



UCL
Université catholique de Louvain
Faculté des Sciences Appliquées

**NUMERICAL STUDY
OF FREE SURFACE
NEWTONIAN AND VISCOELASTIC
FLOWS**

R. Sizaire

Thèse présentée en vue
de l'obtention du grade de
Docteur en Sciences Appliquées

Promoteur:
Dr. V. Legat

Janvier 1998

THIS PAGE IS INTENTIONALLY LEFT BLANK

The most exciting phrase to hear in science, the one that heralds new discoveries, is not “Eureka!” (I found it!) but “That’s funny...”

Isaac Asimov

THIS PAGE IS INTENTIONALLY LEFT BLANK

Acknowledgements

At the end of four years of research, I would like to thank all people that have contributed to the realization of my thesis.

Professor Marcel Crochet initiated my research on encapsulation and was my supervisor during three years. I also thank him for his confidence, and also for providing an excellent environment for research in MEMA.

Next, all my thanks go to my second supervisor, Doctor Vincent Legat. His availability, and the numerous interesting discussions I have got with him, have been for me powerful stimulants during three years.

I also would like to thank Professor Roland Keunings for numerous advises. He gave me the opportunity to take advantage of his experience.

I also thank Professor Paul Van Dooren and Professor Ken Walters for reading the preliminary version of this text. Many improvements were brought to the final version thanks to their comments and suggestions. Finally, I Thank Professor Pierre Wauters to accept to preside the jury of this thesis.

During the four years I have spent in the Euler building, I have met many people. Most of them are more than colleagues for me. I thank them all for the excellent time we had together. My gratitude also goes to Edmond, Guido, Victor, Edward, Michèle and Brigitte for their help and availability.

Finally I want to thank my whist partners who have done so much to improve my skills in playing cards.

THIS PAGE IS INTENTIONALLY LEFT BLANK

To my parents

THIS PAGE IS INTENTIONALLY LEFT BLANK

Preface

Many problems are so complex that it is impossible to study them analytically. For such problems, the use of numerical methods may be an interesting complement to experimental investigations. During the last years, the development of computational software has gained an increasing interest in industry. Indeed, the use of those softwares by engineers may lead to a dramatic reduction of time and cost in the development of new processes.

For example, for many years, the design of a die has been a work in which the intuition of the engineer has played a major role. In many cases however, intuition was not sufficient to design the die, and several attempts had to be done to obtain an acceptable device. But, the construction of a die is an expensive operation, and the lack of trustworthy methods to predict the corresponding extrudate shape has often led to wasted time and money [Leg92]. In the years to come, we may expect an increase in the use of computational software related to the development of powerful and cheap computers.

Besides the development of computer simulation, research is done to better understand the behaviour of complex fluids such as polymer solutions, polymer melts, paints, rubbers,... Those studies are subjects of the science called “rheology”. That science has led to the development of constitutive equations relating stresses to deformations inside the material. But the use of those models often gives rise to numerical difficulties. This is often the case for viscoelastic models. Special numerical techniques have been (and are still being) developed to deal with the computation of such viscoelastic flows.

But the results of rheological science and numerical developments are not sufficient to give a complete solution to most of the problems of polymer processing. Many problems are so complicated that a pragmatic approach must be adopted. For example, the results of experimental observations and analytical modelling may help the engineer to identify the most relevant parameters of the process, and develop a simplified model reproducing most phenomena of interest of the process.

This text is divided in two parts:

- At the beginning of this research, we thought that encapsulation was the result of the development of an interfacial instability. This has led us to investigate the stability of multilayer flows. Chapter 2 is devoted to that study. In particular, we present the results of time-dependent numerical

calculations of interfacial perturbations growing into the nonlinear domain. We show that it is possible to reproduce nonlinear flow regimes observed experimentally like the bamboo waves in core-annular flows. Those results are obtained with transient calculations of two-dimensional Newtonian flows. But three-dimensional transient calculations are needed to reproduce transient development of instabilities towards encapsulation. The computational cost of those calculations is prohibitive. Therefore, we investigate in chapter 3 another possible explanation of the encapsulation: we study the influence of second normal stress difference on the phenomenon. The advantage of that explanation is that it may be checked with time-independent calculations. Finally, our calculated results are compared to experimental observations for a realistic case of coextrusion.

- In chapter 4, we present the results of a numerical study of a filament stretching device. We determine the conditions under which the device produces trustworthy results and we propose an improved estimate of the extensional viscosity. The effects of material parameters and of the initial gap between the plates are investigated too. The calculations of chapter 4 have been done with FENE-CR model. However, some experimental observations cannot be reproduced with the FENE-CR model. In chapter 5, we investigate the influence of the macromolecular structure on the rheological behaviour of polymer solutions in uniaxial extensional flows. We propose a multimode model, and we show that it is suitable to reproduce many experimental results.

Parts I and II are independent. Consequently, we introduce and conclude them separately. In chapter 1, we present the theoretical background necessary to understand the other chapters of the text.

Several results presented in this text have led to publications. Most results given in chapter 4 have been first presented in

- R. Sizaire and V. Legat. Finite element simulation of a filament stretching rheometer. *Journal of Non-Newtonian Fluid Mechanics*, 71:89–107, 1997.

The study of the influence of the macromolecular structure on the behaviour of polymer solutions in extensional flows (chapter 5) will be published in

- R. Sizaire, G. Lielens, I. Jaumain, R. Keunings, and V. Legat. Influence of non-linearity and dispersity on the behaviour of viscoelastic fluids in rheometrical extensional flows. *to be submitted to the Journal of Non-Newtonian Fluid Mechanics*, 1998.

Finally, the results of our investigation of the influence of second normal stress difference on the encapsulation (chapter 3) will be given in

- R. Sizaire and V. Legat. Calculation of 3D encapsulation flows with the finite element method. *to be submitted to the Journal of Rheology*, 1998.

Contents

Acknowledgements	v
Preface	ix
Contents	xi
Glossary	xv
1 Theoretical background	21
1.1 Conservation equations	21
1.1.1 Conservation of mass	21
1.1.2 Conservation of linear momentum	22
1.1.3 Conservation of angular momentum	22
1.1.4 Conservation of energy	22
1.2 Constitutive equations	22
1.2.1 Newtonian fluids	23
1.2.2 Non-Newtonian fluids	23
1.2.3 General principles for constitutive equations	25
1.2.4 Derivation of models from a molecular theory	29
1.2.5 Dimensionless numbers for viscoelastic flows	33
1.3 Spatial discretization for viscoelastic flows	34
1.3.1 Galerkin method	34
1.3.2 Interpolations	35
1.3.3 Stress-splitting formulations	36
1.3.4 Interpolations for 3D calculations	38
1.3.5 Upwinding	38
1.3.6 Stream function	39
1.3.7 Solution of the nonlinear system	39
1.4 Time discretization	40
1.5 Free surfaces	41
1.5.1 Kinematic conditions	41
1.5.2 Surface tension	42
1.5.3 Remeshing techniques	43
1.5.4 Correction for time derivatives	46

I	Numerical calculation of multilayer flows	47
	Introduction	49
2	Stability of multi-layer Newtonian flows	51
2.1	Linear stability of two-layer planar flows	51
2.1.1	Dimensionless numbers	52
2.1.2	Orr-Sommerfeld equations	53
2.1.3	Solution of the eigenvalue problem	55
2.1.4	Stability of two-layer Poiseuille flows	55
2.2	Transient simulations of periodic flows	60
2.2.1	Definition of the problem	60
2.2.2	Validation of the transient calculations	63
2.2.3	Results analysis	68
2.3	Planar coextrusion in a channel	74
2.3.1	Inflow boundary conditions	75
2.3.2	Periodic perturbations in time	76
2.3.3	Perturbation during a small interval of time	79
2.4	Literature review for core-annular flows	81
2.4.1	Dimensionless numbers	82
2.4.2	Linear stability	83
2.4.3	Experimental results	86
2.5	Transient simulations of core-annular flows	88
2.5.1	Definition of the problem	90
2.5.2	Selection of parameters	91
2.5.3	Transient calculations and bamboo waves	91
2.6	Conclusions	96
3	Numerical calculations of encapsulation	99
3.1	Literature review	99
3.2	Encapsulation in channel flow	103
3.2.1	Transient calculation with Reiner-Rivlin model	103
3.2.2	Static calculation of channel flows	105
3.2.3	Interpretation of results	109
3.3	Numerical calculation of a 3D encapsulation	110
3.3.1	Experiments of Han	110
3.3.2	Rheological data	110
3.3.3	Boundary conditions	115
3.3.4	Interpolations	118
3.3.5	The contact line problem	118
3.3.6	Compensation of pressure	121
3.4	Viscoelastic calculations	122
3.4.1	Strategy of resolution	122
3.4.2	Progressive increase of relaxation time	123
3.4.3	Results for an Oldroyd-B calculation	127
3.4.4	Giesekus with a very large Newtonian component	128

3.5	Reiner-Rivlin calculations	130
3.5.1	Strategy of resolution	130
3.5.2	Results for a first set of parameters	131
3.5.3	Results for other values of the flow rate	132
3.5.4	Comparison with experiments	132
3.6	Giesekus and Reiner-Rivlin models	140
3.7	Conclusions	141
	Conclusions	143
II	Numerical calculation of extensional flows	145
	Introduction	147
4	The filament stretching device	149
4.1	Numerical simulation of the stretching device	149
4.2	Numerical Results	153
4.2.1	Material parameters	153
4.2.2	Dimensionless numbers	153
4.2.3	Stretching flow of a viscoelastic fluid	154
4.2.4	Stretching flow of a Newtonian fluid	156
4.2.5	Inertia, capillarity and gravity	158
4.2.6	Improved estimate of the extensional viscosity	162
4.2.7	Comparison with experimental results	164
4.3	Extensibility of the molecules	166
4.4	Conclusions	171
5	Molecular effects in extensional flows	173
5.1	Multimode approach	174
5.1.1	Fractal structure of polymer macromolecules	174
5.1.2	FENE-PM model	175
5.1.3	A “heuristic” multimode model	176
5.2	Identification of a viscous stress	178
5.2.1	Experiments of Orr and Sridhar	178
5.2.2	Relaxation with the multimode FENE-P model	178
5.2.3	Fit of a relaxation curve	181
5.3	Birefringence experiment	184
5.3.1	Birefringence with the multimode model	184
5.3.2	Birefringence in the filament stretching device	185
5.4	Comparison of multimode and FENE	187
5.4.1	Differences between the models	187
5.4.2	New representation of the multimode model	188
5.4.3	Selection of an extensibility distribution	188
5.5	Conclusions	190

	Conclusions	193
III	Appendices	195
A	Numerical methods in Polyflow	197
	A.1 Constraints in Polyflow	197
	A.2 Resolution of the nonlinear system	198
	A.3 Adaptive time stepping algorithm	199
B	More information on multilayer flows	203
	B.1 Base flows	203
	B.1.1 Two layer planar Poiseuille flow	203
	B.1.2 Core-annular flow	204
	B.2 Nonlinear phenomena	205
	B.2.1 Large amplitude perturbations	205
	B.2.2 Unstable higher order harmonics for $n = 8$	207
	B.2.3 The peculiar case $n = \sqrt{m}$	207
C	Contact line problem in Polyflow	211
	C.1 Line dynamic condition with constraints	211
	C.1.1 Dirichlet boundary conditions and contact force	211
	C.1.2 Contact forces and constraints	212
	C.1.3 Implementation of the line dynamic condition	214
D	More information on molecular effects	217
	D.1 Fit with the sum of two exponentials	217
	D.2 Identification of a viscous stress	217
	D.2.1 Transient viscous and elastic stresses	218
	D.3 Origin of the hysteretic behaviour	219
	Bibliography	223

Glossary

In this glossary, we summarize the notations used in this text. We first present the abbreviations, and then the general notations. Unfortunately, notations may vary from chapter to chapter. This is mainly related to the fact that several subjects have been investigated, and we try to use the standard notations in the text. Therefore, some of the notations are introduced or redefined in sections corresponding to the chapters.

Abbreviations

AVSS	adaptive viscous split stress formulation.....	17
BW	bamboo waves.....	68
CAF	core-annular flow.....	68
DBW	disturbed bamboo waves.....	68
DCAF	disturbed core-annular flow.....	68
DEVSS	discrete elastic viscous split stress formulation.....	17
EVSS	elastic viscous split stress formulation.....	17
FENE-CR	Chilcott and Rallison closure of FENE model.....	13
FENE-PM	closure of Wedgewood et al.....	153
FENE-P	Peterlin closure of FENE model.....	13
FENE	finitely extensible nonlinear elastic (dumbbell).....	12
LBB	Ladyzhenskaya, Babuska and Brezzi condition of stability..	15
LDPE	low density polyethylene.....	90
MIX	MIX formulation.....	15
PCJ	Preziosi, Chen and Joseph.....	62
PS	polystyrene.....	90
PTT	Phan-Thien-Tanner model.....	8
SAM	Spiegelberg, Ables and McKinley.....	138
SUPG	streamline upwind Petrov-Galerkin formulation.....	18
SU	streamline upwind formulation.....	18

General notations

A	configuration tensor.....	13
---	---------------------------	----

α_G	one of the parameters of Giesekus model	8
Bo	Bond number	133
Ca	capillary number	133
C_p	heat capacity	2
D/Dt	material derivative	1
De	Deborah number	14
Δt	time step	44
δ	unit tensor	99
:	scalar product of two tensors	2
\mathbf{D}	rate of deformation tensor	3
$\dot{\epsilon}$	extension rate	4
ϵ_{PTT}	one of the parameters of PTT model	8
$\bar{\eta}^+$	transient extensional viscosity	133
η_E	extensional viscosity in regime	4
η_N	Newtonian part of the shear viscosity	7
η	shear viscosity	3
η_V	viscoelastic part of the shear viscosity	7
\mathbf{F}^b	brownian forces on a dumbbell	11
\mathbf{F}^c	connector force between the beads	11
F	Froude number	32
\mathbf{F}^h	hydrodynamic drag forces on a dumbbell	11
4×4	4×4 element of Marchal and Crochet	16
\mathbf{f}	volumic force	2
Γ	boundary of the computational domain Ω	191
$\dot{\gamma}$	velocity gradient	3
γ	surface tension	22
g	magnitude of dimensionless gravity	72
H	stiffness factor for the spring	12
$h(x, t)$	displacement of the interface	24
\mathbf{I}	unit tensor	2
k	Boltzmann constant	11
k_{slip}	slip coefficient	84
k	thermal conductivity	2
λ	relaxation time	6
λ_R	retardation time	7
$\langle B \rangle$	average value of B	11
L^2	extensibility of the dumbbells	13
μ	viscosity	32
$\nabla \cdot$	divergence of a vectorial field	1
∇^2	Laplacian operator	19
$\nabla \cdot$	divergence of a tensorial field	2
∇	gradient of a scalar function	2
n	number of dumbbells per unit of volume	11
N_1	first normal stress difference	4
\mathbf{n}	outward unit normal vector	15
N_2	second normal stress difference	4

ν	kinematic viscosity	62
Ω	computational domain	15
$\partial\Omega$	boundary of the computational domain Ω	15
p	pressure	2
ψ_1	first normal stress coefficient	4
$\psi(\mathbf{R}, t)$	distribution of configuration of dumbbells	11
ψ	stream function	19
ψ_2	second normal stress coefficient	4
\mathbf{q}	energy transported by conduction	2
Q	flow rate	55
\mathbf{R}	configuration vector of a dumbbell	10
R_e	characteristic dumbbell length	13
r	energy produced in the fluid	2
ρ	density	1
\Re	real value of a complex number	52
R	Reynolds number	13
R_0	maximum length of a nonlinear dumbbell	12
s	curvilinear coordinate	15
$\boldsymbol{\sigma}$	Cauchy stress tensor	2
$\overset{\square}{\mathbf{T}}$	linear combination of $\overset{\nabla}{\mathbf{T}}$ and $\overset{\Delta}{\mathbf{T}}$	7
\mathbf{t}	contact force along the boundary	15
\mathbf{T}	extra-stress tensor	2
θ	parameter controlling the implicit character of θ methods	20
\mathbf{T}_N	Newtonian part of the extra-stress tensor	7
$\overset{\nabla}{\mathbf{T}}$	upper-convected derivative of \mathbf{T}	6
$\overset{\Delta}{\mathbf{T}}$	lower-convected derivative of \mathbf{T}	6
tr	trace of a tensor	164
Tr	Trouton ratio	133
T_{shear}	shear stress in rheometrical flow	106
T	temperature	2
t	time	1
\mathbf{T}^T	transposition of tensor \mathbf{T}	2
\mathbf{T}_V	viscoelastic part of the extra-stress tensor	7
U	internal energy	2
u, v, w	components of velocity field	3
\mathbf{v}	velocity field	1
We	Weissenberg number	14
\mathbf{x}	coordinate field	1
ξ	weighting coefficient for the linear combination $\overset{\square}{\mathbf{T}}$	7
x, y, z	components of coordinate field	3
ζ	friction factor on beads	11
ζ_l	parameter controlling the line kinematic condition	22

Stability of multilayer Newtonian flows

A	amplitude of the perturbation.....	46
A_{init}	initial amplitude of the perturbation.....	43
αc_i	growth rate of the perturbation.....	33
α	wavenumber of the perturbation.....	33
A_p	amplitude of harmonic p	46
a	radius ratio.....	62
B	amplitude of the perturbation on flow rates.....	55
c	eigenvalue of the problem.....	33
$\chi(y)$	eigenfunction in Orr-Sommerfeld equations (lower layer) ...	34
$\Delta t_{\text{perturb}}$	duration of perturbation on the flow rates.....	55
f_n	pushing force on the inlet section.....	42
\mathbf{G}	dimensionless gravity.....	32
\mathbf{g}	gravity.....	32
H	height of the mesh for axisymmetric calculations.....	70
h	hold-up ratio.....	71
J^*	dimensionless surface tension of Preziosi, Chen and Joseph.....	62
L	length of the computational domain.....	40
m	viscosity ratio.....	32
n	thickness ratio.....	32
ω	frequency of the perturbation on the flow rates.....	55
$\phi(y)$	eigenfunction in Orr-Sommerfeld equations (upper layer) ...	33
S	dimensionless surface tension.....	32, 63
$\hat{u}, \hat{v}, \hat{p}$	perturbed quantities on u, v and p	33
u', v', p'	perturbations on u, v and p	33
V_o	superficial velocities of oil.....	68
V_w	superficial velocities of water.....	68
ζ	density ratio.....	32

Numerical calculations of encapsulation

δ_{II}	projection tensor onto the local tangent plane.....	99
\mathbf{F}_l	contact force along the contact line.....	100
F_r	radial component of the contact force.....	100
\mathbf{F}_t	tangential component of the contact force.....	99
κ	parameter of the Bird-Carreau law for ψ_2	94
λ_{N}	parameter of the Bird-Carreau viscosity law.....	92
m	power law index for ψ_2	94
n	power-law index for the Bird-Carreau viscosity law.....	92
\mathbf{r}	radial vector.....	100
u_n	normal component of the velocity.....	99
u_t	tangential component of the velocity.....	99

The filament stretching device

$\dot{\epsilon}_{\text{pl}}$	“plate” estimate of the strain rate.....	130
$\dot{\epsilon}_{\text{rad}}$	radial estimate of the strain rate.....	142
ϵ_{pl}	“plate” estimate of the Hencky strain.....	130
ϵ_{rad}	radial estimate of the Hencky strain.....	142
$\bar{\eta}_{\text{pl}}^+$	plate estimate of extensional viscosity.....	142
$\bar{\eta}_{\text{rad}}^+$	radial estimate of extensional viscosity.....	143
F	force measured on the lower plate.....	141
L	length of the filament.....	130
L_0	initial length of the filament.....	130
R	minimum radius of the filament.....	130
R_0	initial radius of the sample.....	130
τ	tension in the filament.....	142

Molecular effects in extensional flows

\mathbf{a}_i	new dimensionless configuration tensor.....	168
\mathbf{A}_{max}	configuration tensor of the largest extensibility mode.....	164
Δt_{stop}	time necessary to stop the upper plate.....	160
$\dot{\epsilon}_{\text{up}}$	strain rate during elongation.....	160
$\boldsymbol{\kappa}^\dagger$	transposition of tensor $\boldsymbol{\kappa}$	157
$\boldsymbol{\kappa}$	rate of deformation tensor.....	157
L_2^i	extensibility parameter of mode i	157
L_{max}^2	maximum extensibility parameter.....	157
L_{min}^2	minimum extensibility parameter.....	157
\mathbf{Q}_j	vector connecting two consecutive beads.....	156
Q_0	equilibrium length for the springs in the chain model.....	156
t_{stop}	time at which the upper plate is stopped.....	160
w_e	weighting parameter for the distribution function.....	157

Chapter 1

Theoretical background

The mathematical modelling of flows is described by the theory of continuum mechanics. The governing equations consist of conservation equations and constitutive equations. The equations are derived from the principle of conservation of mass, the principle of balance of linear momentum, and the principle of balance of energy. Constitutive equations are relating the stresses in the fluid to the deformation history.

Whereas conservation equations apply whatever the material studied, the constitutive equations depend from the material. In the section devoted to constitutive equations, we introduce the generalized Newtonian model, and the differential viscoelastic models.

The conservation and constitutive equations are used to calculate flows in complex geometries. For such problems, it is generally not possible to calculate an analytical solution of the governing equations. We use finite elements to solve that kind of problems. The principles of the finite elements, and their application to the calculation of viscoelastic flows is shortly presented. We also describe how solutions on moving domains are calculated.

Of course this chapter is mainly a literature overview. Most information presented here has been found in [Mac94, CAD⁺95a, Pur96, BHAC77, BCAH87, Lar88, Bod94, Leg92, War96]. The preceding list is not exhaustive.

1.1 Conservation equations

1.1.1 Conservation of mass

Let $\rho(\mathbf{x}, t)$, $\mathbf{v}(\mathbf{x}, t)$ be respectively the volumic mass and the velocity defined at a material point of coordinates \mathbf{x} and at time t . The principle of conservation of mass is expressed as

$$\frac{D\rho}{Dt} + \rho \nabla \cdot \mathbf{v} = 0,$$

where D/Dt denotes the material derivative and $\nabla \cdot$ is the divergence. Usually, most liquids may be considered as incompressible. This equation is usually called

“continuity equation”. If the fluid is incompressible, the density is a constant, and the continuity equation reduces to

$$\nabla \cdot \mathbf{v} = 0. \quad (1.1)$$

1.1.2 Conservation of linear momentum

The equation of motion arises from the principle of balance of linear momentum. It is written as

$$\rho \frac{D\mathbf{v}}{Dt} = \nabla \cdot \boldsymbol{\sigma} + \mathbf{f}, \quad (1.2)$$

in which \mathbf{f} is the resultant of volumetric forces, and $\boldsymbol{\sigma}(\mathbf{x}, t)$ is the Cauchy stress tensor.

1.1.3 Conservation of angular momentum

The balance of angular momentum requires the Cauchy stress tensor to be symmetric:

$$\boldsymbol{\sigma} = \boldsymbol{\sigma}^T. \quad (1.3)$$

1.1.4 Conservation of energy

The energy equation balances the internal energy of the fluid U , the viscous dissipation $\boldsymbol{\sigma} : \nabla \mathbf{v}$, the energy produced in the fluid r (for example by a chemical reaction), and the energy transported by conduction \mathbf{q} :

$$\rho \frac{DU}{Dt} = \boldsymbol{\sigma} : \nabla \mathbf{v} + r - \nabla \cdot \mathbf{q}. \quad (1.4)$$

If we only consider the thermal energy (i.e. the energy corresponding to the temperature of the fluid), and assuming that the conduction satisfies the Fourier law $\mathbf{q} = -k\nabla T$, equation (1.4) becomes

$$\rho C_p \frac{DT}{Dt} = \nabla \cdot (k\nabla T) + \boldsymbol{\sigma} : \nabla \mathbf{v} + r. \quad (1.5)$$

In equation (1.5), we have introduced the temperature T , the heat capacity C_p , and the thermal conductivity k .

1.2 Constitutive equations

The Cauchy stress tensor may be separated into two contributions:

$$\boldsymbol{\sigma} = -p\mathbf{I} + \mathbf{T},$$

in which p is the pressure, \mathbf{I} is the unit tensor and \mathbf{T} is the extra-stress tensor.

The conservation equations presented in section 1.1 are not sufficient to determine the unknowns corresponding to the flow. Constitutive equations are introduced to relate the history of a material point to its extra-stress tensor \mathbf{T} .

1.2.1 Newtonian fluids

For an incompressible Newtonian viscous fluid, the extra-stress tensor is given by

$$\mathbf{T} = 2\eta\mathbf{D}, \quad (1.6)$$

in which η is the constant shear viscosity, and \mathbf{D} is the rate of deformation tensor

$$\mathbf{D} = \frac{\nabla\mathbf{v} + \nabla\mathbf{v}^T}{2}.$$

Most small molecule liquids such as water, oil, gases obey the constitutive law (1.6). But other liquids have a more complex behaviour. The study of those liquids is the subject of the science called “rheology”.

1.2.2 Non-Newtonian fluids

The peculiar properties of non-Newtonian fluids may be observed in rheometrical flows. We present here the main non-Newtonian effects in steady simple shear flow, and in uniaxial extensional flow.

In order to simplify the following expressions, we introduce here the notations for the components of velocity and coordinate fields: $\mathbf{v} = (u, v, w)^T$, $\mathbf{x} = (x, y, z)^T$.

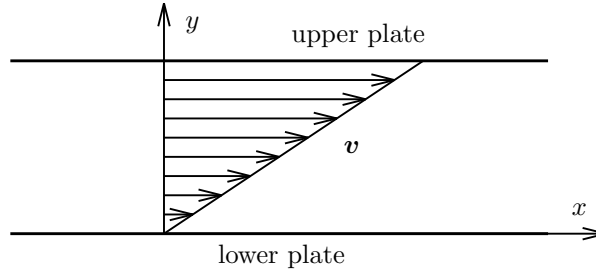


Figure 1.1: *Steady Couette flow.*

In steady simple shear flow (Figure 1.1), the velocity components are given by

$$u = \dot{\gamma}y, \quad v = w = 0, \quad (1.7)$$

in which $\dot{\gamma}$ is the constant velocity gradient. The shear rate $\dot{\gamma}$ may also be defined for complex flows. It is related to the second invariant $\mathbf{D} : \mathbf{D}$ of the rate of deformation tensor \mathbf{D} by

$$\dot{\gamma} = \sqrt{2\mathbf{D} : \mathbf{D}}.$$

Replacing the velocity field (1.7) in the constitutive relation (1.6), we find a Cauchy stress tensor, the components of which satisfy the relations

$$\sigma_{xy} = \eta\dot{\gamma}, \quad \sigma_{xx} - \sigma_{yy} = 0, \quad \sigma_{yy} - \sigma_{zz} = 0. \quad (1.8)$$

In the case of non-Newtonian fluids, the measurements will give other results:

$$\sigma_{xy} = \eta(\dot{\gamma})\dot{\gamma}, \quad \sigma_{xx} - \sigma_{yy} = N_1(\dot{\gamma}), \quad \sigma_{yy} - \sigma_{zz} = N_2(\dot{\gamma}). \quad (1.9)$$

Three differences arise from the comparison of the Newtonian predictions (1.8) and the non-Newtonian observations (1.9):

- The measured shear viscosity $\eta(\dot{\gamma})$ depends on the shear rate $\dot{\gamma}$. Usually $\eta(\dot{\gamma})$ is a monotonically decreasing function of the shear rate, and the behaviour of the fluid is said to be “shear-thinning”. However, in some few cases, the viscosity increases with the shear rate, and the fluid is “shear thickening”.
- The first normal stress difference $N_1(\dot{\gamma})$ is positive for polymeric liquids. The first normal stress difference gives rise to the most typical demonstrations of non-Newtonian behaviours, such as the rod-climbing (or Weissenberg) effect, and the very large extrudate swelling at the exit of a die.
- The second normal stress difference $N_2(\dot{\gamma})$ is negative. That quantity is difficult to measure for it is very small. (Approximately an order of magnitude smaller than the first normal stress difference.)

For small values of the shear rate, the first normal stress difference is proportional to $\dot{\gamma}^2$. This is the reason why, in the literature, the normal stress coefficients $\psi_1(\dot{\gamma})$ and $\psi_2(\dot{\gamma})$ are often used instead of $N_1(\dot{\gamma})$ and $N_2(\dot{\gamma})$ to characterize the normal stress differences. The normal stress coefficients are related to the normal stress differences by

$$N_1(\dot{\gamma}) = \psi_1(\dot{\gamma})\dot{\gamma}^2, \quad N_2(\dot{\gamma}) = \psi_2(\dot{\gamma})\dot{\gamma}^2.$$

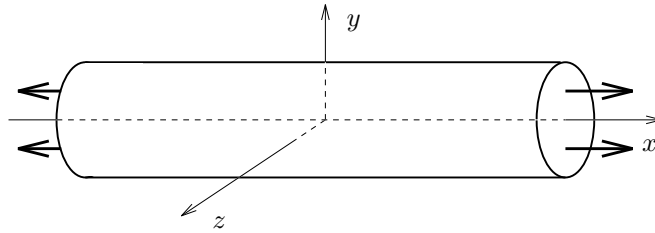


Figure 1.2: *Steady uniaxial extensional flow.*

In steady uniaxial extensional flow (Figure 1.2), the components of the velocity field may be written

$$u = \dot{\epsilon}x, \quad v = -\frac{\dot{\epsilon}}{2}y, \quad w = -\frac{\dot{\epsilon}}{2}z,$$

where $\dot{\epsilon}$ is the constant elongational rate. The non-vanishing stresses may be written

$$\sigma_{xx} - \sigma_{yy} = \sigma_{xx} - \sigma_{zz} = \eta_E(\dot{\epsilon})\dot{\epsilon},$$

in which we have introduced $\eta_E(\dot{\epsilon})$ the extensional viscosity.

For Newtonian fluids, Trouton demonstrated that $\eta_E(\dot{\epsilon})$ is a constant equal to thrice the shear viscosity [Tro06]. For non-Newtonian fluids η_E is a function of the extension rate $\dot{\epsilon}$. The qualitative behaviour of the extensional viscosity is often dramatically different from the behaviour of the shear viscosity. For example, the extensional viscosity of highly elastic polymeric fluids usually exhibits a very large increase with the extension rate while the shear viscosity decreases with the shear rate.

Another difference with Newtonian fluids is the “memory” of some non-Newtonian fluids; because of their memory, such fluids behave like elastic materials when submitted to rapid deformations, and more like Newtonian fluids for slow deformations. Such fluids are called “viscoelastic”.

A common way to measure the viscoelasticity is by stress relaxation. When a polymeric liquid is submitted to a step increase in strain, the stress also increases in a step, and then decreases exponentially [Mac94]. This behaviour is often represented as a series combination of springs (elastic elements) and dashpots (viscous elements) as represented in Figure 1.3.

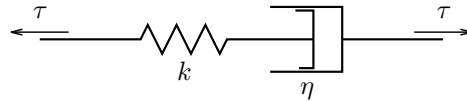


Figure 1.3: *Spring and dashpot representation of a viscoelastic fluid.*

1.2.3 General principles for constitutive equations

The search for constitutive equations describing rheologically complex fluids is the purpose of theoretical rheology. The constitutive equations must satisfy four admissibility conditions:

- The *principle of determinism of stress* states that the stress in a non-Newtonian body is determined by the history of the motion of that body [TN65].
- The *principle of local action* states that the stress at a material point is determined by the history of the deformation of an arbitrarily small neighbourhood around that material point [TN65].
- The *principle of coordinates invariance* states that the constitutive equation must be independent of the frame of reference used to describe them. Expressing the equations in consistent tensorial form will ensure that this principle is automatically satisfied.
- According to the *principle of invariance under superposed rigid body motion*, the rheological equations must have a significance which is independent of absolute motion in space [Old50]. If the equation is correct, any

superimposed rigid body motion cannot affect the basic response of the material.

Although there exists a plethora of constitutive equations in the literature, we will only mention a few ones

Maxwell models

The one-dimensional linear equation of Maxwell is obtained by putting an Hookean spring of constant k and a Newtonian dashpot of viscosity η in series (Figure 1.3). By noting $\dot{\gamma}$ the strain rate of the series, τ will satisfy the differential equation

$$\tau + \lambda\dot{\tau} = \eta\dot{\gamma}, \quad (1.10)$$

with $\lambda = \eta/k$ a relaxation time.

The generalisation of relation (1.10) has to satisfy the principle of objectivity. This leads respectively to the “upper-convected” and “lower-convected” Maxwell models, given respectively by

$$\mathbf{T} + \lambda \overset{\nabla}{\mathbf{T}} = 2\eta\mathbf{D}, \quad (1.11)$$

and

$$\mathbf{T} + \lambda \overset{\Delta}{\mathbf{T}} = 2\eta\mathbf{D}. \quad (1.12)$$

In equations (1.11) and (1.12), the symbols ∇ and Δ stand respectively for the upper-convected and lower-convected derivatives defined by

$$\overset{\nabla}{\mathbf{T}} = \frac{D\mathbf{T}}{Dt} - \mathbf{L} \cdot \mathbf{T} - \mathbf{T} \cdot \mathbf{L}^T, \quad (1.13)$$

$$\overset{\Delta}{\mathbf{T}} = \frac{D\mathbf{T}}{Dt} + \mathbf{T} \cdot \mathbf{L} + \mathbf{L} \cdot \mathbf{T}^T. \quad (1.14)$$

The upper-convected and lower-convected Maxwell models are also called respectively “Maxwell-B” and “Maxwell A”.

Both Maxwell-A and Maxwell-B have a constant shear viscosity η , and a first normal stress difference quadratic in $\dot{\gamma}$: $N_1(\dot{\gamma}) = 2\eta\lambda\dot{\gamma}^2$. The Maxwell-B model predicts $N_2 = 0$, but for the Maxwell-A model, we have $N_2 = -N_1$. This value of second normal stress difference is much larger than what is experimentally observed. Therefore, the Maxwell-A model is generally not considered. The steady state extensional viscosity of Maxwell-B fluid is

$$\eta_E(\dot{\epsilon}) = \frac{2\eta}{1 - 2\lambda\dot{\epsilon}} + \frac{\eta}{1 + \lambda\dot{\epsilon}}. \quad (1.15)$$

With this formula, an infinite value of the extensional viscosity is obtained for $\dot{\epsilon} = 1/2\lambda$. For higher values of $\dot{\epsilon}$, the expression of the extensional viscosity is meaningless. Indeed, for $\dot{\epsilon} > 1/2\lambda$ it is not possible to reach the steady state value (1.15) by a transient calculation starting from vanishing initial stresses because extensional stress grows towards infinity.

Oldroyd-B model

In order to model the behaviour of a polymer solution in a Newtonian solvent, the extra-stress tensor \mathbf{T} is often split in two components: a viscoelastic one \mathbf{T}_V , and a purely viscous one \mathbf{T}_N . The components \mathbf{T}_V and \mathbf{T}_N satisfy respectively the relations

$$\begin{aligned}\mathbf{T}_V + \lambda \overset{\nabla}{\mathbf{T}}_V &= 2\eta_V \mathbf{D}, \\ \mathbf{T}_N &= 2\eta_N \mathbf{D}.\end{aligned}$$

The constitutive equation of the Oldroyd-B model may also be written

$$\mathbf{T} + \lambda \overset{\nabla}{\mathbf{T}} = 2\eta \left(\mathbf{D} + \lambda_R \overset{\nabla}{\mathbf{D}} \right), \quad (1.16)$$

in which $\eta = \eta_V + \eta_N$ is the constant shear viscosity and $\lambda_R = \eta_N \lambda / \eta$ is a retardation time. The normal stress differences of the Oldroyd-B model are $N_1(\dot{\gamma}) = 2\eta_V \lambda \dot{\gamma}^2$ and $N_2 = 0$. The steady extensional viscosity is given by

$$\eta_E(\dot{\epsilon}) = \frac{2\eta_V}{1 - 2\lambda\dot{\epsilon}} + \frac{\eta_V}{1 + \lambda\dot{\epsilon}} + 3\eta_N.$$

Johnson-Segalman model

The second normal stress difference may be related to the presence of a lower convected derivative in the constitutive equations. The Johnson-Segalman model is defined by the constitutive equation

$$\mathbf{T} + \lambda \overset{\square}{\mathbf{T}} = 2\eta_0 \mathbf{D}, \quad (1.17)$$

in which $\overset{\square}{\mathbf{T}}$ is a convex combination of the upper and lower convected derivatives:

$$\overset{\square}{\mathbf{T}} = \left(1 - \frac{\xi}{2} \right) \overset{\nabla}{\mathbf{T}} + \frac{\xi}{2} \overset{\triangle}{\mathbf{T}},$$

ξ being a scalar parameter ($0 \leq \xi \leq 2$).

The Johnson-Segalman model predicts shear-thinning viscosity, first and second normal stress differences:

$$\begin{aligned}\eta(\dot{\gamma}) &= \frac{\eta_0}{1 + \xi(2 - \xi)\lambda^2 \dot{\gamma}^2}, \\ \psi_1(\dot{\gamma}) &= \frac{2\lambda\eta_0}{1 + \xi(2 - \xi)\lambda^2 \dot{\gamma}^2}, \\ \psi_2(\dot{\gamma}) &= \frac{-\xi\lambda\eta_0}{1 + \xi(2 - \xi)\lambda^2 \dot{\gamma}^2}.\end{aligned}$$

For this model, $N_2/N_1 = -\xi/2$. The value $\xi = 0.2$, gives a ratio $N_2/N_1 = -0.1$ corresponding to what is experimentally observed. The steady extensional viscosity exhibited by the Johnson-Segalman model is equal to that of the Maxwell-B model. The shear viscosity tends towards zero when the shear rate tends towards infinity. This problem may be avoided by adding a purely viscous component to the extra-stress tensor.

Phan-Thien-Tanner model

The extensional viscosity of the Johnson-Segalman model tends towards infinity when the extension rate tends towards $1/2\lambda$. The constitutive equation (1.17) may be modified to avoid that problem:

$$\exp\left(\frac{\epsilon_{\text{PTT}}\lambda}{\eta_0}\right) \mathbf{T} + \lambda \overset{\square}{\mathbf{T}} = 2\eta_0 \mathbf{D}. \quad (1.18)$$

Here again, a purely viscous component may be added to the extra-stress tensor. In general, no analytical expression may be found for the viscosities and normal stress differences with the PTT model.

Giesekus model

The constitutive equation defining the Giesekus model is given by

$$\mathbf{T} + \lambda \overset{\nabla}{\mathbf{T}} + \frac{\alpha_G \lambda}{\eta_V} \mathbf{T} \cdot \mathbf{T} = 2\eta_V \mathbf{D}. \quad (1.19)$$

This model exhibits both first and second normal stress differences. With this model, one obtains excellent fits in shear flows, but the extensional behaviour is not very good.

Criminale-Ericksen-Filbey model

The Criminale-Ericksen-Filbey model is a generalisation of the second-order fluid [BHAC77, Lar88]:

$$\mathbf{T} = 2\eta_0 \mathbf{D} - \psi_{10} \overset{\nabla}{\mathbf{D}} + 4\psi_{20} \mathbf{D} \cdot \mathbf{D}. \quad (1.20)$$

The generalisation is obtained by replacing the constants η_0 , $\psi_{1,0}$ and $\psi_{2,0}$ by functions of the shear rate $\dot{\gamma}$:

$$\mathbf{T} = 2\eta(\dot{\gamma}) \mathbf{D} - \psi_1(\dot{\gamma}) \overset{\nabla}{\mathbf{D}} + 4\psi_2(\dot{\gamma}) \mathbf{D} \cdot \mathbf{D}. \quad (1.21)$$

The Criminale-Ericksen-Filbey model is not a viscoelastic model, for the model exhibits no memory effect: the extra-stress tensor \mathbf{T} at a given time only depends on the velocity field at the same time. The model cannot be expected to predict time-dependent phenomena.

Reiner-Rivlin model

The Criminale-Ericksen-Filbey model may be simplified by neglecting ψ_1 in (1.21). This leads to the Reiner-Rivlin model:

$$\mathbf{T} = 2\eta(\dot{\gamma}) \mathbf{D}(\mathbf{v}) + 4\psi_2(\dot{\gamma}) \mathbf{D}(\mathbf{v}) \cdot \mathbf{D}(\mathbf{v}). \quad (1.22)$$

This model may be easier to use for numerical calculations: equation (1.22) only involves first order spatial derivatives of the velocity field. This allows us to substitute \mathbf{T} in the momentum equations with the right member of (1.22). With such a substitution, the weak form of the momentum equation only involves first order spatial derivatives of the velocity field.

As a comparison, the extra-stress tensor of the Criminale-Ericksen-Filbey model, though exhibiting no memory effects, involves second order spatial derivatives of \mathbf{v} because of the upper-convected derivative of \mathbf{D} . Therefore, to calculate a complex flow with the finite element method with such a model, an extra field \mathbf{D} must be added to the variables of the model.

1.2.4 Derivation of models from a molecular theory

Several reasons justify the molecular approach. First, the rheological properties of polymer solutions and polymer melts depend on the molecular architecture of the constituent molecules (molecular weight, molecular weight distribution, chain stiffness). Second, solute-solvent interactions can play a role in the motion of the polymers and affect their macroscopic behaviour. Third, in the neighbourhood of fluid-solid interface, the motion of the polymer molecules is restricted, with the result that wall slip can arise. Finally, useful relationships can be derived between the rheological properties and other physico-chemical properties, such as the diffusional, optical and electrical properties.

The theories deal either with dilute solutions or with concentrated solutions and molten polymers. In dilute solutions theories, each particle interacts only with the solvent and not with the other suspended particles, while in the concentrated fluid theories there are particle-particle interactions, which may form molecular entanglements.

This section is mainly inspired from Bird et al. [BHAC77], and from the thesis of Bruno Purnode [Pur96]. We first present the Rouse chain and dumbbells molecular models. Then we introduce the kinetic theory for elastic dumbbells. In particular, we develop the macroscopic model corresponding to Hookean dumbbells, and to finitely extensible dumbbells. We will not discuss the network and reptation theories for concentrated solutions and polymer melts.

Let us remark that all constitutive models may be derived from molecular theories. Thus the models presented in section 1.2.3 may also be justified by molecular arguments, and actually, some of them have been derived from a molecular theory. The only purpose of this section is to show how a macroscopic constitutive equation may be derived from a kinetic theory.

Molecular models

Following the theory of Rouse [Rou53], polymer coil can be thought of as a series of spherical beads equally spaced and connected one to the next by springs. Each spring models the elastic forces generated by a portion of the polymer macromolecule called a submolecule (Figure 1.4). The polymer solution is sufficiently dilute to allow us to make the assumption that each molecule is isolated

from the others.

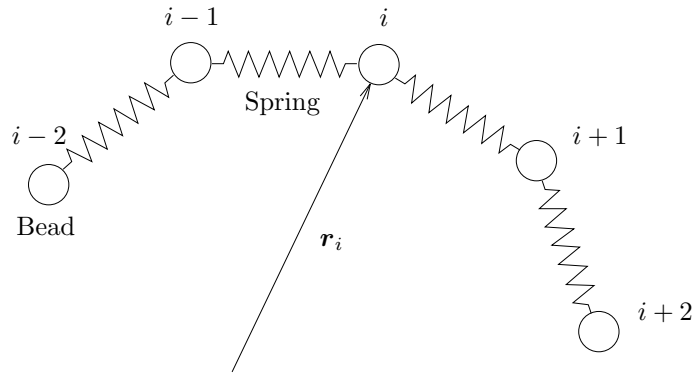


Figure 1.4: *The Rouse bead and spring model for a polymer macromolecule.*

We will here only treat the case of two beads joined by a non-bendable spring: the elastic dumbbell (Figure 1.5). The reason is that the dumbbell theory qualitatively reproduces most features of the Rouse theory. The beads of masses m are labeled with “1” and “2”. Their instantaneous location in space are called \mathbf{r}_1 and \mathbf{r}_2 . The configuration vector $\mathbf{R} = \mathbf{r}_2 - \mathbf{r}_1$ specifies the instantaneous distance between the beads centers and the angular orientation of the dumbbells in space. There are n dumbbells per unit volume suspended in a Newtonian solvent of viscosity η_N .

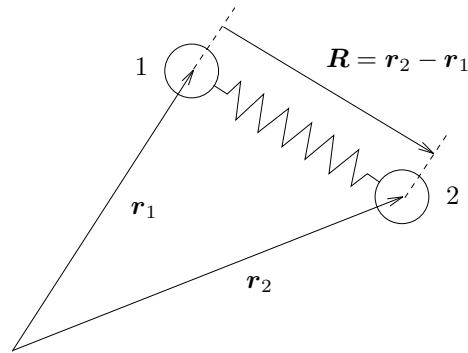


Figure 1.5: *Elastic dumbbell composed of two beads connected by an elastic spring.*

Kinetic theory for dumbbells

The purpose of this section is to show how macroscopic constitutive equations may be derived from a molecular theory. Thus, we do not present the theory and results of stochastic calculations.

In order to derive a macroscopic model, a distribution function $\psi(\mathbf{R}, t)$ is defined. This function gives the probability to find a dumbbell at a given configuration \mathbf{R} and for a given time t . The conservation equation for the dumbbells may be written as a function of the distribution function ψ :

$$\frac{\partial \psi}{\partial t} + \frac{\partial}{\partial \mathbf{R}} \cdot (\psi \dot{\mathbf{R}}) = 0.$$

Taking into account the hydrodynamic drag forces \mathbf{F}^h , the brownian forces \mathbf{F}^b and the connector force \mathbf{F}^c in the spring, an equation of change may be written for the average $\langle \mathbf{R}\mathbf{R} \rangle$:

$$\langle \overset{\nabla}{\mathbf{R}\mathbf{R}} \rangle + \frac{4}{\zeta} \langle \mathbf{R}\mathbf{F}^c \rangle = \frac{4kT}{\zeta} \mathbf{I},$$

in which we have introduced the notation

$$\langle B \rangle = \int B(\mathbf{R})\psi(\mathbf{R}, t)d\mathbf{R},$$

$B(\mathbf{R})$ being a dynamical property depending on \mathbf{R} , k the Boltzmann constant, n the number of dumbbells per unit of volume and T the temperature. ζ is a friction factor relating the hydrodynamic drag force on a bead to the relative velocity of the bead and the solvent:

$$\mathbf{F}^h = \zeta(\mathbf{v} - \dot{\mathbf{r}}).$$

The dumbbells contribute to the momentum equation by the force of their connector spring, and by the amount of momentum they carry with them. This results in a contribution to the extra-stress tensor given by

$$\mathbf{T}_V = n \langle \mathbf{R}\mathbf{F}^c \rangle - nkT\mathbf{I}. \quad (1.23)$$

The last expression is usually called the Kramers expression for the extra-stress tensor [Kra44].

We will introduce the notations R for the end-to-end distance of the vector \mathbf{R} , and F such that

$$\mathbf{F}^c = F(R)\mathbf{R}.$$

With these new notations, the evolution equation for the dumbbells and the expression of the extra-stress tensor are given by

$$\langle \overset{\nabla}{\mathbf{R}\mathbf{R}} \rangle + \frac{4}{\zeta} \langle F(R)\mathbf{R}\mathbf{R} \rangle = \frac{4kT}{\zeta} \mathbf{I}, \quad (1.24)$$

$$\mathbf{T}_V = n \langle F(R)\mathbf{R}\mathbf{R} \rangle - nkT\mathbf{I}. \quad (1.25)$$

Up to this point, the theory has been developed for dumbbells with any kind of elastic connector. Now we will characterize the connector force law. Although a great number of spring types can be used, we will only consider the Hookean and the Warner force laws.

Hookean dumbbells

Let us first assume that the spring is Hookean, i.e. that the tension in the spring is directly proportional to the separation of the beads:

$$F(R) = H.$$

Then, the Kramers expression for the stress tensor (1.23) gives:

$$\mathbf{T}_V = nH \langle \mathbf{RR} \rangle - nkT\mathbf{I},$$

whereas the evolution equation for $\langle \mathbf{RR} \rangle$ is given by:

$$\langle \overset{\nabla}{\mathbf{RR}} \rangle + \frac{4H}{\zeta} \langle \mathbf{RR} \rangle = \frac{4kT}{\zeta} \mathbf{I}.$$

Eliminating $\langle \mathbf{RR} \rangle$ from those equations leads to the following rheological equation of state:

$$\mathbf{T}_V + \frac{\zeta}{4H} \overset{\nabla}{\mathbf{T}}_V = \frac{n\zeta kT}{2H} \mathbf{D},$$

As one defines the characteristic time constant $\lambda = \zeta/4H$ and $\eta_V = n\zeta kT/4H$, this model is the well-known Maxwell-B fluid. By adding a purely viscous component to the constitutive equation, one obtains the Oldroyd-B model.

Fene dumbbells

Let us now consider the Warner force law that avoids the unphysical feature of infinitely extending dumbbells:

$$F(R) = \frac{H}{1 - R^2/R_0^2}.$$

A spring with this force law will be linear for small extensions, but will get ever stiffer as the spring is extended. Furthermore, the spring cannot be extended beyond a separation R_0 . This dumbbell with limited extension is also called *Finitely Extensible Nonlinear Elastic* (FENE) dumbbell. Replacing the Warner force law in the evolution equation and the Kramers expression gives:

$$\langle \overset{\nabla}{\mathbf{RR}} \rangle + \frac{4H}{\zeta} \left\langle \frac{1}{1 - R^2/R_0^2} \mathbf{RR} \right\rangle = \frac{4kT}{\zeta} \mathbf{I}, \quad (1.26)$$

$$\mathbf{T}_V = nH \left\langle \frac{1}{1 - R^2/R_0^2} \mathbf{RR} \right\rangle - nkT\mathbf{I}. \quad (1.27)$$

It is not possible to eliminate the average values, as it was done for the case of Hookean dumbbells. However, replacing the average of the ratio by the ratio of the averages as suggested by Peterlin [Pet66]:

$$\left\langle \frac{H}{1 - R^2/R_0^2} \mathbf{RR} \right\rangle = \frac{H}{1 - \langle R^2/R_0^2 \rangle} \langle \mathbf{RR} \rangle,$$

leads to a tractable rheological equation of state. Indeed, defining a non-dimensional configuration tensor \mathbf{A} and a characteristic dumbbell length R_e as follows:

$$\mathbf{A} = \frac{3 \langle \mathbf{R}\mathbf{R} \rangle}{R_e^2},$$

$$R_e^2 = \frac{3kT}{F(R_e)},$$

and replacing in the equations 1.26 and 1.27 we obtain the following governing equations for fields \mathbf{A} and \mathbf{T}_V :

$$\mathbf{A} + \lambda(1 - \text{tr}\mathbf{A}/L^2)\overset{\nabla}{\mathbf{A}} = \frac{1 - \text{tr}\mathbf{A}/L^2}{1 - 3/L^2}\mathbf{I}, \quad (1.28)$$

$$\mathbf{T}_V = \frac{\eta_V}{\lambda} \left(\frac{1}{1 - \text{tr}\mathbf{A}/L^2}\mathbf{A} - \frac{1}{1 - 3/L^2}\mathbf{I} \right), \quad (1.29)$$

where $L^2 = 3R_0^2/R_e^2$ is a measure of the extensibility of the dumbbells, λ is the relaxation time, and η_V is the viscoelastic part of viscosity. The relaxation time and the zero-shear viscosity are defined by:

$$\lambda = \frac{\zeta}{4H}, \quad \eta_V = \frac{n\zeta kT}{4H}(1 - 3/L^2).$$

This fluid is called the FENE-P model [BDJ80]. This formulation, based on the configuration tensor, is known to offer stable numerical properties [AH94]. The fluid exhibits shear thinning behaviour, and for high shear rates, η is proportional to $\dot{\gamma}^{-2/3}$. At high shear rates, the first normal stress difference scales as $\dot{\gamma}^{2/3}$. The second normal stress N_2 is vanishing. In extensional flow, the model also exhibits an extensional thickening behaviour, and reaches a plateau at high extension rates.

Chilcott and Rallison [CR88] proposed some further modifications in the evolution for \mathbf{A} in order to obtain a fluid with a constant viscosity in steady shear flow:

$$\mathbf{A} + \lambda(1 - \text{tr}\mathbf{A}/L^2)\overset{\nabla}{\mathbf{A}} = \mathbf{I}. \quad (1.30)$$

The equation giving the extra-stress tensor is identical to (1.29). Equations (1.29) and (1.30) define the FENE Chilcott-Rallison model (FENE-CR). This model shows a first normal stress difference that changes from quadratic to linear behaviour as shear rate increases.

1.2.5 Dimensionless numbers for viscoelastic flows

Dimensionless numbers are generally used to characterize fluid mechanics problems. For example, the Reynolds number defined by

$$Re = \frac{\rho VL}{\eta}$$

in which V and L are characteristic velocity and length of the problem respectively. \mathcal{R} characterizes the importance of inertia forces with respect to viscous forces. It may be used to characterize both Newtonian and non-Newtonian flows.

The viscoelasticity of a flow may be characterized by the Weissenberg number, We . It is defined as

$$We = \frac{\lambda V}{L},$$

in which λ is a characteristic relaxation time. It may be interpreted as a ratio of normal stresses and shear stress.

For transient flow, The Deborah number De is often used. It is defined as the ratio of a characteristic time λ of the fluid and a characteristic time of the flow t_c :

$$De = \frac{\lambda}{t_c}.$$

1.3 Spatial discretization for viscoelastic flows

1.3.1 Galerkin method

In this section, we wish to describe the numerical problem of the simulation of viscoelastic fluids. For convenience, we will limit ourselves to the steady flow of a Maxwell fluid in a differential form, and to the finite element formulation. The strong formulation of the system of partial differential equations is then given by

$$\begin{aligned} \mathbf{T} + \lambda \nabla \mathbf{T} &= 2\eta_V \mathbf{D}(\mathbf{v}), \\ -\nabla \cdot p + \nabla \cdot \mathbf{T} + \mathbf{f} &= \mathbf{0}, \\ \nabla \cdot \mathbf{v} &= 0. \end{aligned}$$

We assume that the flow domain is discretized by means of a mesh of finite elements and we approximate the viscoelastic stresses, the velocity and the pressure by means of the finite expansions

$$\begin{aligned} \mathbf{T}^h &= \sum_{i=1}^{N_T} \mathbf{T}_i \phi_i, \\ \mathbf{v}^h &= \sum_{j=1}^{N_v} \mathbf{v}_j \psi_j, \\ p^h &= \sum_{k=1}^{N_p} p_k \pi_k, \end{aligned}$$

in which ϕ_i , ψ_j and π_k are the shape functions and \mathbf{T}_i , \mathbf{v}_j and p_k are the unknown nodal values.

In order to calculate the nodal variables, the classical Galerkin procedure imposes that the governing equations are orthogonal to the set of shape functions. Finally, an integration by parts in the momentum equations is used to yield the discrete problem:

$$\begin{aligned} \int_{\Omega} \phi_i \left(\mathbf{T}^h + \lambda \nabla \mathbf{T}^h - 2\eta_V \mathbf{D}(\mathbf{v}^h) \right) d\Omega &= 0 & i = 1 \cdots N_T, \\ \int_{\Omega} \left(\nabla \psi_j \cdot \left(-p^h \boldsymbol{\delta} + \mathbf{T}^h \right) - \psi_j \mathbf{f} \right) d\Omega &= \int_{\partial\Omega} \psi_j \boldsymbol{\sigma} \cdot \mathbf{n} ds & j = 1 \cdots N_v, \\ \int_{\Omega} \pi_k (\nabla \cdot \mathbf{v}^h) d\Omega &= 0 & k = 1 \cdots N_p, \end{aligned} \tag{1.31}$$

where Ω is the domain on which the calculations are done, $\partial\Omega$ is the boundary of the domain, \mathbf{n} is the outward unit normal vector, and s is the curvilinear coordinate along the boundary. This procedure reduces the continuity requirements imposed for the discrete velocity field and it allows the specification of natural boundary conditions in terms of the contact force $\mathbf{t} = \boldsymbol{\sigma} \cdot \mathbf{n}$ along the boundary. Essential (or Dirichlet) boundary conditions also may be imposed on the momentum equations (i.e. on the velocities). (More details on the imposition of Dirichlet boundary conditions are given in section C.1). The set of equations (1.31) defines formulation MIX-1 [KT77, CK80].

1.3.2 Interpolations

The precision of the solution obtained by the finite element method depends on the choice of interpolant for the unknown fields. The observation of the discretized equations (1.31) shows that the shape functions for the extra-stresses and velocities must be continuous, but the shape functions for pressure only have to be piece-wise continuous.

If we consider a classical mixed velocity-pressure formulation, the mixed interpolation must satisfy a compatibility condition derived by Ladyzhenskaya, Babuska and Brezzi [Bre74] in order to provide stable results. The popular choice of quadratic velocity interpolation with a linear pressure may be justified by the so-called LBB condition.

For the MIX-1 formulation, the first most widely used mixed interpolation, in the case of quadrilateral elements was the following:

- The viscoelastic extra-stress was approximated by means of biquadratic polynomials.
- The basis function for the pressure and the velocity fields are respectively bilinear and biquadratic polynomials. This choice was directly inspired by the LBB condition for the velocity-pressure formulation.

For this choice, all fields were continuous over the flow domain.

In the Newtonian limit $\lambda \rightarrow 0$, and for a quadratic interpolation for the extra-stresses, equations (1.31) are not equivalent to the classical Galerkin for-

mulation of the Navier-Stokes equations. Moreover, Newtonian results of MIX-1 are oscillatory in flows with high gradients.

This fact has been used by Marchal and Crochet [MC86] in the special case of rectangular elements. They found that a sufficient condition for the mixed method to reproduce results identical to those of the velocity-pressure formulation in the Newtonian case was that the discrete stress space must contain the gradient of the discrete velocity space [MC87]. In particular, they modified the stress interpolation as follows: the basic nine-nodes element for the velocity is subdivided into 4×4 bilinear subelements for the stresses (Figure 1.6). Such a mixed finite element was found to give excellent results for the Newtonian case, even near stress boundary layers. This particular element defines the so-called 4×4 formulation which does not however break the high Weissenberg number problem (i.e. the calculation of a flow with the finite element methods become generally difficult when We is increased).

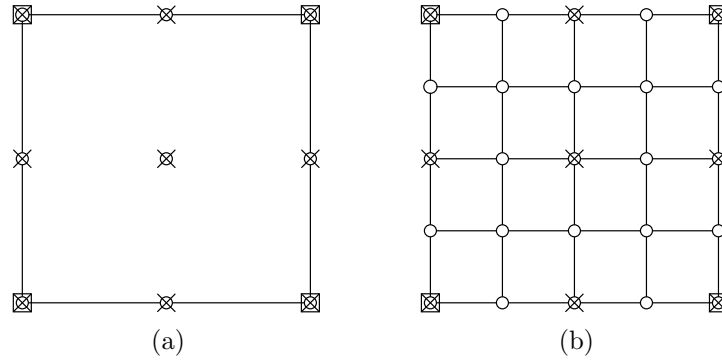


Figure 1.6: Description of mixed interpolants for the finite element simulation of viscoelastic flows: MIX-1 formulation (a) and 4×4 element (b). The circles represent the extra-stress nodes, the crosses the velocities and the squares the pressure.

The main drawback of this method is its large computational cost. Other methods like the EVSS formulation have been proposed to calculate viscoelastic flows (section 1.3.3).

1.3.3 Stress-splitting formulations

In the limit of Newtonian flows ($\lambda = 0$), the MIX formulation in terms of $(\mathbf{T}, \mathbf{v}, p)$ is not equivalent to the usual (\mathbf{v}, p) formulation of the Stokes equations. When we introduce the discretization, this fact has detrimental numerical implications [Keu89] and can be circumvented with the following change of variables:

$$\mathbf{S} = \mathbf{T} - 2\eta\mathcal{D}(\mathbf{v}).$$

A convected derivative of $\mathcal{D}(\mathbf{v})$ is then introduced in the constitutive equation, involving second-order spatial derivatives of \mathbf{v} . But, these derivatives can be

eliminated by considering a $(\mathbf{S}, \mathbf{v}, p, \mathbf{D})$ approximation. In order to define the *Elastic Viscous Split Stress formulation* (EVSS), Rajagopalan et al. [RBA90] introduced the modified stress tensor \mathbf{S} and the rate of deformation \mathbf{D} as additional unknowns, in the following way:

$$\begin{aligned}\mathbf{S} &= \mathbf{T} - 2\eta\mathbf{D}, \\ \mathbf{D} &= \frac{1}{2}(\nabla\mathbf{v} + \nabla\mathbf{v}^T).\end{aligned}\tag{1.32}$$

The discretization of the EVSS formulation provides more stable and accurate solutions than the discretization of the MIX formulation. Those good numerical properties are due both to a new elliptic stabilizing term in the momentum equation and to the least-square approximation of $\mathcal{D}(\mathbf{v})$ by a new variable \mathbf{D} .

In order to further improve the numerical properties, Sun et al. [SPTT96] proposed a modified version of the EVSS formulation to compute the flow of the upper-convected Maxwell fluid. Their so-called reference viscosity scheme formulation can be written as follows:

$$\mathbf{S} = \mathbf{T} - 2\beta\mathbf{D},\tag{1.33}$$

where the reference viscosity β is a function of the coordinates and can be much larger than η used in the usual EVSS formulation. In other words, the EVSS formulation is a particular case of this formulation. They also proposed an adaptive procedure to select β so as to obtain a viscous stress $2\beta\mathcal{D}(\mathbf{v})$ at least of the same order as the elastic stress \mathbf{S} . This scheme defines the so-called *Adaptive Viscous Stress Splitting formulation* (AVSS).

In order to introduce a similar elliptic stabilizing term in the momentum equations for other models, Guénette and Fortin [GF95] considered a modified stress splitting formulation. No change of variable is applied but the momentum equations are modified as follows:

$$\nabla \cdot \sigma(\mathbf{T}, p) + 2\alpha\nabla \cdot (\mathcal{D}(\mathbf{v}) - \mathbf{D}) = \mathbf{0}.$$

Obviously, $\mathcal{D}(\mathbf{v}) - \mathbf{D}$ vanishes in the continuous formulation, but it is introduced here as a stabilization term in the momentum equations. It acts exactly as the additional term generated by the change of variable of the EVSS formulation. This is sometimes known as the *Discrete Elastic Viscous Stress Splitting formulation* (DEVSS) or as the extended EVSS formulation of Guénette and Fortin.

All those formulations are particular cases of the following generic problem:

Find $(\mathbf{S}, \mathbf{v}, p, \mathbf{D})$ such that

$$\begin{aligned}\mathbf{S} + \lambda(\overset{\nabla}{\mathbf{S}} + 2\beta\overset{\nabla}{\mathbf{D}}) - 2(\eta - \beta)\mathcal{D}(\mathbf{v}) &= \mathbf{0}, \\ \nabla \cdot (-p\mathbf{I} + \mathbf{S} + 2\beta\mathcal{D}(\mathbf{v})) + 2\alpha\nabla \cdot (\mathcal{D}(\mathbf{v}) - \mathbf{D}) &= \mathbf{0}, \\ \nabla \cdot \mathbf{v} &= \mathbf{0}, \\ \mathbf{D} - \mathcal{D}(\mathbf{v}) &= \mathbf{0}.\end{aligned}$$

Note that we only present the generic problem on the example of the Maxwell model. But the generic formulation may easily be generalized to more complicated constitutive equations.

The MIX formulation corresponds to the case $\alpha = \beta = 0$ (the field \mathbf{D} is then not required and the field \mathbf{S} becomes \mathbf{T}) and the standard EVSS method (1.32) can be obtained with $\alpha = 0$, $\beta = \eta$. We obtain the reference viscosity AVSS formulation (1.33) with $\alpha = 0$ and the extended EVSS formulation of Guénette et al. with $\beta = 0$.

1.3.4 Interpolations for 3D calculations

There is no general mathematical theory that would give the choice of the approximations of the extra-stress tensor to be used with the various viscoelastic formulations. In this thesis, we only use the DEVSS formulation for the 3D coextrusion calculations (chapter 3).

An interesting property of the extended EVSS formulation is that, after integration by parts of the momentum equation, the tensor \mathbf{D} appears under an algebraic form in the formulation. This allows us to use a discontinuous interpolation for that field, and may lead to dramatic reduction of computational cost, especially for 3D calculations.

Thus, for those calculations, we use a trilinear interpolation for the extra-stress tensor. For the velocities and pressure, we use the mini-element of Fortin [For81] (pressure is discontinuous and constant on the elements, velocities are trilinear, but one adds a normal degree of freedom at the center of each face). For the tensor \mathbf{D} we use the same type of interpolation as for the pressure.

Note that for the 3D Newtonian and Reiner-Rivlin calculations, the mini-element of Fortin is also used for the velocity and pressure discretization.

1.3.5 Upwinding

It is possible to demonstrate that the classical Galerkin formulation is optimal for the discretization of elliptic equations. But the equations governing viscoelastic flows are hyperbolic. The streamline upwind Petrov-Galerkin (SUPG) method has been developed by Brooks et al. [BH82] in order to provide stable and accurate formulation for advection-diffusion equations. This technique consists in replacing the weight function ψ_i of the constitutive equation by

$$\hat{\psi}_i = \psi_i + k\mathbf{v} \cdot \nabla \psi_i,$$

where k is a scalar of the order of the finite element size h .

Numerical experiments and mathematical analysis establish that, for a given velocity field, the SUPG is more accurate and stable. However, when Marchal and Crochet have incorporated the 4×4 interpolation and the SUPG technique for the problem of the full set of viscoelastic equations, they have obtained oscillatory extra-stress and velocity at relatively small values of the Weissenberg number, even if interesting accurate results can be obtained for the flow around a sphere or in undulated channels.

Therefore, Marchal and Crochet used the SU method. In this approach, the additional term of the test function affects only the purely advective term $\mathbf{v}^h \cdot \nabla \mathbf{T}^h$ of the upper convective derivative. The SU method has very good stability properties, but is only first-order accurate. In other words, the artificial diffusion of the SU algorithm introduces an error proportional to the size of elements. But with SU, solutions have been obtained at very high Weissenberg numbers using Maxwell and Oldroyd-B fluids in flows with and without stress singularities [CAD⁺95a].

1.3.6 Stream function

For two-dimensional calculations, if the divergence of velocity field vanishes (incompressible flow), the components of the velocity may be derived from a scalar stream function ψ . For example, for a planar flow, we have

$$u = \psi_{,y} \text{ and } v = -\psi_{,x},$$

in which $\{x, y\}^T$ are the coordinate components, and $\{u, v\}^T$ the velocity components.

This function is often used to visualize flows, for isolines of the stream function given by the solution of

$$\psi(x, y) = \text{constant}$$

are parallel to the direction of velocity vectors.

It easily can be shown that ψ is the solution of a Poisson equation. Indeed, by defining the vector

$$\begin{Bmatrix} \psi_{,x} \\ \psi_{,y} \end{Bmatrix} = \begin{Bmatrix} -v \\ u \end{Bmatrix},$$

and calculating its divergence, one obtains

$$\nabla^2 \psi = -v_{,x} + u_{,y}. \quad (1.34)$$

A similar transformation may be done for axisymmetric flows.

An interesting characteristic of equation (1.34) is that ψ is the solution of an elliptic Poisson equation. This ensures that isolines are generally smooth, even when the velocity field presents wiggles.

1.3.7 Solution of the nonlinear system

The discretization of the governing equations with the finite element method leads to a system of nonlinear equations. Two basic approaches have been adopted to solve the nonlinear system:

- In the *coupled* approach, the equations are solved simultaneously for the whole set of variables. The advantage of this approach lays in the possibility of deriving Newton-Raphson's or Picard's equations for solving the nonlinear problem (section A.2). Its disadvantage is the relatively high computer cost caused by fairly large number of variables.

- In the *decoupled* approach, the calculation of the viscoelastic extra-stress is performed separately from the flow kinematics: from known velocity and pressure, one calculates the extra-stress by integrating the constitutive equations; then, the kinematics is updated by solving the conservation equations for a given extra-stress. With this approach, the number of variables is much lower than in the coupled approach, but the number of iterations is also much larger because it does not enjoy the quadratic convergence properties of Newton's method (section A.2).

1.4 Time discretization

In this section, we present the methods used to discretize the equations in time. This discretization in time has to be done if a time derivative appears in the governing equations. A general form of the time dependent equations is

$$\mathbf{M}(\mathbf{z})\dot{\mathbf{z}} + \mathbf{g}(\mathbf{z}) = \mathbf{0}, \quad (1.35)$$

where \mathbf{z} is the vector containing the nodal values, \mathbf{M} is the mass matrix, and $\mathbf{g}(\mathbf{z})$ is a vector. An initial condition is given to the solution at time t_0 :

$$\mathbf{z}(t_0) = \mathbf{z}_0.$$

The time discretization of equation (1.35) consists in finding numerical approximations \mathbf{z}^n of the unknown theoretical solution $\mathbf{z}(t)$ at discrete times t_n defined by $t_0 < t_1 < \dots < t_n < \dots < t_N$.

In this thesis, we only use algorithms derived from the θ methods. Equation (1.35) also may be written

$$\dot{\mathbf{z}} = -\mathbf{M}^{-1}(\mathbf{z})\mathbf{g}(\mathbf{z}). \quad (1.36)$$

The discretization of this equation with a θ scheme gives

$$\frac{\mathbf{z}^{n+1} - \mathbf{z}^n}{\Delta t_{n+1}} = -\theta \mathbf{M}^{-1}(\mathbf{z}^{n+1})\mathbf{g}(\mathbf{z}^{n+1}) - (1 - \theta)\mathbf{M}^{-1}(\mathbf{z}^n)\mathbf{g}(\mathbf{z}^n), \quad (1.37)$$

in which $\Delta t_{n+1} = t_{n+1} - t_n$ is the time step and θ controls the implicit character of the time discretization.

The values $\theta = 0$ and $\theta = 1$ give the explicit and implicit Euler schemes respectively. Both Euler schemes are first order schemes. The value $\theta = 1/2$ gives the second order Crank-Nicolson method. The value $\theta = 2/3$ gives a first order scheme called "Galerkin method". More informations about the implementation of the θ methods are given in section A.3.

It is important to know whether a transient method is stable or not. For advection equations, it has been shown that among the θ methods, the criterion of stability is $\theta \geq \frac{1}{2}$. This means that Crank-Nicolson, Galerkin and implicit Euler schemes are unconditionally stable; but explicit Euler scheme is unconditionally unstable. This is related to the fact that the time discretization

of an advection equation with the explicit Euler schemes introduces an artificial negative diffusion. with Galerkin and implicit Euler schemes, the artificial diffusion is positive. Numerical diffusion vanishes for $\theta = \frac{1}{2}$. Consequently, the Crank-Nicolson scheme is adapted to the study of stability by transient integration.

1.5 Free surfaces

In this thesis, we calculate flows on geometries with free surfaces or interfaces. Kinematic conditions are used to calculate the motion of those moving boundaries. In order to avoid overdistorted elements inside the computational domain, the motion of the boundaries must be propagated inside the mesh. This is done with an appropriate remeshing technique.

1.5.1 Kinematic conditions

The kinematic condition expresses the condition that fluids do not flow across free surfaces or interfaces. The simplest way to express such a condition is the following:

$$(\mathbf{v} - \dot{\mathbf{x}}) \cdot \mathbf{n} = 0, \quad (1.38)$$

in which \mathbf{v} is the fluid velocity, $\dot{\mathbf{x}}$ is the time derivative of eulerian coordinates and \mathbf{n} is the normal vector to the moving surface. Thus, \mathbf{n} depends on the coordinates on this surface. The difference $\mathbf{v} - \dot{\mathbf{x}}$ is the fluid velocity relative to the mesh. By multiplying this relative velocity by the normal to the boundary we obtain the flow rate through this surface. Thus, we impose this surface flow rate to vanish at each point along this surface. Equation (1.38) may be discretized using a Galerkin formulation for two- and three-dimensional flows. It will be referred to as “surface kinematic condition” in the next chapters. For time independent flows, $\dot{\mathbf{x}} = \mathbf{0}$ and (1.38) reduces to $\mathbf{v} \cdot \mathbf{n} = 0$.

To calculate the motion of a free surface, another type of kinematic condition called “line kinematic condition” may be used; the mesh of the moving surface is divided in lines. Each line is constrained to be parallel to the velocity (Figure 1.7). It is possible to show that this method is optimal because the kinematic condition leads to hyperbolic equations. The use of this method requires the structure of the mesh to be such that it can easily be divided in lines parallel to the main direction of flow. Thus, it also requires a good knowledge of the main direction of flow prior to its calculation. Those two characteristics of the line kinematic condition restrict its use to the calculation of free surface extrusion flows.

Let us define a unit vector $\boldsymbol{\tau}$ tangent to a mesh line with

$$\boldsymbol{\tau} = \frac{\mathbf{x}_s}{\|\mathbf{x}_s\|},$$

in which s is a curvilinear coordinate following the mesh line. The equation

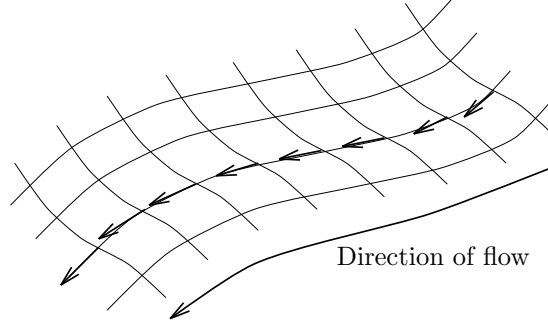


Figure 1.7: *Schematic representation of the line kinematic condition.*

defining the line kinematic condition is

$$\mathbf{c} - c_\tau \boldsymbol{\tau} = \mathbf{0}, \quad (1.39)$$

where \mathbf{c} is a quantity closely related to the fluid velocity and c_τ is its component tangential to the line ($c_\tau = \mathbf{c} \cdot \boldsymbol{\tau}$). Note that $\boldsymbol{\tau}$, and thus c_τ are functions of the nodal coordinates on the line. Thus equation (1.39) involves the coordinates as unknowns.

An interesting feature of the line kinematic condition is that it allows the use of a continuation method on a parameter ζ_l . This allows to progressively model the kinematic condition. This is done by calculating vector \mathbf{c} with

$$\mathbf{c} = \zeta_l \mathbf{v} + (1 - \zeta_l) \|\mathbf{v}\| \boldsymbol{\tau}_{\text{ref}}, \quad (1.40)$$

in which \mathbf{v} is the fluid velocity, and $\boldsymbol{\tau}_{\text{ref}}$ is a reference vector tangential to the initial mesh line. By putting ζ_l to 0, \mathbf{c} remains parallel to the initial mesh line, and the line does not move. By progressively increasing ζ_l , the kinematic condition is introduced in the equation. for $\zeta_l = 1$ the full kinematic condition is obtained.

1.5.2 Surface tension

Along a free surface, the modelling of surface tension leads to a normal force applied on the interface:

$$\mathbf{f}_n = \gamma \left(\frac{1}{R_1} + \frac{1}{R_2} \right) \mathbf{n}, \quad (1.41)$$

in which \mathbf{n} is the normal vector to the surface, R_1 and R_2 are the principal radii of curvature of the surface, and γ is the surface tension coefficient. For an

axisymmetric flow around x axis, the principal radii of curvature are given by

$$R_1 = \left[1 + \left(\frac{\partial h}{\partial x} \right)^2 \right]^{\frac{3}{2}} / \frac{\partial^2 h}{\partial x^2},$$

$$R_2 = -h \left[1 + \left(\frac{\partial h}{\partial x} \right)^2 \right]^{\frac{1}{2}}.$$

For a planar flow, the formula giving R_1 remains unchanged and R_2 becomes infinite.

After discretization and integration by parts of equation (1.41), two different types of boundary conditions may be imposed to the free surface: Dirichlet or Neumann boundary conditions. In some case, the attachment position of the free surface on the wall is known a priori. This is the case when the free surface attaches to a corner. For such cases, Dirichlet conditions are imposed. In other cases, the attachment point is the result of a dynamic equilibrium of contact forces. For such situations, one usually imposes a force equal to surface tension and oriented towards a specified direction (Figure 1.8). Such problems are discussed in [Rus80, Keu86, Leg92].

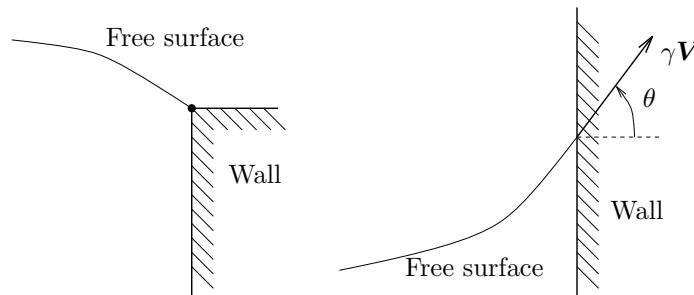


Figure 1.8: *Different types of boundary conditions that may be imposed at the attachment point of the free surface and a wall.*

Note that it is often easier to derive the discretized equations of surface tension from a minimization principle, the function to minimize being the energy associated with the total free surface: $E = \gamma S$.

1.5.3 Remeshing techniques

In order to avoid overdistortion of elements, a remeshing technique is used to propagate the motion of the free surface into the mesh. In this section we only mention the method of spines, a remeshing based on a Thompson transformation and a remeshing based on the minimization of the deformation energy of a grid (called Optimesh in Polyflow).

Method of spines

Let us first define a height function $h(x, t)$ representing the displacement of free surface nodes towards a specified direction \mathbf{d} . The kinematic condition may be expressed as a function of h . In the method of spines, a one dimensional finite element approximation is constructed for the height function h on the free surface (Figure 1.9). We only present the method here for two-dimensional calculations, but it is easy to generalize the calculation to three-dimensional flows.

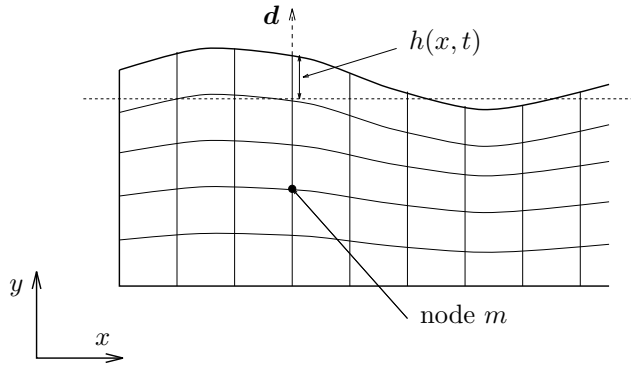


Figure 1.9: Schematic representation of the method of spines.

The mesh is then divided into “slices”. In a given slice, the nodal displacement of each node is a linear function of the nodal displacement of the free surface node of that slice. It may thus be expressed as a function of h :

$$\Delta \mathbf{x}_{mn}(t) = c_{mn} h_m(t) \mathbf{d}_m, \quad (1.42)$$

in which m is a nodal index in the horizontal direction of slicing, n is a nodal index in the vertical direction, and c_{mn} is a constant parameter related to the initial position of the node (m, n) in the undeformed mesh.

In general, \mathbf{d}_m may be updated at each time step (or continuation step). For example, the vector may be calculated at the beginning of each time step in order to have it normal to the mesh before any other calculation. But \mathbf{d}_m may also be determined only once at the beginning of the calculation; that is what we are doing in chapter 2 where director vector \mathbf{d} is vertical or horizontal.

Note that an interesting advantage of the method of spines is that each coordinate unknown is a linear function of one single variable $h_m(t)$. Thus equation (1.42) may be expressed with constraints. This leads to an important decrease of the computational cost of the remeshing for coordinate unknowns are eliminated of the system before the Gaussian elimination. Therefore, the method of spines is a very cheap remeshing technique. But its use is limited to problems in which the deformation of the mesh is not too large.

Remeshing based on a Thompson transformation

When we use the Thompson transformation, we take advantage of the smoothing properties of an elliptic operator [TWM85, TWM82]. As a first step, a generalised coordinate system is defined on the moving domain. For a two-dimensional domain, one builds a mapping between the two-dimensional domain and a “parent element”. In Polyflow the use of Thompson remeshing is limited to problems in which the domain to remesh as a quadrilateral topology, and the parent element is square.

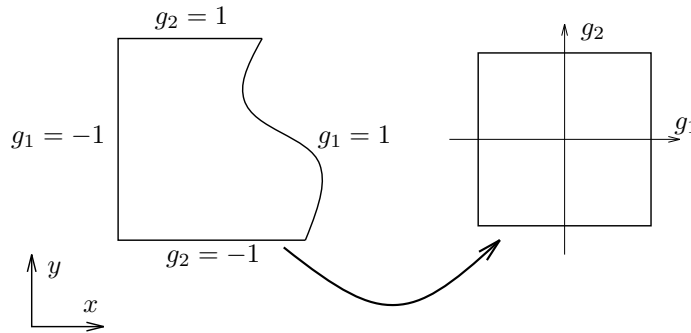


Figure 1.10: *Schematic representation of the mapping between the domain to remesh and the square parent element for the Thompson transformation.*

The mapping is obtained by solving

$$\nabla^2 \mathbf{g} = \mathbf{0},$$

in which \mathbf{g} is a vectorial function $\{g_1, g_2\}^T$ of the coordinates. For that problem, Dirichlet boundary conditions are imposed on the components of \mathbf{g} . Those conditions are indicated in Figure 1.10. The components of \mathbf{g} may be interpreted as generalised coordinates. In Figure 1.10, they are such that the parent element is a square centered on the origin, and of side length 2.

The field \mathbf{g} contains information on the initial distribution of the elements in the domain. This information is used to calculate the motion of the nodes when the boundaries of the domain move. More precisely, we solve

$$\nabla^2 \mathbf{g} = \mathbf{0},$$

but here, the field \mathbf{g} is a data of the problem, and the coordinates are the unknowns. Thus we search $\{x, y\}^T$ such that relation $\nabla^2 \mathbf{g} = \mathbf{0}$ is conserved. This leads to a nonlinear set of equations with coordinate as unknowns. This set of equations is solved with a Newton-Raphson algorithm. The equations involving the nodal coordinates along the boundaries are cancelled and replaced by essential boundary conditions (fixed coordinates), or tangential Thompson remeshing and kinematic conditions, or any other equation depending on the peculiarity of the problem being solved.

The main advantage of the Thompson remeshing resides in the fact that the elliptic operator has smoothing properties on the deformation of the mesh. This allows very large deformations. But the computational cost of the method also is larger than that of the method of spines.

Remeshing based on an energetic approach

In the “Optimesh” remeshing technique of Polyflow, the mesh is considered as a deforming elastic grid. An elastic response corresponds to the angular deformation of the corners, of the diagonal of elements, and of the side of elements. An energy may be associated with the deformation of the grid, and the remeshing is the result of the minimization of that energy: one solves an elastic problem.

Some parameters allow the user to modify the contribution of the various elements of the elastic response (angular, diagonal or side deformations). It is also possible to consider the initial grid as a reference for the elastic deformations.

More details about this remeshing technique may be found in [Ber91].

1.5.4 Correction for time derivatives

Special care must be taken in the evaluation of time derivatives when the Galerkin procedure is used on a moving grid algorithm. For example, the material derivative of the extra-stress tensor becomes

$$\frac{DT}{Dt} = \dot{T} + (\mathbf{v} - \dot{\mathbf{x}}) \cdot \nabla T.$$

If the discretization is done on a fixed mesh, $\dot{\mathbf{x}} = \mathbf{0}$, and the material derivative reduces to its usual expression. Another special case corresponds to the Lagrangian approach in which nodes are fluid particles and $\mathbf{v} = \dot{\mathbf{x}}$. In that case the material derivative reduces to the time derivative [Keu86].

Part I

Numerical calculation of multilayer flows

THIS PAGE IS INTENTIONALLY LEFT BLANK

Introduction

Coextrusion is the simultaneous extrusion from a single die of two or more homogeneous melts which form a laminar structure. This process has gained wide recognition as an approach to achieving unique product performance by combining properties of different materials, and lower costs through combination of different valued materials. Coextrusion simplifies the manufacturing process by avoiding many of the processing steps required by conventional lamination and coating processes. Moreover, coextrusion enables the production of very thin layers and ensures better layer adhesion since the melts are brought together under pressure inside the die [CAD⁺95b].

Two different phenomena related to the multilayer character of the flows are often observed during coextrusion:

- In many cases, the extrudate exhibits wavy interfaces related to interfacial instabilities occurring in the die. Those instabilities may be caused by the combination of inertia and viscosity differences. But in most situations, the elasticity of the fluids is responsible for the problem [SK92, WK93a, WK93b].
- The less viscous fluid exhibits a tendency to surround the more viscous one. This phenomenon may eventually lead to a total “encapsulation” of the more viscous fluid. The phenomenon, represented in Figure I.1, has been investigated both experimentally and theoretically by a large number of researchers [SB73, SB75, Eve75].

Interfacial instabilities and encapsulation have also been observed in multilayer Newtonian flows. For such flows, it has been shown that the viscosity ratio of the fluids plays a major role. Indeed, as has been observed for polymer melts, the less viscous fluid encapsulates the more viscous one. The encapsulation phenomenon may have both positive and negative consequences. In oil pipelining, water is sometimes added to oil. Then water migrates to the walls while oil gathers in the core layer. In such a configuration of oil and water, water acts as a lubricant and reduces the energy losses in the pipe [JR93a, JR93b]. However, when polymer melts are coextruded in dies, encapsulation is generally an undesirable phenomenon. For example, in order to produce multilayer film products, the multilayered structure flows through a runner and then a coat hanger die which spreads the layer to the desired width. If encapsulation phenomenon

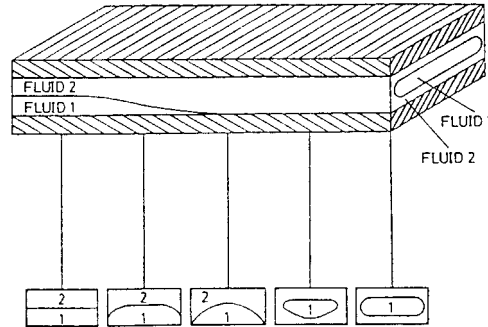


Figure I.1: Progressive encapsulation during coextrusion in a rectangular die. The lower part of the picture represents successive cross-sections in the die (From [CAD⁺95b]).

occurs in the flow, the layered structure presents serious nonuniformities. Generally, the material near the edges of the die must be cut from the film and discarded or recycled [THV⁺93].

For multilayer Newtonian flows, it has been shown that a thin layer of small viscosity fluid is favorable to the stability of long wavelength perturbations (see section 2.1). This phenomenon is called “thin-layer effect”. It is interesting to relate the thin-layer effect to the encapsulation phenomenon. The fact that the more viscous fluid is encapsulated by the less viscous one has suggested a principle of minimization of the viscous dissipation to explain the encapsulation. This principle states that the flow tends to reach a configuration in which the viscous dissipation is minimal for a fixed total flow rate. When encapsulation occurs, the layer of small viscosity fluid acts as a lubricant and reduces viscous dissipation. In the thin-layer effect, the small viscosity fluid acts precisely in the same way: it seems that the lubricated flow is “satisfied” with its configuration, and does not want to be “disturbed” (at least by large wavelength perturbations) if the lower viscosity layer is thin.

This relation between the thin-layer effect and the encapsulation has suggested to some authors the idea that encapsulation could arise from the transient development of an interfacial instability in the stratified flow. In order to check that assumption, we study in chapter 2 the stability of multilayer Newtonian flows. In particular, we investigate the behaviour of perturbations growing into the nonlinear domain. This allows us to calculate the bamboo waves nonlinear flow regime. But, that investigation only gives us some elements of answer, for it is difficult to use the methods described in that chapter to simulate a three-dimensional encapsulation flow. We investigate in chapter 3 another possible explanation of the phenomenon for viscoelastic coextrusion flows. We study the effect of normal stress differences on encapsulation. Results of three-dimensional static calculations with non-Newtonian models are presented and discussed.

Chapter 2

Stability of multi-layer Newtonian flows

In order to know whether encapsulation may be a result of the growth of interfacial instabilities into the nonlinear domain, we calculate the transient evolution of perturbed flows with a finite element method. The results of Yiantsios and Higgins [YH88b] are used to select the parameters of our transient periodic planar calculations. In order to validate our modelling of the problem, we first try to reproduce the results of linear stability analyses with transient calculations of periodic flows. Then we investigate the behaviour of perturbations growing in the nonlinear domain.

However, infinite periodic perturbations in space do not model realistically the perturbed flows observed experimentally. Indeed, the dies (or pipes) have always a finite length, and perturbations are never infinitely periodic in space. Therefore, we also model the more realistic problem of the coextrusion of two fluids in a planar channel. In that case, the perturbation is imposed on the flow rates and is a periodic function of time.

Finally, a realistic model problem is obtained with an axisymmetric periodic flow rather than a planar one. This allows us to calculate some nonlinear flow regimes like the “bamboo waves regime”.

2.1 Linear stability of two-layer planar flows

The first significant study of the linear stability of two-layer shear flows has been done by Yih [Yih67]. He studies two layer Couette and Poiseuille flows slightly perturbed with long wavelength periodic perturbations. In other papers devoted to the study of the stability of multilayer flows, short, long and intermediate wavelength perturbations are considered.

To study the linear stability of flows, the equations governing the linear behaviour of the perturbations have to be written. In our case, for periodic perturbations, those equations are the “Orr-Sommerfeld equations”.

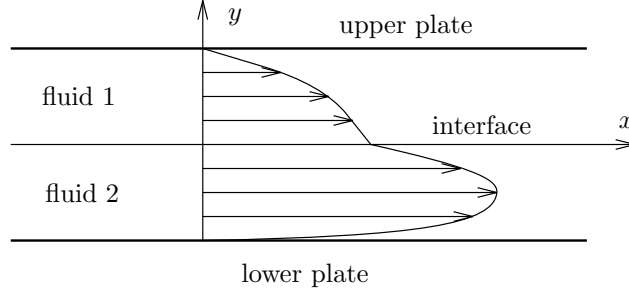


Figure 2.1: Two layer planar Poiseuille flow between parallel plates.

The Orr-Sommerfeld equations result in an eigenvalue problem. Eigen solutions may be calculated analytically for small or large wavelength perturbations by asymptotic analysis. For intermediate wavelengths, numerical methods have to be used to solve the eigenvalue problem. The stability or instability of a perturbation is related to the eigenvalue of its fastest growing mode.

The results obtained by Yiantsios and Higgins are probably the most complete to this date [YH88b]. They are presented and discussed at the end of the section.

2.1.1 Dimensionless numbers

To calculate the flow, the Navier-Stokes are solved in both layers with appropriate boundary and interfacial conditions. The momentum equations in both layers are

$$\rho_1 \frac{D\mathbf{v}_1}{Dt} = -\nabla p_1 + \mu_1 \nabla^2 \mathbf{v}_1 + \rho_1 \mathbf{g},$$

$$\rho_2 \frac{D\mathbf{v}_2}{Dt} = -\nabla p_2 + \mu_2 \nabla^2 \mathbf{v}_2 + \rho_2 \mathbf{g},$$

in which the subscripts 1 and 2 denote the upper and lower layers respectively. In all our calculations, gravity \mathbf{g} is parallel to the y axis and oriented towards the negative direction. The velocity field also must satisfy the incompressibility equation in both layers: $\nabla \cdot \mathbf{v}_1 = 0$ and $\nabla \cdot \mathbf{v}_2 = 0$.

To adimensionalize the governing equations, we use the thickness and the density of the upper layer, and the velocity u_0 at the interface in the base flow. We also introduce the viscosity ratio $m = \mu_2/\mu_1$ and the density ratio $\zeta = \rho_2/\rho_1$.

The other dimensionless numbers arising from the adimensionalisation are the thickness ratio $n = d_2/d_1$, the Reynolds number $\mathcal{R} = \rho_1 u_0 d_1 / \mu_1$, the adimensional gravity $\mathbf{G} = d_1 \mathbf{g} / v_0^2$, the Froude number $F = (\zeta - 1) g d_1 / u_0^2$ and a number expressing the interfacial tension $S = \gamma / \rho_1 d_1 u_0^2$.

To simplify the notations, we use identical symbols for the velocities and the pressure in the dimensional and dimensionless equations. The dimensionless

momentum equations governing the flow are

$$\frac{D\mathbf{v}_1}{Dt} = -\nabla p_1 + \frac{1}{\mathcal{R}}\nabla^2\mathbf{v}_1 + \mathbf{G}, \quad (2.1)$$

$$\zeta\frac{D\mathbf{v}_2}{Dt} = -\nabla p_2 + \frac{m}{\mathcal{R}}\nabla^2\mathbf{v}_2 + \zeta\mathbf{G}, \quad (2.2)$$

The kinematic condition is used to calculate the motion of the interface. Along the interface, the velocity field and the tangential component of the shear stress are continuous. Surface tension results in a discontinuity of the normal component of the Cauchy stress tensor.

Let us note that the adimensionalisation is done differently in some studies. For example, Hooper and Boyd distinguish various definitions of the Reynolds number and surface tension parameters in their analysis [HB87].

2.1.2 Orr-Sommerfeld equations

In the Poiseuille flow represented in Figure 2.1, the y component of the velocity is zero. We use u , v and p to denote respectively the x and y components of the velocity, and the pressure in the base flow. A small amplitude perturbation is added to the base flow. Thus

$$\hat{u} = u + u', \quad \hat{v} = v', \quad \hat{p} = p + p', \quad (2.3)$$

in which \hat{u} , \hat{v} and \hat{p} give the perturbed flow and u' , v' and p' denote the perturbation quantities. The perturbation satisfies the incompressibility equation. This allows us to use a stream function ψ such that $u' = \psi_{,y}$ and $v' = -\psi_{,x}$. We then assume that the perturbation is periodic in the x direction and that it depends exponentially on t . We have

$$\{\psi, p'\} = \{\phi(y), f(y)\} \exp i\alpha(x - ct),$$

in which α is the wave number of the perturbation, and c is its complex wave speed: $c = c_r + ic_i$. α is always positive, and proportional to the inverse of the wavelength of the perturbation. The stability or instability of the perturbation is related to the sign of the imaginary part c_i : if $c_i > 0$, the amplitude of the perturbation increases with t , otherwise the perturbation is stable. Actually, αc_i is the growth rate of the perturbation.

By substituting (2.3) in the dimensionless momentum equations (2.1-2.2), and neglecting the terms pertaining to the base flow and the quadratic terms in perturbation quantities, the momentum equations may be expressed in terms of ϕ and f :

$$i\alpha\{(u - c)\phi_{,y} - u_{,y}\phi\} = -i\alpha f + \frac{1}{\mathcal{R}}(\phi_{,yyy} - \alpha^2\phi_{,y}),$$

$$\alpha^2(c - u)\phi = f_{,y} + \frac{i\alpha}{\mathcal{R}}(\phi_{,yy} - \alpha^2\phi).$$

The elimination of f from the two last equations produces the well-known Orr-Sommerfeld equation

$$\phi_{,yyyy} - 2\alpha^2\phi_{,yy} + \alpha^4\phi = i\alpha\mathcal{R}\{(u_1 - c)(\phi_{,yy} - \alpha^2\phi) - u_{1,yy}\phi\}. \quad (2.4)$$

(We add the subscript 1 to the velocity u to denote the fact that the equation is relative to the upper layer of the flow.) A similar equation is derived for the lower layer:

$$\chi_{,yyyy} - 2\alpha^2\chi_{,yy} + \alpha^4\chi = \frac{i\alpha\zeta\mathcal{R}}{m}\{(u_2 - c)(\chi_{,yy} - \alpha^2\chi) - u_{2,yy}\chi\}, \quad (2.5)$$

in which $\chi(y)$ is the eigenfunction defined in the lower layer and corresponds to $\phi(y)$ in the upper layer.

Boundary and interfacial conditions are imposed to equations (2.4) and (2.5). The velocity is imposed along the upper and lower plates. Therefore, the perturbation velocity vanishes along the upper and lower plates. This leads to the conditions

$$\phi(1) = \phi_{,y}(1) = 0, \quad (2.6)$$

$$\chi(-n) = \chi_{,y}(-n) = 0. \quad (2.7)$$

The continuity of u' and v' on the interface respectively involve the conditions

$$\phi_{,y}(0) - \chi_{,y}(0) = \frac{\phi(0)}{c - u(0)}(u_{2,y}(0) - u_{1,y}(0)), \quad (2.8)$$

$$\phi(0) = \chi(0). \quad (2.9)$$

The continuity of shear stress is expressed by

$$\phi_{,yy}(0) + \alpha^2\phi(0) = m\{\chi_{,yy}(0) + \alpha^2\chi(0)\}. \quad (2.10)$$

The normal stress equilibrium at the interface leads to the condition

$$\begin{aligned} & -i\alpha\mathcal{R}\{(c - u(0))\phi_{,y}(0) + u_{1,y}(0)\phi(0)\} - (\phi_{,yyy} - \alpha^2\phi_{,y}(0)) \\ & + 2\alpha^2\phi_{,y}(0) + i\alpha\mathcal{R}\{(c - u(0))\chi_{,y}(0) + u_{2,y}(0)\chi(0)\} \\ & + m(\chi_{,yyy} - \alpha^2\chi_{,y}(0)) - 2\alpha^2m\chi_{,y}(0) = i\alpha\mathcal{R}\left(\frac{1}{F^2} + \alpha^2S\right)\frac{\phi}{c - u(0)}. \end{aligned} \quad (2.11)$$

Equations (2.4), (2.5), (2.6), (2.7), (2.8), (2.9), (2.10) and (2.11) define an eigenvalue problem in which c is the eigenvalue and $\{\phi(y), \chi(y)\}$ is the eigenfunction.

2.1.3 Solution of the eigenvalue problem

Asymptotic solution of the eigenvalue problems

Exact analytical solutions of the eigenvalue problem described in section 2.1.2 are generally very difficult to obtain. Instead, numerical or approximate solutions are often calculated. In this section, we present analytical solutions obtained for very small or very large wavelength perturbations. The principle of the method used to solve the eigenvalue problem is briefly described. More information about the resolution of the eigenvalue problem for small or large wavelength perturbations can be found in [Yih67, JR93a].

For long wavelength perturbations, $\alpha \ll 1$. Thus the solution may be expanded in an infinite power series:

$$\begin{aligned}\phi(y) &= \phi_0(y) + \alpha\phi_1(y) + \alpha^2\phi_2(y) + \dots \\ \chi(y) &= \chi_0(y) + \alpha\chi_1(y) + \alpha^2\chi_2(y) + \dots \\ c &= c_0 + \alpha c_1 + \alpha^2 c_2 + \dots\end{aligned}$$

These approximations of the solution are substituted in the equations defining the eigenvalue problem. Thus, those equations also may be written as a power series of α .

A zeroth order estimate of the eigensolution is obtained by neglecting all terms containing α^2 or higher orders of α . The first estimate of c , c_0 , is purely real and may be interpreted as a translation velocity of the perturbation. A better estimate of c is obtained by adding the second order powers of α in the equations. To the first estimate, we add the correction αc_1 , in which c_1 is imaginary and related to the stability or instability of the perturbation. The estimate of the eigen solution may still be improved by adding higher order terms in the expansion.

For small wavelength perturbations ($\alpha \gg 1$), the principle of the asymptotic resolution of the eigenvalue problem is the same, except that ϕ , χ and c are expanded in negative power series of α .

Numerical solution of the eigenvalue problems

Yiantsios and Higgins use a numerical technique to discretize the eigenvalue problem [YH88b, YH87a]. The functions $\phi(y)$ and $\chi(y)$ are discretized with a finite element technique. This leads to an algebraic eigenvalue problem. For small wavenumbers and moderate Reynolds numbers, the problem is solved using a QR algorithm. For large wavenumbers or Reynolds numbers, the eigen problem becomes numerically “stiff”, and special numerical techniques are used to calculate some eigensolutions of the problem [YH88a].

2.1.4 Stability of two-layer Poiseuille flows

We present here some results of linear stability analyses of the two layer planar Poiseuille flow represented in Figure 2.1 (velocity and pressure fields in the base

flow are given in section B.1.1). Most results given in this section have been published by Yiantsios and Higgins [YH88b, YH87a]. They solve the eigenvalue problem numerically to estimate the eigenvalues c for a wide range of wavenumbers α , and of the parameters \mathcal{R} , S , F , ... Then, the selection of the eigenvalue presenting the largest imaginary part allows them to determine whether the flow is stable for all perturbations or not.

We summarize here the conclusions of Yiantsios and Higgins about the influence of thickness ratio, wavenumber of the perturbations, inertia, surface tension and gravity. We present neutral stability curves in plane (n, α) (i.e. thickness ratio vs. wavenumber). Stable and unstable areas are denoted with “s” and “u”. Neutral stability curves separate stable and unstable areas.

Neutral stability curves and thin layer effect

In Figure 2.2, the neutral stability curves are plotted for the case $m = 20$, $\mathcal{R} = 10$, and for vanishing gravity and surface tension. The first neutral stability curve is the straight line of equation $n = \sqrt{20} = \sqrt{m}$. This corresponds to a base flow in which the velocity gradient vanishes at the interface.

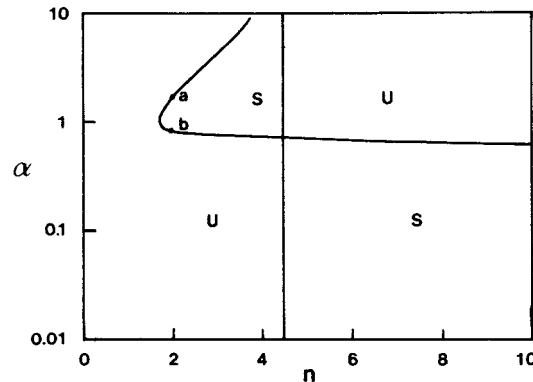


Figure 2.2: *Neutral stability curve for a planar Poiseuille flow ($m = 20$, $\zeta = 1$, $\mathcal{R} = 10$, $F = 0$ and $S = 0$). Stable and unstable areas are denoted with “s” and “u”. (From [YH88b]).*

For large wavelengths (small values of α), the perturbations are unstable for small values of n , and stable if n is sufficiently large (i.e. $n > \sqrt{m}$). This behaviour has also been predicted in other studies devoted to large wavelength perturbations [Yih67, Hoo89, Hoo85, APW90, HB87]: a thin layer of low viscosity fluid is favorable to the stability of the flow, while a thin layer of high viscosity fluid has a destabilizing influence. This phenomenon is usually called “thin-layer effect”.

However, for short wavelengths ($\alpha > \mathcal{O}(1)$), the second neutral stability curve tends asymptotically towards the straight line $n = \sqrt{m}$, and the per-

turbations become unstable for all values of the thickness ratio save $n = \sqrt{m}$. Here again, this result is confirmed by asymptotic analyses for short wavelength perturbations [HB83, HB87].

Influence of Reynolds number

Yiantsios and Higgins investigate the influence of the Reynolds number on neutral stability curves (Figure 2.3). Unfortunately, for the presentation of their results, they do not adopt conventions identical to those of Figure 2.2: the relation between the diagrams of Figures 2.3 and 2.2 is given by $\mathcal{R}' = \mathcal{R}n/m$, $\alpha' = \alpha n$, $n' = 1/n$ and $m' = 1/m$. The points a' and b' in Figure 2.3 correspond to a and b in Figure 2.2.

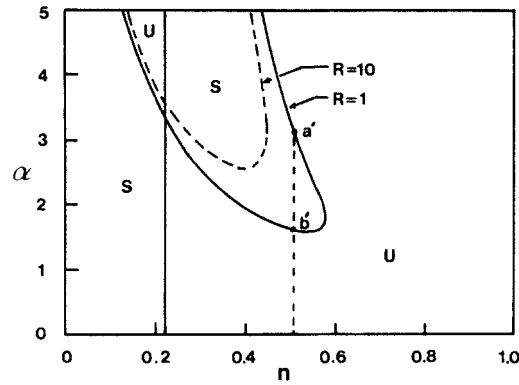


Figure 2.3: Influence of the Reynolds number on the neutral stability curve for a planar Poiseuille flow ($m = 0.05$, $\zeta = 1$, $\mathcal{R} = 10$, $F = 0$ and $S = 0$). Only one neutral stability curve is affected by modification of inertia. (From [YH88b].)

The neutral stability curves is not altered appreciably by a change of Reynolds number, at least for small values of \mathcal{R} ($\mathcal{R} < 20$). In its linear asymptotic analysis, Yih predicts a growth rate proportional to the Reynolds number [Yih67]. According to this result, the neutral stability curves should not be modified by a change of Reynolds number, and this agrees more or less with the results of Yiantsios and Higgins.

Influence of surface tension

The influence of surface tension is investigated in Figure 2.4. An increase of S has always a stabilizing influence on the flow. This stabilizing influence decreases rapidly as $\alpha \rightarrow 0$ (long wavelength perturbations). But for short wavelength perturbations, the stabilizing effect of surface tension is very important. A small quantity of surface tension is sufficient to create an interval of thickness ratios

$[n_{\text{inf}}, n_{\text{sup}}]$ for which all periodic perturbations are stable. If $S \rightarrow 0$, the interval reduces to the single value $n = \sqrt{m}$.

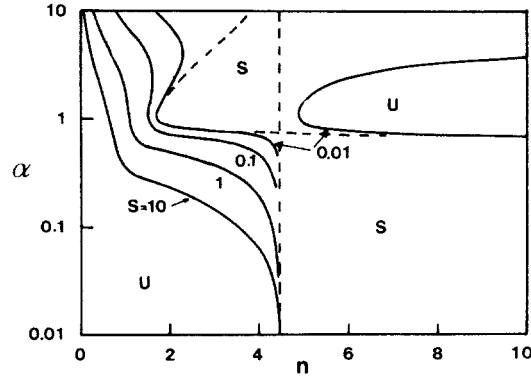


Figure 2.4: Influence of surface tension on the neutral stability curves for a planar Poiseuille flow ($m = 20$, $\zeta = 1$, $R = 10$, $F = 0$). An increase of surface tension always has a stabilizing effect on interfacial instabilities. (From [YH88b].)

The fact that surface tension always has a stabilizing influence on the flow may easily be explained. Surface tension may be interpreted as a membrane stretched along the interface. The tension of the membrane acts in such a way that the membrane tries to shrink and minimize its area. For a slightly perturbed interface, the interface may be described by a function $y = h(x)$ giving the vertical displacement as a function of x . Then, surface tension results in a normal force given by $f_n = -\gamma h_{,xx}$ which acts on the interface to make it as flat as possible. For our periodic perturbations, the interface is given by functions like $h(x) = h_0 \exp i\alpha(x - ct)$, and we find $f_n(x) = -\alpha^2 \gamma h(x)$. This explains the strong dependence of the stabilizing effect of surface tension on the wavelength of the perturbations.

Influence of gravity

In Figures 2.5 and 2.6, the neutral stability curves are plotted for various values of the Froude number. Gravity stabilizes the flow if the upper layer has a lower density than the lower layer. This can be understood intuitively: the flow tries to reach a configuration that minimizes the potential energy.

Here again, if gravity is stabilizing, an interval of thickness ratios $[n_{\text{inf}}, n_{\text{sup}}]$ on which the flow is stable for all wavelength perturbations appears. If the upper layer has a higher density, gravity is destabilizing and short wavelength perturbations are unstable for all values of n . The influence of gravity on the neutral stability curves does not seem to depend on the wavelength of the perturbations.

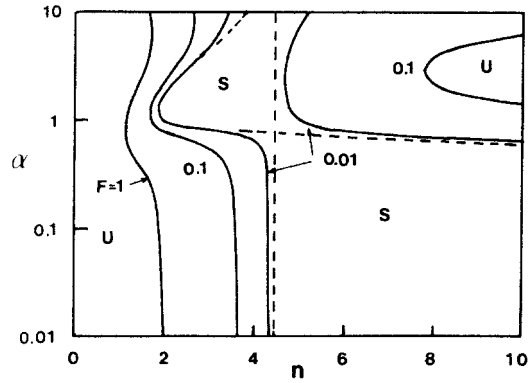


Figure 2.5: *Stabilizing influence of the gravity for a planar Poiseuille flow when the lower layer has a higher density ($m = 20$, $\mathcal{R} = 10$, $S = 0$, $F > 0$ and $\zeta > 0$). (From [YH88b].)*

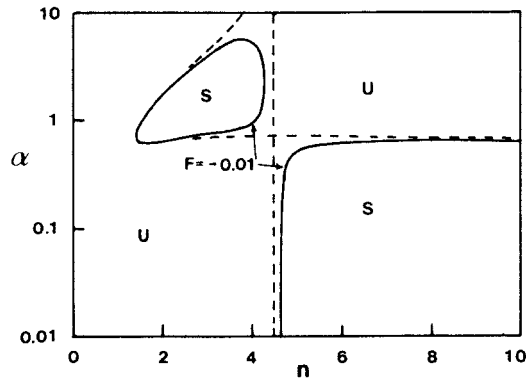


Figure 2.6: *Destabilizing influence of the gravity for a planar Poiseuille flow when the upper layer has a higher density ($m = 20$, $\mathcal{R} = 10$, $S = 0$, $F < 0$ and $\zeta < 0$). (From [YH88b].)*

2.2 Transient simulations of periodic flows

We have seen in section 2.1 how the linear stability or instability of a periodic perturbation of planar Poiseuille flow may be predicted by the resolution of an eigenvalue problem. Another way to predict the behaviour of a perturbation consists in calculating its transient evolution by numerical computation of the perturbed flow. By calculating the transient evolution, we also may predict the behaviour of the perturbed flow when perturbation grows into the nonlinear domain. The present section is devoted to the transient simulation of periodically perturbed Poiseuille flows.

2.2.1 Definition of the problem

In this section, we briefly describe how the periodicity of the problem is modelled and how the parameters of the transient calculations are selected. Then we explain how the initially perturbed flow is obtained and we describe the boundary conditions used for the transient calculations.

Periodicity constraints

All the stability results presented in section 2.1 have been obtained for infinite flows in the x direction. The flows are also periodic in that direction. This allows us to limit our study to a computational domain of finite length.

In order to model the periodicity of the flow, appropriate constraints are imposed on the velocities and on the interface position. The constraints are given by

$$\begin{aligned} \mathbf{v}(0, y) &= \mathbf{v}(L, y), \\ h(0) &= h(L). \end{aligned}$$

Only the pressure field is not strictly periodic. This is due to the fact that, in the base flow, the pressure field is a linear decreasing function of x . However, the perturbation on the pressure field $\Delta p = p - p_0$ (in which p_0 is the pressure in the base flow) is a periodic function of x .

We do not impose any condition on the pressure field: it seems that the absence of periodicity conditions on the pressure does not affect sensibly the behaviour of the flow. The periodicity condition for the pressure seems to be implicitly included in the velocity and interface periodic conditions.

Selection of the parameters

To select the parameters of our transient calculations, we use the results obtained by Yiantsios and Higgins for their stability analysis [YH87a]. In Figure 2.7, we plot the isostability curves corresponding to the case $m = 20$, $\zeta = 1$, $\mathcal{R} = 10$, $F = 0$ and $S = 0$.

For the first calculation, we select a point such that the growth rate $\alpha c_i = 0.4$. For $\alpha = 0.4$, this gives $n \approx 2.63$. We also select parameters for a neutrally stable perturbation ($\alpha = 0.4$ and $n = \sqrt{20} = \sqrt{m}$), and for a stable perturbation

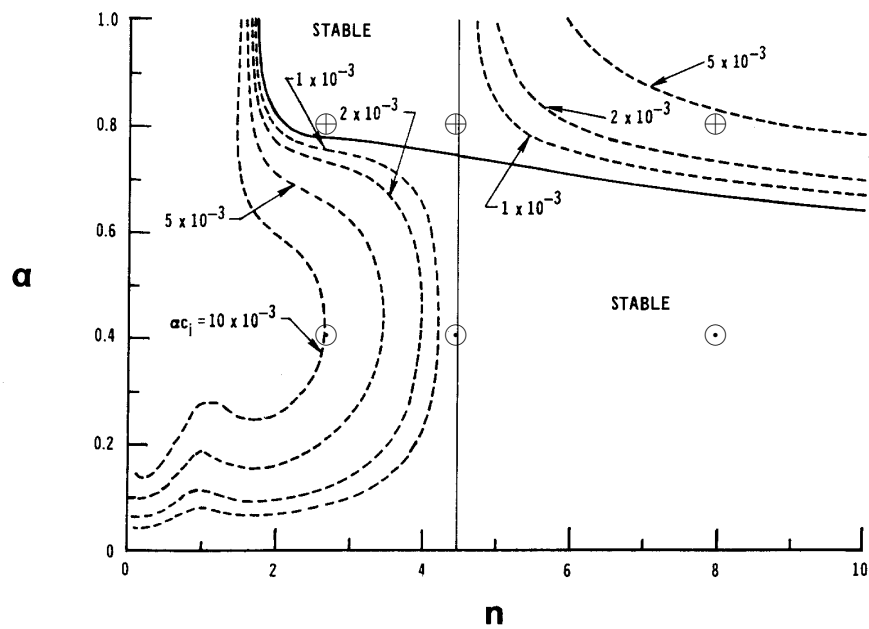


Figure 2.7: Isostability curves for a planar Poiseuille flow ($m = 20$, $\zeta = 1$, $R = 10$, $F = 0$ and $S = 0$). (From [YH87a].) The symbols \ominus represent the points selected for the transient calculations, and the \oplus are the corresponding second harmonics. α_{c_i} is the growth rate of the perturbation.

($\alpha = 0.4$ and $n = 8$). The selected perturbations are located in Figure 2.7 with the symbols \ominus . The second harmonic corresponding to each perturbation are represented with \oplus .

Initially perturbed flow

We wish to calculate the evolution of a slightly perturbed flow for the case $\mathcal{R} = 10$, $m = 20$, $\zeta = 1$, $n = 2.63$ and $\alpha = 0.4$. Gravity and surface tension are not taken into account. For our choice of parameters, we try to obtain a growth rate close to 0.01. The length of the wave corresponding to the wave number $\alpha = 0.4$ is $L = 2\pi/\alpha = 5\pi$. L is also the length of our computational domain (Figure 2.8).

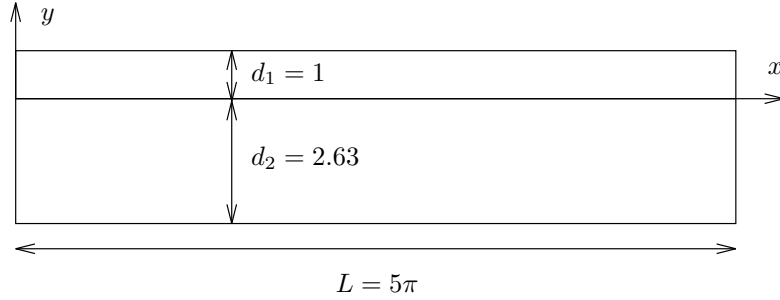


Figure 2.8: Dimensions of the undisturbed computational domain ($\alpha = 0.4$ and $n = 2.63$).

The fluids are pushed between the two plates by a normal force per unit of surface, f_n applied on the left boundary of the domain. To calculate the force, we use the equation (B.1) giving the horizontal pressure gradient in the undisturbed Poiseuille flow. The pressure drop between the inlet and outlet sections is given by the product of the pressure gradient and of the distance between the two sections. Indeed the force applied on the left boundary must compensate the pressure drop due to the viscous dissipation. So

$$f_n = -\frac{\partial p}{\partial x}L = \frac{2(m+n)}{n(n+1)}L.$$

Our first calculations are done on a relatively coarse mesh of 130 elements (Figure 2.9).

Several possibilities may be used to add a small perturbation to the base flow. Our initial flow is obtained by the resolution of the stationary Navier-Stokes equations on a deformed mesh, obtained by the addition of a sinusoidal perturbation on the interface position. The function $h(x)$ describing the position of the interface is initially given by

$$h_{\text{init}}(x) = A_{\text{init}} \sin(\alpha x),$$

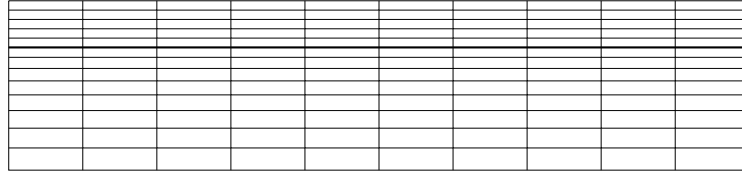


Figure 2.9: *Unperturbed mesh for the first calculations ($\alpha = 0.4$ and $n = 2.63$).*

where A_{init} is the initial amplitude of the perturbation. In our example $A_{\text{init}} = 0.1$. The perturbation of the interface is propagated in the two layers of the mesh with a remeshing rule such that only the y coordinate of the nodes is changed (Figure 2.10).

Inertia terms are neglected for the computation of the initial flow. Along the interface, we impose that the fluids flow tangentially to the fixed interface ($v_n = 0$). The positions of all nodes of the mesh are imposed.

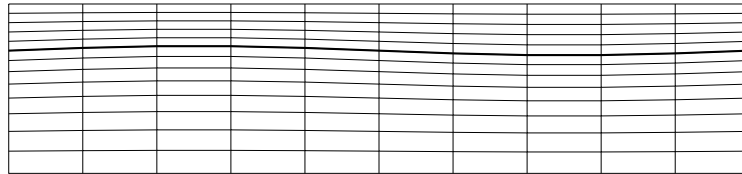


Figure 2.10: *Slightly initial deformed mesh for the transient calculation. ($\alpha = 0.4$, $n = 2.63$ and $A_{\text{init}} = 0.1$.)*

Time-dependent calculations

Once the initial perturbed flow has been obtained, the transient evolution may be calculated. The problem is nearly identical to the problem solved to obtain the perturbed flow, except that inertia terms are taken into account in the momentum equations, and that a kinematic condition is used to calculate the motion of the interface. A summary of the boundary conditions is presented in Figure 2.11.

To propagate the deformation of the interface in the mesh, we use a method of spines. The direction of motion of the nodes is vertical (parallel to y). A Crank-Nicolson scheme is used for the time discretization. The time-step is fixed at 0.25.

2.2.2 Validation of the transient calculations

We present in this section the results obtained for the peculiar case $n = 2.63$ and $\alpha = 0.4$. For that perturbation, a growth rate $\alpha c_i = 0.01$ is expected. We

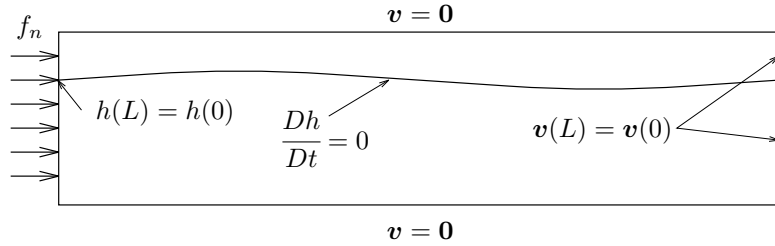


Figure 2.11: *Boundary conditions for the transient simulation of the perturbed flow.*

explain how the calculated results may be analysed and interpreted. For example, we describe how the amplitude of the perturbations is calculated. We also check whether our results are converged by performing numerical calculations with other meshes and time-stepping schemes, and with various values of the time step.

Results for $n = 2.63$

The observation of the interface gives information on the behaviour of the perturbation (Figure 2.12). The shape of the interface is plotted for three values of the time t . In order to make the observation easier, three consecutive space periods have been plotted for each time. It can be seen that the perturbation moves from the left to the right at an approximately constant speed.

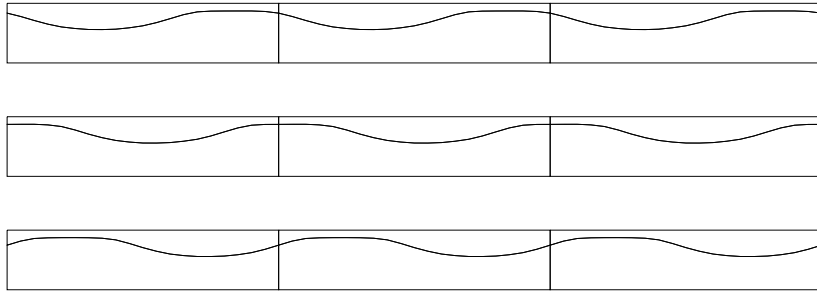


Figure 2.12: *Horizontal movement of the perturbation. The shape of the interface is given at $t = 250$, $t = 252.5$ and $t = 255$ ($\alpha = 0.4$, $n = 2.63$, $m = 20$, $R = 10$, $A_{init} = 0.1$ and $\Delta t = 0.25$).*

The perturbation amplitude is an increasing function of time (Figure 2.13). At the beginning of the calculation, the shape of the interface remains approximately sinusoidal. But for larger values of t (approximately 200), the upper part of the interface flattens. The departure from a sinusoidal shape proves that for large amplitudes, the behaviour of the perturbation no longer is linear.

The velocity and pressure fields are represented for $t = 225$ in Figure 2.14.

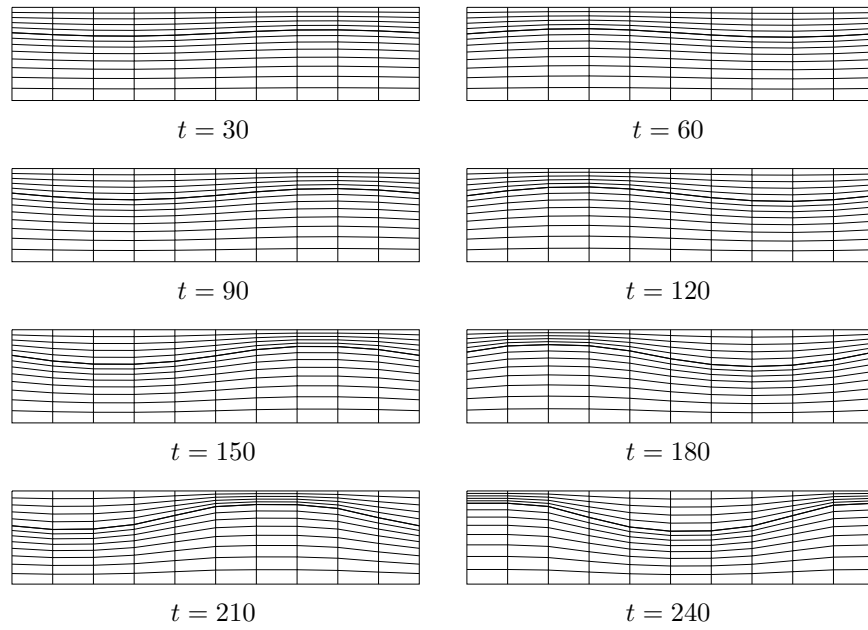


Figure 2.13: *Development of the perturbation of a planar Poiseuille flow ($\alpha = 0.4$, $n = 2.63$, $m = 20$, $\mathcal{R} = 10$, $A_{init} = 0.1$ and $\Delta t = 0.25$).*

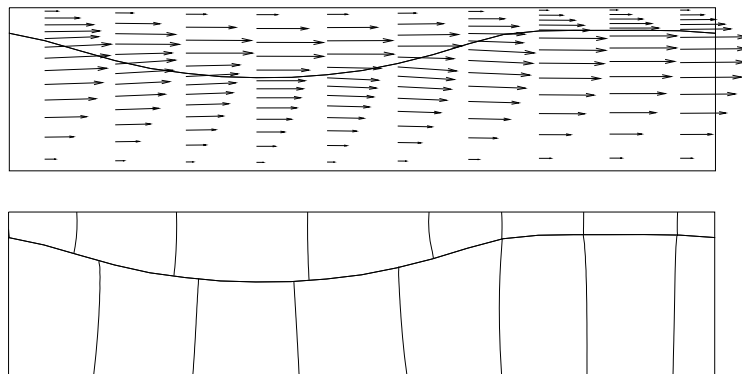


Figure 2.14: *Representation of the flow. The upper part gives the velocity field, and in the lower part, iso values of the pressure are plotted ($\alpha = 0.4$, $n = 2.63$, $m = 20$, $\mathcal{R} = 10$, $A_{init} = 0.1$ and $t = 225$).*

Estimate of the perturbations amplitude

Assuming that the behaviour of the perturbation is linear, we may estimate its amplitude A by the use of the following set of equations:

$$h_1 = \frac{\alpha}{\pi} \int_0^{\frac{2\pi}{\alpha}} h(x) \sin \alpha x dx,$$

$$h_2 = \frac{\alpha}{\pi} \int_0^{\frac{2\pi}{\alpha}} h(x) \cos \alpha x dx,$$

$$A = \sqrt{h_1^2 + h_2^2}.$$

If the interface departs from a sinusoidal shape, other informations are needed to describe its shape. The expansion of $h(x)$ in a Fourier series will also provide harmonics, the order of which is larger than one. The amplitude of the higher order harmonics present in the perturbation may be estimated with the following equations

$$h_1^p = \frac{\alpha}{\pi} \int_0^{\frac{2\pi}{\alpha}} h(x) \sin p\alpha x dx, \quad (2.12)$$

$$h_2^p = \frac{\alpha}{\pi} \int_0^{\frac{2\pi}{\alpha}} h(x) \cos p\alpha x dx, \quad (2.13)$$

$$A_p = \sqrt{(h_1^p)^2 + (h_2^p)^2}, \quad (2.14)$$

in which p denotes the harmonic number. However, the amplitude A_1 of the first harmonic gives interesting informations if the perturbation is small. To simplify the notations we write $A = A_1$.

The amplitude as a function of time is represented in Figure 2.15. We also plot the function $0.1 \exp(t/100)$ giving the amplitude we would obtain for a perturbation growing exponentially. For small amplitudes, the two curves are nearly parallel. But for higher values of t , the growth rate of the perturbation progressively decreases. That is normal, for the amplitude of the perturbation cannot exceed 1, the thickness of the upper layer. Thus, the decrease of the growth rate is a nonlinear phenomenon related to the flattening of the upper part of the interface observed in Figure 2.13. More information on nonlinear phenomena in perturbed flows is given in section B.2.

Influence of the time-stepping scheme

For the time discretization, we use a Crank-Nicolson scheme. In Figure 2.16, we present the curves of the amplitude of the perturbation as a function of time for the Crank-Nicolson scheme and for the Galerkin scheme with various values of the time step.

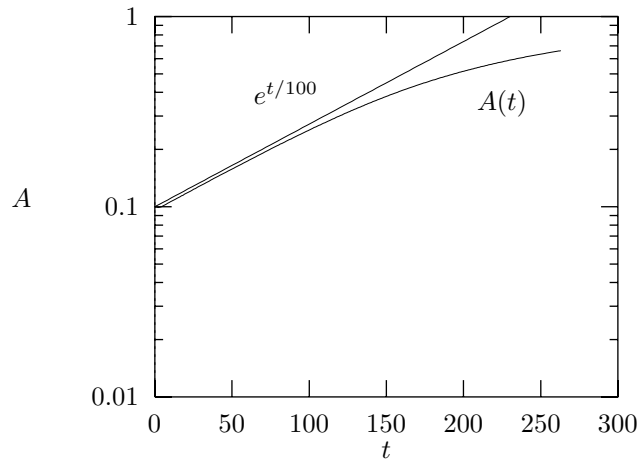


Figure 2.15: *Amplitude of the perturbation as a function of time* ($\alpha = 0.4$, $n = 2.63$, $m = 20$, $\mathcal{R} = 10$, $A_{\text{init}} = 0.1$ and $\Delta t = 0.25$).

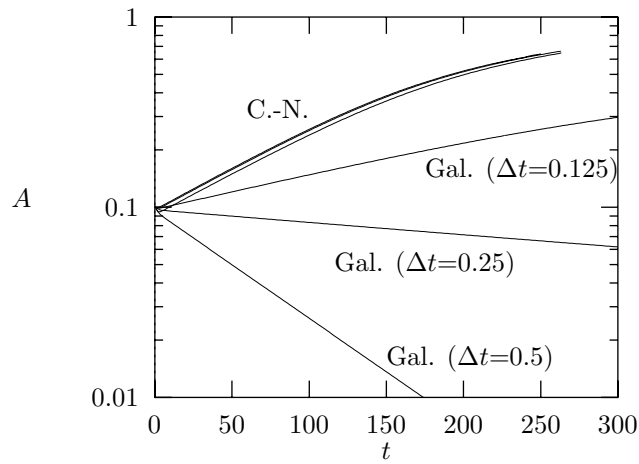


Figure 2.16: *Influence of the time-stepping scheme on the calculation of the amplitude of the perturbation* ($\alpha = 0.4$, $n = 2.63$, $m = 20$, $\mathcal{R} = 10$ and $A_{\text{init}} = 0.1$).

It is well known that the Galerkin scheme has damping properties when used to discretize hyperbolic equations. We see that for $\Delta t = 0.5$ or $\Delta t = 0.25$, the use of the Galerkin scheme leads to a predicted amplitude decreasing with time. Only for small values of the time step, an increasing amplitude may be obtained. Very small time steps should be used to produce a curve close to the Crank-Nicolson curves. A similar comparison could be made between the Crank-Nicolson scheme and the implicit Euler scheme, the damping properties of which are still more important than that of the Galerkin scheme.

Small differences may also be observed between the amplitude curves calculated with a Crank-Nicolson scheme. But the differences are very small and we are satisfied with the curves obtained with $\Delta t = 0.25$.

Influence of the mesh

We calculate the growth rate of the perturbation on a more refined mesh in the x direction. The coarse and refined meshes are plotted in Figure 2.17 for comparison.

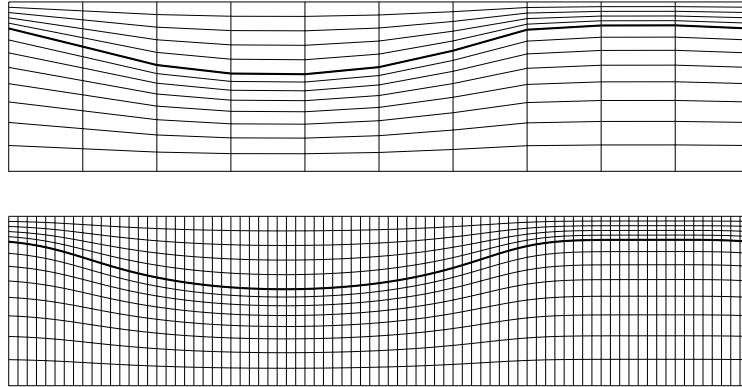


Figure 2.17: *Comparison of the coarse and refined meshes used for the transient calculations ($\alpha = 0.4$, $n = 2.63$, $m = 20$, $\mathbb{R} = 10$, $A_{\text{init}} = 0.1$ and $t = 225$).*

The growth rates obtained with both meshes are plotted in Figure 2.18. The two curves are nearly superposed and cannot be distinguished. The maximum relative difference between the two curves is approximately 0.25 %. We conclude that the results obtained with the coarse mesh are good. However all amplitude curves given in the rest of the chapter have been plotted from results of calculations done with refined meshes.

2.2.3 Results analysis

In this section, we analyse the results of the transient calculations. We first calculate the transient evolution of perturbed flows for other values of the thickness ratio n . The interpretation of those results is not straightforward, because

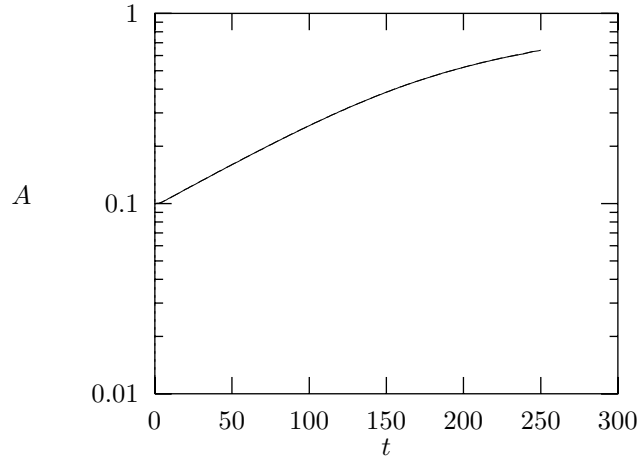


Figure 2.18: *Influence of the mesh on the calculation of the amplitude of the perturbation ($\alpha = 0.4$, $n = 2.63$, $m = 20$, $\mathcal{R} = 10$, $A_{\text{init}} = 0.1$ and $\Delta t = 0.125$). The two curves are nearly superposed and cannot be distinguished.*

unexpected oscillations are observed in amplitude curves, and higher order harmonics also may be observed in the flow. Those observations have led us to study the behaviour of higher order harmonics present in the flow. We also investigate the consequences of interference between the various modes simultaneously observed in the perturbed flow.

Results for other values of the thickness ratio n

Transient calculations of initially perturbed flows also may be done for other values of the parameters defining the base flow. For example, we plot in Figure 2.19 the amplitude of the perturbation as a function of time for various values of the thickness ratio n . The value $n = \sqrt{20} = \sqrt{m}$ is such that the linear stability analyses predict a neutral stability (i.e. a zero growth rate of the perturbation). For $n = 8$ we expected a decreasing curve (and obtained it, at least for small values of t).

However, because of the small amplitude of the perturbation, we expected straight lines for $n = \sqrt{20}$ and $n = 8$, but we obtain wavy curves. The amplitude curves do not seem to vary with modification of the mesh and time step.

Another surprising phenomenon may be observed for $n = \sqrt{20}$, the interface does not keep its sinusoidal shape. It appears clearly in Figure 2.20, where two local maxima of the position of the interface may be seen. This proves that smaller wavelength periodic modes are present in the perturbed flow.

Note that the results presented in section 2.2.2 for $n = 2.63$ were in good agreement with linear stability analyses results and physical intuition. But, at first sight, the results for $n = \sqrt{20}$ and $n = 8$ are in contradiction with the theoretical results given in section 2.1.

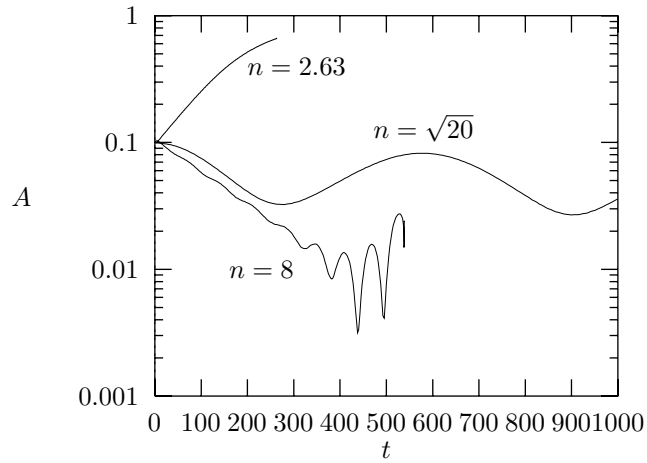


Figure 2.19: Amplitude of the perturbation as a function of time for various values of n ($\alpha = 0.4$, $m = 20$, $\mathcal{R} = 10$, $A_{\text{init}} = 0.1$ and $\Delta t = 0.25$).

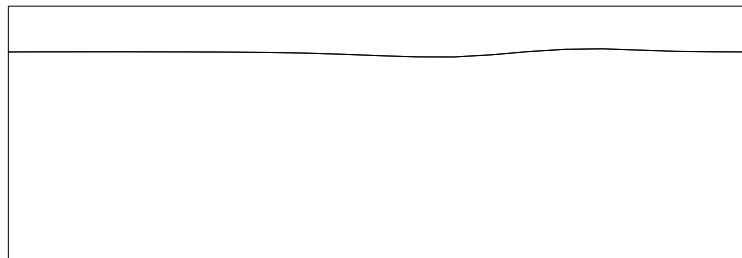


Figure 2.20: Configuration of the layers for $t = 185$ ($\alpha = 0.4$, $m = 20$, $\mathcal{R} = 10$, $m = \sqrt{20}$, $A_{\text{init}} = 0.1$ and $\Delta t = 0.25$).

Now, the questions that arise are: how do the smaller wavelength perturbations appear in the perturbed flow? How can we explain the oscillations of amplitude curves in Figure 2.19? Can those problems be related to discretization or modelling errors? If a satisfying answer may be found for the first two questions, the third question will be answered too. In order to explain the surprising behaviour of the perturbed flow, we investigate the behaviour of higher order perturbation harmonics.

Observation of higher order harmonics

The amplitude of the higher order harmonics present in the flow are estimated with equations (2.12-2.14). We plot in Figure 2.21 the amplitude of the second harmonic as a function of time for three values of n .

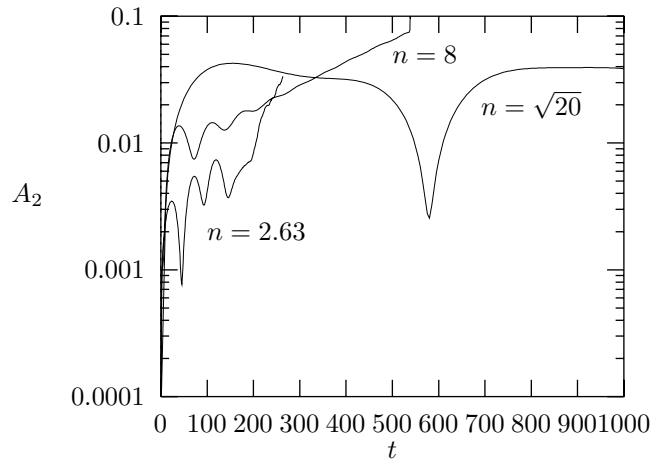


Figure 2.21: Amplitude of the second harmonic of the perturbation as a function of time for various values of n ($\alpha = 0.4$, $m = 20$, $\mathcal{R} = 10$ and $A_{\text{init}} = 0.1$).

The examination of Figures 2.19 and 2.21 leads to the following observations:

- The amplitude of the second harmonic is zero for $t = 0$ and grows rapidly towards a finite value for $t \lesssim 15$.
- For $n = 2.63$ and $n = 8$, the oscillations seem to be associated with small amplitude of the corresponding harmonic. They have a large frequency.
- For $n = \sqrt{m}$, the amplitude oscillates at a small frequency around an approximately constant value. The amplitude curves qualitative behaviour is very different for $n = \sqrt{m}$ than for other values of n .

In the next section, we try to explain the presence of oscillations in amplitude curves by interference phenomena.

Interference between two modes

We have seen that various wavelength perturbations are present in the flow. But even if only one wavelength was present, we could not conclude that only one mode is present. Indeed, we have seen in section 2.1 that in their linear stability study, Yiantsios and Higgins calculate the growth rate of various modes of wavenumber α . Then, they select the fastest growing mode to determine whether the flow is stable or not for the selected value of α .

This means that several modes of identical wavelength $2\pi/\alpha$ may be present in the flow at a given time. Provided the amplitude of these modes is small, they are essentially decoupled and behave linearly. Each mode perturbs the interface independently. The interface has a sinusoidal shape given by the sum of the contributions of the various modes.

We will show that the various modes present in the flow may give rise to interference phenomena in the amplitude curves.

For only one mode present in the perturbation, and assuming that its behaviour is linear, the position of the interface is given by a function of x and t of the form

$$\begin{aligned} h(x, t) &= \Re \left\{ g e^{i\alpha(x - c_r t - i c_i t + \beta)} \right\} \\ &= g e^{\alpha c_i t} \{ \cos \alpha x \cos[\alpha(\beta - c_r t)] - \sin \alpha x \sin[\alpha(\beta - c_r t)] \}, \end{aligned}$$

In which g is the amplitude of the mode, \Re is the real value of a complex number and β is a horizontal shift parameter. The amplitude of the perturbation on the interface may be computed with the usual formulas:

$$\begin{aligned} h_1(t) &= \frac{\alpha}{\pi} \int_0^{\frac{2\pi}{\alpha}} h(x, t) \cos(\alpha x) dx, \\ &= g e^{\alpha c_i t} \cos[\alpha(c_r t - \beta)]. \end{aligned}$$

$$\begin{aligned} h_2(t) &= \frac{\alpha}{\pi} \int_0^{\frac{2\pi}{\alpha}} h(x, t) \sin(\alpha x) dx, \\ &= g e^{\alpha c_i t} \sin[\alpha(c_r t - \beta)]. \end{aligned}$$

$$\begin{aligned} A(t) &= \sqrt{h_1^2(t) + h_2^2(t)}, \\ &= g e^{\alpha c_i t}. \end{aligned}$$

We obtain of course an amplitude increasing (or decreasing) exponentially with time.

If several modes of wavenumbers α are present in the flow, the two components of the amplitude are given by

$$h_1(t) = \sum_{l=1}^n g_l e^{\alpha c_i^l t} \cos[\alpha(c_r^l t - \beta_l)],$$

$$h_2(t) = \sum_{l=1}^n g_l e^{\alpha c_i^l t} \sin[\alpha(c_r^l t - \beta_l)].$$

and the amplitude is

$$A(t) = \sqrt{\left(\sum_{l=1}^n g_l e^{\alpha c_i^l t} \cos[\alpha(c_r^l t - \beta_l)] \right)^2 + \left(\sum_{l=1}^n g_l e^{\alpha c_i^l t} \sin[\alpha(c_r^l t - \beta_l)] \right)^2}.$$

If only two modes are present in the flow, the last equation may be developed as follows:

$$A(t) = \sqrt{g_1^2 e^{2\alpha c_i^1 t} + g_2^2 e^{2\alpha c_i^2 t} + 2g_1 g_2 e^{\alpha(c_i^1 + c_i^2)t} \cos\{\alpha[(c_r^1 - c_r^2)t - (\beta_1 - \beta_2)]\}}. \quad (2.15)$$

In this expression, g_1 and g_2 give the amplitudes of the two modes. c_i^1 and c_i^2 are related to their respective growth rates αc_i . The difference $c_r^2 - c_r^1$ is proportional to the difference of translation velocity of the modes. The oscillation frequency of the amplitude curves is given by $\alpha \|c_r^2 - c_r^1\|/2\pi$. In the square root, the first two terms correspond respectively to the amplitudes of the first and second modes. The last term is related to the interference between the two modes. This term generates the oscillations observed in Figure 2.19.

In order to check the validity of our explanation, we try to find two modes of the first harmonic that interfere to give the curve $n = \sqrt{20}$ in Figure 2.19. We search the parameters g_1 , g_2 , c_i^1 , c_i^2 , $c_r^2 - c_r^1$ and $\beta_2 - \beta_1$ of equation (2.15) that minimize

$$\int_{t_0}^{t_f} (A_{\text{approx}}(t) - A_{\text{fem}}(t))^2 dt,$$

in which A_{approx} is the amplitude of our approximating two modes perturbation, and A_{fem} is the amplitude given by the transient numerical calculation. For the various parameters, we find the values given in table 2.1. The curve approximating the amplitude of the perturbation on the interface corresponding to the parameters is given in Figure 2.22.

Table 2.1: Parameters describing the two interfering modes of Figure 2.22.

parameters	values
g_1	0.03065941059219
g_2	0.06194600564449
c_i^1	-0.00074933164247
c_i^2	-0.00070911707249
$c_r^2 - c_r^1$	0.02696972599487
$\beta_2 - \beta_1$	0.18015331517018

It appears clearly in Figure 2.22 that more than two modes of the first harmonic have to be introduced in the approximating perturbation to better

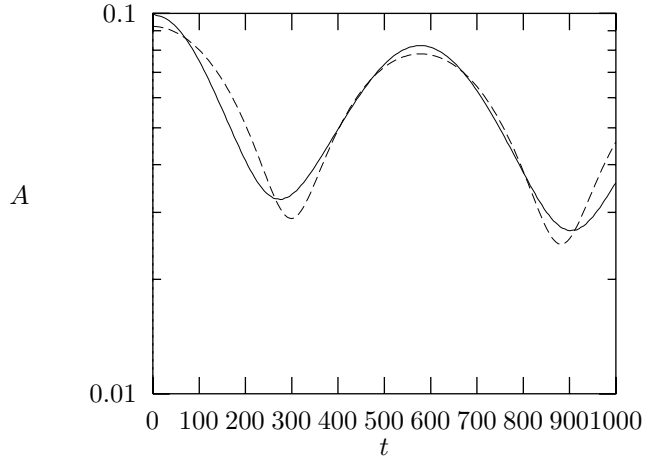


Figure 2.22: Approximation of the interference phenomenon for two interfering modes. The continuous curve gives the results of the finite element calculation A_{fem} , and the dashed line corresponds to the approximating curve with two modes A_{approx} . The parameters describing the interfering modes are given in table 2.1.

approximate the finite element amplitude curve. But the interference of only two modes gives a good approximation of the oscillations of the amplitude curve. The growth rates of the modes given respectively by αc_i^1 and αc_i^2 are negative and small compared to the growth rate for $n = 2.63$.

2.3 Planar coextrusion in a channel

In the previous sections of this chapter, we have investigated the behaviour of flows periodic in the x direction. Actually, in practical situations, the observed flows are never periodic in space. In coextrusion processes, the die in which the fluids are flowing has a finite length, and the amplitude of the perturbations depends on the distance to the inlet section. In this section, we investigate the stability of the interface between two fluids coextruded in a long channel (Figure 2.23).

The thickness of the upper layer is fixed to one. The thickness of the lower layer is equal to n . The length of the channel is 250. The vertical distribution of the elements in the mesh is identical to the distribution used for the periodic calculations. Horizontally, the mesh is divided in 320 equally distributed elements.

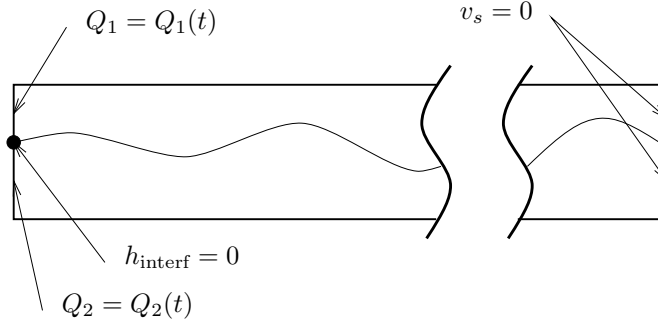


Figure 2.23: *Geometry of the computational domain for the two layer coextrusion in a channel. The fluids are injected at the left, and exit at the right.*

2.3.1 Inflow boundary conditions

In order to perturb the flow, we make the flow rates of both fluids depend on time, the total flow rate remaining constant. Basically, two kinds of perturbations may be added to the base flow:

- The flow may be perturbed periodically in time. For example, by adding a sinusoidal perturbation $\sin(\omega t)$, for $t \in [0, \infty]$.
- The perturbation may be added during a small interval of time $t \in [0, t_{\max}]$.

In our calculations, the general form for the dependence of the flow rates on time is given by

$$Q_1(t) = \begin{cases} Q_{10} + B \sin(\omega t) & \text{if } 0 < t < \Delta t_{\text{perturb}}, \\ Q_{10} & \text{if } t > \Delta t_{\text{perturb}}, \end{cases}$$

$$Q_2(t) = \begin{cases} Q_{20} - B \sin(\omega t), & \text{if } 0 < t < \Delta t_{\text{perturb}}, \\ Q_{20} & \text{if } t > \Delta t_{\text{perturb}}, \end{cases}$$

in which B is related to the amplitude of the imposed perturbation, ω to its wavelength, and $\Delta t_{\text{perturb}}$ is the interval of time during which the perturbation is added to the base inflows. We assume that before entering into the channel, the fluids are separated by a plate. Therefore, the position of the interface on the inlet section is fixed ($h = 0$). At the outlet section, we impose $f_n = 0$ and $v_s = 0$. For other boundary conditions, the problem is very similar to the periodic problem described in section 2.2, and the characteristic dimensionless numbers are those presented in section 2.1.1.

We select ω such that the wavelength of the perturbations is approximately equal to 5π , corresponding to the wavenumber $\alpha = 0.4$ used so far. Thus, ω is related to the translation velocity of the perturbation αc_r by $2\pi\alpha c_r = 5\pi = 2\pi/\alpha$ or $\omega = \alpha^2 c_r$.

Four different calculations have been done: the varying parameters used for each calculation are summarized in table 2.2. (The symbol “#” corresponds

Table 2.2: Parameters of the four calculations of perturbed coextrusion flows in a channel.

#	n	B	ω	$\Delta t_{\text{perturb}}$
1	2.63	0.15	0.550	∞
2	8.00	0.25	0.328	∞
3	2.63	0.15	0.550	11.424
4	8.00	0.25	0.328	19.156

to the referring number of the calculation.) The upper and lower flow rates imposed on the inlet section are given by the two terms of equation (B.2). In order to impose the inlet velocity fields, we calculate on each part of the inlet a parabolic profile. This parabolic profile is imposed as a boundary condition on the velocity for the resolution of the Navier-Stokes equations in both layers. For calculations 3 and 4, the value of interval of time $\Delta t_{\text{perturb}}$ is approximately the duration of one time period of the sinusoidal oscillation.

In sections 2.3.2 and 2.3.3, we analyse the results respectively for perturbations periodic in time, and for perturbations added during a small interval of time.

2.3.2 Periodic perturbations in time

In this section, we present the results for the calculations 1 and 2. The thickness ratios are $n = 2.63$ and $n = 8$. They correspond respectively to a stable and an unstable perturbation. To represent the evolution of the perturbation, we only will plot the height h of the interface as a function of the horizontal position x and for various values of the time t .

The aspect ratio $(y_{\text{max}} - y_{\text{min}})/(x_{\text{max}} - x_{\text{min}})$ of the computational domain being very small, we use different scales for the coordinates x and y . For the x (i.e. horizontal) direction, 52 mm on the plots represent a dimensionless length of 250. For the y (vertical) direction 14 mm on the plots represent a dimensionless height of 1.09. To recover the aspect ratio of the calculations, the vertical distances should be divided by approximately 62.

For $n = 8$, the perturbation imposed on the inflows is expected to be stable (i.e., the amplitude of the oscillations is expected to decrease with the distance to the inlet section). In the last plot of Figure 2.25 ($t = 240$), we see that the amplitude of the perturbations is roughly independent of the horizontal position in the channel. But one observes that the shape of the oscillations depends on the position: close to the inlet section (left side), the oscillations are more regular, and their wavelength is larger than the oscillations on the right side of the channel.

This may easily be explained if we remember that for $n = 8$, the first harmonic of the perturbation is stable, and that the higher order harmonics are unstable. In our channel flow, the first harmonic dominates close to the inlet section, but its amplitude progressively decreases. However, the higher order

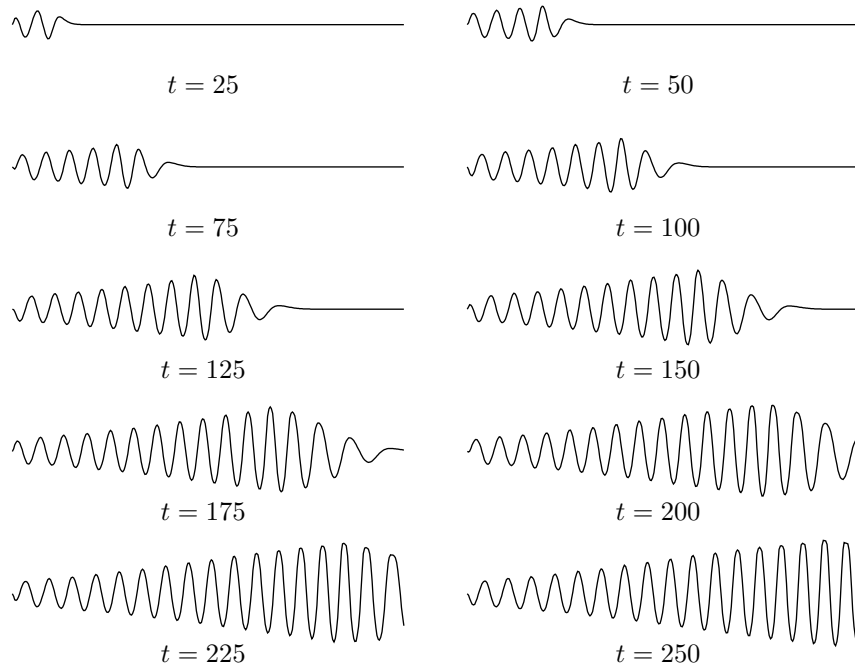


Figure 2.24: *Development of a perturbation in a two layer Poiseuille flow in a channel ($\omega = 0.55$, $n = 2.63$, $m = 20$, $\mathcal{R} = 10$, $B = 0.15$, and $\Delta t = 0.25$). The results correspond to calculation 3 in table 2.2.*

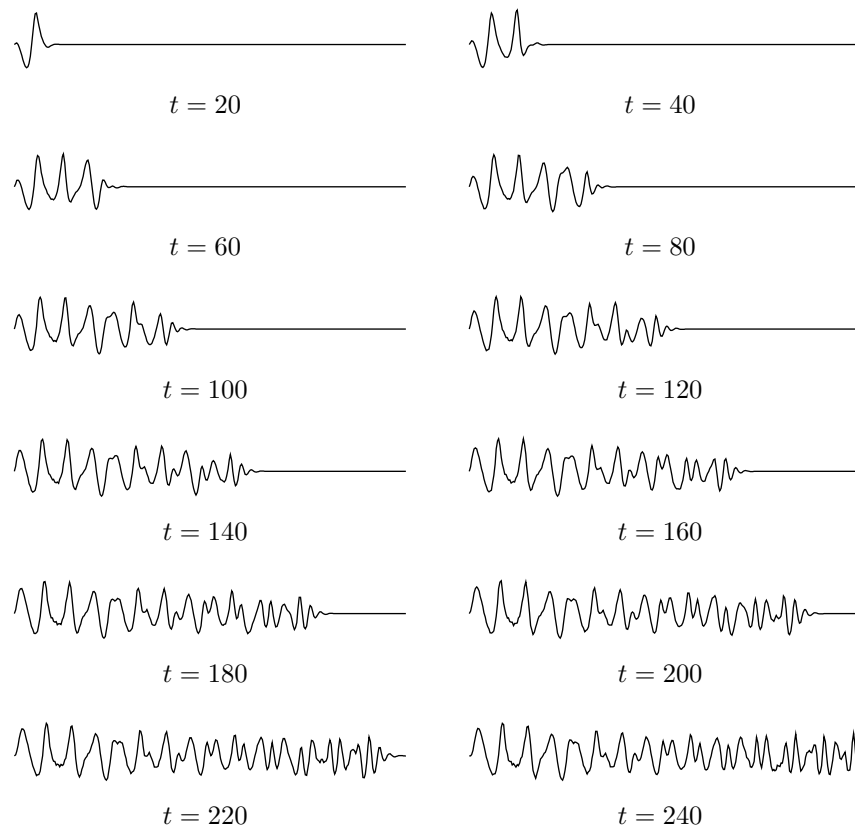


Figure 2.25: *Development of a perturbation in a two layer Poiseuille flow in a channel ($\omega = 0.328$, $n = 8$, $m = 20$, $\mathcal{R} = 10$, $B = 0.25$ and $\Delta t = 0.25$). The results correspond to calculation 2 in table 2.2.*

harmonics are present close to the inlet section because of the nonlinearities of the flow. Their respective amplitudes are small in that area, but they grow while being translated towards the exit. During that process, the first harmonic is progressively “replaced” by interacting higher order harmonics. The interaction between those harmonics is responsible for the “chaotic” behaviour of the interface.

2.3.3 Perturbation during a small interval of time

In this section, we present the results for the calculations 3 and 4. Here again, the thickness ratios are $n = 2.63$ and $n = 8$ respectively in Figures 2.26 and 2.27.

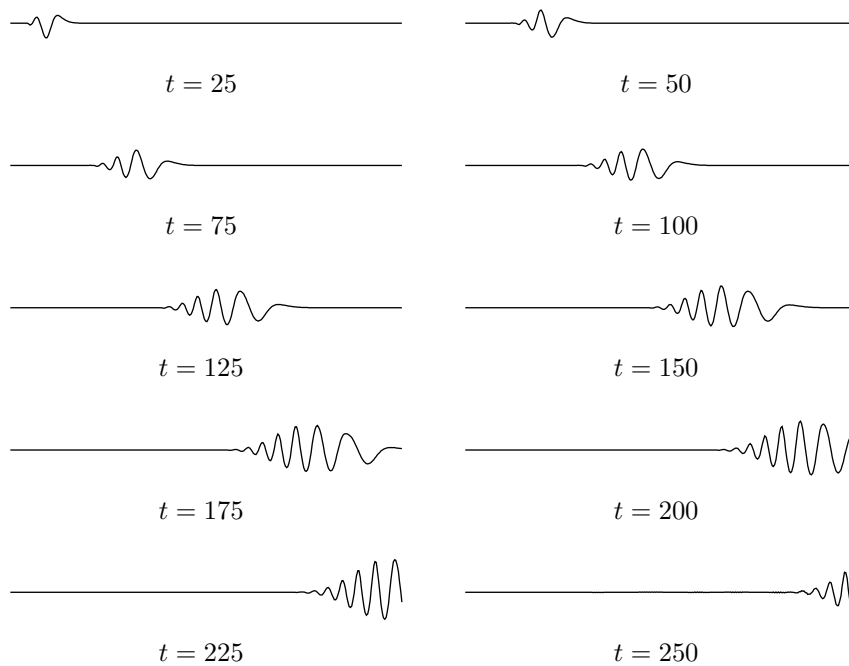


Figure 2.26: *Development of a perturbation in a two layer Poiseuille flow in a channel ($\omega = 0.55$, $n = 2.63$, $m = 20$, $\mathcal{R} = 10$, $B = 0.15$, $\Delta t_{\text{perturb}} = 11.424$ and $\Delta t = 0.25$). The results correspond to calculation 3 in table 2.2.*

For $n = 2.63$, the initial wave packet is translated towards the exit. During its displacement, the amplitude of the waves increases, and the packet disperses. The wavelength of the oscillations remains approximately constant during the calculation. Observing the interface at a selected point in the channel (for example the mid point $x = 125$), we see that after the passage of the wave packet, the interface recovers its original shape. It seems that no wavy interface

may be observed in our calculations without imposing any perturbation on the inlet section.

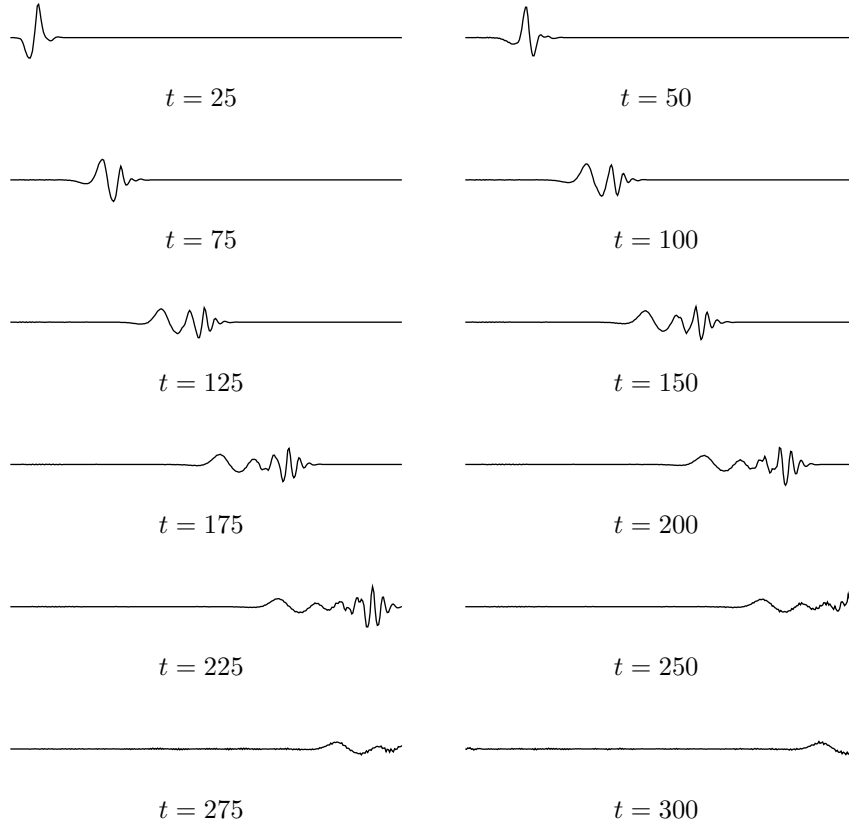


Figure 2.27: *Development of a perturbation in a two layer Poiseuille flow in a channel ($\omega = 0.55$, $n = 8$, $m = 20$, $\mathcal{R} = 10$, $B = 0.15$, $\Delta t_{\text{perturb}} = 11.424$ and $\Delta t = 0.25$). The results correspond to calculation 4 in table 2.2.*

For $n = 8$, the perturbation of the inflow during a small interval of time leads to a slightly different qualitative behaviour (Figure 2.27). The wave packet is split into two sets: a short wavelength one and a large wavelength one. The short wavelength packet has a larger translation velocity than the long wavelength one, and exits the channel first. Its amplitude increases while the amplitude of the long wavelength oscillations progressively decreases. This observation is consistent with the conclusions of the linear stability analyses and with our transient periodic calculations.

We also observe very small wavelength oscillations of the interface. But the wavelength of those oscillations is identical to the length of the elements of the mesh. It is possible that those oscillations are related to an interfacial instability. Indeed, we have seen in section 2.1.3, that for vanishing surface tension and

gravity, and for small wavelength perturbations (large values of α), the area of stability is limited to a very small interval of thickness ratio n . In order to correctly model the growth of those very short wavelength perturbations, the mesh should be refined both in horizontal direction and vertical direction close to the interface. This would result in an important increase of computational cost of the calculations. Actually, with only one calculation, it is difficult to obtain information on phenomena occurring both at very small and intermediate length scales. Moreover, the very small wavelength oscillations observed in Figure 2.27 have probably been initiated by discretization errors. Therefore, we do not try to further investigate those very small wavelength perturbations.

2.4 Literature review for core-annular flows

In former sections, comparisons were done between linear stability analyses, and the results of our transient calculations. It is also interesting to compare the results of transient calculations with experimental observations of the non-linear growth of perturbations. However, for planar flows, such a comparison would probably give very disappointing results for the assumption of two-dimensionality only may be approximately satisfied in practical situations. The problem arises mainly from the fact that the flow is always limited in the third direction z . A very large experimental device should be used to eliminate the effect of lateral walls.

In order to avoid this difficulty, we investigate now the stability of core-annular flows. For such flows, results of experimental observations of oil and water flowing in tubes have been published [CGH61, MBD⁺92, CBJ90, BCJ92, JR93b], and assuming that the flow is axisymmetric, comparisons can be done with the results of our transient calculations on two-dimensional computational domains. Actually, the fluids have different densities, and the assumption of axisymmetric flow only is valid for vertical flows. Thus, the comparisons are done with vertical flows experiments. We have an “up”-flow when the fluids are pushed against gravity, and a “down”-flow when they flow towards the same direction as gravity. The aim of this section is to prove that our transient calculations allow us to predict the evolution of an unstable small amplitude perturbation towards a nonlinear flow regime.

The configuration of the base core-annular flow we are going to study is given in Figure 2.28. The internal radius of the pipe is R_2 . The radius of the core layer is R_1 . We assume that in all our calculations, the axis of the pipe is vertical and that gravity is parallel to this axis, oriented towards the bottom (negative values of z), and that its value is g . In following sections, we often denote the core and annular layer fluids with “oil” and “water”, because those two fluids were used in most experiments.

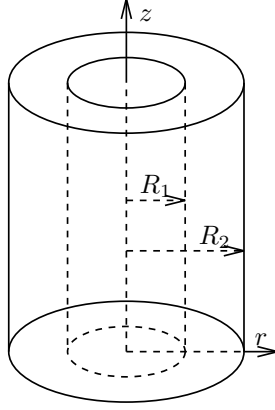


Figure 2.28: Configuration of the core-annular flow.

2.4.1 Dimensionless numbers

In our calculations, we solve dimensionless equations. Lengths are scaled with R_1 , velocity is scaled with the centerline velocity v_0 , time with R_1/v_0 , pressure with $\rho_1 v_0^2$, gravity with v_0^2/R_1 , surface tension with $\rho_1 v_0^2 R_1$, and the flow rates with $v_0 R_1^2$. In order to simplify the notations, we use the same symbols to write the dimensional and dimensionless equations. The momentum equations are

$$\begin{aligned}\frac{D\mathbf{v}_1}{Dt} &= -\nabla p_1 + \frac{1}{\mathcal{R}_1} \nabla^2 \mathbf{v}_1 + \mathbf{g}, \\ \zeta \frac{D\mathbf{v}_2}{Dt} &= -\nabla p_2 + \frac{1}{\mathcal{R}_2} \nabla^2 \mathbf{v}_2 + \zeta \mathbf{g},\end{aligned}$$

where

$$\zeta = \frac{\rho_2}{\rho_1}, \quad \mathcal{R}_1 = \frac{v_0 R_1 \rho_1}{\mu_1}, \quad \mathcal{R}_2 = \frac{v_0 R_1 \rho_1}{\mu_2}.$$

The radius ratio is noted $a = R_2/R_1$.

The difference between our dimensionless equations, and the equations of Preziosi, Chen and Joseph [PCJ89], comes from the fact that they use respectively ρ_1 and ρ_2 to adimensionalize their equations in each layer. The correspondence between the Reynolds numbers is given by

$$\mathcal{R}_1 = \mathcal{R}_1^{\text{PCJ}}, \quad \mathcal{R}_2 = \frac{\mathcal{R}_2^{\text{PCJ}}}{\zeta}.$$

Moreover, their dimensionless surface tension is given by

$$J^* = \frac{\gamma R_2}{\rho_1 \nu_1^2},$$

in which ν_1 is the kinematic viscosity of the upper layer ($\nu_1 = \mu_1/\rho_1$). The advantage of this choice is that their surface tension parameter is related to

the radius of the pipe and material parameters characterizing the fluids. Our dimensionless surface tension is given by

$$S = \frac{\gamma}{\rho_1 v_0^2 R_1},$$

and thus also depends on the oil and water flow rates.

2.4.2 Linear stability

We summarize in this section some results of studies of the linear stability of Newtonian core-annular flows. The methods used for these studies are similar to what we have presented in section 2.1. We essentially present the results of Preziosi, Chen and Joseph [PCJ89], and discuss the effects of surface tension and inertia.

Perturbations

In order to study the linear stability of axisymmetric Poiseuille flows, small amplitude perturbations are added to the base flow, and the Orr-Sommerfeld equations for core-annular flows are established. As has been shown in section 2.1.3, the Orr-Sommerfeld equations lead to an eigenvalue problem that can be solved analytically for large or small wavelength perturbations or numerically for intermediate wavelengths.

The general form of the periodic perturbations is

$$\begin{pmatrix} \mathbf{v}' \\ p' \end{pmatrix} (r, \theta, z, t) = \begin{pmatrix} \mathbf{v}_0 \\ p_0 \end{pmatrix} (r) \exp(i\alpha(z - ct) + in\theta),$$

$$h'(\theta, z, t) = h_0 \exp(i\alpha(z - ct) + in\theta),$$

in which \mathbf{v}' , p' and h' are the perturbations on the velocity, the pressure and the interface position respectively, θ is the azimuthal coordinate, α and n are the axial and azimuthal wavenumbers respectively, and $c = c_r + ic_i$ is a complex number related to the growth rate and the translation velocity of the perturbations.

Depending on the value of n , we may distinguish two different kinds of perturbations: the axisymmetric perturbations ($n = 0$) and the non-axisymmetric ones ($n > 0$). Our aim being to calculate the transient nonlinear evolution of perturbations, we limit our investigations to axisymmetric perturbations. This allows us to calculate the flow on a two-dimensional domain. However, non-axisymmetric flows are often observed in experimental studies, especially in down flows [CBJ90, BCJ92, JR93b].

Linear stability results for core-annular flows

Preziosi, Chen and Joseph use a numerical technique to discretize and solve the eigenvalue problem and investigate the linear stability for intermediate wavelength perturbations [PCJ89]. They investigate the effects of the wavenumber

α , of the Reynolds numbers, surface tension and gravity. They plot neutral curves in the plane (α, \mathcal{R}_1) and for various values of the viscosity ratio m (Figure 2.29).

Let us first examine the curve $m = 0.7$. For such a value of the viscosity ratio, the unstable areas are located in the lower left, and upper right corners of the plot:

- In the lower left corner, the instability occurs at small Reynolds numbers and for small values of the wavenumber α (i.e. large values of the axial wavelength). The instability is caused by capillarity: the interface tries to reach a configuration for which its area is minimum for given volumes of oil and water. It easily may be demonstrated that such an instability cannot occur for values of α larger than one, and the neutral stability curves confirm this result.
- In the upper right corner, the instability occurs at larger values of the wavenumber α and of the Reynolds number \mathcal{R}_1 . This instability is caused by inertia.
- There exists an interval $[\mathcal{R}_L, \mathcal{R}_U]$ in which the flow is stable for all values of the axial wavenumber α . In that area, the small wavelength capillary instability is compensated by a “thin layer effect” (see section 2.1.4).

Two conditions are needed to produce a thin-layer effect: the viscosity difference between the two fluids must be sufficiently large, and the thickness of the lower viscosity layer must be sufficiently small compared to the thickness of the other layer (here, the core layer of radius R_1). When the viscosity ratio m progressively tends towards one, the difference of the viscosities of the two layers progressively vanishes. Therefore, the interval $[\mathcal{R}_L, \mathcal{R}_U]$ becomes progressively smaller and finally disappears around $m \approx 0.77$. Of course, when the larger viscosity fluid is in the annular layer, the flow is unstable as has been shown by Hickox and Joseph, Renardy and Renardy [Hic71, JRR84].

The results plotted in Figure 2.29 are calculated for a radius ratio $a = 1.25$. If this ratio increases, the thin-layer effect progressively disappears. Joseph, Renardy and Renardy and Preziosi, Chen and Joseph show that the stabilizing thin-layer effect cannot compensate instabilities for a radius ratio larger than approximately 1.5 (this value may vary with other parameters like the viscosity ratio and surface tension).

For large values of the Reynolds number \mathcal{R}_1 , surface tension prevents the growth of small wavelength perturbations. But the stabilizing effect of surface tension progressively decreases when \mathcal{R}_1 increases. Therefore, the maximum wavelength for which a perturbation may be unstable increases with the Reynolds number \mathcal{R}_1 . Joseph, Renardy and Renardy showed that, in the absence of surface tension, small wavelength perturbations are unstable. Their result agrees with a similar observation made by Hooper and Boyd about the stability of unbounded Couette flows [HB83].

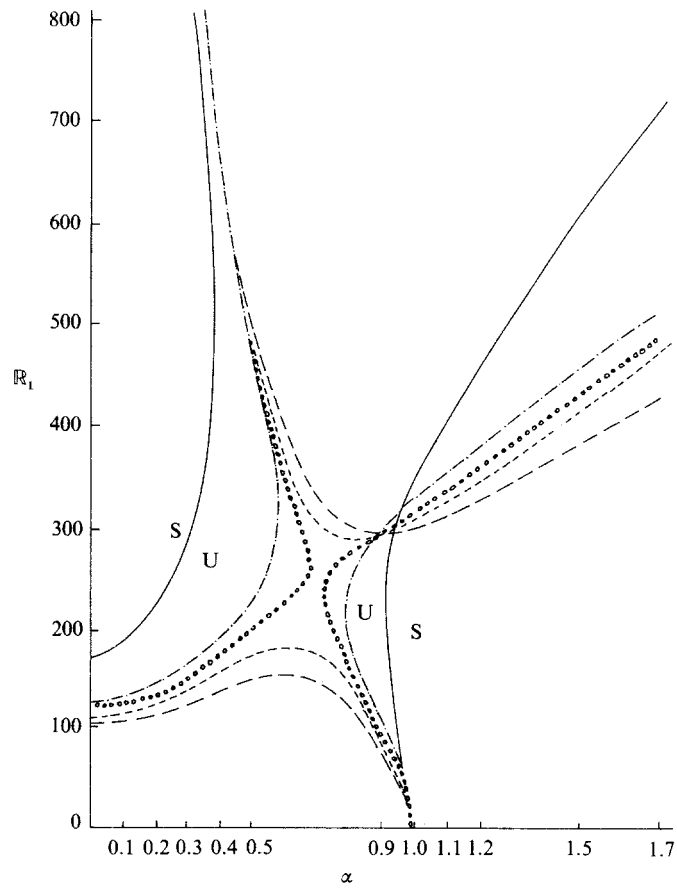


Figure 2.29: Neutral stability curve $R_c(a, m, J^*)$, $J^* = 930$, $a = 1.25$. The curves are plotted for various values of the viscosity ratio m : $m = 0.9$ (—), $m = 0.8$ (-.-.), $m = 0.78$ (ooooo), $m = 0.75$ (- - - -), $m = 0.7$ (- - - -). (from [PCJ89]).

2.4.3 Experimental results

We briefly summarize the experimental results of Charles, Govier and Hodgson [CGH61] and Bai, Chen and Joseph [CBJ90, BCJ92, JR93b]. In particular, we are looking for a disturbed flow regime that can be calculated by transient simulations.

Charles, Govier and Hodgson

Preziosi, Chen and Joseph [PCJ89] try to correlate the results of their numerical linear stability analyses with experimental results of Charles, Govier and Hodgson [CGH61]. In their paper, Charles, Govier and Hodgson present pictures of eleven different flow regimes (Figure 2.30).

Preziosi, Chen and Joseph calculate the neutral stability curves for parameters corresponding to the eleven pictures of Figure 2.30. For each selection of flow parameters, they calculate the wavelength of the fastest growing axisymmetric perturbation, and they try to correlate that length with the size of bubbles and slugs observed in the experiments.

More precisely, we note $\tilde{\alpha}$ the wavenumber of the fastest growing perturbation, and $\tilde{\lambda} = 2\pi/\tilde{\alpha}$ the corresponding wavelength. Preziosi, Chen and Joseph make the assumption that as the growth of the perturbation proceeds, an initially cylindrical portion of the core of length $\tilde{\lambda}$ and radius R_1 will break either in bubbles or in slugs, depending on the wavelength $\tilde{\lambda}$. If $\tilde{\lambda}$ is small enough, the cylinder breaks in spherical bubbles. Assuming that the volume of the cylinder of length $\tilde{\lambda}$ is conserved during the break-up process, the radius of the bubbles may be estimated:

$$l_{\text{theor}} = \frac{R_b}{R_2} = \left(\frac{3\pi}{2\tilde{\alpha}}\right)^{\frac{1}{3}} \frac{1}{a}, \quad (2.16)$$

in which R_b is the radius of the bubble. If the value of l_{theor} calculated with this formula is too large (i.e. $l \gtrsim 0.85$), bubbles also are too large to fit in the pipe, and they become slugs. Slugs seem well lubricated for $R_2/R_s \approx 1.2$. Therefore, a cylinder portion of the core fluid of length $\tilde{\lambda}$ and radius R_1 will gather in a slug of radius $R_s = R_2/1.2$ and length l_{theor} , in which l_{theor} is given by

$$l_{\text{theor}} = 1.44\tilde{\lambda}/a^3 = 2.88\pi/\tilde{\alpha}a^3. \quad (2.17)$$

Using equations (2.16) and (2.17), Preziosi, Chen and Joseph predict the size of bubbles and slugs that may be expected in experimental flows, and they compare their results with the observations of Charles, Govier and Hodgson. The comparison is summarized in table 2.3. The qualitative agreement between predicted and observed values of the dimensions of bubbles or slugs is surprisingly good.

Bai, Chen and Joseph

Bai, Chen and Joseph [CBJ90, BCJ92, JR93b] use an experimental device composed of a pipe describing a “U” loop, The curved section of the pipe being on

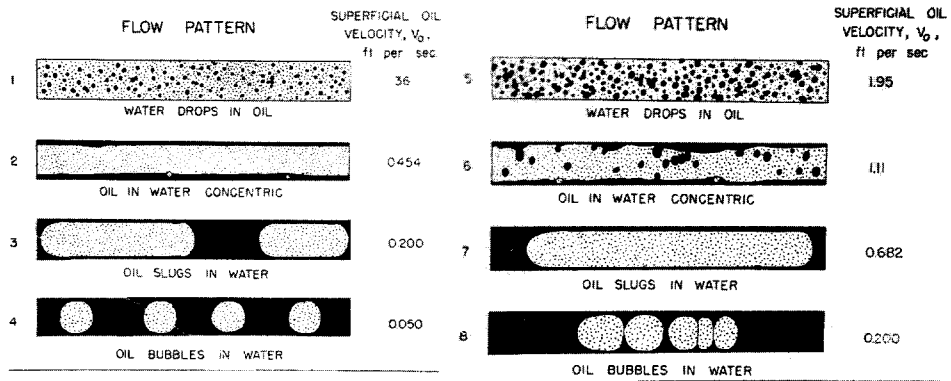


Figure 3 — Drawings prepared from photographs of the 16.8 viscosity oil flowing in the presence of water and showing the variation in flow pattern with oil velocity for a low fixed water velocity of 0.10 ft./sec.

Figure 4 — Drawings prepared from photographs of the 16.8 centipoise viscosity oil flowing in the presence of water and showing the variation in flow pattern with oil velocity for a fixed water velocity of 0.682 ft./sec.

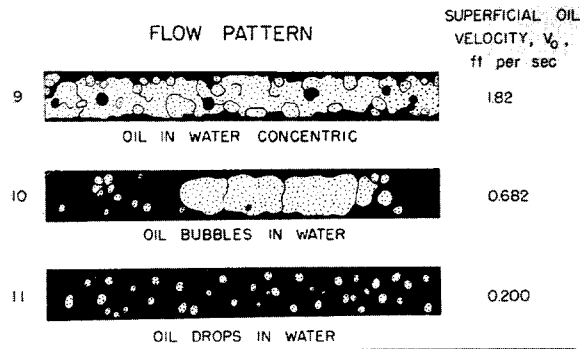


Figure 5 — Drawings prepared from photographs of the 16.8 centipoise viscosity oil flowing in the presence of water and showing the variation in flow pattern with oil velocity for a high fixed water velocity of 2.04 ft./sec.

Figure 2.30: *Eleven different flow types observed by Charles, Govier and Hodgson (from [CGH61, PCJ89]).*

Table 2.3: Comparison of theory and experiments for the prediction of the flow patterns observed by Charles, Govier and Hodgson. The numbers in the first column refer to the numbers of the flow patterns in Figure 2.30. $\sigma(\tilde{\alpha})$ is the growth rate of the perturbation predicted with the linear theory. (From [PCJ89].)

#	Experimental results			Theoretical results		
	a	R_1	l_{exp}	$\tilde{\alpha}$	$\sigma(\tilde{\alpha})$	l_{theor}
3	1.42	69.80	4.5 (short slug) 7.5 (long slug)	0.6	$7.83518 \cdot 10^{-2}$	5.2665
4	2.24	26.98	0.85 (bubble)	0.66	$2.91616 \cdot 10^{-2}$	0.8596
6	1.5	406.90	> 15.75 (slug)	0.22	$5.85969 \cdot 10^{-2}$	12.1856
7	1.74	287.41	13.1 (slug)	0.08	$2.34665 \cdot 10^{-3}$	21.4686
8	2.80	134.50	0.69 (bubble)	0.61	$5.23881 \cdot 10^{-2}$	0.7060
9	1.81	795.97	6.0 or > 15.75 (slug)	0.32	$6.84020 \cdot 10^{-2}$	4.7682
				0.023	$5.39895 \cdot 10^{-4}$	66.3405
10	2.65	433.70	2.70 (slug)	0.11	$1.82720 \cdot 10^{-2}$	4.4199
11	4.63	221.69	0.3125 (bubble)	0.64	$2.41483 \cdot 10^{-2}$	0.4202

the top. Oil and water are injected in the pipe at the left bottom end of the loop, and exit at the right bottom end. A pressure gradient is imposed to force the flow. The flow rates of both liquids are adjustable separately.

Bai, Chen and Joseph distinguish various regimes depending on the relative flow rates of oil and water: Oil bubbles in water, slugs of oil in water, bamboo waves (BW), disturbed bamboo waves (DBW), disturbed core-annular flow or corkscrew waves (DCAF) and other regimes.

The results are given as a function of oil and water superficial velocities. The superficial velocities are defined as the ratio of the flow rates Q_o and Q_w and of the area of the pipe $A = \pi R_2^2$: $V_o = Q_o/A$ and $V_w = Q_w/A$.

The various regimes observed by Bai, Chen and Joseph are summarized in a flow chart (Figure 2.31). The approximate length of bamboo waves, if such waves are present, is given in Figure 2.32 for various values of the oil and water flow rates.

2.5 Transient simulations of core-annular flows

From the good agreement between experimental results and linear stability analyses, it has been concluded that the flow patterns observed by Charles, Govier and Hodgson arise from the growth of an initially small amplitude perturbation. Therefore, the transient calculation of an unstable perturbation should allow us to calculate the transition towards the experimental flow patterns.

However, it is not possible to calculate the complete evolution towards the breaking into small bubbles or droplets with our method because of the topological difficulties and large deformations of the mesh involved by such calculations.

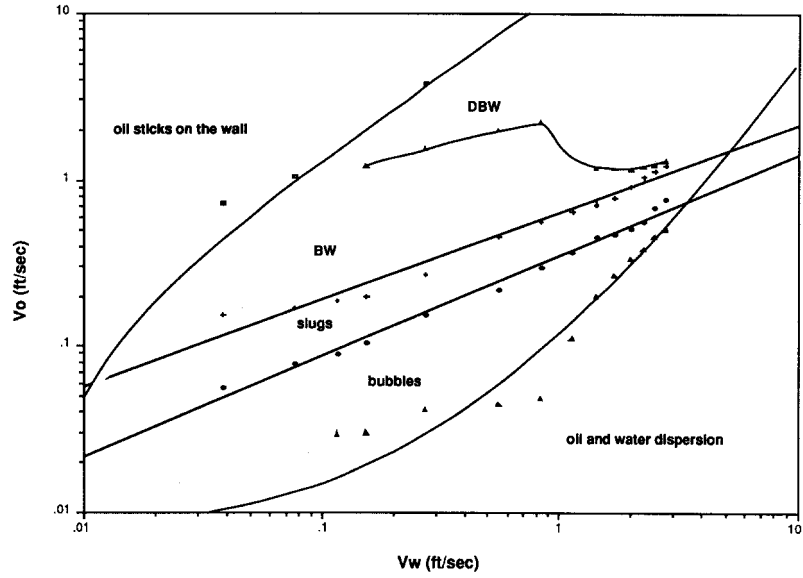


Figure 2.31: Flow chart in up flow giving the types of flow as a function of the oil and water flow rates. (From [BCJ92, JR93b].)

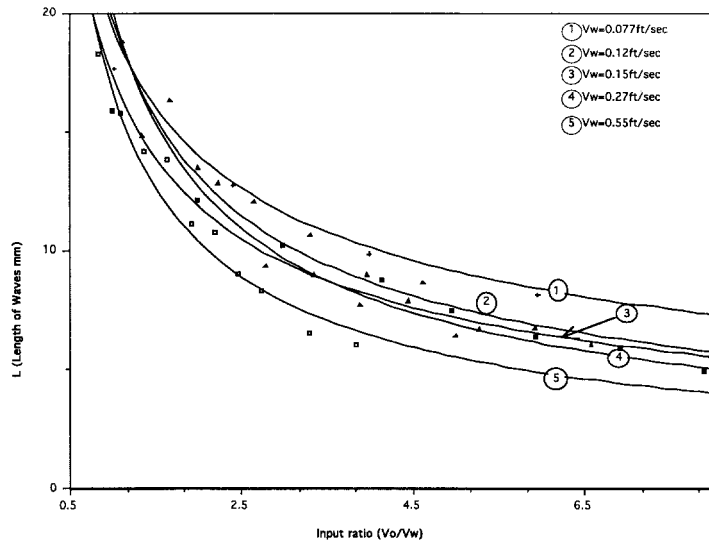


Figure 2.32: Average length of the bamboo waves in an up flow for various values of the oil and water flow rates. (From [BCJ92, JR93b].)

Therefore, we only present the results for a transient evolution towards the bamboo waves regime observed by Bai, Chen and Joseph.

2.5.1 Definition of the problem

In this section, a method similar to the one used for planar periodic flows is used to calculate the transient evolution of periodic perturbations of the base flow.

Geometry and boundary conditions

The geometry of the problem, and the boundary conditions are summarized in Figure 2.33. Periodic conditions are imposed on the velocity and the radial displacement of the interface between the inlet and outlet sections. The velocity vanishes along the pipe wall, and symmetry conditions are imposed along the axis of symmetry. The height of the mesh H is equal to the wavelength of the perturbation we want to study.

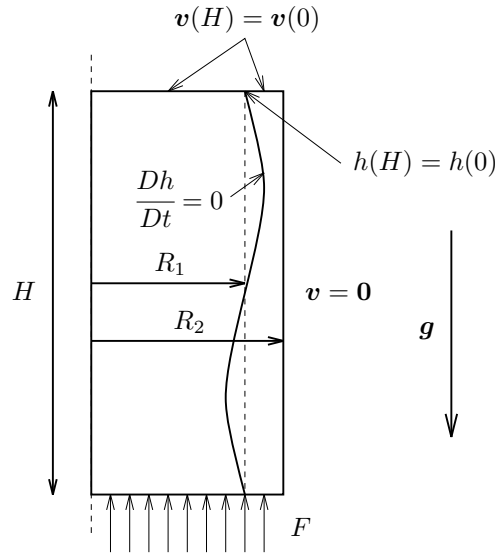


Figure 2.33: Definition of the subdomains and of the boundaries for the calculation of the transient calculation of the perturbed core-annular flow.

A kinematic condition is used to calculate the motion of the interface, and we use the method of spines for the remeshing. In this case, the direction of motion of the nodes is horizontal (parallel to r axis). Surface tension results in a normal force applied on the interface. An a priori unknown force $F(t)$ is imposed on the lower section of the pipe. Its value is such that the total flow rate Q is equal to the prescribed value.

The initial perturbation of the base flow is obtained by adding a sinusoidal radial displacement to the interface and calculating a flow on the deformed geometry. During the calculation, inertia terms are neglected and the normal component of the velocity field vanishes along the interface. For the initial perturbation of the interface, we select a horizontal displacement

$$h_0(z) = A_0 \sin(\alpha z),$$

in which A_0 is the amplitude of the initial perturbation. Here again, a Crank-Nicolson scheme is used for the implicit correction of the time stepping scheme.

2.5.2 Selection of parameters

Some parameters of the computations are selected directly according to the experimental conditions described by Preziosi, Chen and Joseph. The diameter of the pipe is 3/8 inches. The densities of oil and water are respectively $\rho_o = 0.905$ and $\rho_w = 0.995$. The viscosities are $\mu_o = 6.01$ poise and $\mu_w = 0.01$ poise. The surface tension between oil and water is $T = 8.54$ dyn/cm.

It is not possible to select the other parameters in order to match exactly experimental conditions. The experimental parameters are given for flows in a nonlinear regime. For disturbed flows, the volumes ratios of oil and water in the pipe are not univoquely determined by the flow rates. Therefore, approximations are done to estimate the core radius R_1 of the base flow. According to observation of Preziosi, Chen and Joseph, the core radius is given by

$$R_2 = R_1 / \sqrt{1 + hV_w/V_o}, \quad (2.18)$$

in which h is the hold-up ratio first introduced by Charles, Govier and Hodgson, and defined by

$$h \triangleq \frac{Q_o/Q_w}{\Omega_o/\Omega_w} = \frac{V_o/V_w}{H_o/H_w} \approx 1.39, \quad (2.19)$$

Once the values of the core radius and total flow rates known, the base flow and the axial velocity may be estimated with the analytical results of section B.1.2, and the dimensionless numbers are calculated as explained in section 2.4.1.

2.5.3 Transient calculations and bamboo waves

We select the parameters in such a way that the wavelength of the bamboo waves is approximately 1 cm. From Figures 2.31 and 2.32 we see that such a wavelength may be obtained with $V_w = 0.125$ ft s⁻¹ and $V_o = 3V_w$.

After adimensionalization, we have $R_1 = 1$ and $R_2 = a \approx 1.2097$. The axial wavenumber of the perturbation is $\alpha \approx 2.4737$, and the height of the mesh is $H = 2\pi/\alpha$. The material parameters for the calculation are

$$\rho_1 = 1, \quad \rho_2 = \zeta = 1.099448,$$

$$\mu_1 = \frac{1}{R_1} = 0.85366746, \quad \mu_2 = \frac{1}{R_2} = 1.4204117 \cdot 10^{-3},$$

$$g = -0.98920145, \quad \gamma = 6.1390097 \cdot 10^{-2}.$$

The total flow rate is $Q \approx 0.7713$. For the initial amplitude of the perturbation, we take $A_{\text{init}} = 0.05$.

The initially deformed mesh is represented in Figure 2.34.

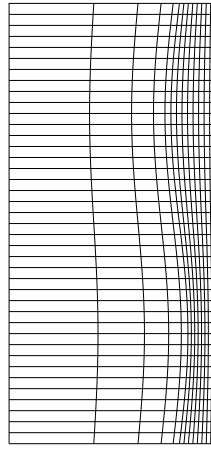


Figure 2.34: Configuration of the initially deformed mesh corresponding to $R_2 \approx 1.2097, \alpha \approx 2.4737$ and $A_0 = 0.05$.

In Figure 2.35, we plot the mesh for six different values of time. We see that the bamboo wave regime is rapidly obtained. In Figure 2.36, the shape of the interface is plotted for two consecutive axial wavelengths, and for three values of the time close to the end of the calculation: the bamboo waves move in the upward direction without deforming.

The flow corresponding to the last calculated solution is represented in Figure 2.37. In each layer, the pressure gradient is approximately a constant. The gradient is essentially related to gravity. Close to the crest, and in both layers, the pressure gradient has a more complicated shape because of the larger viscous dissipation in that area. Velocity is nearly a constant in the oil core: oil has a very large viscosity compared to water, and moves in the flow nearly as a rigid body. Along the filaments connecting the crests, water seems to follow oil, in the sense that the velocity in that area is approximately equal to the velocity of oil and does not seem to vary in that layer. The shearing in the annular layer concentrates in a thin layer close to the walls.

But here again, an interesting phenomenon appears in the water layer, close to the crest: the vertical component of the velocity becomes very small. We even observe vectors pointing downwards. This may be better seen in a zoom of the area of the crest (Figure 2.38).

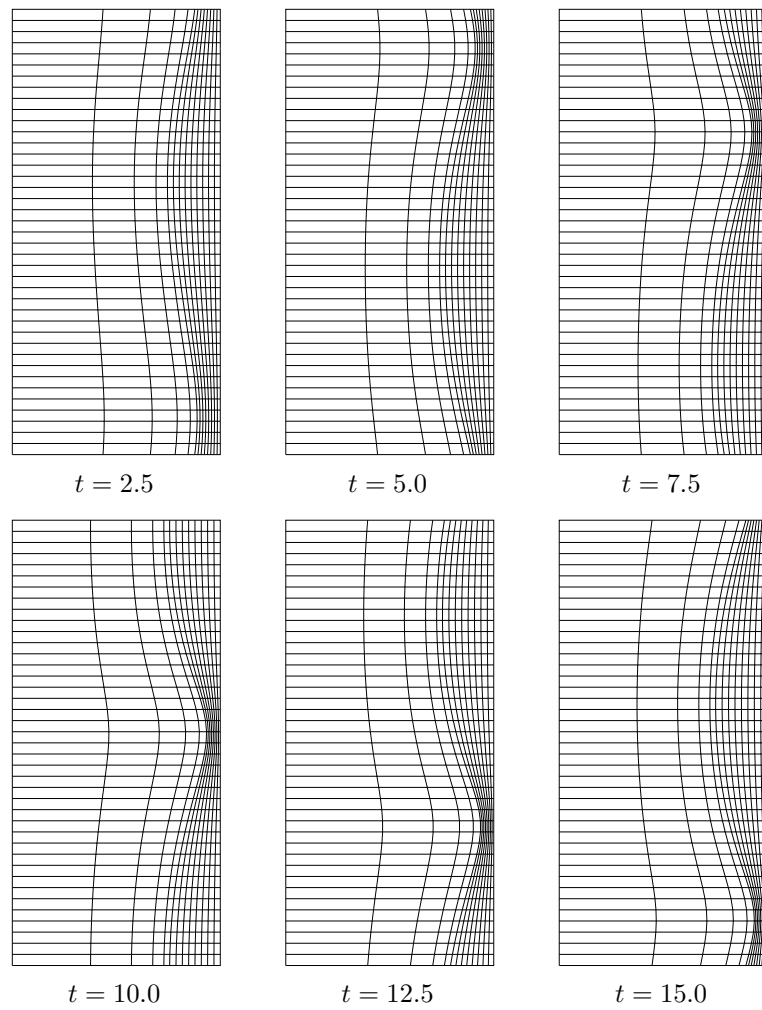


Figure 2.35: *Development of a bamboo wave in a vertical axisymmetric Poiseuille up flow.*

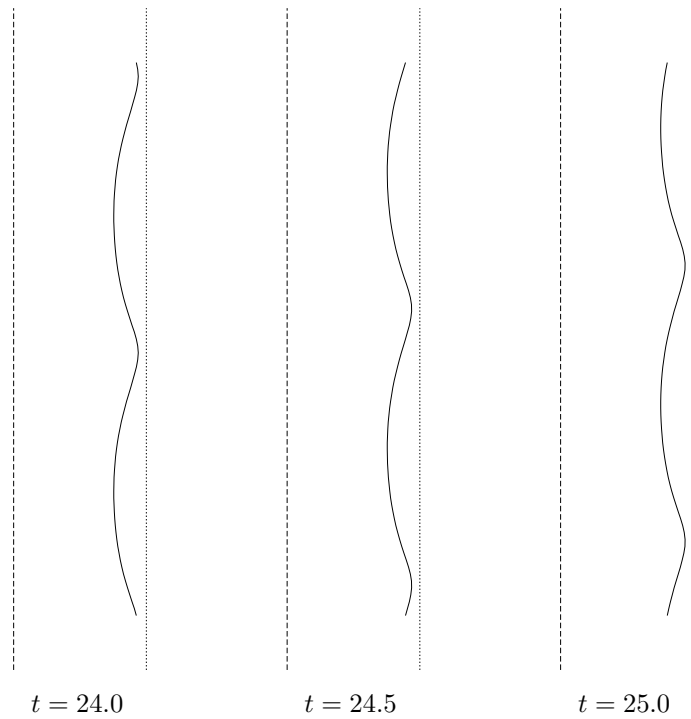


Figure 2.36: *Bamboo waves for three different of time and for an up flow. The waves move progressively upwards. The continuous line represents the interface, the dashed line, the axis of symmetry, and the dotted line corresponds to the wall ($R_2 \approx 1.2097, \alpha \approx 2.4737$ and $A_0 = 0.05$).*

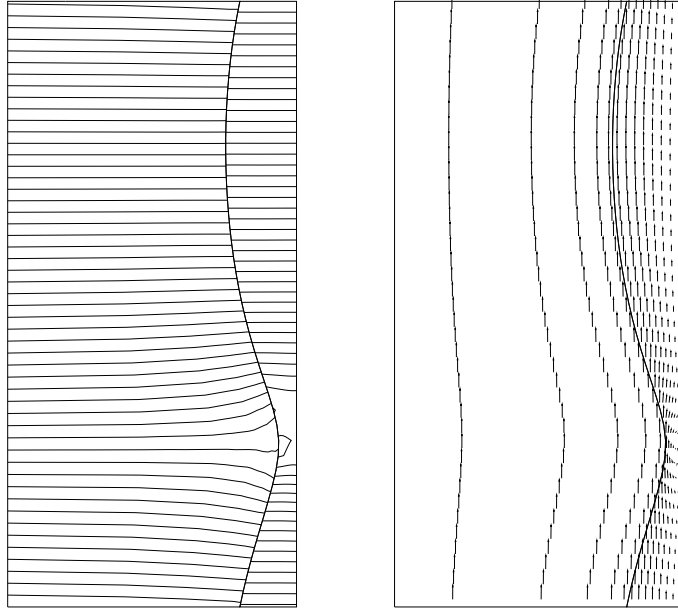


Figure 2.37: Representation of the flow for an established regime of bamboo waves ($R_2 \approx 1.2097, \alpha \approx 2.4737$ and $A_0 = 0.05$). The left part gives the pressure field. Pressure is maximum at the bottom and the increment of pressure between two consecutive isolines is $\Delta p = 0.2$. On the right hand side, we represent the velocity field. The vectors are centered on the elements.

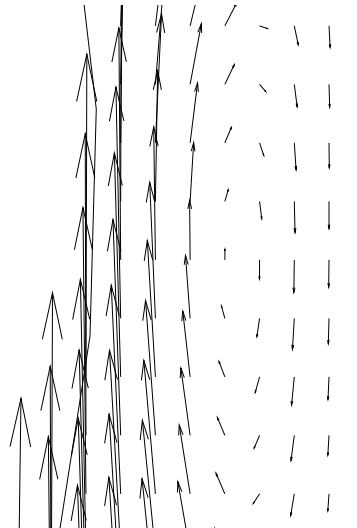


Figure 2.38: Velocity field in the area of the crest of the bamboo wave and in the annular layer. ($R_2 \approx 1.2097, \alpha \approx 2.4737$ and $A_0 = 0.05$).

It is easier to understand what happens in the area of the crest if we plot the velocity field observed in a coordinate system moving with the bamboo waves. Indeed, in such a coordinate system, the geometry does not change with time. We estimate the wave translation velocity from the position of the crest at various values of t and find $V_{\text{wave}} \approx 1.22$. To obtain the new velocity field, we make the following transformation:

$$\begin{aligned} u_{\text{new}} &= u_{\text{old}}, \\ v_{\text{new}} &= v_{\text{old}} - V_{\text{wave}}. \end{aligned}$$

We also can transform the pressure field by adding a constant pressure gradient to the solution, in order to eliminate the hydrostatic pressure gradient. To calculate the new pressure field, we use the expression

$$p_{\text{new}} = p_{\text{old}} - G \frac{z}{H},$$

in which G is the total weight of oil and water contained in the pipe divided by its total volume. With such a transformation, the pressure profile at the inlet section nearly is equal to the profile at the outlet section. The transformed velocities and pressure are plotted in Figure 2.39.

In the new coordinate system, the oil velocity nearly vanishes. That means that the waves move approximately at the same velocity as oil. The velocity in the water layer is essentially oriented towards the negative direction. Its amplitude is maximum close to the crest, for the water flow rate flows in a narrower “channel”. In that area, the velocity gradient and viscous dissipation are maximum. It induces a pressure drop in the area of the crest: the pressure is higher just over the crest than under it.

2.6 Conclusions

In this chapter, we use the transient calculation of multilayer flows to investigate their stability. Our results are compared with linear stability analyses. In general, the agreement between the two methods is good. But it is difficult to compare linear stability analyses and time-dependent numerical calculations. This is related to interference and nonlinear phenomena, and to the fact that our initial perturbation is not an eigen-solution of the Orr-Sommerfeld equations.

We also investigate the behaviour of planar perturbations growing into the nonlinear domain. This behaviour cannot be studied with linear theories, and it is interesting to compare the results of our transient calculations with experimental observations. This is done for the bamboo waves regime of core-annular flows and the numerical method is proved to be suitable for such calculations. Attempts have been done to reproduce other flow regimes, but the computational cost of those calculations was too large because very refined meshes were required.

Note that the transient calculation of perturbed flows also may be used to investigate the stability of multilayer viscoelastic flows. For such flows, it

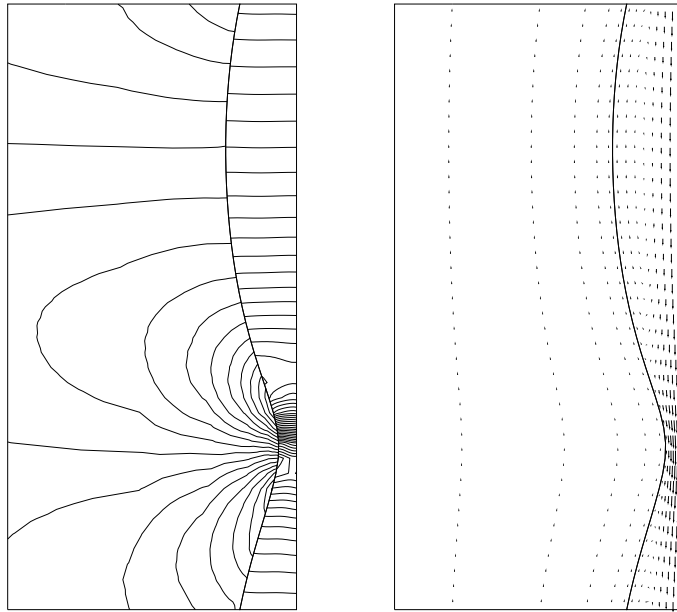


Figure 2.39: Representation of the flow for an established regime of bamboo waves ($R_2 \approx 1.2097, \alpha \approx 2.4737$ and $A_0 = 0.05$). The left part gives the modified pressure field (see the transformation equation page 96). The increment of pressure between two consecutive isolines is $\Delta p = 0.01$. On the right hand side, we represent the velocity field in a coordinate system moving with the waves. The vectors are centered on the elements.

has been shown that the elasticity of fluids has an important influence on the stability. But, here again, the computational cost of the calculations would be very important because an additional field must be discretized.

Finally, in order to reproduce encapsulation, three-dimensional transient multilayer-layer flows have to be calculated. The computational cost of such calculations is prohibitive. That is the reason why we abandon this way to try to reproduce the phenomenon.

Chapter 3

Numerical calculations of encapsulation

In this chapter we present the results of a numerical study of encapsulation. In particular, we investigate the influence of second normal stress difference on the phenomenon. Actually, the assumption that N_2 may be the cause of encapsulation had been done formerly [WUDP72, Uwa95]. But no quantitative comparisons of numerical results and experimental observations have been done so far. Here, we compare the results of calculations with experiments of Han [Han73]. The main advantage of the “ N_2 assumption” compared to the “interfacial instability assumption” is that it may be investigated numerically by time independent calculations.

Calculations are done with Giesekus and Reiner-Rivlin models. The rheometrical data used to fit the parameters of Giesekus model are the shear viscosity and first normal stress difference. To fit the parameters of Reiner-Rivlin model, we need an estimate of the second normal stress difference as a function of the shear rate. However, no experimental measurements of N_2 are available. Therefore, we use the Giesekus model to produce the missing data.

In order to solve the problem, we develop an original solution to calculate the motion of the contact line of the interface and the cylindrical wall. A good agreement is obtained between numerical calculations and experiments. This confirms the assumption that N_2 is the main factor influencing encapsulation.

The results presented in this chapter will be submitted to the Journal of Rheology [SL98].

3.1 Literature review

The conclusions of some experimental studies suggest that viscosity differences alone cause interface shape change, with the less viscous fluid always tending to encapsulate the more viscous fluid [SB73, SB75, Eve73, Eve75, LW74].

Theoretical studies have been done to try to study the influence of viscosity and elasticity ratios on encapsulation [WUDP72, KH76]. But the calculations are generally very complicated and many approximations are done. Thus the conclusions of those studies are to be taken with much care.

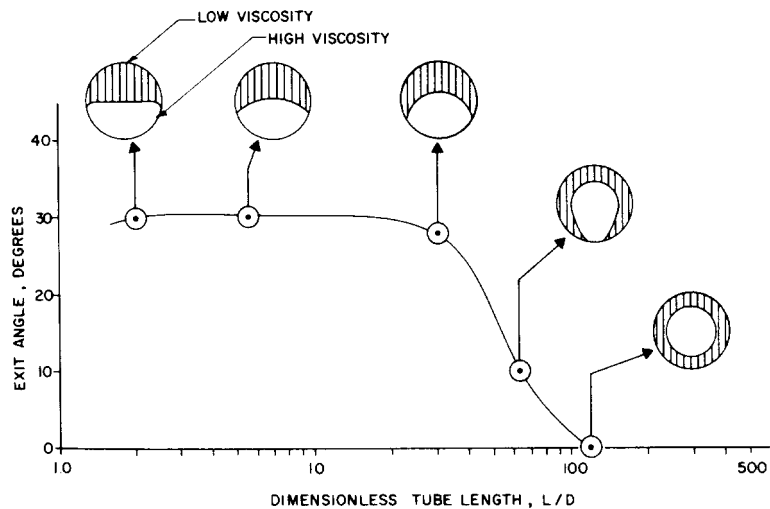


Figure 3.1: *Exit angle of the extrudate as a function of the die length. The assumed arrangement of the fluids in the section of the die is given for various values of the distance to the merging area. (From [Eve75]).*

Some results of Everage [Eve75] indicate that the encapsulation process may be divided into two parts. The first part of the encapsulation is the result of fluid rearrangement when the two coextruded fluids merge in the die. This rearrangement occurs close to the merging area. Then, a very slow encapsulation process occurs along the tube (Figures 3.1 and 3.2). Everage reports a length of die equal to 120 times the diameter in order to obtain a new equilibrium with the slow encapsulation process. But he does not give a satisfactory explanation of the cause of this slow encapsulation. Moreover, he assumes that the contact line keeps the position of the separating edge in the rearrangement area without justifying his assumption.

Few results of three dimensional multilayer flow calculations have been published so far. For such complicated calculations, numerical techniques like the finite element method must be used. Some results have been published for Newtonian flows (Karagiannis et al. [KHV90]). Non-isothermal calculations also have been performed [CAD⁺95b]. The results seem to confirm that the more viscous fluid is encapsulated by the less viscous one, but the results obtained show very small degree of encapsulation (Figure 3.3). Moreover, it seems that in all numerical studies, the small degree of encapsulation that has been obtained occurs in the first characteristic length of flow after the fluids have

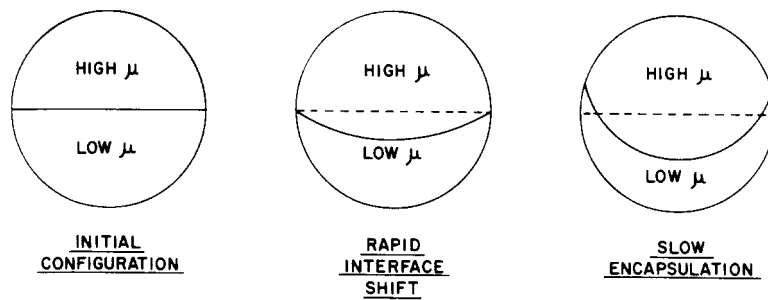


Figure 3.2: Distinction proposed by Everage between the rapid rearrangement of the fluids close to the merging area, and the slow encapsulation process occurring along the die. (From [Eve75]).

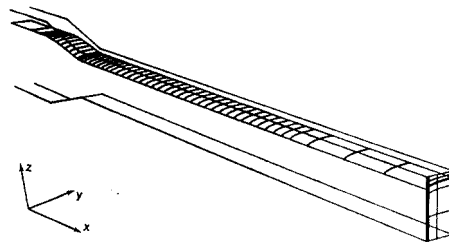


Figure 3.3: Two layer coextrusion flow calculated by Karagiannis et al. in a square die with a Newtonian model. (From [KHV90]).

been brought together in the die [KHV90]. To explain this, Karagiannis et al. incriminate problems with the boundary conditions and a too short downstream length of the mesh.

By theoretical development, White et al. show that for two fluids of equal viscosity flowing in a channel, the fluid with the largest second normal stress difference must have a convex shape [WUDP72]. That means that it is encapsulated by the other fluid. But the analysis of White does not predict steady state results, and nothing is said for two fluids of different viscosities. Actually, it is well known that N_2 is the cause of secondary recirculations when one viscoelastic fluid is extruded in a rectilinear die. Thus, it is not surprising that progressive interface shape changes occur when two fluids are coextruded in a die. However, in their experimental study of bicomponent stratified flow in tubes, Lee and White [LW74] show that the less viscous fluid encapsulates the more viscous one, and that the encapsulation is independent of the relative elasticities of the fluids. They conclude that the dominating factor for the encapsulation is the difference of viscosity of the fluids. Their conclusion has been confirmed by Khan, Han and Kim [KH76, HK76a, HK76b].

The effect of second normal stress difference on encapsulation has been investigated by Uwaji both numerically and experimentally [Uwa95]. Let us summarize his results:

- In his experiments, Uwaji shows that when two Newtonian fluids are coextruded, the rearrangement occurs in the merging area. But no slow encapsulation process is observed with Newtonian fluids. This confirms the results of the Newtonian calculations of Karagiannis et al. [KHV90, CAD⁺95b].
- Only in viscoelastic coextrusion experiments, slow encapsulations have been observed. This indicates that the elasticity of the fluids is the key factor to explain the progressive encapsulation observed by Everage.
- When viscoelastic and Newtonian fluids are coextruded, the viscoelastic fluid is encapsulated by the Newtonian one. This phenomenon does not seem to depend on the viscosity ratio.
- Numerical calculations corresponding to the aforementioned experiments have been performed with Newtonian and viscoelastic (PTT) models. They confirm qualitatively the experimental results. Moreover, by modifying the parameter ξ of PTT model, Uwaji shows that second normal stress difference causes the progressive encapsulation observed by Everage.

Those results seem to indicate that second normal stress difference is the cause of encapsulation.

Here, it is interesting to remark that when the influence of elasticities on encapsulation is investigated, the estimates of elasticities are not based on measures of second normal stress differences. Actually, we can say that the influence of N_2 has not really been investigated experimentally so far. From the experimental results of Uwaji, it is not possible to determine whether the factor that

causes encapsulation is N_1 , N_2 or some other property related to the elasticity of fluids. Numerical calculations only, allow Uwaji to determine that the slow encapsulation process may be caused by N_2 . But his numerical results only may be considered as qualitative investigations of the effect of N_2 . Indeed, with one single mode, PTT model only poorly approximates the behaviour of viscoelastic fluids. Moreover, some experimental results of Uwaji are in contradiction with many formerly published experimental observations.

In this chapter, we try to explain those contradictions.

3.2 Encapsulation in channel flow

We have seen in section 3.1, that White et al. have shown that when two fluids of identical constant viscosities are coextruded in a channel, the fluid that exhibits the largest second normal stress difference should have a convex shaped interface [WUDP72]. But it also appears from experimental studies that encapsulation is mainly influenced by the viscosity ratio, and that normal stress differences are of secondary importance.

In this section, we investigate the influence of the viscosities and of the second normal stress difference on two layers channel flows. This has been done to illustrate the effect of N_2 on that kind of flows.

For the calculations presented here, we use the Reiner-Rivlin model. The use of the Reiner-Rivlin model has two main advantages. First, this model is cheaper to use in numerical calculations than the viscoelastic models. Second with the Reiner-Rivlin model, we have a very good control on the viscosities and second normal stress coefficients of both fluids. In particular, each fluid may have constant shear viscosity and second normal stress coefficient. This is not possible with the Phan-Thien-Tanner and Giesekus models. The use of a viscoelastic model for our numerical investigations would make the interpretation of results very problematic.

3.2.1 Transient calculation with Reiner-Rivlin model

We calculate a transient two-layer channel flow on the computational domain represented in Figure 3.4. Note that, in this section, we just perform a qualitative investigation. Thus all quantities are dimensionless, and we do not try to reproduce any realistic case.

In a “channel flow”, the main direction of the velocities is perpendicular to the computational domain (direction z). All partial derivatives with respect to coordinate z , save $p_{,z}$ vanish. Note that the possible presence of first normal stress difference in the model has no effect on planar channel flows. Indeed, N_1 results in a stress τ_{zz} parallel to the direction of flow. The assumption that $\tau_{zz,z} = 0$ makes that the contribution of τ_{zz} to the momentum equations vanish.

In this case, a constant normal pressure gradient is imposed on the whole computational domain in order to have a total flow rate equal to $Q_0 = 1000$. The viscosity is identical for both fluids: $\eta = 20$. The second normal stress

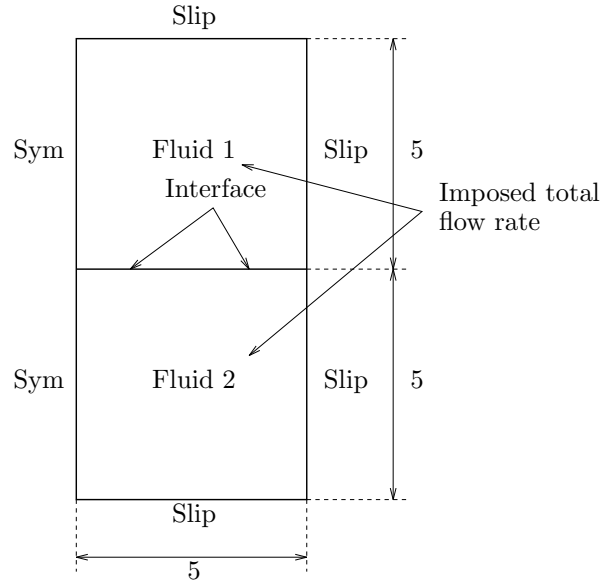


Figure 3.4: Schematic representing the geometry and the boundary conditions of the two-layer channel flow problem.

coefficient in the upper layer, $\psi_2 = -2$ is twice that of the lower layer. This second normal stress difference is the cause of secondary recirculations in the flow. Those recirculations will move the interface.

A kinematic condition is used to calculate the motion of the interface. In order to avoid too large deformations of the mesh, surface tension is modelled along the interface: its value has been selected in such a way that an equilibrium of the stresses between the two layers is progressively reached. When that equilibrium is reached, the difference of normal components of contact forces on both sides of the interface is compensated by surface tension. For our calculations, $\gamma = 30$ gives a satisfying equilibrium configuration.

Along the walls, slip conditions are applied in order to allow the motion of the contact point:

$$\begin{aligned} \mathbf{v}_t &= k_{\text{slip}} \mathbf{f}_t, \\ v_n &= 0. \end{aligned}$$

The value of the slip coefficient is $k_{\text{slip}} = 20$ along the four walls on which that condition is used.

Finally, symmetry boundary conditions are applied on the left boundary. Actually the computational domain given in Figure 3.4 represents a square channel in which two fluids are coextruded. The symmetry of the problem has been used to reduce the computational cost of the calculation.

For the time discretization, we use an implicit Euler scheme (section 1.4). The mesh on which the calculations are done is represented in Figure 3.5. To

propagate the motion of the interface into the meshes of both subdomains, we use the method of spines. The direction of motion of all nodes is vertical.

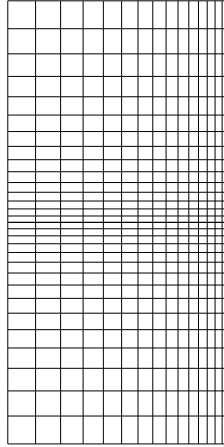


Figure 3.5: *Mesh on which the two-layer channel flows are calculated.*

We plot in Figure 3.6 the configuration of the layers and the stream function for various values of time. The upper layer (high $|\psi_2|$ fluid) pushes progressively into the lower layer (low $|\psi_2|$ fluid). The lower layer creeps along the right wall and tends to surround the upper layer. An equilibrium position of the interface is reached for approximately $t = 60$. Note that at equilibrium, the isolines of the stream function do not cross the interface. This is normal for at equilibrium, the position of the interface does not change, and the velocities are parallel to that interface.

3.2.2 Static calculation of channel flows

We plot in Figure 3.7 the velocity vector field for $t = 2.5$. Clearly, it is possible to see which fluid is encapsulating the other fluid, only by the observation of the velocities. Actually, the velocity field calculated at the first time step may tell us which is the encapsulating fluid.

This fact suggests us a way to investigate the influence of viscosity and second normal stress difference on encapsulation at a very low computational cost. Among the governing equations of the transient problem described in section 3.2.1, only the kinematic condition involves time derivatives: the momentum equation contains no time derivatives of the velocity field for inertia has been neglected; moreover, in our constitutive equation, the extra-stress tensor is an algebraic function of the rate of deformation tensor \mathbf{D} , and thus is an explicit function of \mathbf{v} .

Therefore, taking into account the fact that we only need the initial velocity field to determine which fluid is the encapsulating one, we conclude that a static calculation (i.e. not time dependent) is sufficient to investigate the influence of

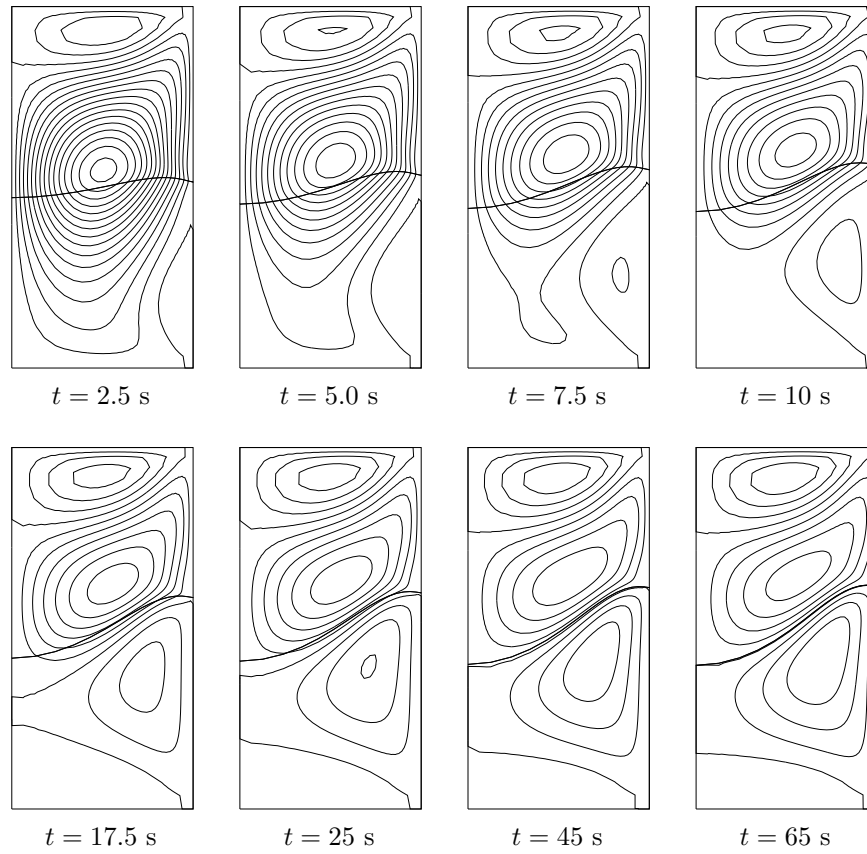


Figure 3.6: Configuration of the layers and stream function for various values of the time t .

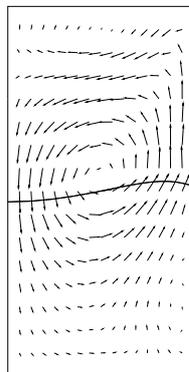


Figure 3.7: velocity vector field for the two-layer channel flow at $t = 2.5$.

material parameters on encapsulation. For such static calculations, we are not looking for the motion of the interface. Thus, we do not need slip at the walls.

A summary of the results of our calculations is given in table 3.1. The corresponding initial flows are represented in Figure 3.8. The material parameters used for calculation (a) are identical to those of the transient calculation presented in section 3.2.1. For calculation (b) the upper and lower fluids have identical properties. This explains why no encapsulation phenomenon may be observed.

Table 3.1: *Summary of the parameters used for the various static calculations of two-layer channel flows, and of the results. In the column titled “Calc.,” each letter represent the index of the corresponding calculation. The last column indicates which fluid encapsulates the other fluid (E. F. as “encapsulating fluid”).*

Calc.	η^{upper}	ψ_2^{upper}	η^{lower}	ψ_2^{lower}	E. F.
(a)	20	-2.0	20	-1.0	lower
(b)	20	-2.0	20	-2.0	(-)
(c)	10	-1.0	20	-1.0	lower
(d)	10	-1.0	20	-2.0	upper
(e)	10	-1.0	20	-1.5	lower
(f)	10	-1.0	20	-1.6	upper
(g)	10	-1.0	30	-3.0	upper
(h)	10	-1.0	30	-2.0	lower

Now let us first investigate the effect of an increase of the second normal stress coefficient. We compare successively the results of calculations (c), (e), (f) and (d). For (c) and (d), only one recirculation may be observed. Note that those two recirculations have different directions of rotation: in (c), the fluids rotate counter-clockwise, while the direction of rotation in (d) is clockwise. We observe that by progressively increasing the second normal stress coefficient of the lower layer, a second recirculation is created in the bottom of that layer. This recirculation grows and progressively embraces the whole computational domain. We also observe that for situations (c) and (e), the lower viscosity fluid is encapsulated by the higher viscosity fluid. This result is in contradiction with most experimental observations.

An observation still more surprising may be done by comparing situations (d) and (h). For those two calculations, the second normal stress coefficients are identical. Only the shear viscosity of the lower layer fluid has been increased in (h). It seems that a consequence of that increase is that the lower layer encapsulates the upper layer. This too is in contradiction with experimental results.

In all our calculations, when the fluids have same shear viscosity and second normal stress coefficient ratios, $\eta^{\text{upper}}/\psi_2^{\text{upper}} = \eta^{\text{lower}}/\psi_2^{\text{lower}}$, the more viscous fluid is encapsulated by the less viscous one (calculations (b), (d) and (g)). At

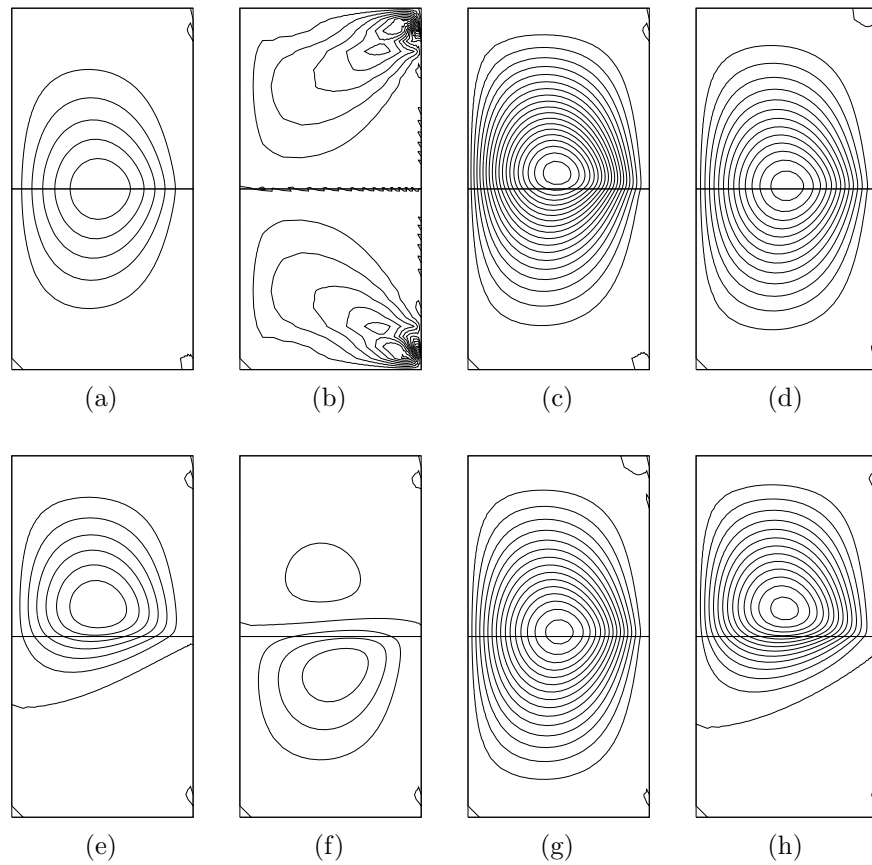


Figure 3.8: Configuration of the initial recirculations for various sets of material data (see table 3.1). Note that the distance between two consecutive lines is different for each plot, and thus cannot be used to estimate the amplitude of the recirculations.

last, we have one observation in line with experimental results!

3.2.3 Interpretation of results

Note that the comparisons done in the preceding section have been done on the basis of shear viscosity and second normal stress coefficient. We also could have made our comparison on the basis of second normal stress difference and shear stress. This is not easy to make for the shear rate is not a constant on the computational domain. But now, let us examine intuitively the effect of a variation of the shear viscosity in one layer on shear stresses and second normal stress differences.

Let us first remark that for fixed shear viscosity and second normal stress coefficient, shear stress is a linear function of shear rate, while second normal stress difference is a quadratic function of the shear rate.

Let us start from a situation similar to (b), in which the two fluids have identical material properties ($\eta = 10$ and $\psi_2 = -1$). For those parameters, the initial flow is identical to that presented in part (b) of Figure 3.8: secondary recirculations appear in both layers, but the vertical component of the velocity vanishes along the interface.

Let us now increase the lower fluid viscosity to $\eta^{\text{lower}} = 20$. Thus, we calculate the flow with the parameters of (c). The total flow rate is identical to that of the preceding calculation, but the flow rate of the lower fluid decreases, and that of the upper layer increases. Consequently, the shear rate increases in the upper layer and decreases in the lower layer. The second normal stress coefficient remaining unchanged in both layers, this results in a decrease of the second normal stress difference in the lower layer and an increase of it in the upper layer. If we accept the assumption that the fluid that exhibits the largest second normal stress difference is encapsulated, this could explain qualitatively why an increase of the viscosity of one fluid may lead this fluid to encapsulate the other fluid.

Note that the assumptions of constant shear viscosities and second normal stress coefficients are in contradiction with all experimental observations. Moreover, it is interesting to remark that Phan-Thien-Tanner and Giesekus models, reduce to Maxwell-B model when parameters ξ or α_G are put to zero (i.e. when second normal stress difference vanishes). A consequence of a progressive increase of α_G and ξ parameters is that second normal stress difference appears, and that the models exhibit a shear thinning character. Thus, PTT and Giesekus models cannot have second normal stress difference without exhibiting a shear thinning character. For that reason too, the model used in our calculations is a very peculiar model.

Thus our calculations have been done with an unrealistic model. It should be interesting to make calculations with a more realistic model. This is done for one peculiar case in section 3.3.2, in which encapsulation flows are calculated using material parameters fit from experimental data.

3.3 Numerical calculation of a 3D encapsulation

3.3.1 Experiments of Han

In one of his papers, Han presents results about the encapsulation of polystyrene (PS) by low density polyethylene (LDPE) in circular dies [Han73]. The results obtained with circular dies are particularly interesting for us: they allow us to make numerical calculations without solving the topological difficulties related to the presence of corners in the geometry. Indeed, if we make that kind of calculation in square dies, when high degrees of encapsulation are achieved, the contact line encounters the corners of the die section, and modifications of the mesh topology must be performed to deal with that problem.

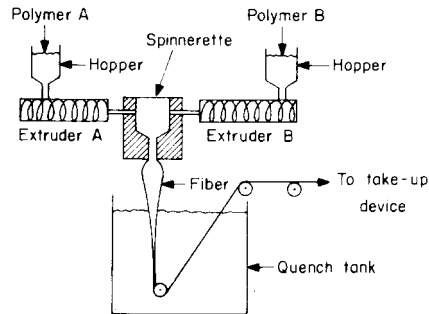


Figure 3.9: *Experimental device used by Han and Kim for the coextrusion of LDPE and PS (from [HK76a]).*

An experimental device similar to the one used by Han is represented in Figure 3.9, and a closer view of the die is represented schematically in Figure 3.10. Two extruders are used to bring the fluids together in the die. At the die inlet, a separating edge ensures that the interface is flat where the two fluids merge. The extrudate is collected and rapidly cooled in a quench tank (This last part was not present in the first version of the device used by Han [Han73]).

Han uses three different circular dies described in table 3.2. The two melt streams are combined at a point very close to the inlet of a die which is divided by a knife-edged flow divider. Figure 3.11 shows the position of the flow divider. In order to obtain quantities numerically easy to handle, we express all lengths in mm. A similar transformation has been done for the other physical quantities: viscosities are given in $\text{kg mm}^{-1}\text{s}^{-1}$, stresses in $\text{kg mm}^{-1}\text{s}^{-2}$ and normal stress coefficients in kg mm^{-1} .

3.3.2 Rheological data

Han presents the viscoelastic properties of the molten polymers used in his experiments. For the LDPE and PS, he gives the shear viscosity and first

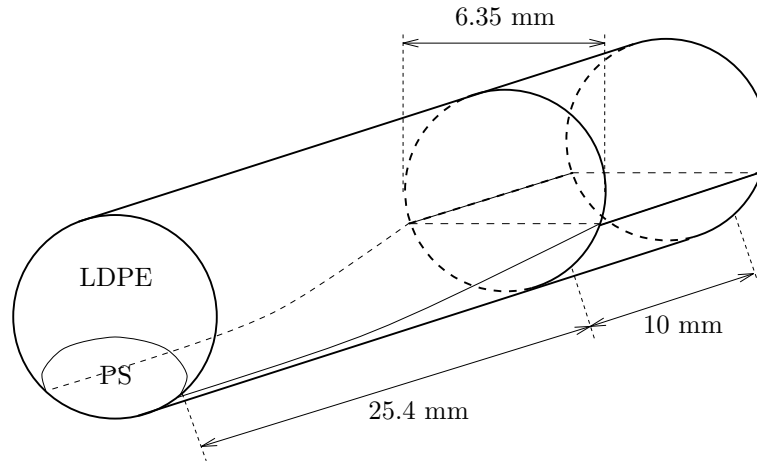


Figure 3.10: Schematic representing the encapsulation of polystyrene by low density polyethylene in the experiments of Han [Han73].

Table 3.2: Dimensions of the capillary dies used by Han to investigate the encapsulation.

Die	D , in.	L , in.	L/D
A	0.250	1.000	4
B	0.250	2.750	11
C	0.250	4.500	18

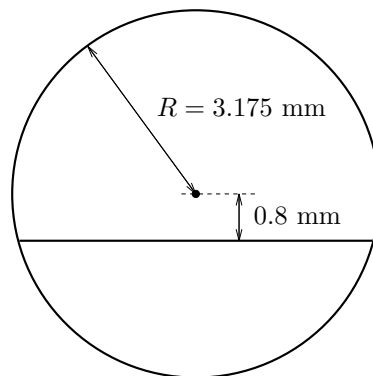


Figure 3.11: Schematic which shows how two molten polymers meet at the die inlet in the experiments of Han [Han73].

normal stress difference as a function of the shear rate. We use those data to find the material parameters of our viscoelastic models.

Several attempts of fit of experimental curves have been done with the Phan-Thien-Tanner model without giving satisfactory results. With PTT model, shear viscosity and first normal stress difference decrease too fast to fit the shear data. Maybe the problem could be solved using several modes in the model, but the computational cost associated with such a choice would be prohibitive.

Instead of using PTT model, we try to fit the data with the Giesekus model defined by

$$\mathbf{T} + \lambda_G \overset{\nabla}{\mathbf{T}} + \frac{\alpha_G \lambda_G}{\eta_V} \mathbf{T} \cdot \mathbf{T} = 2\eta_V \mathbf{D}. \quad (3.1)$$

The parameters of the model are the relaxation time λ_G , the shear viscosity η_V and the last parameter is α_G . For the fit, we use a hybrid procedure:

- We first try to fit the experimental first normal stress difference. For that step, we select the viscoelastic part of the shear viscosity at about 80% of the viscosity plateau. This gives $\eta_V = 20$ (kg mm⁻¹s⁻¹) for the polystyrene and $\eta_V = 8$ (kg mm⁻¹s⁻¹) for the low density polyethylene. Then, we try to find the parameters α_G and λ_G that minimize the difference between the first normal stress difference corresponding to the Giesekus model, and the measured first normal stress difference.
- Then, the difference between the measured shear viscosity and the shear viscosity predicted with the Giesekus model is calculated. (By selecting η_V equal to 80% of the viscosity plateau for the Giesekus model, we ensure that the aforementioned viscosity difference is positive for all values of the shear rate.) We fit the difference of viscosity with a Bird-Carreau viscosity law:

$$\eta_N(\dot{\gamma}) = \eta_0 \left(1 + \lambda_N^2 \dot{\gamma}^2\right)^{\frac{n-1}{2}}. \quad (3.2)$$

Here, the parameters we want to determine are η_0 , λ_N and n .

The result of our procedure is a model that fits reasonably well both shear viscosities and first normal stress differences. The fit parameters are given in table 3.3, and the corresponding curves for the shear viscosities and first normal stress coefficients in Figures 3.12 and 3.13 respectively.

Table 3.3: *Parameters for the fit of the measurements of Han with a Giesekus model*

	η_V (kg.mm ⁻¹ s ⁻¹)	λ_G (s)	α_G (-)	η_N (kg.mm ⁻¹ s ⁻¹)	λ_N (s)	n (-)
LDPE	8	5.7471	0.2241	1.8379	0.2575	0.4639
PS	20	3.7792	0.5167	5.1429	0.2338	0.3203

Now, it is interesting to remark that the second normal stress coefficient predicted by the Giesekus model with the parameters given in table 3.3 seem to

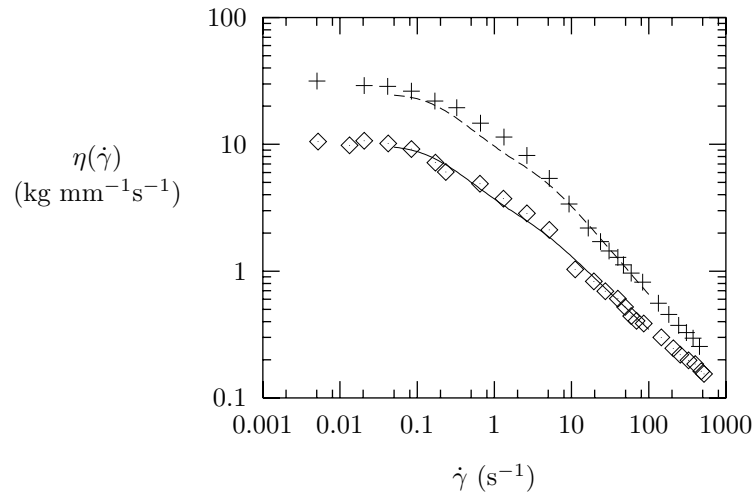


Figure 3.12: *Fit of the shear viscosity curves. The continuous curve corresponds to LDPE and the dashed line to PS.*

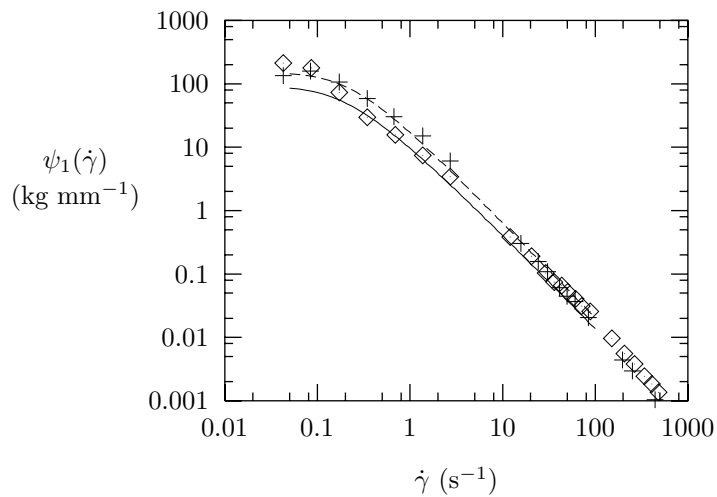


Figure 3.13: *Fit of the first normal stress difference. The continuous curve corresponds to LDPE and the dashed line to PS.*

be essentially related to the viscosities of the fluids (Figure 3.14): the fluids have very similar first normal stress coefficients, but the ratio $\psi_2^{\text{LDPE}}/\psi_2^{\text{PS}}$ is similar to $\eta_V^{\text{LDPE}}/\eta_V^{\text{PS}}$. That means that, in this case, our Giesekus fit predicts that the more viscous fluid also is the fluid that exhibits the largest second normal stress difference coefficient.

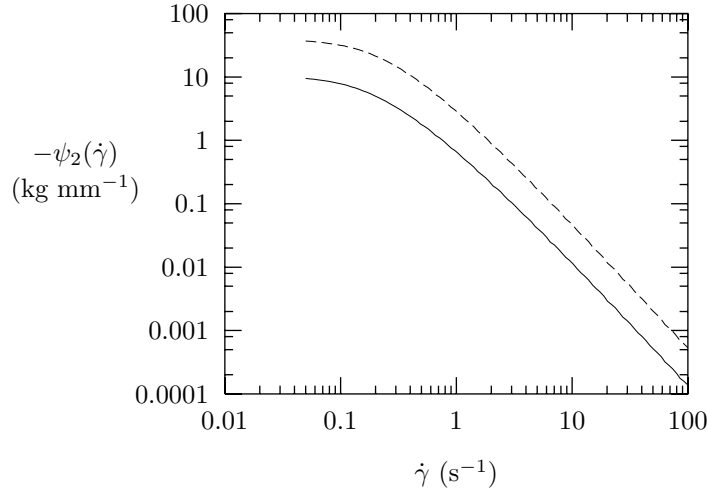


Figure 3.14: *Second normal stress difference of the Giesekus model for the set of parameters given in table 3.13. The continuous curve corresponds to LDPE and the dashed line to PS.*

Numerical simulations also will be done with the Reiner-Rivlin model:

$$\mathbf{T} = 2\eta(\dot{\gamma})\mathbf{D}(\mathbf{v}) + 4\psi_2(\dot{\gamma})\mathbf{D}(\mathbf{v}) \cdot \mathbf{D}(\mathbf{v}). \quad (3.3)$$

For the functions $\eta(\dot{\gamma})$ and $\psi_2(\dot{\gamma})$, we use Bird-Carreau laws:

$$\eta(\dot{\gamma}) = \eta_0 \left(1 + \lambda_N^2 \dot{\gamma}^2\right)^{\frac{n-1}{2}}, \quad (3.4)$$

$$\psi_2(\dot{\gamma}) = \psi_{20} \left(1 + \kappa^2 \dot{\gamma}^2\right)^{\frac{m-1}{2}}. \quad (3.5)$$

For the fit of the shear viscosity, we may use the experimental data of Han. But he does not give experimental measurements of the second normal stress difference. Thus, we have to find a way to estimate second normal stress difference. In order to “produce” the missing data, we make an assumption: we assume that Giesekus model with the fit parameters given in Table 3.3 correctly predicts the second normal stress differences of PS and LDPE. Thus, we adopt a two step procedure:

1. The shear viscosities and first normal stress differences are used to fit the parameters of Giesekus model.

2. The Giesekus model is used to predict second normal stress differences as a function of the shear rate $\dot{\gamma}$. The second normal stress differences predicted with Giesekus model are used to fit the parameters of the functions $\psi_2(\dot{\gamma})$ of the Reiner-Rivlin model (3.3).

The results of the Reiner-Rivlin fits are given in table 3.4 and Figures 3.15 and 3.16.

Table 3.4: Parameters for the fit with Reiner-Rivlin model of the measurements of the shear viscosities and second normal stress differences predicted by the Giesekus model with parameters given in table 3.3.

	η_0 ($\text{kg}\cdot\text{mm}^{-1}\text{s}^{-1}$)	λ_N (s)	n (-)	ψ_{20} ($\text{kg}\cdot\text{mm}^{-1}$)	κ (s)	m (-)
LDPE	9.3330	5.7939	0.4985	-8.5305	3.9212	-0.8252
PS	23.119	3.9894	0.4343	-33.973	3.5959	-0.8613

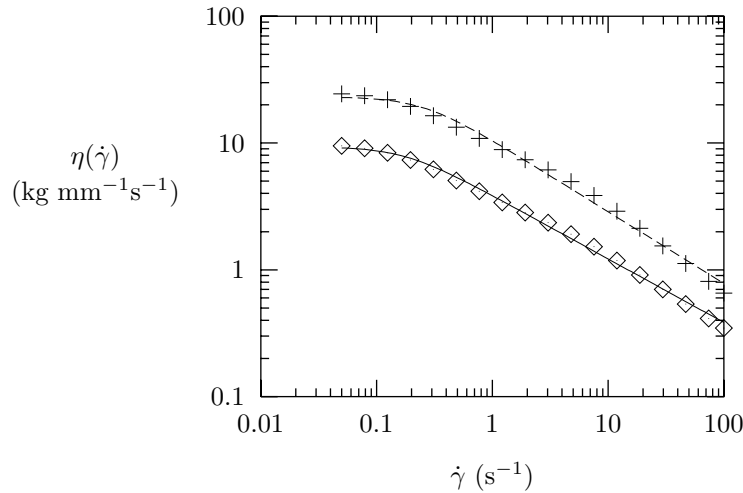


Figure 3.15: Fit with a Bird-Carreau law of the shear viscosity predicted with the Giesekus model. The continuous curve corresponds to LDPE and the dashed line to PS.

3.3.3 Boundary conditions

In order to reduce the computational cost, the calculations are done on half of the computational domain (Figure 3.17). Boundary conditions are imposed on the velocities for the momentum equations, on the coordinates for the remeshing equations, and on the extra-stress tensor for the constitutive equations (viscoelastic calculations only).

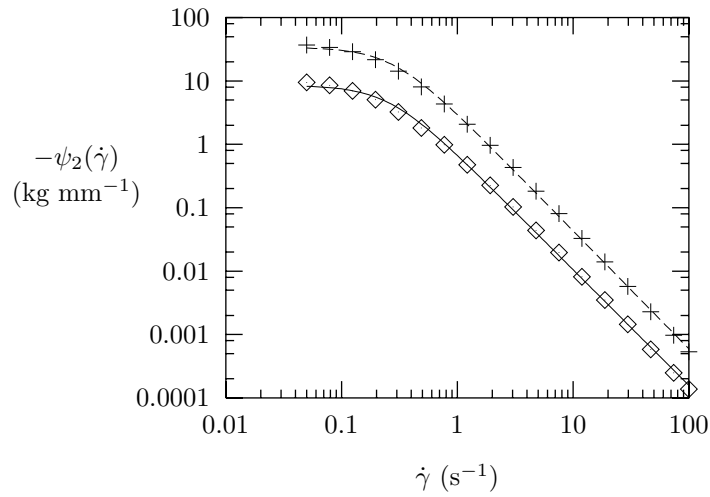


Figure 3.16: Fit with a Bird-Carreau law of the second normal stress coefficients predicted with the Giesekus model. The continuous curve corresponds to LDPE and the dashed line to PS.

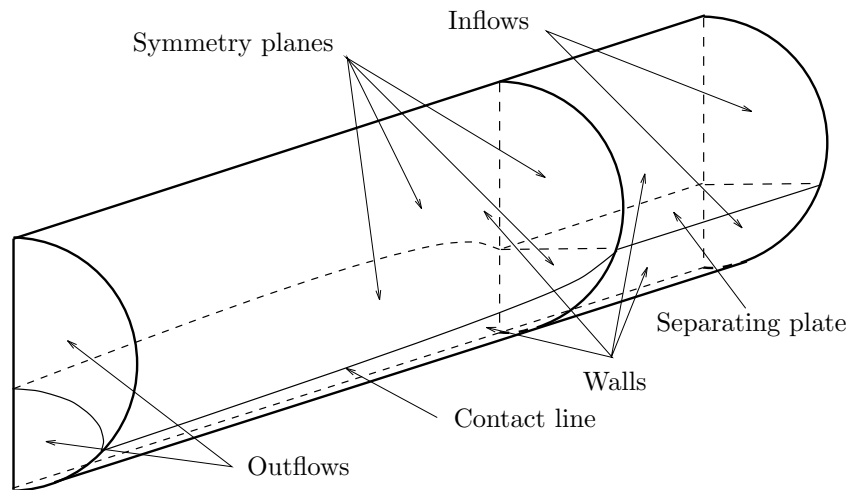


Figure 3.17: Computational domain and boundary sets for the numerical calculation of a three dimensional encapsulation.

1. For the momentum equation, vanishing normal velocities and tangential contact forces are applied along the symmetry plane. The velocities vanish along the walls and the separating plate.

For the inflows, the flow is first calculated separately (one calculates a channel flow on the inlet section). Then, the calculated velocities are imposed as Dirichlet boundary conditions for the three dimensional calculation.

Along the outlet section, we impose vanishing tangential velocities; this has been done to avoid a too large deformation of the interface close to the exit of the die.

For the viscoelastic calculations, we also impose Neumann boundary conditions at the momentum equation along the output section. The contact force imposed is

$$\mathbf{t} = \mathbf{T} \cdot \mathbf{n},$$

in which \mathbf{n} is the normal vector to the outlet section. Actually, only the normal component of \mathbf{t} influences the flow, for Dirichlet conditions are imposed on the tangential components of the velocity on the outlet section.

2. For the remeshing, the position of the nodes of the free surface is determined with the line kinematic condition. The remeshing technique is such that the axial coordinate of each node (z coordinate) is conserved by the remeshing. The nodes may move along the walls and along the symmetry plane. On those surfaces, we impose a vanishing displacement towards the normal direction. This forces the nodes located on the cylindrical walls to move tangentially to that surface.

In all calculations, the second normal stress difference is progressively introduced in the calculations by the use of a continuation technique. This is done in order to progressively increase the degree of encapsulation. In our first calculations, we observed that the walls progressively departed from the cylindrical shape. Thus, the imposition of a vanishing displacement in the normal direction was not sufficient to keep the cylindrical shape. In order to solve that problem, the wall nodes are repositioned on the cylinder at the end of each continuation step.

3. For the viscoelastic calculations only, boundary conditions are imposed on the constitutive equation. As has been done for the momentum equation, the inflow is calculated separately: velocities and extra-stress tensor are calculated by solving a channel flow problem on the inlet section. Then the calculated fields are used to impose Dirichlet conditions for the three-dimensional calculation of the viscoelastic flow.

3.3.4 Interpolations

In order to reduce the computational cost of the calculations, we use the mini-element of Fortin for the spatial discretization of velocities and pressure [For81]. We use a trilinear interpolation of the coordinates.

For viscoelastic calculations, we use the DEVSS formulation of Guénette and Fortin. The extra-stress tensor, is discretized with a trilinear interpolation. For the additional tensor \mathbf{D} , we use a constant and discontinuous interpolation per element (thus the shape function of \mathbf{D} are identical to those of the pressure field).

3.3.5 The contact line problem

Along the walls, the velocity vanishes, and consequently, the kinematic condition vanishes too. Therefore, we have no equation to predict the position of the contact line between the free surface and the walls. In order to circumvent this difficulty, we propose a “line dynamic condition” in which the contact force is used instead of the velocity to calculate the kinematic condition. This condition is approximately equivalent to a slip condition in which the slip coefficient is very small.

Slip boundary conditions in the literature

It is interesting to remark that the words “contact line” are used in various contexts in the literature. For example, they are used to describe the separating line of the extrudate at the exit of a die [SS80]. In that context, the fluids flow perpendicularly to the line, and stress singularities appear close to the die lip when stick boundary conditions are used. Silliman and Scriven suggest the introduction of slip conditions in order to avoid those singularities. The problem of stick and slip boundary conditions has been discussed in many other publications, either from molecular or continuum viewpoints. The continuum aspect of the problem only, is interesting for us.

We are interested in a problem in which the flow is parallel to the contact line. The contact line is defined as a fluid-fluid-solid intersection. The position of the line is *a priori* unknown, but located on the solid surface. It seems that in that case, no stress singularities are observed [SS80]. Anyway, we are not interested in the problem of stress singularities, but in the problem of the calculation of the position of the contact line. In this case, when slip conditions are introduced, the aim is to have an equation to calculate the kinematic condition, and not to avoid stress singularities.

The introduction of slip boundary conditions to calculate the motion of the contact line in 3D coextrusion flow calculations has been done by Torres et al. [THV⁺93]. They compare results obtained with the extrapolation method of Dheur and Crochet [DC87], with slip conditions on the contact line and with stick boundary conditions. Unfortunately, several errors have been done in the writing of slip boundary conditions. For example, they use the two-dimensional

simplified version of the Navier's slip condition of Silliman and Scriven [SS80] instead of the general Navier's condition

$$-\frac{1}{k_{\text{slip}}}\boldsymbol{\delta}_{\text{II}} \cdot (\mathbf{u} - \mathbf{u}_s) = \boldsymbol{\delta}_{\text{II}} \cdot (\boldsymbol{\sigma} \cdot \mathbf{n}), \quad (3.6)$$

in which k_{slip} is the slip coefficient, \mathbf{n} the normal to the wall, \mathbf{u} the fluid velocity, \mathbf{u}_s the wall velocity, $\boldsymbol{\delta}_{\text{II}} = \boldsymbol{\delta} - \mathbf{n}\mathbf{n}$ the geometric tensor that projects vectors onto the local tangent plane to the surface. But it is clear that the simplified version of Silliman and Scriven cannot be used in this context; indeed, the simplification of Silliman and Scriven is based on the planar flow assumption while in this case, we have a three-dimensional flow.

Line dynamic condition as a limit case of slip condition

We have seen that slip conditions may be used to avoid vanishing kinematic condition along a wall. Assuming that the wall velocity \mathbf{u}_s vanishes, equation (3.6) may be written

$$\mathbf{u}_t = -k_{\text{slip}}\mathbf{F}_t, \quad (3.7)$$

in which \mathbf{F}_t and \mathbf{u}_t are tangential components of the wall force and wall velocity respectively. The normal component of the velocity field along the walls, u_n is of course equal to zero. The advantage of (3.7) compared to (3.6) is that the projection tensor $\boldsymbol{\delta}_{\text{II}}$ no longer appears in the equation.

When a condition of the type (3.7) is used, the velocity $\mathbf{u} = \mathbf{u}_t$ along the wall is different from $\mathbf{0}$ and may be used in the line kinematic condition. This will give good results, even with very small values of k_{slip} , for only the direction of \mathbf{u}_t is important for the kinematic condition. It is clear that the contact line is parallel to \mathbf{u}_t and thus parallel to \mathbf{F}_t . Thus, we could use \mathbf{F}_t to “feed” the line kinematic condition. That is the basic idea of the “line dynamic condition”.

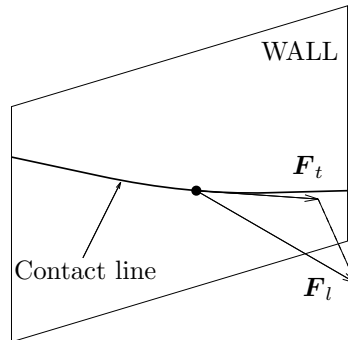


Figure 3.18: Representation of the line dynamic condition. For each point, the contact line is parallel to the tangential component of the contact force.

In order to avoid the ambiguities of the paper of Torres et al. [THV⁺93] we try to describe and justify in section C.1 with as much details as possible

the way we calculate the position of contact lines in our computational software. Actually, when we use the line dynamic condition a small velocity appears along the contact line. Thus, the way we implement the dynamic condition is approximately equivalent to introducing a small amount of slip for the nodes of the contact line. But the velocity for the other nodes of the wall vanish. (For this aspect, our condition is similar to the one used by Torres et al.) Another original aspect of our “slip” condition is that it is calculated node-by-node (i.e. we do not write its weak formulation); thus, the nodal velocities are a representation of the nodal contact forces.

Contact line on a cylindrical wall

In our problem, the wall is cylindrical, and the component of the contact force tangential to that wall (i.e. its projection on the wall) is calculated by adding a radial compensating force to the initial contact force along the line (Figure 3.19). More precisely, the radial vector is defined as

$$\mathbf{r}(x, y) = \frac{(x, y, 0)^T}{x^2 + y^2}.$$

The compensating force is oriented towards the radial direction, and is the Lagrange multiplier of the constraint on the contact force:

$$\text{Equation } \mathbf{F}_t: \quad \mathbf{F}_t - F_r \mathbf{r} = \mathbf{F}_l,$$

$$\text{Equation } F_r: \quad \mathbf{F}_t \cdot \mathbf{r} = 0.$$

In other words, the compensating radial force F_r is calculated in such a way that $\mathbf{F}_l + F_r \mathbf{r}$ is tangent to the wall. This may be better seen on Figure 3.19 on which we represent the geometric construction of the compensation radial force, and the resulting tangential component of the contact force.

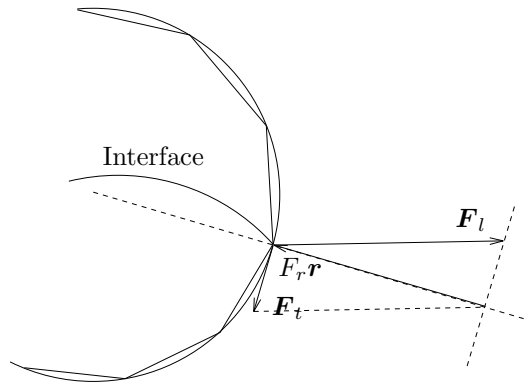


Figure 3.19: Calculation of the tangential component of the contact force to the wall by imposition of a compensating radial force.

3.3.6 Compensation of pressure

But when the wall has a cylindrical shape, other problems have to be solved in order to use the line dynamic condition. Among those problems, the fact that the mesh is generally coarse, induces pressure to contribute significantly to the tangential component of the contact force (Figure 3.20). This numerical effect is related to the fact that the boundary of the geometry is not well approximated by the spatial discretization.

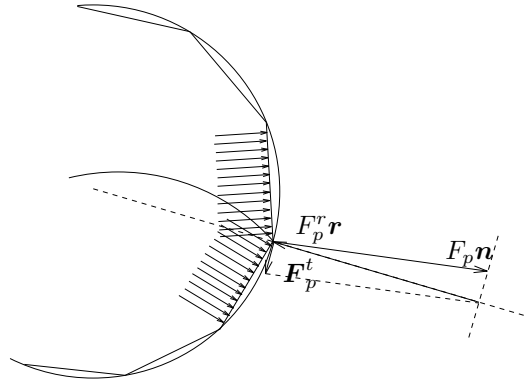


Figure 3.20: *Problem for the line dynamic condition caused by the pressure.*

The origin of this problem comes from the fact that the pressure contributions may result in a contact force that is not oriented towards the radial direction. Therefore, the radial compensation of those contributions leaves a non-vanishing tangential component. Of course, this tangential component of the pressure contribution to the contact force is totally unphysical: for a non-discretized problem, the pressure only leads to contact forces normal to the surface.

This problem may be solved by a refinement of the mesh, or by the use of a higher order of interpolation for the geometrical unknowns. Unfortunately, those two solutions may lead to a very important increase of the computational cost. Therefore, we prefer to cancel the unphysical contributions of the pressure in the momentum equations along the cylindrical surface. This is done by applying a compensating normal force on the cylindrical surface. This force is equal to the pressure in the fluid, and oriented towards the axis of the cylinder (Figure 3.21).

Note that the problem of pressure also occurs when slip conditions are imposed on a curved boundary in contact with an interface.

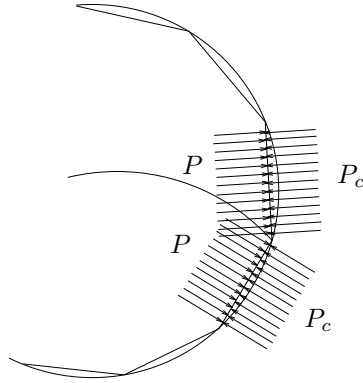


Figure 3.21: *Compensation of pressure applied on the cylindrical surface.*

3.4 Viscoelastic calculations

3.4.1 Strategy of resolution

The equations governing the encapsulation problem are strongly nonlinear. The nonlinearities are related to the nonlinear character of the models, to the presence of convected derivatives in the constitutive equations, to the presence of free surfaces, and to the techniques of remeshing used in both layers. The nonlinearities are so important that continuation techniques have to be used to calculate the encapsulation flow. Therefore, we separate the calculation of the final flow into three steps:

1. We calculate a flow without introducing any remeshing rule, and thus without modelling the motion of the interface. For this calculation, we also neglect all viscoelastic effects. Thus, we put the relaxation time λ to 0.

Note that for this step, the fluid may flow across the interface. This, of course, is totally unphysical, for it means that the material properties of a fluid particle change instantaneously when this particle changes of layer. For that reason, we do not present any result of the first step calculation.

When we put $\lambda = 0$ for the viscoelastic calculations, the Giesekus constitutive equation reduces to a Newtonian model. Nevertheless, we calculate the initial flow with a MIX formulation (we discretize pressure, velocity and extra-stress fields). This does not increase the total computation cost significantly for we may do this calculation without using any continuation method, because the governing equations of this step are quasi linear.

2. The mobility of the interface is introduced in the calculations at the second step. Here again, because of the nonlinearities of the remeshing equations and kinematic conditions, a continuation method is used. Indeed, it is

possible to select flow rates such that the motion of the interface is very large, even for Newtonian calculations.

An advantage of the line kinematic condition, is that it is possible to use a continuation method for the motion of the interface, thanks to the evolution parameter ζ_l of the line kinematic condition (equation 1.40). We progressively increase the deformation of the initial interface by making ζ_l vary from 0 to 1:

$$\zeta_l(s_2) = s_2, s_2 : 0 \rightarrow 1.$$

3. In the third step of the calculation the viscoelasticity is progressively introduced in the model. This is the most difficult part of the calculation, and we have made several attempts to find the right path to reach the final solution. Those attempts are presented in the next section.

We first present in Figure 3.22 the layers configuration obtained at the end of the second step. This corresponds to a Newtonian fluid, though calculated with a MIX formulation. The kinematic condition is fully modelled.

For the calculations, we only use the shortest die of Han (die “A” in table 3.2). The reason of this choice is that the calculation of encapsulations in longer dies generally leads to very high degrees of encapsulation. This leads to very large deformations of the mesh, and generally the calculation fails before the end of the continuation on parameter s_3 . The flow rates for LDPE and PS are $276.67 \text{ mm}^3\text{s}^{-1}$ and $69.17 \text{ mm}^3\text{s}^{-1}$ respectively.

A layer rearrangement occurs in the merging area, just after the separating edge. The lower layer fluid (i.e. the high viscosity polystyrene layer) has a convex shape. This may be interpreted as follows: just after the separating edge, both fluids try to swell; but the strongest fluid (in this case PS) imposes its will to the weaker one (LDPE). It pushes into the low viscosity fluid and imposes its convex shape. The low viscosity fluid is just “allowed” to wet the walls.

Note that the layer rearrangement occurs close to the end of the separating edge. The free surface reaches very rapidly a new equilibrium shape, and this shape does not seem to vary with the distance from the merging area. In other words, with a Newtonian model, we obtain the rapid rearrangement in the merging area, but not the slow encapsulation observed by Everage. This confirms results obtained for the numerical calculations of encapsulation in a square die [KHV90, Uwa95].

3.4.2 Progressive increase of relaxation time

The most evident way to introduce viscoelasticity in the model is to increase the relaxation time λ . Thus, we have

$$\begin{aligned}\lambda_{\text{LDPE}} &= \lambda_{\text{LDPE}}^{\text{final}} s_3, s_3 : 0 \rightarrow 1, \\ \lambda_{\text{PS}} &= \lambda_{\text{PS}}^{\text{final}} s_3, s_3 : 0 \rightarrow 1,\end{aligned}$$

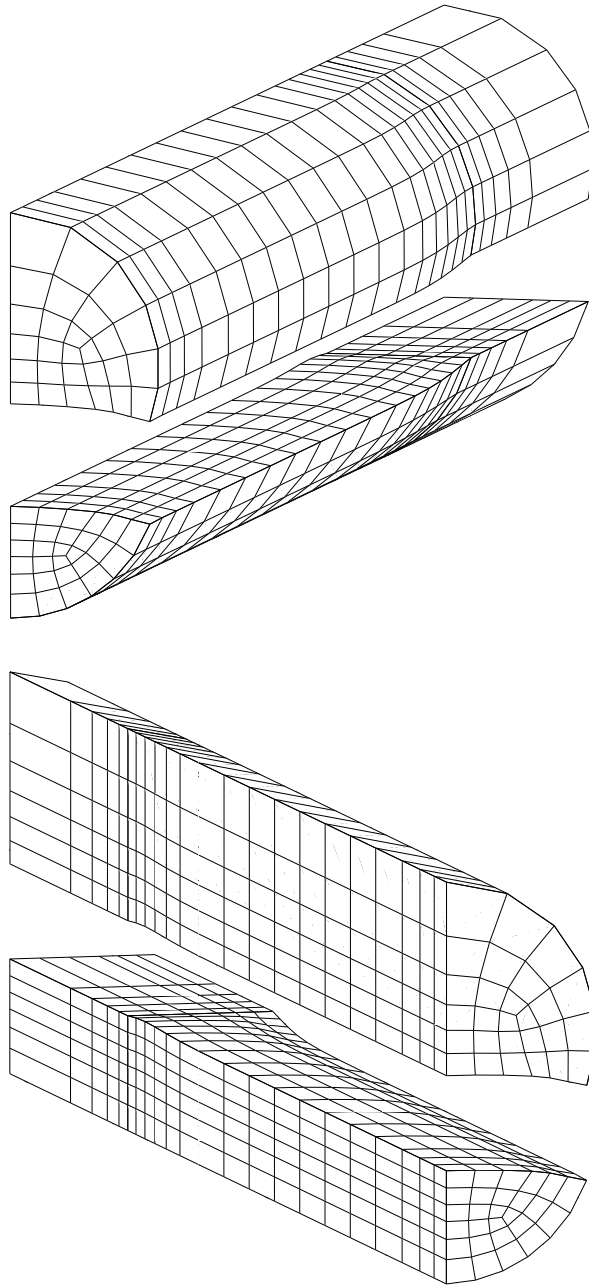


Figure 3.22: Configuration of the layers for $\lambda = 0$ at the end of the second step of viscoelastic calculations (Newtonian fluid). The upper part represents the two layers seen from one side. The lower part gives the layers observed from the other side.

in which $\lambda_{\text{LDPE}}^{\text{final}}$ and $\lambda_{\text{PS}}^{\text{final}}$ correspond to the values given in table 3.3.

By increasing the relaxation time, we increase both the convected derivatives and the last term of the constitutive equation 3.1, responsible for the second normal stress difference of the model. Thus, we also increase the degree of encapsulation.

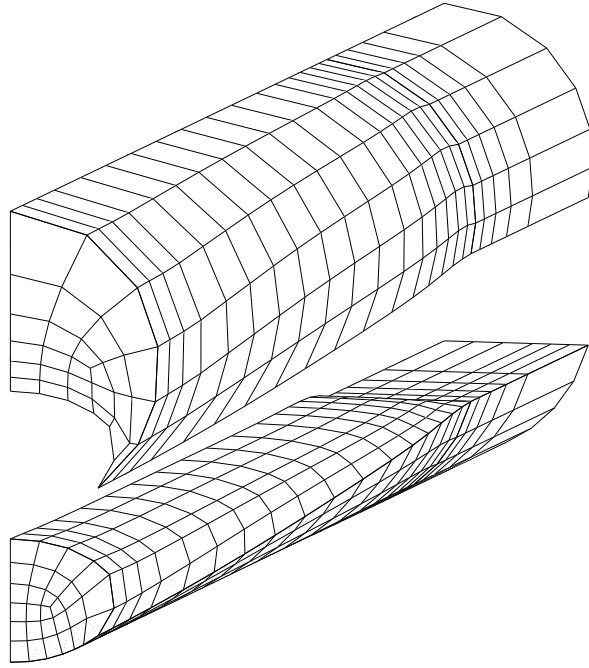


Figure 3.23: *Configuration of the layers at the end of the evolution on relaxation times for a Giesekus model. The evolution parameter is $s_3 \approx 0.01166$.*

The last result obtained with our continuation method corresponds to $s_3 \approx 0.01166$. A little more than 1 % of the path has been done, and that is not much! The configuration of the layers corresponding to the last calculation are presented in Figure 3.23. We see that, even though only 1 % of the path to the final value of s_3 has been done, a relatively high degree of encapsulation has been obtained.

We made an investigation in order to find the reason why we failed to reach higher values of s_3 . It seems that the extra-stress field is well approximated (but we do not present the results here). The only explanation we have found to the failure of the calculation is that the deformation of the mesh is too important for our remeshing technique. It is surprising that at only 1% of the continuation on s_3 , we obtain a so large degree of encapsulation. We know that for $s_3 = 0$, the Giesekus model exhibits no normal stress differences, and the encapsulation is clearly related to the increase of λ . But, which results would we obtain for $s_3 = 1$

if it was possible to reach such a large value of the continuation parameter?

In this chapter, we have adopted the assumption that second normal stress difference is responsible for encapsulation. Thus the high degree of encapsulation should be related to the value of the ratio N_2/T_{shear} . In order to see how the degree of encapsulation depends on the relaxation time λ , we plot in Figure 3.24 the ratio of the second normal stress difference and shear stress in a planar shear flow as a function of s_3 (and thus of the relaxation time λ). All other parameters are those of the polystyrene in table 3.3. To select the value of $\dot{\gamma}$, we first calculate a mean value of the velocity in the die, and divide it by the radius to estimate a mean value of the shear rate. We find $\langle \dot{\gamma} \rangle \approx 6.88 \text{ s}^{-1}$. To take into account the fact that the shear rate is larger along the walls, we plot the results for $\langle \dot{\gamma} \rangle \approx 15 \text{ s}^{-1}$.

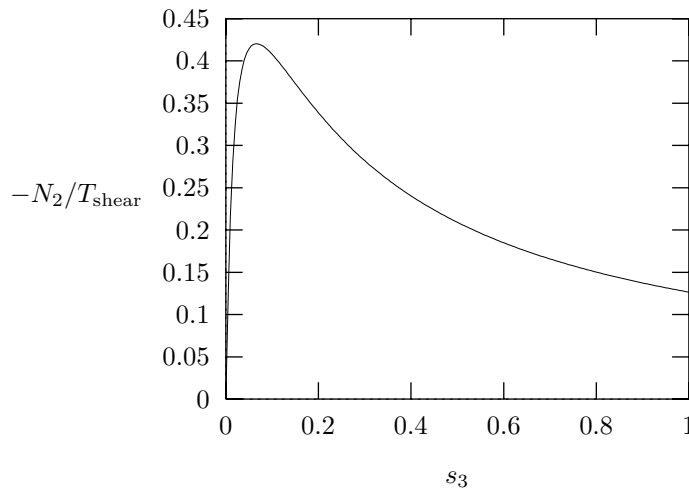


Figure 3.24: *Ratio of the second normal stress difference and of the shear stress as a function of parameter s_3 that controls relaxation time λ and for $\dot{\gamma} = 15 \text{ (s}^{-1}\text{)}$.*

For small values of s_3 the ratio increases very fast. It reaches a maximum at $s_3 \approx 0.065$, and then slowly decreases. For $s_3 = 0.01$ we find 0.2174. That means that when 1 % of the continuation on s_3 has been performed, the degree of encapsulation is nearly twice as large as what we would obtain for $s_3 = 1$. Thus we tried to follow a path in which we obtain very fast a high degree of encapsulation that would later decrease if it was possible to continue the calculation. But actually, the calculation fails because of the too large deformation of the mesh.

Note that the problem is essentially related to the first initial increase of the normal stress differences with the relaxation time (see Figure 3.25).

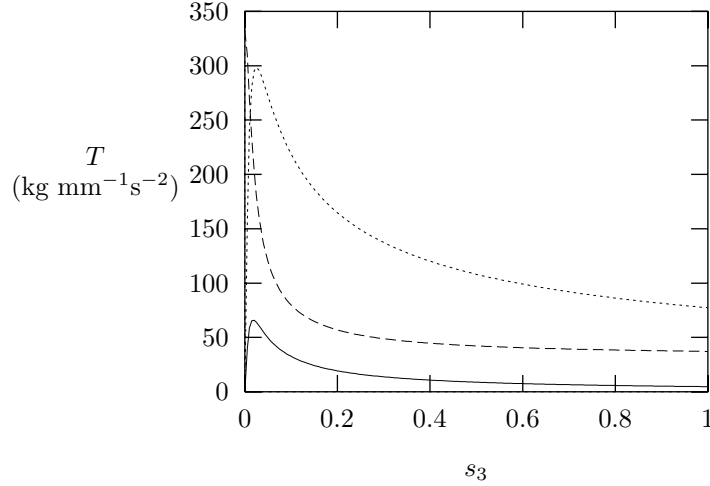


Figure 3.25: *Second normal stress difference (continuous line), shear stress (dashed line), and first normal stress difference (dotted line) as a function of parameter s_3 that controls relaxation time λ and for $\dot{\gamma} = 15$ (s^{-1}).*

3.4.3 Results for an Oldroyd-B calculation

There is one way to avoid the fast initial increase of the degree of encapsulation with parameter λ . By putting α_G in the Giesekus model to zero, we obtain an Oldroyd-B model that exhibits no second normal stress difference, and thus no secondary recirculation in a channel flow. The third step of the calculation would then be divided into two sub-steps:

1. The relaxation times λ are increased, but α_G is put to 0:

$$\begin{aligned}\lambda_{\text{LDPE}} &= \lambda_{\text{LDPE}}^{\text{final}} s_3, \quad s_3 : 0 \rightarrow 1, \\ \lambda_{\text{PS}} &= \lambda_{\text{PS}}^{\text{final}} s_3, \quad s_3 : 0 \rightarrow 1.\end{aligned}$$

2. Then, a fourth step is performed, in which the parameters α_G are progressively increased to their final values:

$$\begin{aligned}\alpha_{\text{G,LDPE}} &= \alpha_{\text{G,LDPE}}^{\text{final}} s_4, \quad s_4 : 0 \rightarrow 1, \\ \alpha_{\text{G,PS}} &= \alpha_{\text{G,PS}}^{\text{final}} s_4, \quad s_4 : 0 \rightarrow 1.\end{aligned}$$

Unfortunately, the evolution on the relaxation times λ failed for $s_3 = 0.0389$. The corresponding configuration of the layers is represented in Figure 3.26. It clearly appears that the swelling of polystyrene just after the separating edge is very important (much more important than what is observed for the Newtonian and Giesekus calculations). This is related to the large values of the first normal stress difference of the Oldroyd-B model.

When one single fluid is extruded in a die, the swelling at the exit of the die may be very important when the fluid exhibits large values of the first normal

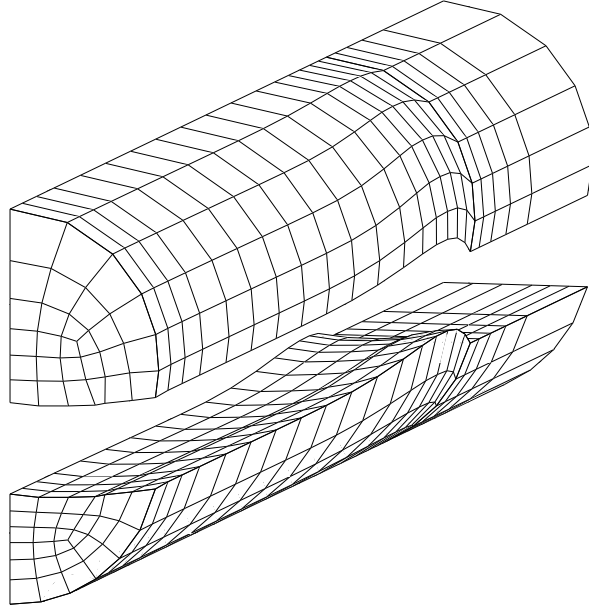


Figure 3.26: *Configuration of the layers at the end of the evolution on relaxation times for an Oldroyd-B model. The evolution parameter is $s_3 \approx 0.0389$.*

stress difference. In this case, when LDPE and PS are brought together in the die, each fluid tries to swell, and the strongest fluid (the fluid that exhibits the largest first normal stress difference) wins. Here again, the strongest fluid is polystyrene.

The reason why our calculation failed for small values of the relaxation time λ , is that in the merging area, and close to the interface, the fluid particles are submitted to a high elongation. This results in a thin layer of fluid in which the axial component of the extra stress tensor is very large. We see in Figure 3.27 that the phenomenon is particularly important for LDPE, which cannot swell. In order to capture the correct solution in that area, we should refine the mesh close to the interface. But we need a so important refinement that the computational cost would be prohibitive.

Actually, the Oldroyd-B model leads to numerical difficulties. In many cases, the Giesekus model is easier to use, because it exhibits saturation effects: the stresses cannot grow infinitely with this model.

3.4.4 Giesekus with a very large Newtonian component

A third attempt has been done to try to calculate the final flow with Giesekus model. We have seen in section 3.4.2 that the very high degree of encapsulation occurring at small values of λ with the Giesekus model may be related to the large values of the ratio N_2/T_{shear} for small values of the relaxation time.

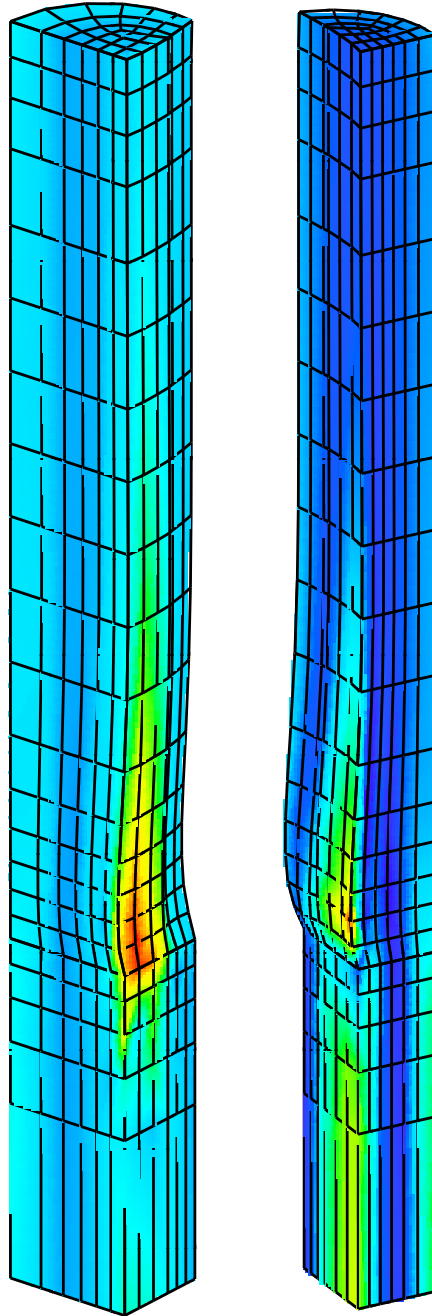


Figure 3.27: zz component of the extra stress tensor in both layers for an Oldroyd- B model. The evolution parameter is $s_3 \approx 0.0389$.

This problem may be avoided by artificially increasing T_{shear} . It may be done by adding an artificial viscous component to the Cauchy stress tensor. The relaxation time may then be increased to its final value. Then, the artificial viscous component may be progressively cancelled in a last continuation.

In practice, we proceed as follows:

1. During the continuation on the relaxation times, the parameter η_N is put to ten times its value given in table 3.3. Moreover, the shear thinning character of the viscous component is cancelled by putting n to 1. We have thus

$$\begin{aligned}\lambda_{\text{LDPE}} &= \lambda_{\text{LDPE}}^{\text{final}} s_3, \quad s_3 : 0 \rightarrow 1, \\ \lambda_{\text{PS}} &= \lambda_{\text{PS}}^{\text{final}} s_3, \quad s_3 : 0 \rightarrow 1.\end{aligned}$$

2. Then, a new continuation is required to progressively restore the parameters given in table 3.3 for the viscous component. This is done as follows

$$\begin{aligned}\eta_{\text{NLDPE}} &= 10\eta_{\text{NLDPE}}^{\text{final}}(0.1)^{s_4}, \quad s_4 : 0 \rightarrow 1, \\ n_{\text{LDPE}} &= (1 - s_4) + n_{\text{LDPE}}^{\text{final}} s_4, \quad s_4 : 0 \rightarrow 1, \\ \eta_{\text{NPS}} &= 10\eta_{\text{NPS}}^{\text{final}}(0.1)^{s_4}, \quad s_4 : 0 \rightarrow 1, \\ n_{\text{PS}} &= (1 - s_4) + n_{\text{PS}}^{\text{final}} s_4, \quad s_4 : 0 \rightarrow 1.\end{aligned}$$

Actually, the calculation fails during the continuation on λ at $s_3 \approx 0.2$. We do not represent the examples of layer configurations for that calculation, for the results are very similar to those of the Newtonian calculations. The fact that the calculation fails indicates that the nonlinear character of the constitutive equation also may be responsible of numerical difficulties. This problem probably may be solved by using a refined mesh for the calculations, but here again, this would result in a very large increase of computational cost.

Compared to viscoelastic calculations, Reiner-Rivlin calculations give rise to very few numerical problems. Moreover, their computational cost is small. We present the results obtained with those calculations in section 3.5.

3.5 Reiner-Rivlin calculations

3.5.1 Strategy of resolution

In the Reiner-Rivlin calculations, the nonlinearities arise from the presence of free surfaces, from the remeshing technique, and from the constitutive equation.

We separate the calculation of the final flow into three steps:

1. We calculate a flow without introducing any remeshing rule, and thus without modelling the motion of the interface. For this calculation, we also neglect second normal stress differences: $\psi_2(\dot{\gamma}) = 0$.

Note that, here again, the fluids may flow across the interface (see section 3.4.1).

Because of the shear thinning character of the viscosity, this first step already involves strong nonlinearities, and a continuation method is used to calculate the flow. We progressively make the shear thinning character of the fluids increase by making the power law index m vary from 1 to its final value given in table 3.4. More precisely, we make a parameter s_1 vary from 0 to 1, and the power law index is calculated from that parameter with the formula

$$m(s_1) = (1 - s_1) + m_{\text{final}}s_1,$$

in which m_{final} is replaced by the corresponding value given in table 3.4.

2. The mobility of the interface is introduced in the calculations at the second step. This step is equivalent to what has been done at the second step of viscoelastic calculations (section 3.4.1).
3. The second normal stress difference is introduced in the model at the third step of the calculation. For the Reiner-Rivlin model, the parameter ψ_{20} is progressively increased with parameter s_3 :

$$\psi_{20}(s_3) = \psi_{20}^{\text{final}} s_3, \quad s_3 : 0 \rightarrow 1.$$

Note that, for this step, the nonlinearities are introduced both in the constitutive and remeshing equations.

The parameters that will change from one calculation to another are the relative flow rates. We also perform a mesh convergence analysis. The parameters of our calculations are summarized in table 3.5. The flow rates of calculation ‘‘A’’ are identical to those used in our viscoelastic calculations.

Table 3.5: *Relative flow rates of LDPE and PS for our calculations.*

Calc.	Q_{LDPE} mm^3s^{-1}	Q_{PS} mm^3s^{-1}
A	276.67	69.17
B	448.33	69.17
C	82.50	90.83

3.5.2 Results for a first set of parameters

We first present the layers configuration for the Newtonian part of calculation A in table 3.5 (upper part of Figure 3.28). As has been observed in Figure 3.22, the layer rearrangement occurs close to the merging area, but after that, the shape of the interface does not change along the die. It is interesting to remark that the shape of the interface is very similar to the shape obtained with the

MIX Newtonian calculation 3.22. This is surprising for the fluids of Figure 3.28 are shear thinning while the viscosities of the fluids in Figure 3.22 are nearly constant.

With our modelling of the problem, we must introduce second normal stress difference in the constitutive model to obtain a progressive encapsulation. The lower part of Figure 3.28 represents the flow configuration when second normal stress difference is introduced in the model.

Very similar results are obtained when the calculations are done on a refined mesh (Figure 3.29). This may be better seen in Figure 3.30 where we compare the output profiles obtained with Newtonian and Reiner-Rivlin models and for coarse and refined meshes respectively. This means that good results may be obtained with a relatively coarse mesh.

3.5.3 Results for other values of the flow rate

The results obtained for the flow rates corresponding to B in table 3.22 are presented in Figure 3.31 for the refined mesh. They are in qualitative agreement with results of calculation A: a rapid rearrangement occurs in the merging area; then a slow encapsulation process takes place. Note that, in this case, the rapid rearrangement in the merging area leads to larger deformations of the interface than in case A, because the flow rates are different.

For calculation C, the flow rates are such that the swelling of polystyrene is very important. For the rest, results are in qualitative agreement with calculations A and B.

3.5.4 Comparison with experiments

The flow rates we have used in our numerical calculations correspond to those of some of the results presented by Han in his paper [Han73]. Han presents cross sections of the LDPE/PS extrudates for various values of the flow rates (and in particular for the flow rates used in our calculations). We compare in Figure 3.33 the extrudate cross sections with the corresponding calculated shapes of the interface at the outlet section.

Discrepancies between the cross sections of Han and our outlet interface profiles may be observed. The most striking difference between calculations and experiments resides in the fact that the area occupied by polystyrene in the calculations is always larger than in the experiments. This may easily be explained. There is a relation between the relative flow rates, mean velocities and areas at the outlet section. This relation may be written

$$\frac{Q_{\text{LDPE}}}{Q_{\text{PS}}} = \frac{\langle V_{\text{LDPE}} \rangle A_{\text{LDPE}}}{\langle V_{\text{PS}} \rangle A_{\text{PS}}},$$

in which $\langle V \rangle$ is the mean value of z component of the velocity and A is the area occupied in the cross section.

In all our calculations, the mean velocity of polystyrene is smaller than that of polyethylene. But out of the die, the flow rapidly tends towards a plug flow,

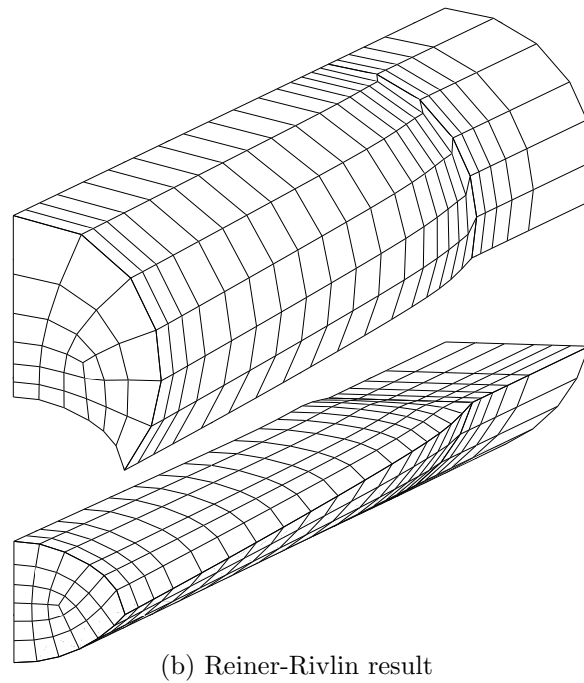
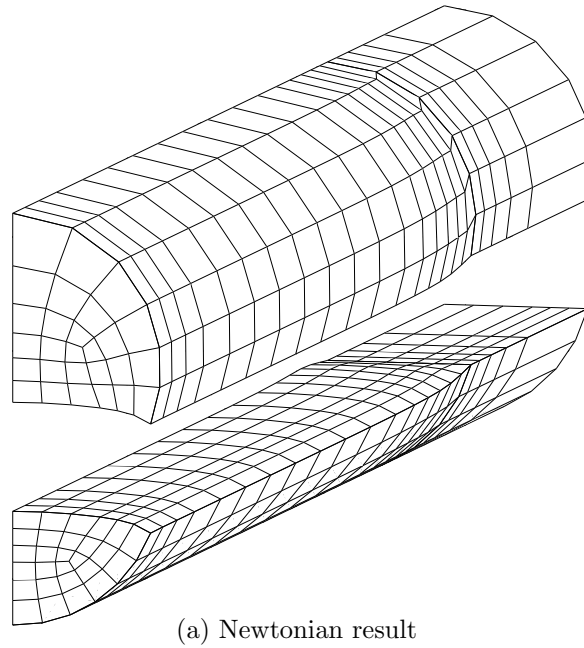
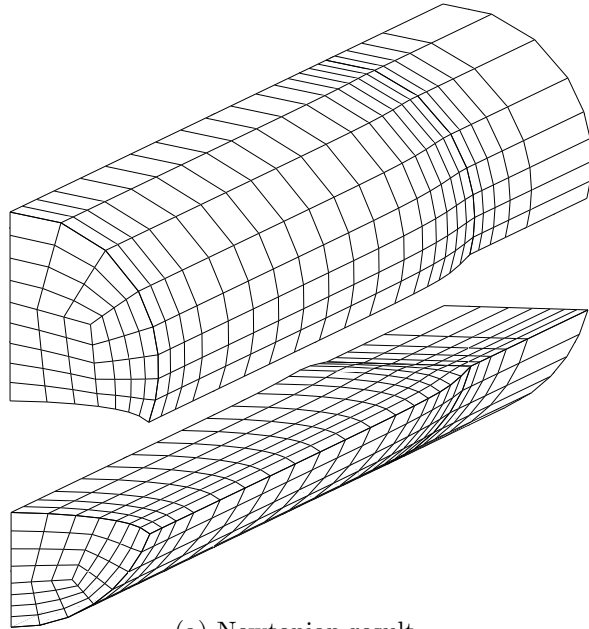
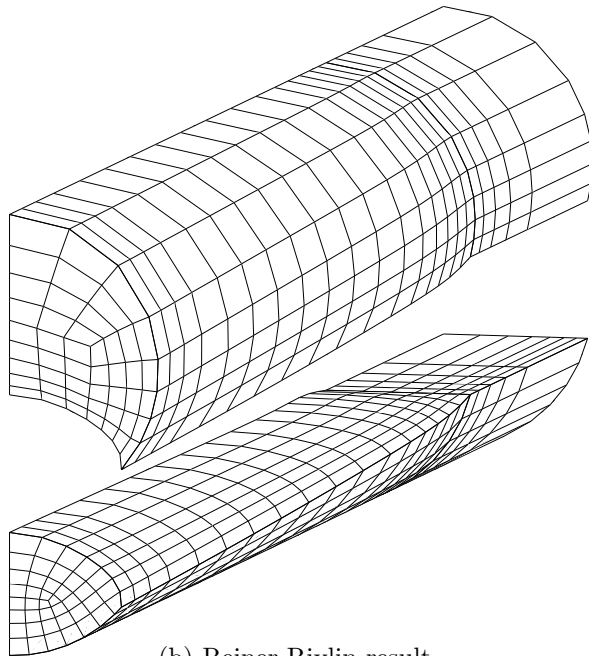


Figure 3.28: Configuration of the layers for the Newtonian and Reiner-Rivlin parts of calculation A (coarse mesh).



(a) Newtonian result



(b) Reiner-Rivlin result

Figure 3.29: Configuration of the layers for the Newtonian and Reiner-Rivlin parts of calculation A (refined mesh).

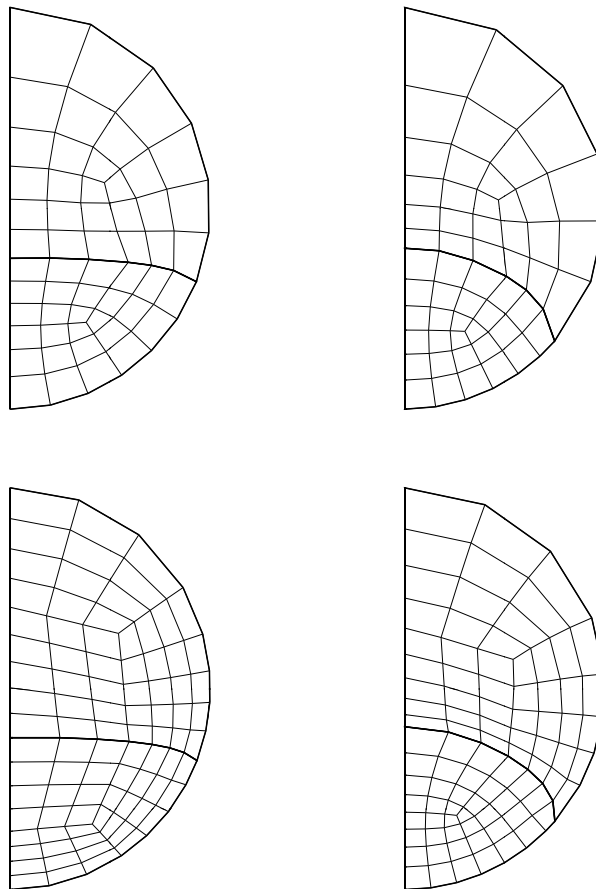


Figure 3.30: Comparison of the output profiles for coarse (upper part) and refined (lower part) meshes, and for Newtonian (left part) and Reiner-Rivlin (right part) models.

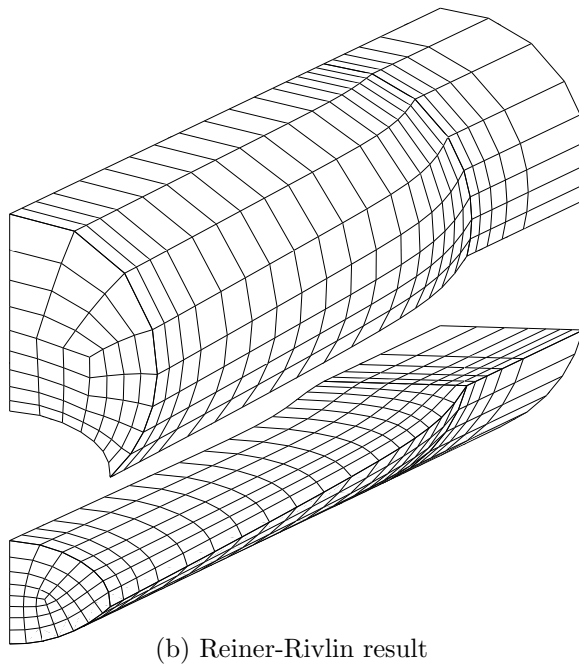
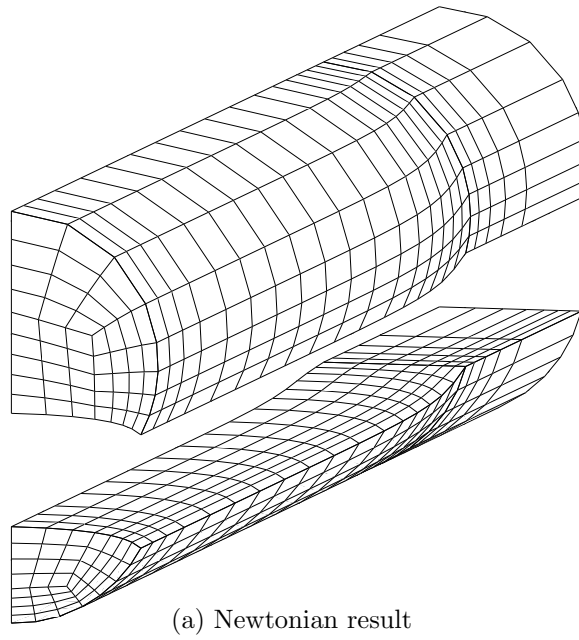


Figure 3.31: Configuration of the layers for the Newtonian and Reiner-Rivlin part of calculation B (refined mesh).

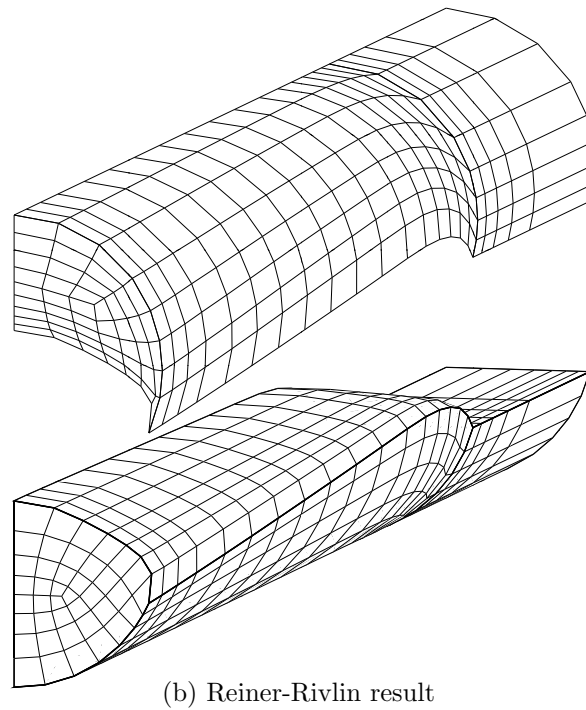
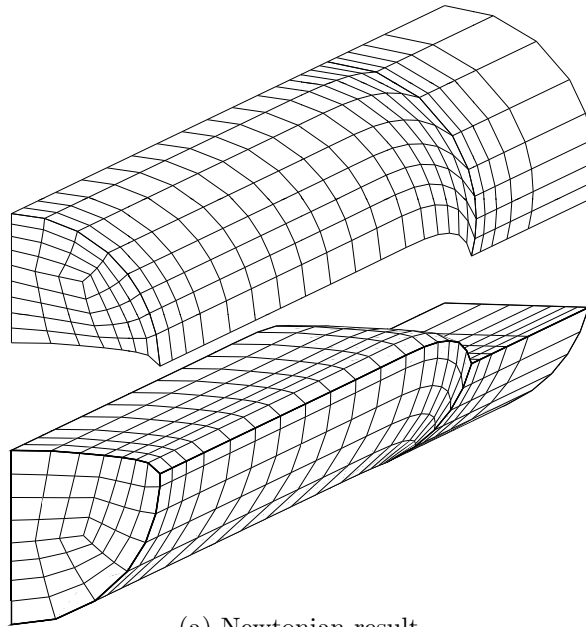


Figure 3.32: Configuration of the layers for the Newtonian and Reiner-Rivlin parts of calculation C (refined mesh).

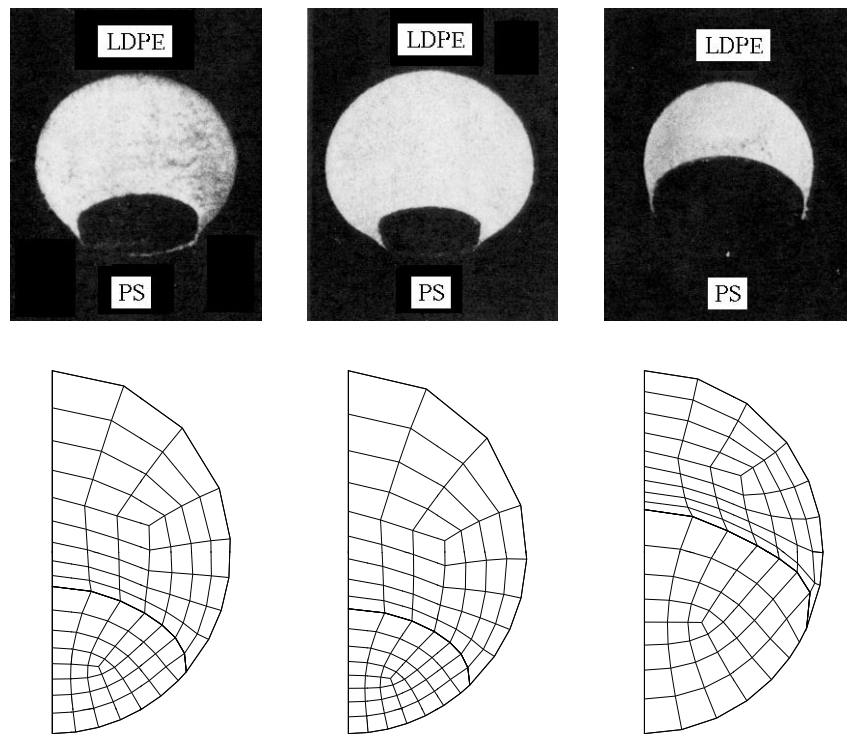


Figure 3.33: Comparison of experimental results of Han [Han73] with the configuration of the layers along the outlet section obtained with our numerical calculations.

and the velocity profile becomes flat in the whole cross section. Thus the mean velocity becomes identical for both fluids. Consequently, in the extrudate, the proportion of the cross section area occupied by PS is equal to its flow rate divided by the total flow rate. In the die, PS occupies a larger proportion of the cross section area.

Therefore, the comparison given in Figure 3.33 only may be qualitative. If we observe the way polystyrene is surrounded by LDPE at the outlet section and in the extrudate cross sections, we see that the degree of encapsulation is approximately the same for each flow rate ratio. It is interesting to remark that this result has been obtained without using any artificial trick, and without manipulation of data.

This means that the estimation of second normal stress difference by a Giesekus fit seems to give good results. This is surprising for we do not know so much about second normal stress difference. This quantity is small compared to other stresses in shear flows. Consequently, it is very difficult to measure with precision. Moreover one does not know what is the microscopic origin of that quantity. But it seems that by fit other rheometrical data with a Giesekus model, one is able to correctly reproduce N_2 effects.

A similar observation has been done by Benoît Debbaut et al. [DADH97]. They study the development of secondary recirculations caused by second normal stress difference both experimentally and numerically. They use a five modes Giesekus model for their calculations, and obtain a very good agreement though they only fit viscosity, G' and G'' .

This indicates that the term in " $\mathbf{T} \cdot \mathbf{T}$ " of the Giesekus constitutive equation correctly models the mechanism by which the second normal stress difference is related to the other stresses in molten polymers and for shear flows. And it explains why by fit the available shear data, one also catches information on the second normal stress difference.

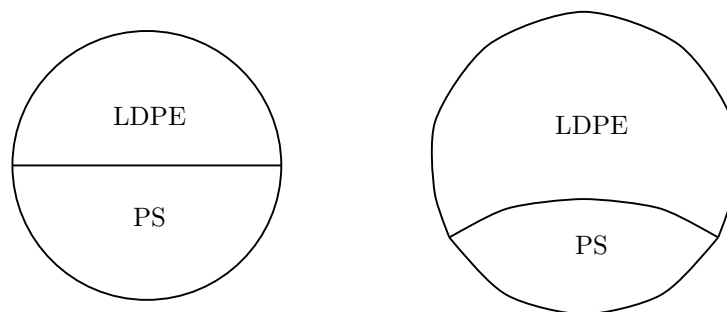


Figure 3.34: Probable rearrangement of an initially flat interface at the exit of a die.

Note that, the layer rearrangement that occurs at the exit of the die probably leads to a further increase of the degree of encapsulation. To illustrate this intuition, we plot in Figure 3.34 the probable rearrangement we would observe at the exit of the die if the interface was initially flat, and each fluid occupied

50 % of the section. The higher swelling of LDPE probably would lead to a curvature of the interface with a convex shape for polystyrene layer.

3.6 Giesekus and Reiner-Rivlin models

After having performed numerous calculations with the Reiner-Rivlin model, we would like to know whether this model correctly reproduces the viscoelastic behaviour of the Giesekus model. There are several differences between Giesekus and Reiner-Rivlin models: Reiner-Rivlin model does not exhibit first normal stress difference, its extensional viscosity is identical to that of a generalized Newtonian fluid, it exhibits no memory effects.

Except in the merging area, extensional effects are not very important for the flows we study in this chapter. They are more a source of numerical difficulties than a factor influencing encapsulation. However, we have seen in section 3.4.3 that first normal stress difference may have an important effect on layer rearrangement. But the effect of extensional stress and first normal stress difference has only been observed in calculations with Oldroyd-B model. Giesekus model is nonlinear and exhibits saturation effects. Consequently extension stresses and normal stresses are smaller with Giesekus model than with Oldroyd-B model and their influence on encapsulation probably will be smaller with Giesekus model.

Another difference between Reiner-Rivlin and Giesekus models resides in the fact that the Reiner-Rivlin model does not exhibit memory effects. With viscoelastic models, memory effects may have a large influence on flow kinematics if relaxation times are large compared to the rate of change of flow characteristics. For example, in our flow, we may compare relaxation times to the mean residence time of the fluids in the die. Unfortunately, the result of that comparison indicates that memory effects play an important role in the flow (the ratio relaxation time / residence time is approximately 4 for calculation A). This may be interpreted as follows: a fluid particle brought into the die, exits before having adapted its stresses to the flow kinematics.

But in the former comparison, we didn't take into account the nonlinear character of the constitutive equation. Most nonlinear viscoelastic models exhibit saturation effects. This is the case for the Giesekus model. In the models exhibiting such saturation effects the parameter λ no longer represents a relaxation time. Actually the more the model enters in the nonlinear domain, the shorter its response time to a modification of the flow kinematics becomes. In our case, this means that the response time decreases with the shear rate.

To illustrate this point, we plot in Figure 3.35 the transient evolution of the second normal stress difference as a function of time for various values of the shear rate (for that calculation, we used the parameters of PS in table 3.3). We see that for all values of time, N_2 is an increasing function of the shear rate. But the most interesting thing that appears in Figure 3.35, is that the regime is reached for smaller values of time when the shear rate is high. For $\dot{\gamma} = 25 \text{ s}^{-1}$ the regime is attained after approximately 0.25 s. For $\dot{\gamma} = 5 \text{ s}^{-1}$ the regime is

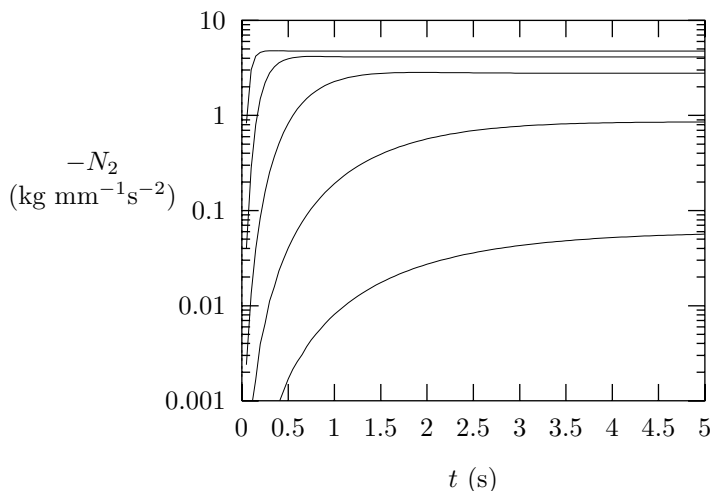


Figure 3.35: *Second normal stress difference as a function of time t for various values of the shear rate: $\dot{\gamma} = 0.04, 0.2, 1, 5, 25$ (s^{-1}) respectively.*

attained after approximately 0.5 s. Only for very small values of the shear rate, the time needed to reach the regime is approximately equal to λ .

In calculation A, the mean value of the shear rate is approximately $7 s^{-1}$. Thus, the response time of the Giesekus model is probably smaller than 0.5 s. This value is clearly smaller than the mean value of the residence time (≈ 1.2 s). Moreover, if we accept the assumption that encapsulation occurs mainly along the walls where the shear rate and residence time are larger, we also may accept that the response time of the fluid particles responsible for encapsulation is large compared to the time they need to respond to the flow kinematics.

We conclude that, for the slow encapsulation process of Everage, the Reiner-Rivlin model probably gives results similar to what we would obtain with the Giesekus model if it was possible to make the calculation with that viscoelastic model.

3.7 Conclusions

In this chapter, we have presented the results of a numerical investigation of the influence of second normal stress difference on encapsulation.

By calculating transient and static two-layer channel flows with Reiner-Rivlin model, we show that second normal stress difference is the origin of secondary recirculations that cause interface motion. In that case, it appears clearly that N_2 is the key factor to explain interface motion.

Then, we simulate the experimental observations of Han [Han73] with Reiner-Rivlin model. With this model, we obtain a good agreement between experimental observations and numerical calculations. The encapsulation obtained by our calculations is related to second normal stress difference only. Indeed,

Reiner-Rivlin model does not exhibit first normal stress difference, and no slow encapsulation process have been obtained with Newtonian model. This result is new: in former calculations of Uwaji, PTT model exhibited both first and second normal stress differences. Moreover, the fits of Uwaji only poorly approximated the behaviour of real fluids. Note that calculations done with the Oldroyd-B model indicate that the layer rearrangement observed in the merging area is influenced by the viscosities and first normal stress differences of the fluids.

The rheological data of Han are used to fit the parameters of Giesekus model. But we have no experimental measurements of the second normal stress difference. Thus, in order to fit the parameters of Reiner-Rivlin model, we propose a two-step procedure in which the missing data are produced by a Giesekus fit.

To calculate the motion of the contact line between the interface and the wall, we propose a “line dynamic condition” in which the value of the contact force is used instead of the velocity in the kinematic condition. The problems related to the curvature of the wall have been solved.

Let us remark that with both Oldroyd-B and Giesekus models, numerical difficulties related to the viscoelasticity of the models prevent us to simulate realistic problems. In comparison, Reiner-Rivlin model is in many cases a very interesting model: it does not lead to important numerical difficulties and is cheap because no extra-stress field is needed to calculate the flow.

Conclusions

In this first part, we have investigated the behaviour of multilayer flows. In chapter 2 the stability of multilayer Newtonian flows has been studied by transient calculations. Chapter 3 was devoted to the study of the influence of second normal stress difference on encapsulation. This second investigation has been done with time independent calculations.

In chapter 2 we show that it is possible to study the stability of multilayer flows by transient numerical calculations. The calculations allow us to compare results of linear stability analyses and transient simulations, and to investigate the nonlinear behaviour of growing perturbations. It is also possible to reproduce with transient calculations some of the flow regimes experimentally observed in axisymmetric flows. In particular, the bamboo waves regime may easily be obtained. In this flow regime, the thin-layer effect stabilizes long wavelength perturbations and compensates capillary instabilities while short wavelength instabilities are compensated by surface tension.

Encapsulation phenomena are often observed experimentally with Newtonian flows in pipes, and the bamboo waves regime may be the result of an encapsulation. Those encapsulations are probably the result of an interfacial instability, related to inertia. In order to check that assumption, three-dimensional multi-layer transient flows should be calculated. In view of their very high computational cost, such calculations have not been performed.

In chapter 3, we try to check whether encapsulation may be related to the secondary recirculations caused by second normal stress difference in channel flows. An advantage of this possible explanation, is that it may be checked by performing time-independent flow calculations. It appears that the rapid rearrangement observed in the merging area is mainly influenced by the viscosities and first normal stress differences. But the slow encapsulation process is only caused by the second normal stress difference exhibited by viscoelastic fluids. This slow encapsulation process generally leads to higher degrees of encapsulation than the rearrangement of the layers observed in the merging area.

One sometimes observe coextrusion flows in which encapsulation and interfacial instabilities occur together. For example Wilson and Khomami report experiments in which the extrudate exhibits encapsulation and wavy interfaces [WK93a]. But this does not prove that encapsulation is a consequence of interfacial instability and it is interesting to remark that Han does not report any wavy interface in his extrudates [Han73].

We conclude that the encapsulations observed in Newtonian and viscoelastic multi-layer flows respectively are, in general, caused by two distinct mechanisms. For Newtonian flows, the thin-layer effect is responsible for the phenomenon, while in viscoelastic flows, second normal stress difference has to be incriminated. Though, in both cases, the more viscous fluid is often encapsulated by the less viscous one.

Part II

Numerical calculation of extensional flows

THIS PAGE IS INTENTIONALLY LEFT BLANK

Introduction

In many process flows, the extensional behaviour of polymer solutions or melts is of critical importance. For example, it is now well established that contraction flows are, in many cases, strongly influenced by extensional behaviour [DC88, PCb]. Therefore, the measurement of extensional stresses is a subject of investigations for rheologists. The measurement of extensional stresses leads to important experimental difficulties, especially for polymer solutions that exhibit generally smaller viscosities than polymer melts. Recently, the filament stretching device has allowed to measure steady state values of the extensional viscosity [TS93, OS94]. The principle of the extensional rheometer is to try to expose the sample to steady uniaxial extensional flow.

But among other difficulties, the fact that the flow only approximates uniaxial extensional flow often prevents us to give a straightforward interpretation of the measurements. Of course, this problem also occurs in other types of rheometrical experiments. Therefore, an analysis of the flow can help to improve the interpretation of the experimental data. This type of analysis has already been made both by experimental observations and by numerical simulations [SDK91, PCc, PN95, SM96a, MC87, Cas96, SAM96].

In chapter 4, we present results of a numerical study of the filament stretching device. In that investigation, we try to derive the optimal operating conditions for the device. we also describe some of the phenomena that may lead to difficulties in the interpretation of the measured quantities. For example, we show that the device leads to non-uniformities of the stretching, both in time and space. We also investigate the effects of the material parameters and of the initial gap between the plates, and comparisons are done with experimental observations. Finally, we propose a way to improve the estimates of the extensional viscosity given by the device.

Finally, the flow in the filament stretching device can be used as an investigation tool. Orr and Sridhar observe a rapid drop of the tensile stress in the filament when extension ceases. They interpret this rapid drop as a vanishing of a viscous polymer stress at the end of stretching [OS96]. Birefringence experiments indicate that there is no unique relation between the stress in the filament and the elongation of the macromolecules [DS97, DSMS97]. Those results may be reproduced by stochastic calculations of extensional flows with FENE model. Those stochastic calculations lead to the development of a new closure of the FENE model: the so-called “FENE-L” model [LHJ+97, LKLon].

In chapter 5 we propose a heuristic multimode model based on a fractal interpretation of the macromolecules. This model allows us to reproduce the rapid drop of tensile stress in the filament and the results of birefringence experiments. We also show that dispersity and nonlinearity are two common aspects of the FENE, FENE-L and multimode models, and that they explain the behaviour of those models in extensional flows.

Chapter 4

The filament stretching device

In this chapter, we present the results of a numerical study of the filament stretching device used by Tirtaatmadja and Sridhar [TS93], Solomon and Muller [SM96a] and McKinley and al. [McK95, Cas96, SAM96]. The device and the free-surface profiles are schematically shown in Figure 4.1. The FENE-CR constitutive equation is selected and we use the material parameters identified by McKinley on the basis of steady shear data. The model is then used to simulate the flow in the filament stretching rheometer.

We present the results obtained with viscoelastic and Newtonian models respectively. The effects of surface tension, gravity and inertia on the rheometrical flows is also investigated for those two models. By a closer observation of the rheometrical flows, we show that purely uniaxial extensional flows are never produced by the device.

Comparisons between numerical calculations and experimental observations are presented for various sets of material parameters and initial gaps between the plates. A good qualitative agreement is obtained between numerical results and experiments. Finally, the influence of the nonlinearity of FENE-CR model is investigated.

The results presented in this chapter have to be published in the Journal of Non-Newtonian Fluid Mechanics [SL97].

4.1 Numerical simulation of the stretching device

Now, we describe the boundary conditions used to calculate the time dependent flow of a viscoelastic fluid in the filament stretching apparatus proposed by Sridhar et al. [TS93]. In such a device, a syringe is used to put a droplet of fluid between the plates. Because of surface tension, the fluid sample has initially a

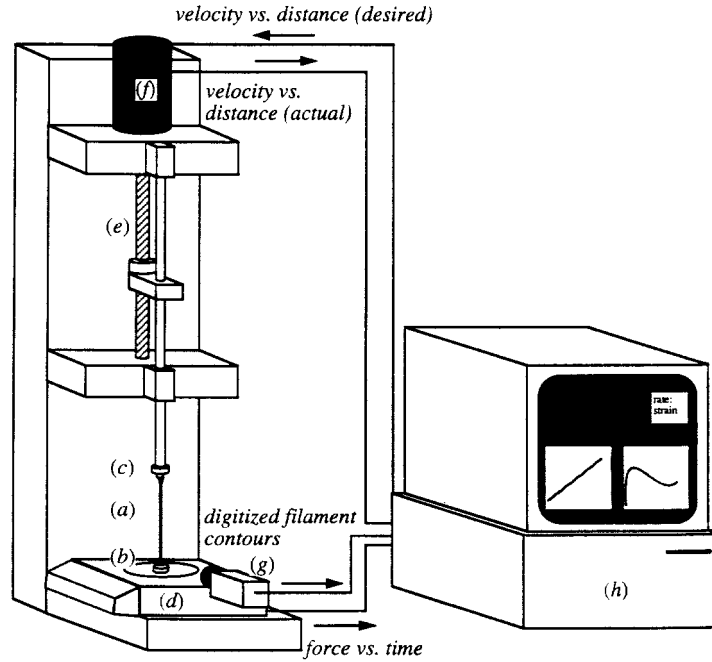


Figure 4.1: Example of filament stretching device: (a) fluid sample; (b) fixed lower plate; (c) moveable upper plate; (d) force transducer; (e) ball screw; (f) servo motor; (h) computer, motion controller (From [SAM96].)

cylindrical shape. Then, it is stretched between the plates. The shape of the fluid column and the force measured along the lower plate as a function of time can be used for the characterization of the extensional viscosity of the sample (Figure 4.1). The basic parameters of the device are shown in Figure 4.2.

The typical function of interest for the rheometer is the Hencky strain as a function of time. The Hencky strain is defined as the logarithm of the extensional deformation of the fluid sample:

$$\epsilon_{\text{pl}} \triangleq \ln \left[\frac{L(t)}{L_0} \right], \quad (4.1)$$

where $L(t)$ is the length of the filament, and $L_0 = L(0)$; the subscript “pl” has been added for the deformation is estimated from the distance between the plates. R_0 is the initial radius of the filament and $R(t)$ is the minimal radius as a function of the time.

By imposing an exponential rate of separation between the two plates, i.e. by assuming that $L(t) = L_0 \exp(\dot{\epsilon}_{\text{pl}} t)$, one hopes to do experiments under constant stretch rate conditions rather than under constant force. The constant stretch rate is denoted by $\dot{\epsilon}_{\text{pl}}$, and the “plate estimate” of the Hencky strain becomes a

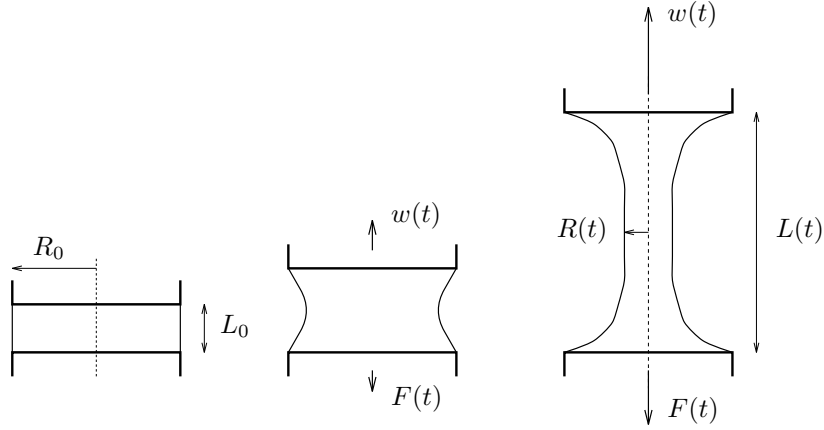


Figure 4.2: Schematic of the filament stretching rheometer.

linear function of time:

$$\epsilon_{\text{pl}} = \dot{\epsilon}_{\text{pl}} t. \quad (4.2)$$

For the constitutive equation of the viscoelastic component of the Cauchy stress tensor, we chose the FENE-CR model introduced by Chilcott and Rallison [CR88] (see section 1.2.4). Our mathematical viscoelastic problem consists of finding the velocities, the pressure and the configuration tensor in the domain Ω such that the conservation (i.e. incompressibility and momentum) and constitutive equations are satisfied under suitable boundary conditions for the velocities and the configuration tensor.

In most calculations, we neglect inertia and gravity. With this assumption, the flow is not only axisymmetric but also exhibits symmetry with respect to an horizontal midplane between the plates. In the next section, we will demonstrate that we can neglect gravity and inertia if the extensional viscosity is very large compared to the stresses induced by shear viscosity. Finally, we also demonstrate that the same condition has to be satisfied in order to obtain useful experimental results from the stretching device. Therefore, the computational domain is reduced to the area depicted in Figure 4.3.

In order to describe the boundary conditions of the viscoelastic free surface problem, we consider the following subsets of the boundary $\partial\Omega$:

- $\partial\Omega_{\text{PLATE}}$, the upper side of the domain, represents the moving plate where the velocity is prescribed. A no-slip condition is applied and the velocity is imposed as follows

$$\begin{aligned} w &= \frac{\dot{\epsilon}_{\text{pl}} L_0}{2} \exp(\dot{\epsilon}_{\text{pl}} t), \\ u &= 0, \end{aligned} \quad (4.3)$$

where L_0 is the initial length of the whole sample.

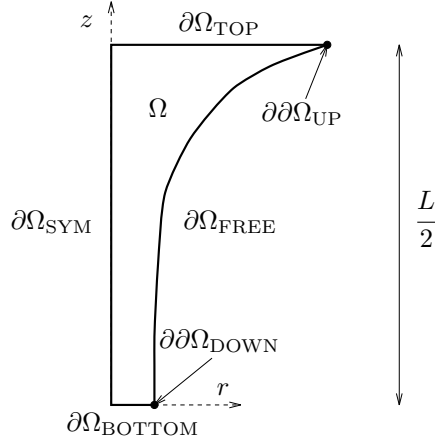


Figure 4.3: *Computational domain and definition of the boundaries for the transient calculation of the filament stretching rheometer.*

- $\partial\Omega_{\text{SYM}}$, is the axis of symmetry. Symmetry conditions are applied, i.e. vanishing normal velocity and tangential stress.
- $\partial\Omega_{\text{BOTTOM}}$, is the lower boundary on which symmetry conditions are applied.
- $\partial\Omega_{\text{FREE}}$, is the free-surface. Along that boundary, surface tension results in a normal force proportional to the sum of the curvatures of the surface. A kinematic condition is used to calculate the motion of the free surface.
- $\partial\partial\Omega_{\text{UP}}$, is the point defined by the intersection of the free-surface and the upper moving plate. The position of this point of the free-surface is prescribed to be attached to the end of the plate. In other words, the free-surface is not allowed to slip along the plate.
- $\partial\partial\Omega_{\text{BOTTOM}}$, is the point defined by the intersection of the free-surface and the horizontal midline. At this point, one prescribes that the free-surface is vertical.

Initially, the computational domain is rectangular, and the fluid is assumed to be at rest. That means that $\mathbf{v} = \mathbf{0}$ and $\mathbf{T}_V = \mathbf{0}$ for $t < 0$. The second equality involves that for the initial \mathbf{A} , we take the tensor unity.

A mixed Finite Element Method (FEM) with the configuration tensor, the velocity, the pressure and the geometrical unknowns as variables, is used. Standard Galerkin weak formulation is derived with the 4×4 element developed by Marchal and Crochet: the pressure, the velocity and the configuration tensor are approximated by linear, quadratic and 4×4 sub-linear interpolations respectively. However, we observe that we obtain the same results by using quadratic interpolation for the configuration tensor. Such a choice is efficient in terms of CPU and memory requirements. Mesh refinement analysis has been performed.

For the time integration, we use an adaptive predictor-corrector time-stepping scheme. At each time step, a prediction of the solution is calculated with the Euler explicit scheme. This first estimate is then corrected with the Euler implicit scheme. The implicit equations are solved by Newton's method. The next time step is then selected such that the difference between predicted and corrected solutions is kept under a specified value. The initial shape of the domain is a rectangle, and the sample is at rest before the beginning of the stretching.

A moving grid algorithm is used to avoid overdistorted elements due to the boundary motion and to maintain a good nodal distribution in the deformed mesh. We solve the Thompson transformation in order to take advantage of the smoothing properties of this elliptic operator. Standard Dirichlet boundary conditions are applied on the coordinates, except along the axis of symmetry where Neumann conditions are introduced for the tangential component. Furthermore, a slight modification of the remeshing rule near the upper plate is introduced in order to maintain a high density of elements where the free-surface shape is more complex. A quadratic continuous representation is used for both the geometrical unknowns and the coordinates.

4.2 Numerical Results

4.2.1 Material parameters

In most calculations, inertia and gravity are neglected and the parameters of both viscoelastic and Newtonian calculations are summarized in Table 4.1. We use material parameters identified on the basis of steady shear data [McK95].

4.2.2 Dimensionless numbers

Now, let us define the dimensionless numbers that can be used for analysing the numerical results. The transient Trouton ratio Tr scales the transient extensional viscosity to the shear viscosity. The Deborah number De characterizes the elastic forces with respect to the viscous terms. The capillary number Ca balances viscous and surface tension forces. The Bond number characterizes the ratio of gravitational forces to capillary forces. Finally, the Reynolds number \mathcal{R} characterizes inertia.

$$Tr = \frac{\bar{\eta}^+}{\eta_0}, De = \lambda \dot{\epsilon}_{pl}, Ca = \frac{\eta \dot{\epsilon}_{pl} R}{\gamma}, Bo = \frac{\rho g L R}{\gamma}, \mathcal{R} = \frac{\dot{\epsilon}_{pl} L^2 \rho}{\eta}.$$

It is obvious that the extensional viscosity is the most appropriate quantity to the study of the present flows. Therefore, we use the ratios \mathcal{R}/Tr , $Ca.Tr$ and $Bo/(Ca.Tr)$ to characterize inertia, surface tension and gravity with respect to extensional stresses.

Table 4.1: *Material parameters for a Polyisobuthylene/Polybutene Boger fluid [McK95].*

ρ (density)	890 (kg.m ⁻³)
$\dot{\epsilon}_{pl}$ (stretch rate)	1.6 (s ⁻¹)
L_0 (initial length)	2 10 ⁻³ (m)
R_0 (initial radius)	3.5 10 ⁻³ (m)
γ (surface tension coefficient)	28.9 10 ⁻³ (N.m ⁻¹)
<i>Newtonian calculations</i>	
η (shear viscosity)	98 (Pa.s)
<i>FENE-CR calculations</i>	
η (shear viscosity)	105 (Pa.s)
η_N (solvent viscosity)	35.7 (Pa.s)
η_V (polymer viscosity)	69.3 (Pa.s)
λ (relaxation time)	2.0 (s)
L^2 (extensibility dumbbell coefficient)	4325.5

4.2.3 Stretching flow of a viscoelastic fluid

The shape of the filament, obtained by numerical simulation with the FENE-CR model, is drawn at different times of the calculation in Figure 4.4. For relatively large values of the time t , we see that the filament nearly has the shape of a cylindrical pillar which enlarges near both plates. The formation of the pillar may be explained by the high extensional viscosity of the fluid:

- As a consequence of the high extensional viscosity, a small increase of the deformation leads to a dramatic increase of the stress. This effect tends to distribute the deformation equally in the filament. Therefore, the fluid sample tends to a cylindrical shape, and one also tends to a perfectly extensional flow.
- On the other hand, the high extensional viscosity of the fluid leads to a sucking effect along the plates: the force in the filament is very important and draws away the fluid adhering to the plates. It follows a very steep transition from the cylindrical portion to the adhesion area, and a very strong deformation of the mesh in that region.

The sucking effect is a source of numerical difficulties. The modification of the remeshing rule has been introduced in order to maintain a high density of elements in the transition area. Nevertheless, this modification of the remeshing rule was not sufficient to avoid a very important distortion of the elements close to the upper plate, and all viscoelastic calculations failed before the time reached the maximum time of the experimental data. In Figure 4.5, we see that some

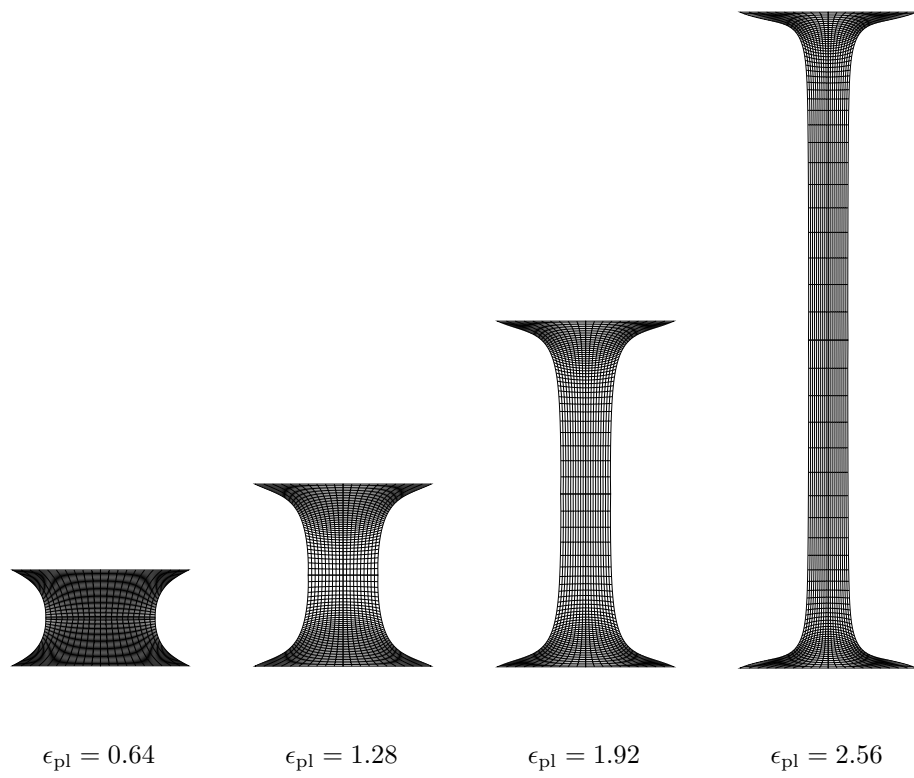


Figure 4.4: *Viscoelastic calculation: deformation of the sample as a function of the Hencky strain.*

elements close to the upper plate become almost triangular at the end of the calculation.

As suggested by a referee, we also believe that the sucking effect may be connected to the instabilities observed by McKinley where the fluid forms fibrils near the end plates [SM96b]. However, when such instabilities are present, the flow does not keep its symmetry around the axis. Therefore, we are unable to predict such phenomena with our method.

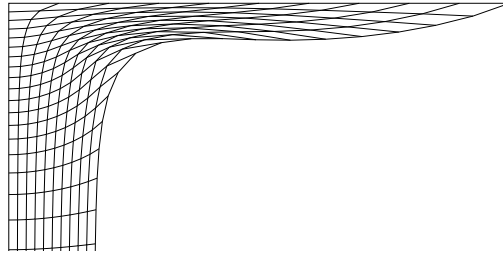


Figure 4.5: *Viscoelastic calculation: closeup view of the mesh at $\epsilon_{pl} = 3.52$. The remeshing rule minimizes the distortion of the elements, when the suction effect takes place near the plate. Nevertheless, some quadrilateral elements nearly degenerate in triangles.*

We also analyse the profile of the extensional component of the tensor \mathbf{A} in Figure 4.7. We plot the ratio A_{zz} as a function of r on the mid-plane section. We see that the stretching is more important along the free surface. This effect is related to the non purely extensional flow at the beginning of the stretching: the fluid located close to the free surface must follow the deformation of the free surface and is submitted to an axial deformation in the middle and a radial one close to the plates.

The almost perfect extensional character of the flow can be observed on the curve of the minimum filament radius as a function of Hencky strain, in Figure 4.8. Close to the end of the numerical simulation, the slope of the curve tends to the slope of the theoretical dashed line corresponding to a perfect extensional flow. However, the slopes of the two curves are quite different at the early stages of the stretching. Let us observe that the inflexion of the curve at $\epsilon_{pl} = 1.6$ probably is the sign of the transition from a more complex flow to an almost perfect extensional flow. In fact, the same observation can be made by analysing the different shapes of Figure 4.4.

4.2.4 Stretching flow of a Newtonian fluid

In Figure 4.9, we draw the shape of the filament obtained for a Newtonian fluid at various values of the Hencky strain. The contours of the free surface are very different than the ones obtained with the viscoelastic model. We no longer see any cylindrical portion. The radius varies everywhere along the filament, and

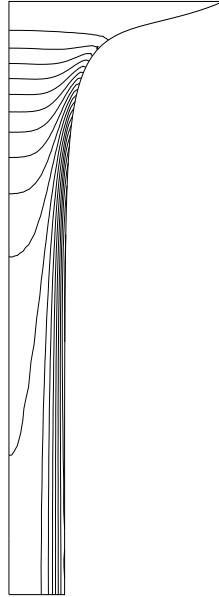


Figure 4.6: Viscoelastic calculation: A_{zz} for $\epsilon_{pl} = 2.24$ is represented with isolines (lines of equal values). The interval of A_{zz} between two consecutive lines is 10. The maximum value of A_{zz} is located on the lower right corner of the sample. This may be better seen in Figure 4.7.

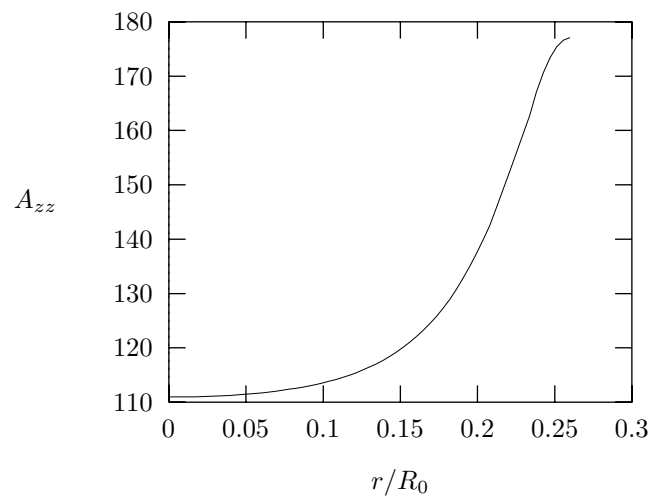


Figure 4.7: Evolution of A_{zz} as a function of the radius along the symmetry plane for $\epsilon_{pl} = 2.24$.

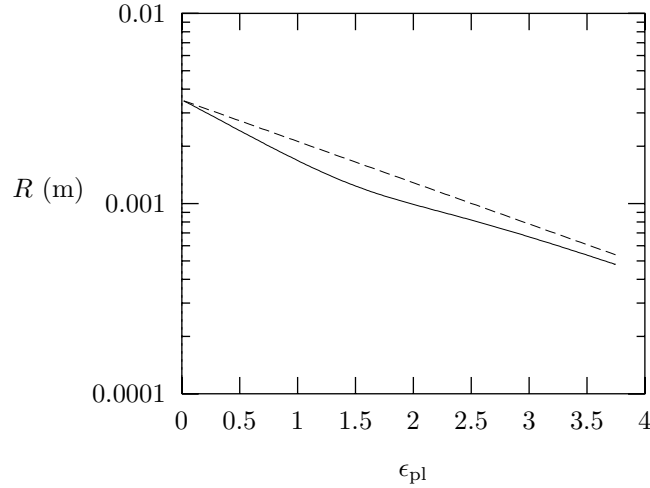


Figure 4.8: *Viscoelastic calculation: minimum filament radius as a function of the Hencky strain. The dashed line represents the theoretical evolution of the radius for a perfectly uniaxial extension. It is a fair approximation of the real behaviour for large values of the Hencky strain.*

has a minimum on the symmetry plane. Similarly, the numerical difficulties due to the suction effect do not appear in this case (Figure 4.10).

In Figure 4.11, we give the minimum filament radius as a function of time. The curve of the minimum radius decreases really faster than the line we could obtain for a purely extensional flow. It follows that the Newtonian flow is very different from the uniformly extensional stretching it previously was assumed to be. Therefore Spiegelberg and al. [SAM96] introduced a simplified lubrication analysis to study the stretching of a Newtonian fluid. They provide an estimate of the effective extension rate, $\dot{\epsilon}_{SAM} \approx 3\dot{\epsilon}_{pl}/2$ from the imposed value $\dot{\epsilon}_{pl}$. In Figure 4.11, we found an excellent agreement between the estimate from the lubrication theory and our large scale calculations at the beginning of the stretching. Due to the assumptions of the simplified model, it is quite normal that we observe discrepancies at larger values of the stretching.

4.2.5 Inertia, capillarity and gravity

In this section, we show that we can neglect inertia and gravity in most calculations. It is clear that if inertia and gravity are taken into account, the filament is not divided by a horizontal symmetry plane. Therefore, the axisymmetric calculation has to be performed on the whole filament, which implies an increase of CPU and memory requirements by a factor two. We consider both the viscoelastic and Newtonian cases studied in the previous sections.

- Using a viscoelastic model, we first perform the calculation neglecting inertia and gravity. Then, we calculate the same problem, taking into

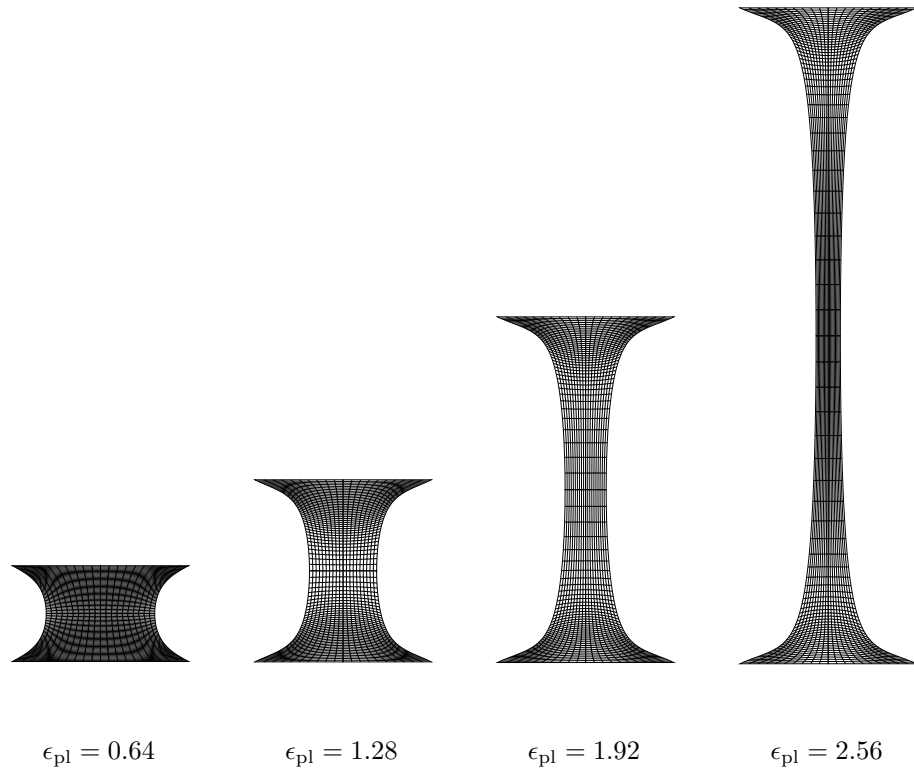


Figure 4.9: *Newtonian calculation: deformation of the sample as a function of the Hencky strain.*

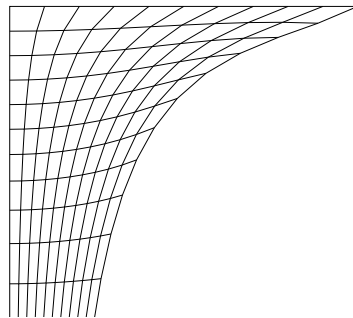


Figure 4.10: *Newtonian calculation: closeup view of the mesh at $\epsilon_{pl} = 4.608$. The deformation of elements remains acceptable.*

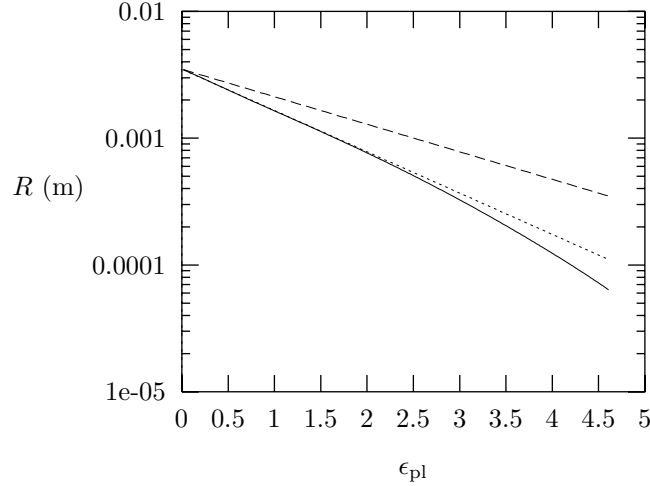


Figure 4.11: *Newtonian calculation: minimum filament radius as a function of the Hencky strain. The dashed line represents the theoretical evolution of the radius for a perfectly uniaxial extension while the dotted line gives the results predicted with the lubricated model.*

account inertia and gravity. In Figure 4.12, we give the force measured on the lower plate as a function of time for both cases. A detailed analysis of the results shows that the shift between the two curves is approximately equal to the weight of the sample divided by two, and is small compared to the value of the force.

- Let us now perform the same numerical experiments with a Newtonian model. Results are given in Figure 4.13. The shift between the two curves is again approximately equal to the sample weight divided by two. We observe that the force measured on the lower plate for the calculation without inertia and gravity decreases very quickly and that the extensional force becomes much smaller than the value of the sample weight at the end of the stretching. Now, if we take inertia and gravity into account, this fact leads to a negative total force for large values of the time.

Inertia and gravity may be neglected in the first calculation with a viscoelastic model, but not in the second with a Newtonian one. This observation is related to the fact that the extensional viscosity of the viscoelastic fluid is very important compared to its shear viscosity, which results in high Trouton ratios, while the extensional and shear viscosities of a Newtonian fluid are related by a constant Trouton ratio. Inertia terms are neglectable in our calculations: the maximum value of R/Tr is approximately 0.2 at the end of the Newtonian stretching. The effect of gravity is very small in viscoelastic calculations ($Bo/(Ca.Tr) \approx 10^{-2}$) and may be important for the Newtonian calculations ($Bo/(Ca.Tr) \approx 4$ at the end of the calculation).

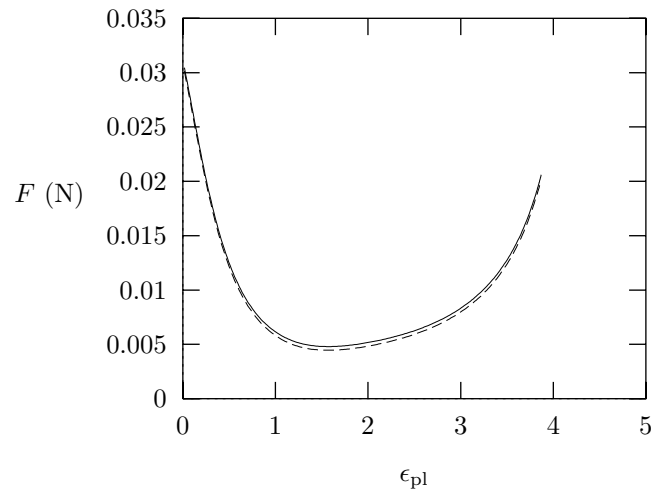


Figure 4.12: *Viscoelastic calculations: force measured on the lower plate as a function of the Hencky strain. The dashed and the continuous lines give the results when inertia and gravity are taken into account or neglected respectively.*

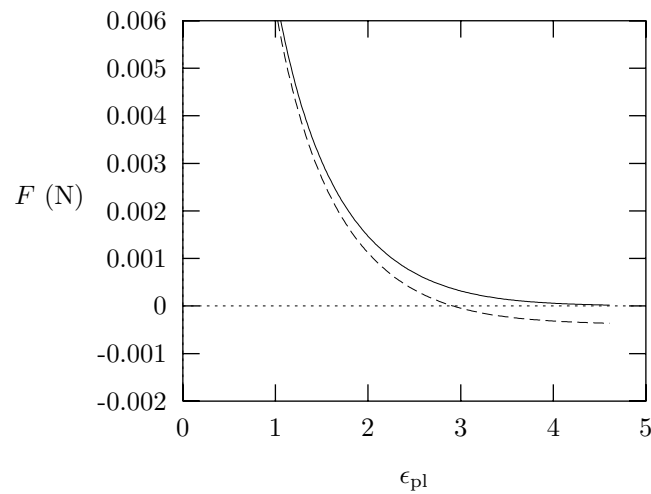


Figure 4.13: *Newtonian calculation: force measured on the lower plate as a function of the Hencky strain. The dashed and the continuous lines give the results when inertia and gravity are taken into account or neglected respectively.*

A similar conclusion can be drawn for the capillary forces: the dimensionless group $Ca.Tr$ ranges from 20 to 400 for the viscoelastic calculation, while at the end of the stretching of the Newtonian fluid, $Ca.Tr$ is approximately 1.

We conclude that when the fluid exhibits strain hardening, the minimum radius of the filament decreases approximately as for a uniaxial extensional flow. But it is difficult to find a good interpretation of the force measured along the lower plate in other cases. Therefore, inertia, capillarity and gravity may be neglected for all cases where the extensional rheometer is able to produce useful results (i.e. when extensional viscosity is high).

4.2.6 Improved estimate of the extensional viscosity

The main quantity of interest from the experimental data provided by the filament stretch rheometer is the extensional viscosity. In order to estimate this quantity, one measures F , the normal force applied to the lower plate. Assuming that the flow is close to uniaxial extension at the median plane, the extensional tension inside the filament is then estimated by

$$\tau \simeq \frac{F}{\pi R^2}, \quad (4.4)$$

where R is the radius of the filament. Finally, approximating the extension rate by the stretch rate $\dot{\epsilon}_{pl}$, one is able to calculate an extensional viscosity by

$$\bar{\eta}_{pl}^+ \simeq \frac{\tau}{\dot{\epsilon}_{pl}}. \quad (4.5)$$

In fact, the flow is not purely extensional (in particular, at the beginning of the stretch). Only the middle of the domain is in extension, and the local extension rate in the middle of the sample is larger than the Hencky strain rate $\dot{\epsilon}_{pl}$. A central question is of course to determine what such an estimate means. The problem can be addressed by the numerical simulation of the whole experiment. It can also be addressed by a better estimate of the extension rate along the center line. For example, we consider only a small material cylindrical part of the filament. If we define l as the length of this cylinder, the volume conservation law leads to the following relationship:

$$lR^2 = l_0R_0^2.$$

Therefore, one is able to derive a better approximation for both the extension strain and the extension rate:

$$\begin{aligned} \epsilon_{rad} &\simeq \ln \frac{l}{l_0} = \ln \frac{R_0^2}{R^2}, \\ \dot{\epsilon}_{rad} &\simeq -2 \frac{\dot{R}}{R}. \end{aligned} \quad (4.6)$$

The subscript “rad” used to denote the new estimates of the extensional deformations denotes a “radial” estimate. A second estimate of the extensional viscosity can be written as

$$\bar{\eta}_{\text{rad}}^+ \approx \frac{\tau}{\dot{\epsilon}_{\text{rad}}}. \quad (4.7)$$

The definition of this estimate can be clearly correlated with the work of Solomon and Muller [SM96a] who demonstrate the difference between radial and axial measures of strain rate.

Finally, a third estimate of the extensional viscosity is provided by the lubrication model of Spiegelberg and al. [SAM96]

$$\bar{\eta}_{\text{SAM}}^+ \approx 3 + \frac{R_0^2}{L_0^2} \exp\left(\frac{-7\epsilon_{\text{pl}}}{3}\right). \quad (4.8)$$

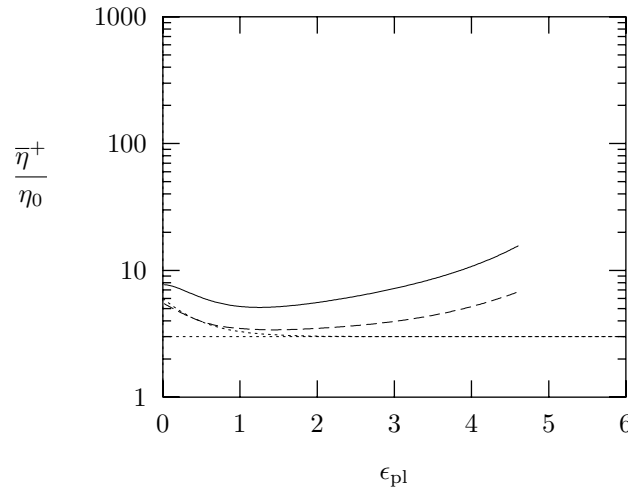


Figure 4.14: *Newtonian calculation: estimated extensional viscosities as a function of the Hencky strain. The continuous and the dashed lines give the extensional viscosity estimated with the “plate” and “radial” estimates of the extension rate. The two dotted lines give respectively the theoretical Trouton ratio ($Tr = 3$) and the results given by the lubricated model.*

In Figure 4.14 the extensional viscosities of a Newtonian fluid as a function of the Hencky strain is drawn from calculations in which gravity and inertia terms have been neglected, using (4.5) and (4.7). We also draw the curve of the lubrication model using (4.8). One can observe that the slopes of all estimates of extensional viscosity are approximately similar. However, the first approximation is distant from the horizontal line corresponding to the Trouton ratio. Therefore, the second estimate of the extensional strain rate appears to be more realistic. We also observe that the lubrication theory agrees with our improved estimate of the Trouton ratio at the beginning of the stretching.

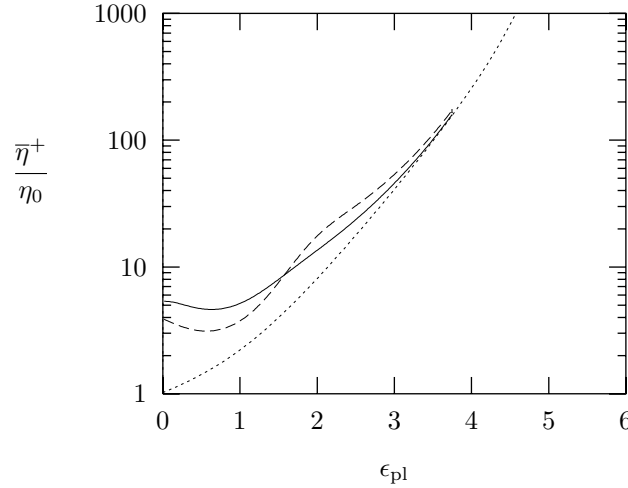


Figure 4.15: *Viscoelastic calculation: estimated extensional viscosities as a function of the Hencky strain. The continuous and the dashed lines give the extensional viscosity estimated with the “plate” and “radial” estimates of the extension rate. Both curves are almost similar, excepted for initial values of the Hencky strain. The dotted line corresponds to the theoretical results we would obtain with a perfectly uniaxial extensional flow.*

The comparison of our two estimates of the Trouton ratio has also been done for the viscoelastic fluid in Figure 4.15. It demonstrates that both approximations of the extensional viscosities are similar for large times. ACTually, they converge towards the theoretical value, and this proves that the device gives good results for viscoelastic fluids. Some people have proposed an approach to avoid the nonuniformities of the radial Hencky strain rate during the stretching [SM96a, SAM96] by selecting a modified evolution for the velocity of the upper plate. (A similar approach is used for the calculations presented in section 4.3.)

4.2.7 Comparison with experimental results

In Figure 4.16, we compare the forces as a function of time for a viscoelastic fluid, obtained respectively by the numerical calculations and by the measurements of McKinley. The large discrepancy at the initial times is due to the delay (100 ms) of the measurement device. The high value of the force at the beginning of the stretching is also explained by the poorly extensional character of the sample deformation.

Now, let us compare in Figure 4.17 both the minimum filament radius as a function of time obtained by the numerical calculations and by image analysis of the experiments. One obtains a very good qualitative agreement and in particular, the numerical simulation reproduces the slope change observed in experimental data.

In Figure 4.18, we investigate the influence of the material parameters of the

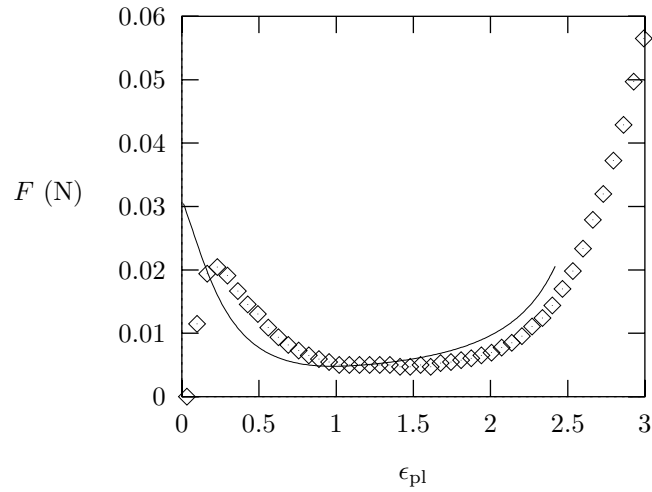


Figure 4.16: Comparison with experimental results: force to be exercised on the plate as a function of time. The lines and the symbols give the numerical results and the experimental data respectively.

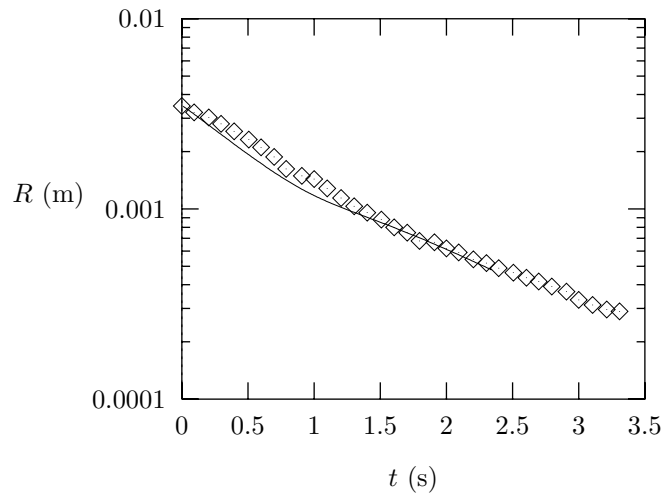


Figure 4.17: Comparison with experimental results: minimum filament radius as a function of time. The lines and the symbols give the numerical results and the experimental data respectively.

constitutive equation for different kind of fluid samples. In particular, we also perform the same calculation for the fluid defined in Table 4.2.

Table 4.2: *Material parameters for a Polyisobuthylene/Polybutene [McK95] Boger fluid.*

η (shear viscosity)	98 (Pa.s)
η_N (solvent viscosity)	32.67 (Pa.s)
η_V (polymer viscosity)	65.33 (Pa.s)
λ (relaxation time)	2.9 (s)
L^2 (extensibility dumbbell coefficient)	4325.5

For $\epsilon_{pl} > 1$, the curves obtained with the numerical calculation are similar to the experimental data given by McKinley.

In Figure 4.19, we also investigate the effect of the initial gap between the plates. The major difference between the curves occurs in the area $\epsilon_{pl} < 1$, and consists mainly of a shift of the initial value. This phenomenon is due to the more non-extensional character of the deformation at the beginning of the stretching when the gap is small. Qualitatively, the influence of a modification of the initial gap is in good agreement with experimental results.

4.3 Extensibility of the molecules

Until here, the viscoelastic calculations have been done with the FENE-CR model, and with $L^2 = 4325.5$. For such a large value of the extensibility of the molecules, the behaviour of the FENE-CR model is very similar to the behaviour of an Oldroyd-B model. In this section, we perform the calculation of the stretching device using several values of L^2 . We compare the estimates of the extensional viscosities obtained from the finite element calculations, with the estimates obtained from a purely uniaxial extensional flow.

Such a comparison is meaningless if the effective strain rates are different in the finite element, and in the theoretical calculations. We already have seen that the estimate of the extensional viscosity may be improved by the use of a radial estimate of the Hencky strain, and of the extension rate.

Another way to improve the estimate of the extensional viscosity, is to adapt the velocity of the upper plate in such a way that the minimum radius decreases exponentially with time. This approach already has been investigated experimentally [SM96a, SAM96]. Numerically, this is easier to do than experimentally. To the set of governing equations, we add an equation expressing the constraint on the radius of the filament. Another unknown is added to the problem: the upper plate velocity V_{pl} . In our formulation, V_{pl} is the Lagrange multiplier of the constraint imposed on the radius.

For such calculations, the ‘‘plate’’ estimate of the stretch rate may be calculated from the velocity of the upper plate, and the distance between the upper

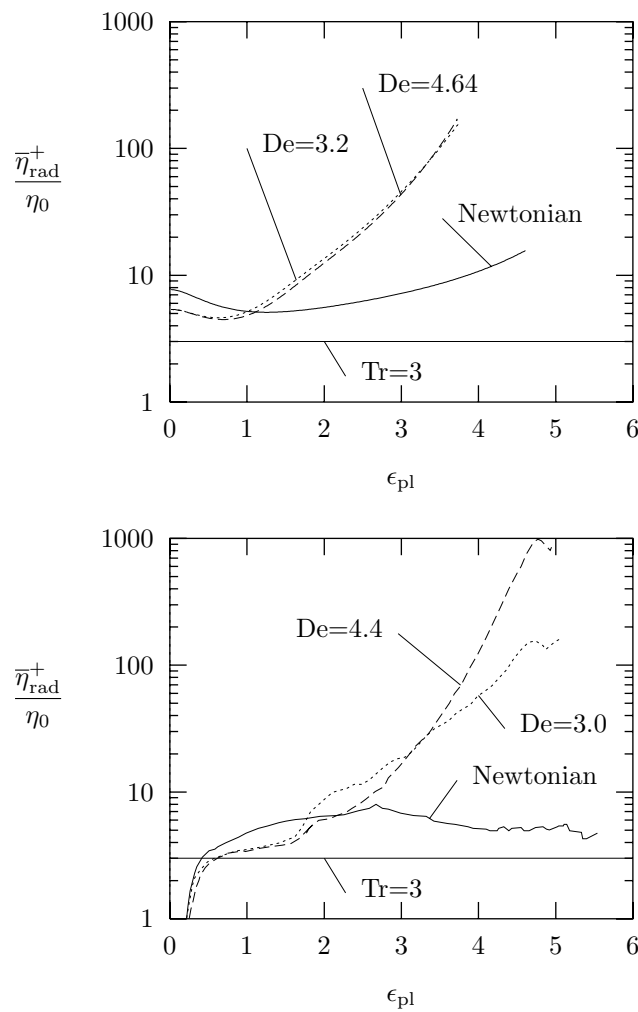


Figure 4.18: Comparison with experimental results for different fluids: estimated extensional viscosities as a function of the Hencky strain. The upper and lower parts give the numerical results and the experimental data respectively.

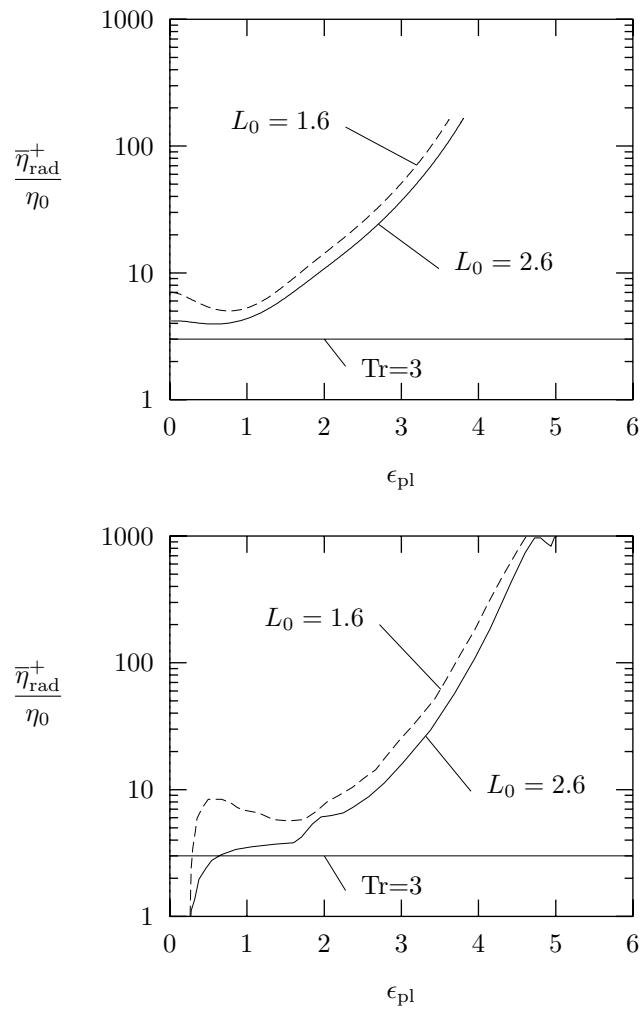


Figure 4.19: Comparison with experimental results for different initial lengths: estimated extensional viscosities as a function of the Hencky strain. The upper and lower parts give the numerical results and the experimental data respectively.

plate and the axis of symmetry:

$$\dot{\epsilon}_{\text{pl}} = \frac{V_{\text{pl}}}{h_{\text{pl}}}.$$

The evolution of $\dot{\epsilon}_{\text{pl}}$ as a function of the radial Hencky strain $\epsilon_{\text{rad}} = \dot{\epsilon}_{\text{rad}}t$ is plotted for an Oldroyd-B model in Figure 4.20.

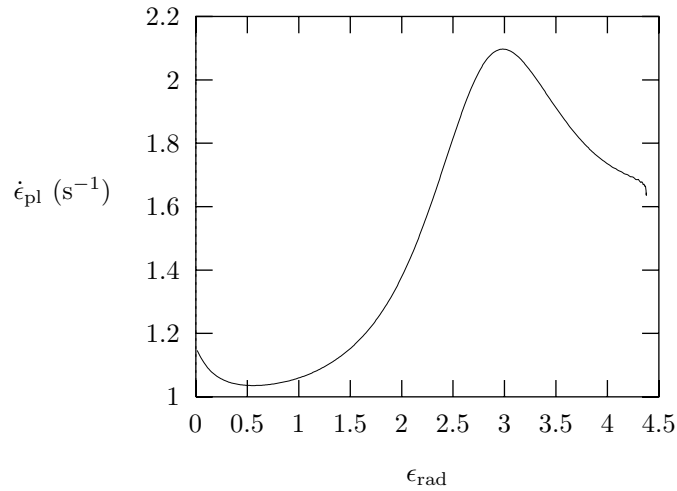


Figure 4.20: Evolution of the “plate estimate” of the Hencky strain rate $\dot{\epsilon}_{\text{pl}}$ as a function of the Hencky strain ϵ_{rad} for an Oldroyd-B model.

For a purely uniaxial extensional flow, we would have a horizontal straight line $\dot{\epsilon}_{\text{pl}} = 1.6 \text{ (s)}^{-1}$. But at the beginning of the stretching, a small increase of the distance between the plates results in a large variation of the minimum radius. This explains why $\dot{\epsilon}_{\text{pl}}$ is small in that area. The maximum of $\dot{\epsilon}_{\text{pl}}$ close to $\epsilon_{\text{rad}} = 3$ corresponds to the transition towards the strain hardening.

In order to compare the results of our finite element calculations with the results for a purely uniaxial extensional flow, we also introduce a correction for surface tension. To calculate the new estimate of the mean value of σ_{zz} on the symmetry plane, we use the following formula:

$$\sigma_{zz} = \frac{F - 2\pi R\gamma}{\pi R^2} + \frac{\gamma}{R}.$$

The extensional viscosity is the ratio of σ_{zz} and the strain rate $\dot{\epsilon}_{\text{rad}} = 1.6 \text{ (s)}^{-1}$. The results are plotted in Figure 4.21.

The agreement between finite element and numerical results is good, except for small values of ϵ_{rad} for which the flow is dominated by shearing. The presence of a horizontal plateau is related to the fact that the trace of \mathbf{A} reaches a maximal value. In our calculation, this length is approximately given by $\text{tr}\mathbf{A} \approx A_{zz} \approx 0.8L^2$. When the trace reaches its maximum value, tension stabilizes, and a horizontal plateau is observed in the extensional viscosity curve.

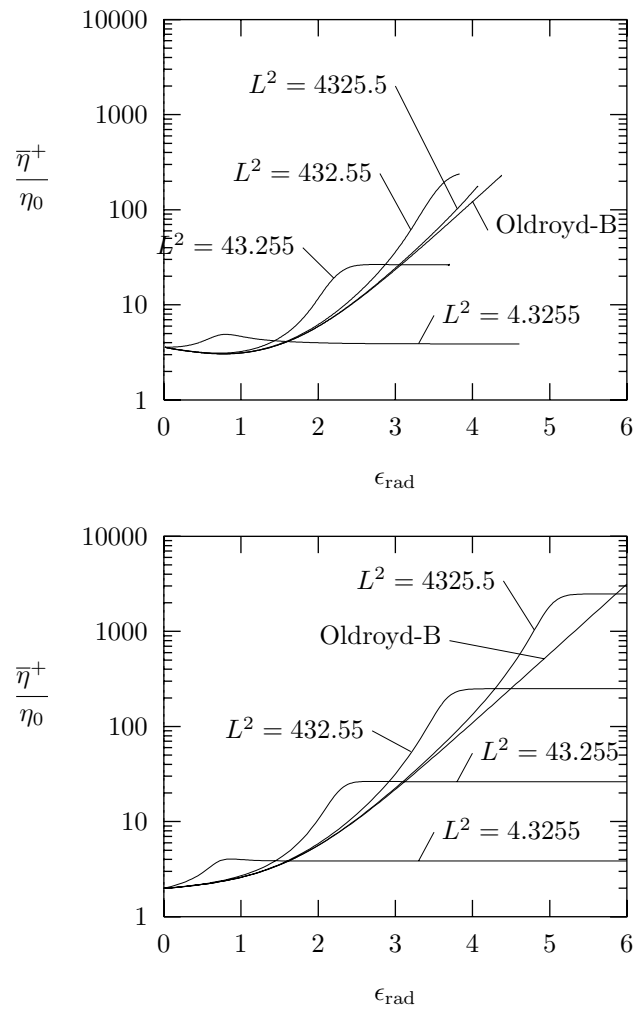


Figure 4.21: Influence of the extensibility L^2 of the molecules on the extensional viscosity as a function of the Hencky strain.

We can see that the transition from the growing parts of the curves to the horizontal plateau is steeper for the theoretical than for the finite element calculations. This may be explained by the non-homogeneity of A_{zz} in the section of the filament. In order to check that assumption, we plot in Figure 4.22 the A_{zz} profiles for various values of the Hencky strain.

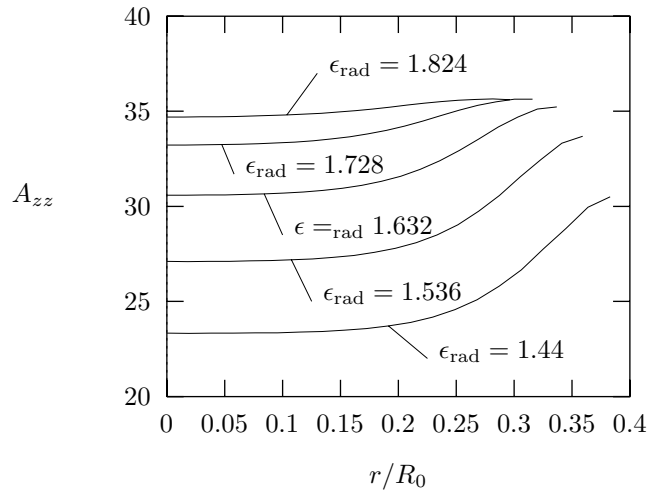


Figure 4.22: A_{zz} profiles for $L^2 = 43.255$ and various values of ϵ_{rad} .

Close to the free surface, the extension is larger than close to the axis of symmetry. As a consequence, the trace of \mathbf{A} does not reach its maximum value at the same time for all positions in the cross section, and the transition to the plateau regime occurs more slowly.

Note that the non-uniformities related to the non-purely extensional character of the flow are still larger for the zz component of the viscoelastic part of the Cauchy stress tensor (Figure 4.23).

4.4 Conclusions

We use the finite element method to calculate the deformation of a fluid sample in a filament stretching rheometer. Calculations have been done with viscoelastic (FENE-CR) and Newtonian models. The strain-hardening behaviour exhibited by viscoelastic fluids is reproduced numerically. This effect leads eventually to large distortion of elements close to the plates and is a source of numerical difficulties. Newtonian calculations do not lead to similar numerical problems.

In our calculations, we show that, when a viscoelastic model is used, a consequence of strain-hardening is that the sample nearly is cylindrical. Thus a nearly purely uniaxial extensional flow is obtained. This type of flow cannot be obtained with a Newtonian model because the extensional viscosity is too small. The conclusion is that the rheometer of Sridhar performs well with fluids exhibiting a high extensional viscosity. We show that for such fluids, the influence

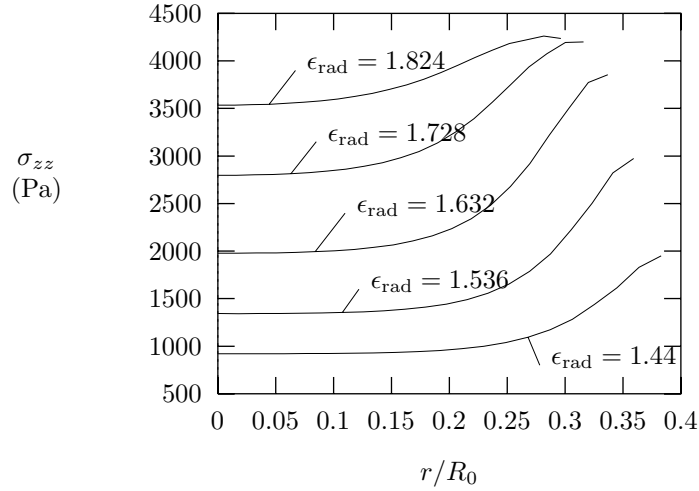


Figure 4.23: $T_{V_{zz}}$ profiles for $L^2 = 43.255$ and various values of ϵ_{rad} .

of gravity, surface tension and inertia may be neglected.

However, we also show that, even for large extensional viscosity fluids, the stretch rate is neither constant in time, nor in the axial and radial directions. Therefore the results must be interpreted with care. We propose an improved estimate of the extensional viscosity based on the observation of the radius rather than the distance between the plates. Comparisons of both estimate show that better results are obtained for small values of the Hencky strain. For larger values of extension, the estimates give similar results.

The influence of material parameters and of the initial gap between the plates has been investigated, and comparisons have been done with experimental data. Qualitative agreement is obtained between numerical calculations and experimental observations.

Note that most calculations have been done with parameters based on shear data. A better agreement between experimental observations and numerical results could be obtained with parameters selected to fit both shear and extensional measurements. Nevertheless, it is not possible to reproduce quantitatively the behaviour of real fluids, with a single mode FENE-CR model.

Chapter 5

Molecular effects in extensional flows

In this chapter we study the influence of the macromolecular structure on the behaviour of polymeric solutions in extensional flows.

We propose a personal and intuitive interpretation of the macromolecular structure in which molecules are considered as “fractal” objects. We assume that to the self-similarity of the structures identified when one looks closer into the molecules corresponds a distribution of characteristic length scales. Then, the fractal structure of molecules allows us to propose a modified version of the FENE-PM model of Wedgewood et al. [WOB91]. Our model is characterized by a distribution of extensibilities rather than a distribution of relaxation times. Our new model is called “multimode FENE-P model”.

By numerical integration of the constitutive equations of our multimode model, we calculate its behaviour in elongation-relaxation flows. The results of our numerical calculations are compared to experimental observations. In particular we give a new interpretation of the “viscous stress” identified by Orr and Sridhar [OS96]. We also explain how our model may reproduce the hysteretic behaviours observed by Doyle et al. [DS97, DSMS97].

A comparison is done between our multimode FENE-P model and the FENE model. It appears that both models have a similar behaviour in extensional flows. The similarities between the models are related to their “dispersive” character. It appears that the dispersity in polymer solutions is one of their fundamental aspects, and that it should be taken into account for the development of new constitutive equations. The qualitative agreement between FENE and multimode FENE-P models in extensional flows may be used to select a distribution of extensibilities of the multimode model such that a good quantitative agreement is obtained. On the other hand, the fact that the hysteretic behaviour of polymer solutions in elongation-relaxation experiments is related to dispersity has led us to identify a similar hysteresis in our macroscopic calculations of the filament stretching device.

The results presented in this chapter are a part of a work done in collaboration with two other researchers (Gregory Lielens and Ingrid Jaumain). This collaboration will lead to a publication [SLJ+98].

5.1 Multimode approach

5.1.1 Fractal structure of polymer macromolecules

We draw in Figure 5.1 the representation of a polymeric macromolecule. The molecule is represented with a large number of spherical beads connected either by rigid rods or by springs.

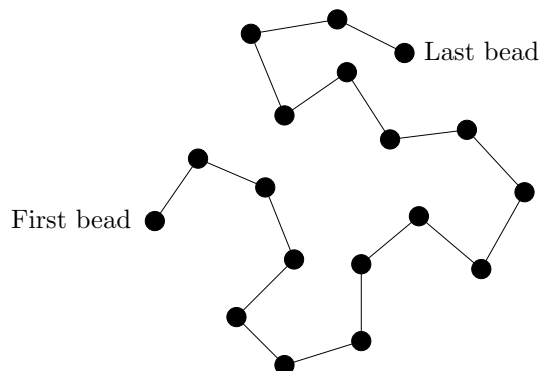


Figure 5.1: *Schematic representation of a polymer macromolecule.*

The FENE-dumbbell type models (i.e. FENE-dumbbell, FENE-P and FENE-CR) are supposed to represent each macromolecule with a single dumbbell composed of two beads connected by a nonlinear spring (section 1.2.4). To make such a simplification is equivalent to concentrate all hydrodynamic interactions on the first and last beads, and assume that the intramolecular interactions may be represented by a spring, the connecting force of which depends on the distance between both ends of the molecule.

With such a simplification, the dynamics of the macromolecules related to intramolecular interactions is lost. For example, only one extensibility of the molecules appears in those models. Intuitively, this extensibility may be thought of as the maximum separability of the two beads divided by their mean distance at rest.

Intuition may help us to better understand the consequences of the macromolecular structure. In our opinion, the macromolecules have a “fractal structure”: by looking closer into the molecule with a microscope, self-similar structures could be observed (Figure 5.2). This is a personal intuitive representation of macromolecules, but this fractal representation catches certainly a part of the reality. The fractal structure of macromolecules in polymer solutions should

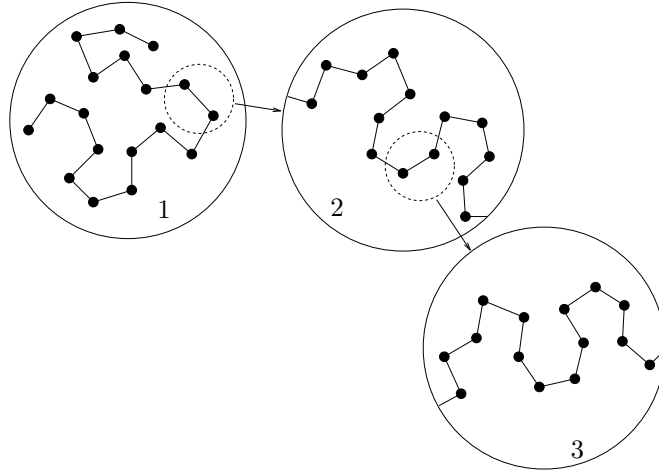


Figure 5.2: Illustration of the “fractal structure” of a polymer macromolecule.

be taken into account in the development of constitutive equations. One of the first constitutive equation based on a “chain” approach is the FENE-PM model.

5.1.2 FENE-PM model

The simplest bead-spring chain model is the Rouse model [Rou53] in which N identical spherical beads are connected by $N - 1$ springs (Figure 5.3). In the original model, the springs connecting two consecutive beads were Hookean, but they may be replaced by FENE springs. However the viscometric properties of the resulting model cannot be studied analytically [BCAH87].

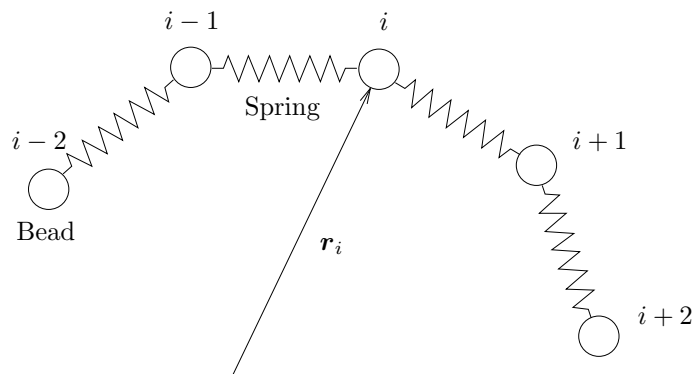


Figure 5.3: The Rouse beads and springs model for a polymer macromolecule.

For FENE-P springs connectors, the connecting force \mathbf{F}_j^c of each spring is

given by

$$\mathbf{F}_j^c = \frac{H\mathbf{Q}_j}{1 - \langle (Q_j/Q_0)^2 \rangle},$$

in which \mathbf{Q}_j is the vector connecting two consecutive beads, H is the stiffness of the spring, Q_j is the length of vector \mathbf{Q}_j and Q_0 is an equilibrium length for the springs. Solutions may be calculated numerically with this model, but the computational cost of the calculations increases rapidly and the problem becomes difficult for a number of beads larger than 25.

In order to find a closure to the model, some approximations have to be introduced. Wedgewood et al. introduce a modification in the force of the spring connecting two beads [WOB91]:

$$\mathbf{F}_j^c = \frac{H\mathbf{Q}_j}{1 - \sum_{k=1}^{N-1} \frac{\langle (Q_k/Q_0)^2 \rangle}{(N-1)}}.$$

They derive a constitutive equation involving a large number of independent FENE-P modes of different relaxation times. This model is called “FENE-PM” where the “M” stands for the mean value that appears in the denominator. But they have only one extensibility parameter L^2 for all modes. This is a result of the pre-averaging step.

5.1.3 A “heuristic” multimode model

Let us have a look to the first circle in Figure 5.2. With the FENE model, interactions with the solvent concentrate in the first and last beads of the polymeric chain, and the whole chain is represented by a single dumbbell. Let us call this dumbbell “dumbbell 1” (“1” because we are looking to the first circle of the figure).

Now, if we look closer into the molecule (circle 2), we also may represent the small piece of chain on which we make a zoom by an elastic dumbbell. Actually, this elastic dumbbell is member of a Rouse chain of the type presented in Figure 5.3. It is interesting to remark that the extensibility of dumbbell “2” is certainly smaller than that of dumbbell “1”.

The same operation may be performed on circle 3 of Figure 5.2. Here again, we identify smaller extensibility springs. Thus we have found various kinds of springs, each one being characterized by its extensibility, and we have the relation

$$L_3 < L_2 < L_1.$$

Thus, it clearly appears that a correct modelling of the interaction of intermediate beads with the solvent leads to the identification of various extensibilities.

We propose here a “heuristic” constitutive equation without trying to derive it from the Rouse chain model. Our model is essentially inspired from the model of Wedgewood et al. in the sense that to each mode corresponds a FENE-P

equation. Its most important feature is that each mode is characterized by its extensibility L_2^i rather than by its relaxation time.

For a N modes model, the equations governing the evolution of the i^{th} configuration tensor \mathbf{A}_i are those of the FENE-P model and may be written

$$\frac{d\mathbf{A}_i}{dt} - \boldsymbol{\kappa} \cdot \mathbf{A}_i - \mathbf{A}_i \cdot \boldsymbol{\kappa}^\dagger = \boldsymbol{\delta} - \frac{\mathbf{A}_i}{1 - \text{tr}\mathbf{A}_i/L_i^2}, \quad (5.1)$$

in which $\boldsymbol{\kappa}$ is the rate of deformation tensor. The Kramers' expression of the contribution of this mode to the polymer stress $\boldsymbol{\tau}$ becomes

$$\boldsymbol{\tau}_i = \eta_V \frac{\mathbf{A}_i}{1 - \text{tr}\mathbf{A}_i/L_i^2} - \boldsymbol{\delta}. \quad (5.2)$$

Finally, the total polymer stress is given by

$$\boldsymbol{\tau} = \sum_{i=1}^N w_i \eta_V \left(\frac{\mathbf{A}_i}{1 - \text{tr}\mathbf{A}_i/L_i^2} - \boldsymbol{\delta} \right), \quad (5.3)$$

in which w_i weights the contribution of the i^{th} mode. The sum of all weights $\sum_{i=1}^N w_i$ is equal to 1.

In our model, we neglect the interaction between the modes (the same approximation has been done for the FENE-PM model). We discuss in section 5.4.3 the problem of the selection of the distribution of extensibilities. The selection of a discrete distribution has been done for the sake of facility, but actually, a model involving a continuous distribution is probably more acceptable from the physical point of view.

For most calculations, two different kinds of distributions are used for the extensibilities: the "geometric" and the "linear" distributions. All modes are assumed to have the same relaxation time ($\lambda_i = \lambda$) and an identical weight for their contribution to the extra-stress tensor ($w_i = 1/N$).

For a geometric distribution, the extensibilities are distributed according to a geometric progression. The maximum and minimum values of the extensibility are noted L_{max}^2 and L_{min}^2 . The L_i^2 parameters are given by

$$L_i^2 = (L_{\text{min}}^2)^{\frac{N-1}{i-1}} (L_{\text{max}}^2)^{\frac{i-1}{N-1}}.$$

In a linear distribution, the extensibilities are distributed linearly between the maximum and the minimum:

$$L_i^2 = \frac{(N-i)L_{\text{min}}^2 + (i-1)L_{\text{max}}^2}{N-1}.$$

With both distributions, the parameters characterizing the model are the viscosity η_V , the relaxation time λ , the maximum and minimum extensibilities L_{max}^2 and L_{min}^2 , and the number of modes N . To those parameters, we add a Newtonian viscosity η_N corresponding to the solvent.

5.2 Identification of a viscous stress

Some experimental results suggest the existence of a viscous component in the polymeric stress. This observation has led some people to propose modified versions of the FENE-type models to fit experimental curves. In this section, after presenting experimental results, we try to demonstrate that experimental observations may be reproduced simply with our modified multimode FENE-P model.

5.2.1 Experiments of Orr and Sridhar

Orr and Sridhar use a filament stretching device to measure the stress relaxation in a filament previously submitted to a large stretching [OS96].

During the first part of their experiment, the fluid sample is submitted to an elongation at constant stretch rate $\dot{\epsilon}$ (s^{-1}). Then the upper plate is suddenly stopped. The time necessary to stop the upper plate is approximately 50 ms, and depends on the velocity of the plate prior to stopping. They observe that rapid changes imposed on the force transducer during the deceleration process cause the initial stress relaxation data to oscillate (Figure 5.4). The oscillations are probably also related to elastic vibrations of the filament.

To eliminate those spurious oscillations, the relaxation data are fitted with the sum of two exponentials. With this interpolation function, Orr and Sridhar try to extrapolate the stress back to the time at which the upperplate came to a halt. They interpret the obtained value as the elastic stress at stopping time. The viscous stress is the difference between the total stress at the end of the stretching, and the elastic stress. (More details about the determination of viscous and elastic stresses are given in Figure 5.4.)

In their experimental study of the stress relaxation in a filament, Orr and Sridhar observe a sudden decrease of stress in the filament after cessation of stretching. The sudden decrease of the stress is interpreted by Orr and Sridhar as the vanishing of a viscous component.

5.2.2 Relaxation with the multimode FENE-P model

In this section, we show that the observed rapid drop of the tensile stress after cessation of stretching may be explained by the rapid decrease of the elastic stress when a nonlinear model is used. By using a multimode FENE-P model with a wide spectrum of extensibilities, we ensure that some of the modes go very fast into the nonlinear domain, even for small values of the Hencky strain. This ensures that the rapid decrease of tensile stress is obtained even for small values of the Hencky strain.

We simulate the experiments of Orr and Sridhar. For the calculations, we use the multimode FENE-P model. We distinguish three different fluids labelled “A”, “B” and “C”. The parameters corresponding to the fluids are summarized in Table 5.1. With such a choice of parameters, we try to approximately reproduce the fluids “A” and “B” used by Orr and Sridhar in their experiments

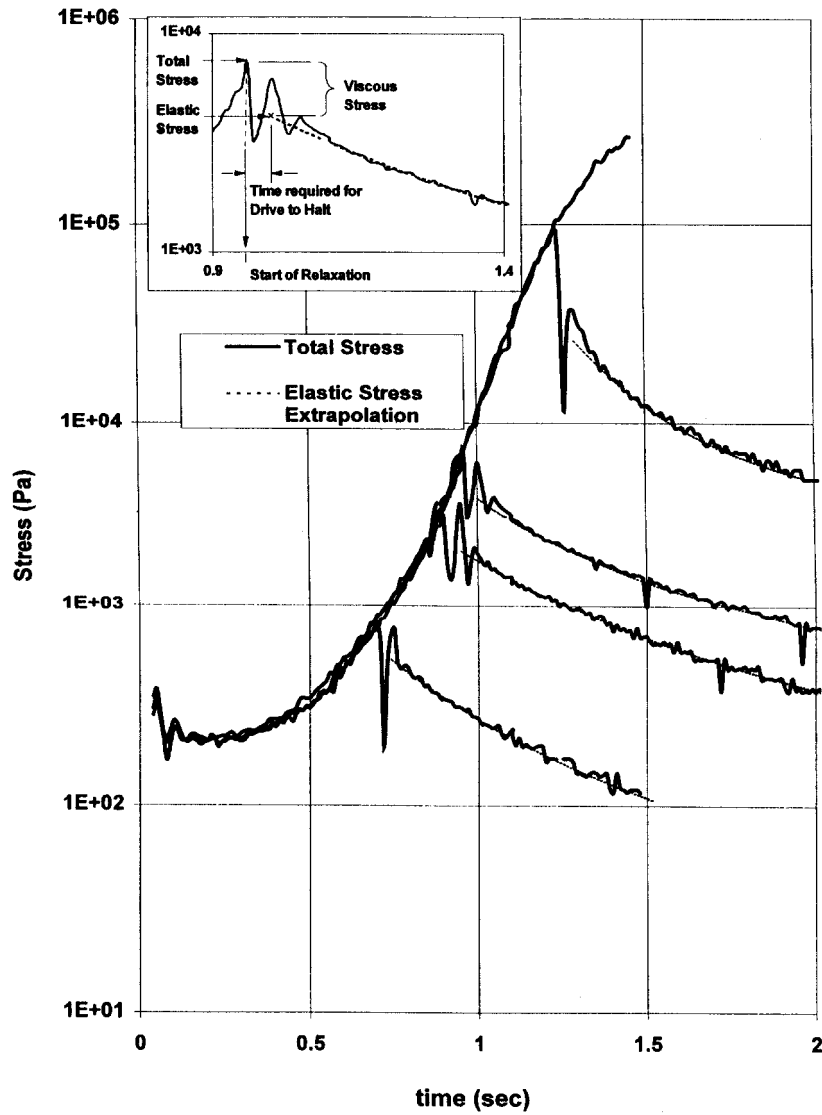


Figure 5.4: Example of result obtained by Orr and Sridhar for their “extension-relaxation” experiment (from [OS96]). The strain rate is 4 s^{-1} . Orr and Sridhar also explain how elastic and viscous stress are determined.

[OS94, OS96]. For fluids “A” and “B”, we choose a geometric distribution of extensibilities. Fluid “C” is identical to “B” except that the distribution of extensibilities is linear.

Table 5.1: *Material parameters for the various fluids used in our numerical calculations.*

fluid	type	N	L_{\min}^2	L_{\max}^2	λ (s)	η_V (Pa.s)	η_N (Pa.s)
A	geometric	20	3.5	20000	1.15	14	20
B	geometric	20	3.5	20000	1.60	25	30
C	linear	20	3.5	20000	1.60	25	30

We integrate equations (5.1) as function of time with a fifth order Runge-Kutta algorithm for a purely extensional flow. The applied strain rate is a function of time. It is given by

$$\dot{\epsilon}(t) = \begin{cases} \dot{\epsilon}_{\text{up}}, & \text{for } t \leq t_{\text{stop}}, \\ \dot{\epsilon}_{\text{up}} \frac{t_{\text{stop}} + \Delta t_{\text{stop}} - t}{\Delta t_{\text{stop}}}, & \text{for } t_{\text{stop}} \leq t \leq t_{\text{stop}} + \Delta t_{\text{stop}}, \\ 0, & \text{for } t_{\text{stop}} + \Delta t_{\text{stop}} \leq t, \end{cases} \quad (5.4)$$

in which $\dot{\epsilon}_{\text{up}}$ is the stretch rate during the stretching, t_{stop} is the time at which the upper plate is stopped, and Δt_{stop} is the time necessary to come to rest.

The viscoelastic part of the tension is calculated with (5.3). To this viscoelastic tension, we add a purely viscous contribution corresponding to the solvent. The tensile stress is thus given by

$$\sigma_{zz} = \tau_{zz} - \tau_{rr} + 3\eta_N \dot{\epsilon}(t).$$

We make four different relaxation experiments at different stopping times. We select $\Delta t_{\text{stop}} = 0.05$ s, and we calculate the relaxation until $t_{\text{end}} = 2$ s. The calculations have been done with fluid “A”, and the results are plotted in Figure 5.5.

Note that the transition of the growing curve towards the horizontal plateau is very abrupt and very different than what is observed in the experimental curve in Figure 5.4. This may be avoided by selecting an appropriate extensibility distribution. But here, we do not try to reproduce exactly the experimental results of Orr and Sridhar.

Now, let us look at the relaxation curve corresponding to $t_{\text{stop}} = 1.2350$ s. At the beginning of the relaxation, the curve decreases very fast, then the relaxation rate progressively decreases. This is related to the fact that, at stopping time, a large number of modes have reached a nonlinear extension. The slow down of the relaxation after some time is related to the progressive return of the modes in the linear domain.

Note that a fast relaxation after cessation of stretching also may be obtained with the FENE-P model. But, as explained by Orr and Sridhar [OS96], this

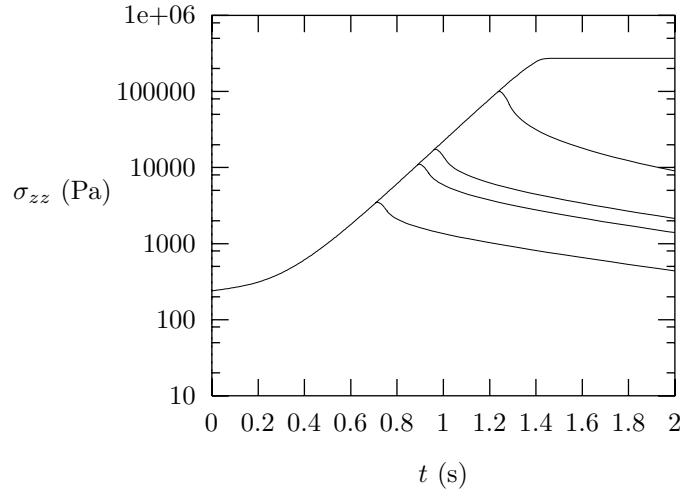


Figure 5.5: *Tension in the filament versus the time for strain-relaxation experiment. The calculations have been done with fluid “A” (see table 5.1 for the material parameters). The relaxation curves are plotted for four different values of time corresponding to $t_{\text{stop}} = 0.7075$ s, $t_{\text{stop}} = 0.8875$ s, $t_{\text{stop}} = 0.9575$ s and $t_{\text{stop}} = 1.2350$ s. $\Delta t_{\text{stop}} = 0.05$ s.*

behaviour may only be observed close to the horizontal plateau of the extension curves. For smaller values of extension, the FENE-P model is very similar to the Oldroyd-B model. Thus we need a distribution of extensibilities to explain the fast relaxation rate after stopping the extension at small values of time.

The tension calculated with the multimode FENE-P model decreases faster than the interpolation dotted lines of Orr and Sridhar (Figure 5.4). The experimental device of Orr and Sridhar cannot detect such a rapid drop of the tensile force. This means that the elastic response of the small extensibility modes explains easily what Orr and Sridhar interpret as an instantaneous drop of the tensile force (and thus a viscous stress).

To illustrate this, we plot in Figure 5.6 a zoom on the upper relaxation curve of Figure 5.4. To this zoom, we add a curve similar to the relaxation curves obtained with our multimode model and referred to as “elastic fit” (though this fit only is an intuitive interpolation). The difference between our “elastic fit” and the fit of Orr and Sridhar appears clearly.

5.2.3 Fit of a relaxation curve

In order to compare quantitatively our relaxation curves with the results of Orr and Sridhar, we try to reproduce the fit procedure of Orr and Sridhar. We consider the calculated relaxation curve corresponding to $t_{\text{stop}} = 1.2350$ s as an experimental result. Then we try to fit this curve with the sum of two

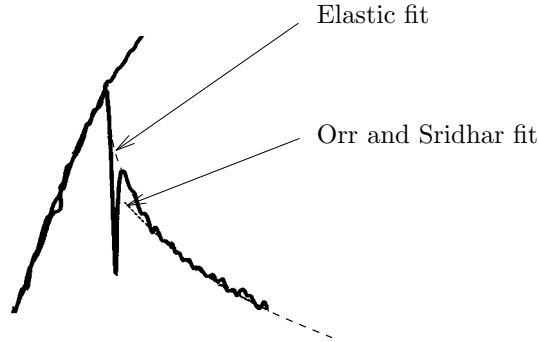


Figure 5.6: Comparison of the fit of Orr and Sridhar with our intuitive “elastic fit”.

exponential functions (as has been done by Orr and Sridhar):

$$f(t) = A \exp(-t/a) + B \exp(-t/b).$$

(Details about the fit procedure are given in section D.1.) The solution of the fit is given in Figure 5.7.

The correspondence between the fit curve and the data points is very good. A “pseudo viscous” component of the tensile stress may be identified on the curve and it corresponds to the relaxation during the stopping of the upper plate. However, there is a major difference between our fit and the fit of Orr and Sridhar: our fit follows the data points after $t_{\text{stop}} + \Delta t_{\text{stop}}$, while the fit of Orr and Sridhar departs from the data points in that area and leads to larger estimates of the viscous polymer stress (Figure 5.4).

This may be related to the large oscillations observed in the measured relaxation curves. In order to check that assumption, we calculate the same fit with modified data points: the second data point is put to 10000 Pa. By making such a modification, we try to reproduce the noise in the tensile stress measured with the filament stretching device. The results of our fit are given in Figure 5.8.

We see that the fit function is very sensitive to errors measurements. The comparison of Figures 5.7 and 5.8 leads to one conclusion: the fit done by Orr and Sridhar is very bad, because of the noise in the measure of the force. For a perfect measure, the fit function would probably remain close to the experimental points.

Because of the sensitivity of the fit to the noise, the “pseudo-viscous” component of the tensile stress estimated by Orr and Sridhar is larger than what they would calculate if their fit was good. Moreover, the residual viscous component they would obtain with a perfect experimental device easily could be explained by the elastic relaxation during the slow down of the upper plate.

We try to check in section D.2 whether the bad fit of Orr and Sridhar is sufficient to explain the presence of a viscous component in the polymer stress.

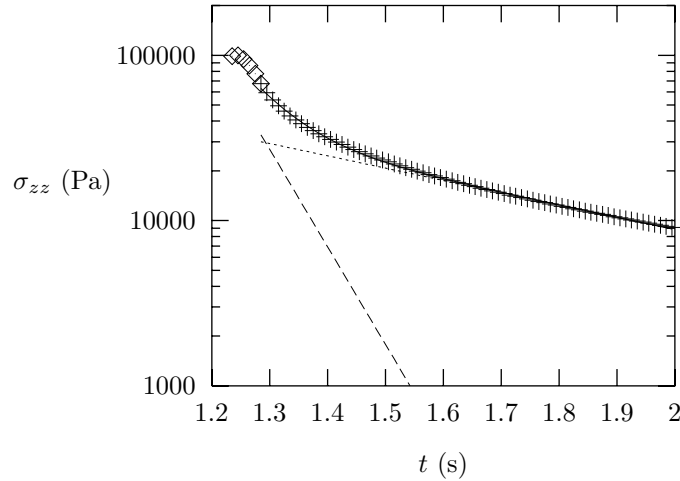


Figure 5.7: Fit of the relaxation curve corresponding to $t_{\text{stop}} = 1.2350$ s. The time necessary to come to a halt is $\Delta t_{\text{stop}} = 0.05$ s. The fit is done between $t_{\text{stop}} + \Delta t_{\text{stop}}$ and $t_{\text{end}} = 2$ s. The diamonds and crosses represent the datapoints during the stopping of the plate and the subsequent relaxation respectively; the continuous line represents the fit function f ; the dashed and dotted lines correspond to the two exponentials.

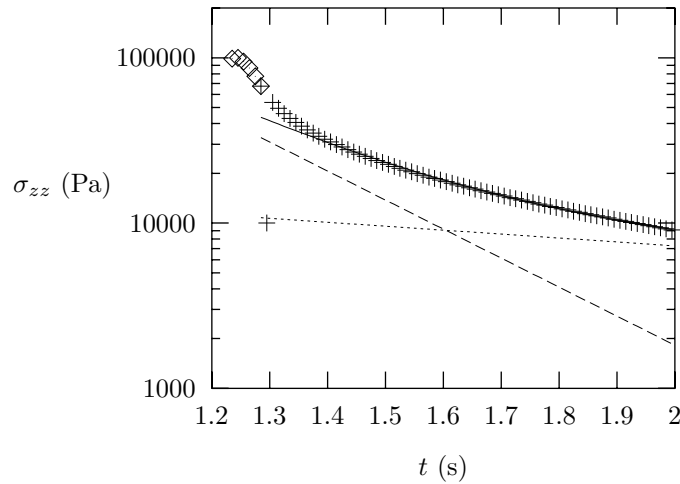


Figure 5.8: Fit of the relaxation curve corresponding to $t_{\text{stop}} = 1.2350$ s. The time necessary to come to a halt is $\Delta t_{\text{stop}} = 0.05$ s. The fit is done between $t_{\text{stop}} + \Delta t_{\text{stop}}$ and $t_{\text{end}} = 2$ s. (fluid "A"). The diamonds and crosses represent the datapoints during the stopping of the plate and the subsequent relaxation respectively; the continuous line represent the fit function f ; the dashed and dotted lines correspond to the two exponentials. The second data point has been put to 10^4 Pa.

This is done by predicting a viscous stress with a linear back reinterpolation from a relaxation curve. The results confirm that the bad fit of Orr and Sridhar explains their viscous stress observations.

5.3 Birefringence experiment

Doyle et al. [DS97, DSMS97] measure the birefringence during the strain and relaxation experiment in the filament stretching device. By plotting the tensile stress versus the birefringence, they find an hysteresis.

5.3.1 Birefringence with the multimode model

The birefringence is related to the elongation of the macromolecules in the solvent. For the FENE-P model, the elongation of the macromolecules is related to the trace of tensor \mathbf{A} . For the multimode FENE-P model, we don't know exactly how the birefringence must be related to the various configuration tensors.

Therefore, we plot in Figure 5.9, the zz component of the Cauchy stress tensor versus the trace of the configuration tensor of the largest extensibility mode (noted $\text{tr}\mathbf{A}_{\text{max}}$). The resulting hysteresis curves are plotted for four different values of the stretch rate $\dot{\epsilon}$. The maximum Hencky strain for the calculations is $\epsilon = 10$. The size of the hysteresis increases with the strain rate. All relaxation curves follow a master curve.

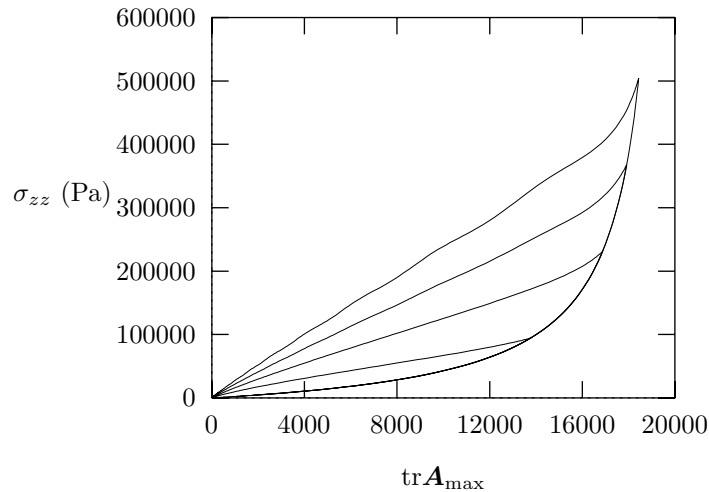


Figure 5.9: *Hysteresis of the zz component of the Cauchy stress tensor as a function of the trace of the configuration tensor of the last mode. The curves have been plotted for $\dot{\epsilon}_1 = 1.0 \text{ s}^{-1}$, $\dot{\epsilon}_2 = 2.0 \text{ s}^{-1}$, $\dot{\epsilon}_3 = 3.0 \text{ s}^{-1}$ and $\dot{\epsilon}_4 = 4.0 \text{ s}^{-1}$. Fluid “B” is used for the calculation.*

The stress may also be plotted as a function of a mean value of the trace of

the configuration tensors of all modes. We calculate the mean value $\text{tr} \langle \mathbf{A} \rangle$ with

$$\text{tr} \langle \mathbf{A} \rangle = \sum_{i=1}^N w_i \text{tr} \mathbf{A}_i.$$

The results corresponding to that mean value are presented in Figure 5.10. Note that the hysteresis obtained when plotting the stress as a function of the largest extensibility mode is larger than when we use the mean value $\text{tr} \langle \mathbf{A} \rangle$.

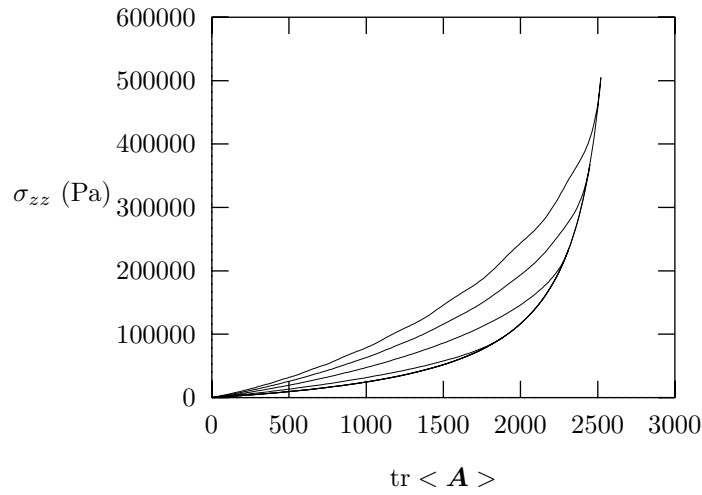


Figure 5.10: *Hysteresis of the zz component of the Cauchy stress tensor as a function of the mean value of the trace of the configuration tensors of all modes. The curves have been plotted for $\dot{\epsilon}_1 = 1.0 \text{ s}^{-1}$, $\dot{\epsilon}_2 = 2.0 \text{ s}^{-1}$, $\dot{\epsilon}_3 = 3.0 \text{ s}^{-1}$ and $\dot{\epsilon}_4 = 4.0 \text{ s}^{-1}$. Fluid “B” is used for the calculation.*

A similar picture is plotted in Figure 5.11 for the “linear” version of the multimode model (fluid “C”). With that fluid, the hysteresis is a little smaller than in Figure 5.9, but the results are qualitatively comparable.

It is interesting to remark that the shape of our hysteresis curves is qualitatively similar to what has been observed by Doyle et al., though the extensibility distributions have only been guessed.

5.3.2 Birefringence in the filament stretching device

We have seen in section 4.3 that for the filament stretching device, the end effects result in larger extension of the macromolecules close to the free surface. For the numerical calculations we used the FENE-CR model, in which the molecules have a maximum extensibility. As a consequence, the molecules located close to the free surface reach a maximum extension before the molecules located close to the axis of symmetry.

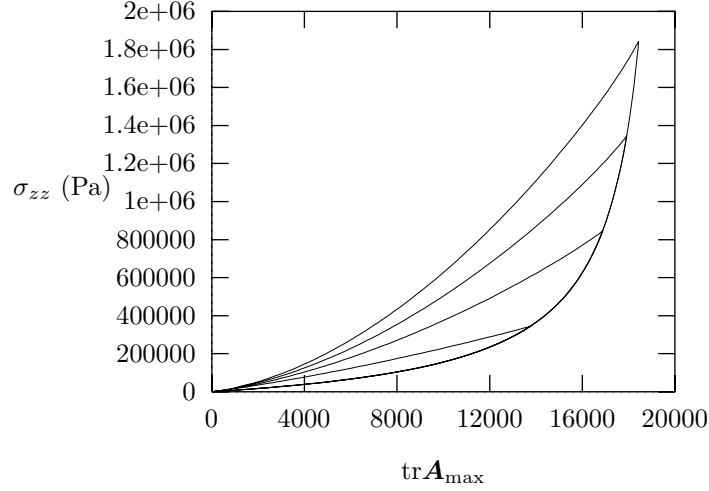


Figure 5.11: *Hysteresis of the zz component of the Cauchy stress tensor as a function of the trace of the configuration tensor of the last mode. The curves have been plotted for $\dot{\epsilon}_1 = 1.0 \text{ s}^{-1}$, $\dot{\epsilon}_2 = 2.0 \text{ s}^{-1}$, $\dot{\epsilon}_3 = 3.0 \text{ s}^{-1}$ and $\dot{\epsilon}_4 = 4.0 \text{ s}^{-1}$. Fluide “C” is used for the calculation.*

The non-uniformities of \mathbf{A} in the section of the filament may result in an hysteresis effect in the curves of the mean value of the tension versus the birefringence. We calculate a mean value $\langle \tau_{zz} \rangle_S$ across the section with

$$\langle \tau_{zz}(t) \rangle_S = \frac{1}{\pi R^2(t)} \int_0^{R(t)} \tau_{zz}(r, t) 2\pi r dr.$$

The factor $2\pi r$ has been introduced in the integral to take into account the axisymmetry of the problem. To calculate the mean values of the components of \mathbf{A} , we use

$$\langle A_{ij}(t) \rangle_D = \frac{1}{R(t)} \int_0^{R(t)} A_{ij}(r, t) dr.$$

Here, the factor $2\pi r$ is not present in the integral for we try to simulate an optical measure with a laser ray crossing the filament. We plot in Figure 5.12 the mean value $\langle \tau_{zz} \rangle_S$ versus the mean value of the trace of \mathbf{A} , and for three different values of the strain rate $\dot{\epsilon}_{\text{rad}}$. It clearly can be seen that during the stress relaxation, to a small decrease of $\text{tr} \langle \mathbf{A} \rangle_D$ corresponds a larger decrease of $\langle \tau_{zz} \rangle_S$ than during the stretching. This comes from the fact that during the relaxation, all molecules relax together while during the stretching, the molecules located close to the free surface reach their maximum length before the other molecules.

Note that the contribution of the end effects to the hysteretic behaviour is too small to explain experimental observations of hysteresis curves.

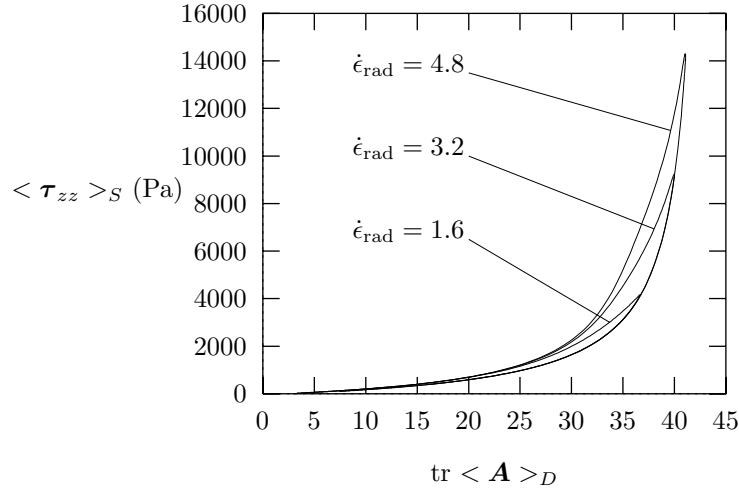


Figure 5.12: *Hysteresis curves calculated with the filament stretching device for three different values of the strain rate.*

5.4 Comparison of multimode and FENE

5.4.1 Differences between the models

The shape of the hysteresis curves obtained with the multimode FENE-P model is surprisingly similar to the shape of hysteresis curves obtained with the FENE model [LHJ⁺97]. But, at first sight, the mechanisms by which the hysteretic behaviour appears are different with both models:

- With the FENE model, the hysteretic behaviour is related to the fact that the elastic dumbbells are already dispersed in length and orientation before the beginning of stretching. When submitted to an extensional flow, the dumbbells elongate according to their initial length in the direction of stretching, until the nonlinear force in the spring compensates hydrodynamic forces. When this saturation of extension occurs, the function representing the distribution of dumbbells gathers progressively into a narrow peak corresponding to the saturation length. During relaxation the dumbbells of the peak relax approximately at the same rate. Actually, Brownian forces widen progressively the narrow peak, but this effect is small compared to the relaxation due to connector forces [LHJ⁺97].
- Let us first remark that for the multimode model, the trace of the configuration tensor of one mode may be interpreted as the average square length of this mode. With the multimode model, all modes start from the same position (the configuration tensors \mathbf{A}_i have all the same value δ before stretching). At the beginning of stretching, they all elongate the same way. But very soon, the small extensibility modes are abandoned along the way, while the larger extensibility modes continue to elongate. When

the stress curve reaches the horizontal plateau, each mode has reached its saturation length. During relaxation, all modes relax approximately at the same rate but they start from various positions. Thus they are dispersed during relaxation.

Thus, for the FENE model, the hysteretic behaviour is related to the fact that the dumbbells are dispersed during stretching and gathered during relaxation, while with the multimode model, the modes are gathered during extension and relax separately. In both cases, the hysteretic behaviour is related to the fact that all modes (or dumbbells) do not reach a maximum extension at the same time.

5.4.2 New representation of the multimode model

In one sense, each FENE-P mode behaves like a single dumbbell: it is elongated during extension, reaches a maximum length, and then relaxes after cessation of the stretching. It is interesting to remark that to a dumbbell of small initial length corresponds a large extensibility FENE-P mode. Indeed, the last modes that reach a maximum length are those of largest extensibility, while the last dumbbells that reach their maximum length are those that have initially the smallest length in the axial direction.

This suggests us an alternative way to represent the multimode model during stretching. By dividing the configuration tensor of each mode by its maximum extensibility L_i^2 , we obtain a new representation of the multimode model. For convenience, we introduce a new notation for the configuration tensor:

$$\mathbf{a}_i = \frac{\mathbf{A}_i}{L_i^2}. \quad (5.5)$$

With this new representation, we can see that the similarities between the FENE and FENE-P multimode models are stronger than it appeared at first sight:

- Before stretching, the various modes of the new version of the multimode model are dispersed in length. Those initial lengths correspond to the traces of the tensors \mathbf{a}_i ; their lengths are thus given by $3/L_i^2$.
- At the end of the stretching, in the horizontal plateau of the stress curve as a function of time, all modes have approximately the same extension and the traces of all tensors \mathbf{a}_i are a little smaller than 1.

5.4.3 Selection of an extensibility distribution

Taking into account that the new representation of the multimode model exhibits many qualitative similarities with the FENE model, we could ask the question: “is it possible to have a quantitative agreement between the two models?”

This question has been investigated in [SLJ⁺98]. It is shown that, with an appropriate change of variables, it is possible to rewrite the equations governing

the motion of FENE dumbbells in such a way that they become very similar to the governing equations of the FENE-P mode in the new representation. The governing equations differ essentially by the presence of a Wiener process in the FENE model.

But, in extensional flows, the rheological behaviour of FENE model depends essentially on the initial distribution of dumbbells [LHJ⁺97, LKLon]. In the new representation of the multimode model, the initial length distribution (trace of \mathbf{a}) of the various modes closely is associated with their distribution in the old representation. This property is used to select a distribution of extensibilities on the basis of the equilibrium distribution of dumbbells at rest.

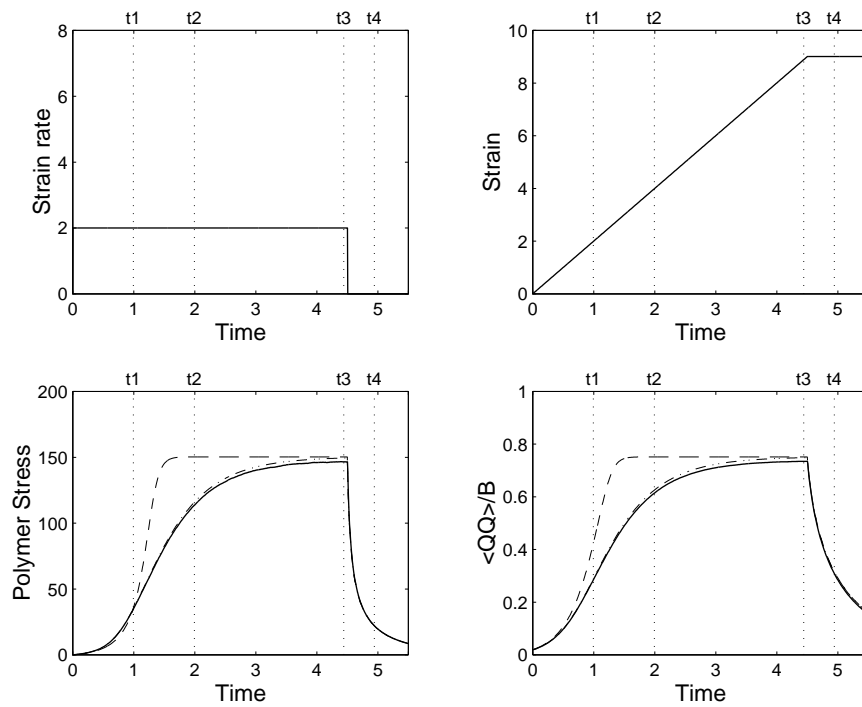


Figure 5.13: *One-dimensional startup of elongation followed by relaxation: comparison between FENE (solid curve), FENE-P (dashed curve) and multimode (dash-dotted curve) results (from [SLJ⁺98]).*

With this new distribution, a very good agreement may be obtained between the FENE and multimode models in uniaxial elongational flows. To illustrate this, we plot in Figure 5.13 a comparison of the stresses obtained with three models in a startup of elongation followed by relaxation. The specified velocity gradient is

$$\kappa(t) = 2(H_0(t) - H_{9/2}(t)). \quad (5.6)$$

Figure 5.13 shows that the early multimode stress and mean square extension

growths remain very close to their FENE counterparts. However, the more pronounced peak-distribution of the multimode model leads at later times to a slight overprediction of both extension and stress values.

Unfortunately the procedure of selection of an extensibility distribution depends on the type of flow: for example a distribution selected for a uniaxial elongational flow gives very disappointing results for biaxial elongational flows. But it is possible to select another distribution of extensibilities that gives very good results for biaxial elongational flows. Thus, we cannot consider the multimode model as a closure approximation of the FENE model.

5.5 Conclusions

We have shown in this chapter, that some essential characteristics of the polymer solutions in elongational flows may be reproduced by the use of a multimode FENE-P model with a spectrum of extensibilities. One of the results we have been able to reproduce is the hysteretic behaviour of solutions in elongation-relaxation experiments. Another important experimental phenomenon is the initial fast decrease of the stress as a function of time after cessation of stretching.

Actually, those two experimental phenomena may be reproduced either with the multimode FENE-P model, or with the FENE model. Moreover a quantitative agreement between both models may be obtained by selection of an appropriate extensibility distribution.

In the multimode stress relaxation curves presented in Figure 5.5, the abrupt transition towards the horizontal plateau may be explained by the fact that the extensibility distribution is not appropriate. With the FENE model, it is possible to obtain a better qualitative agreement between calculations and experimental observations only by adapting the values of relaxation time and extensibility of the model. Thus it is also possible to select a more appropriate extensibility distribution for the multimode model.

It is interesting to remark that a good fit of stress relaxation curves presented in Figure 5.4 with a linear model would require a very large number of modes with various relaxation times, while a good qualitative agreement may be obtained with the FENE model by modifying only two parameters. Thus the combination of dispersity and nonlinearity could explain many rheometrical results without needing a distribution of relaxation times.

Note that, the multimode FENE-P and FENE models are based on two totally different representations of the macromolecules in polymeric solutions. Starting from the fractal interpretation of the macromolecules, we expect to find modes with small extensibilities compared to that of the FENE dumbbells. Moreover, it has been demonstrated in [SLJ⁺98] that the extensibility distribution of the multimode model corresponding to the FENE distribution of dumbbells leads to modes that have small extensibility. If we combine the two ideas, we conclude that, to correctly represent the behaviour of polymer solutions in elongational flows with a multimode model, some very small extensibilities must be introduced in the distribution of the multimode model.

Those very small extensibility modes only influence the rheological behaviour of the model for small values of the Hencky strain. For such values of the stretching, the contribution of those modes to the total stress is not negligible compared to the contribution of the larger extensibility modes because of the nonlinear character of the model. Moreover, the contribution of small extensibility modes to the nonlinearity of the model is predominant at small values of Hencky strain.

It is interesting to remark that Bruno Purnode was obliged to use very small values of the FENE-P extensibility parameter L^2 to reproduce with numerical calculations the flow patterns experimentally observed in 4:1 contractions [PCa, PCb]. This may be explained as follows: the flow patterns are strongly influenced by the nonlinearity of the fluid behaviour. If we consider the multimode model, the modes of small extensibility have the largest contribution to the nonlinearities. To calculate the flow with FENE-P model is equivalent to use the multimode model with only one mode. In order to reproduce the nonlinear behaviour of macromolecules, the extensibility parameter must be very small.

From the behaviour of multimode model, we predict that, when we try to calculate contraction flows with a single mode FENE-P model, the parameter L^2 must depend on the contraction ratio. This dependence of material parameters on the type of flow one wants to calculate may be avoided if a “dispersive” model is used instead of FENE-P. For example, the FENE model with an appropriate selection of parameters could reproduce the observed flow patterns for a wide range of flow rates and contraction ratios. Macroscopic models may also be used provided they are obtained with a closure that takes the dispersive character of polymer solutions into account. For example, it would be interesting to calculate contraction flows with the FENE-L model [LHJ⁺97, LKLon].

Conclusions

This part is devoted to the study of viscoelastic extensional flows.

In chapter 4, we study numerically a filament stretching rheometer. This study allows us to derive the conditions under which the device provides good results. In particular, we show that the filament stretching device only should be used with fluids exhibiting strain hardening. For Newtonian fluids, the device always produces poorly extensional flows, and the measure of the force in the filament is difficult to interpret because it is mainly related to gravitational effects. We show why the flow produced in the device departs from a purely uniaxial extensional flow, and we propose an improved estimate of the extensional viscosity.

Here, it is interesting to remark that two approaches may lead to improvement of rheometrical measurements. We may build more sophisticated devices in which the flows become closer to the rheometrical flows. This approach, though interesting, also leads to a dramatic increase of the complexity of experimental devices, and to a still more dramatic increase of their cost! Another possible approach is to use a relatively simple device in which the rheometrical flow only is approximated. Then a numerical study of the device may help the experimentalist to identify the complex flow, and to interpret the measured data. Taking the dramatic reduction of computational costs into account, this second approach is more promising than the first one.

Finally, we have presented in chapter 5 the results of an intuitive investigation of the influence of the fractal structure of macromolecules on the rheological properties of polymer solutions. Those results confirm that the dispersity of conformation of the molecules may have a large influence on the rheological properties of polymer solutions (and probably polymer melts too). In particular, we have shown that the rapid drop of tensile stress after cessation of stretching, and the hysteresis observed in birefringence experiments may be explained by dispersity and nonlinearity.

It is possible to build closure approximations that take the dispersity into account. This has been done, for example, for the FENE model [LHJ⁺97]. But this gives rise to very complicated models, and much has still to be done to find constitutive equations adapted to a wide range of flows. When such constitutive equations are developed, the mathematical developments are often so complicated, that simplifications must be done in the calculations. But the physical meaning of those simplifications is not always easy to understand. For

example, the modification in the connector force introduced by Wedgewood et al. allows them to close the equations governing the Rouse chain model. But by introducing the simplification, they lose some important characteristics of the chain model, and many experimental observations cannot be reproduced with the FENE-PM model. As a comparison, an intuitive and pragmatic approach, though not based on complicated mathematical developments, has led to the multimode FENE-P model that is able to reproduce many observations in elongation-relaxation experiments.

Therefore, we think that a more pragmatic approach should be used in the development of constitutive equations. And when a simplification is introduced in the mathematical developments, the physical interpretation of that simplification should always be clearly understood. Otherwise, constitutive equations based on physical intuition and experimental observations will generally better reproduce real fluids.

Part III

Appendices

THIS PAGE IS INTENTIONALLY LEFT BLANK

Appendix A

Numerical methods in Polyflow

We present in this appendix some details about the way some numerical techniques presented in chapter 1 are implemented in Polyflow.

A.1 Constraints in Polyflow

Various ways may lead to the imposition of constraints to a set of equations. The introduction of Lagrange multipliers allows to add a condition to the weak formulation of the equations. For example, in the Navier-Stokes equations, the pressure field is the Lagrange multiplier of the incompressibility condition. By modifying the interpolation of the multiplier, the condition may be imposed more or less strongly. In some cases, the Lagrange multiplier method may be used to impose essential boundary conditions (see section 3.3.5). Note that the multiplier may be an interesting result (for example the pressure in Navier-Stokes equations). The method of Lagrange multiplier leads to an increase of the number of equations and unknowns.

There is another way to impose constraints without increasing the number of unknowns of the problem. Let us see for example how the constraint

$$z_n = \beta + \alpha z_1$$

may be added to the linear system

$$\sum_{j=1}^n A_{ij} z_j - b_i = 0, \quad i = 1 \dots n.$$

If this set of equations is the result of the discretization of an elliptic operator, to solve the equations is equivalent to calculate the solution $\sum z_j \phi_j$ in a finite dimension subspace, that minimizes a functional J . When the constraint $z_n =$

$\beta + \alpha z_1$ is imposed on the system, the dimension of the subspace of possible solutions is reduced. In his PHD thesis [Leg92], Vincent Legat explains how the variables of the algebraic linear system may be constrained in such a way that the size of the system is also reduced before the frontal resolution. He justifies the various operations for the simplified example of a Poisson equation. Here, we only give the three steps of the proposed procedure:

1. The n^{th} line of the matrix \mathbf{A} is multiplied by α , and added to the first line. The same operation is done for \mathbf{b} : the n^{th} element of \mathbf{b} is multiplied by α and added to the first element. That is the line operation.
2. From the vector \mathbf{b} , we subtract the n^{th} column of \mathbf{A} multiplied by β . From the first column of \mathbf{A} , we subtract the product of the n^{th} column of \mathbf{A} and α . That is the column operation.
3. The n^{th} line and n^{th} column are cancelled from the system. The $n - 1$ first variables are calculated by inversion of the matrix. The n^{th} variable, z_n is calculated with the constraint $z_n = \beta + \alpha z_1$.

In the data files of Polyflow, constraints of the general form are implemented with “CTRRHS” cards. An “ADD” flag of the CTRRHS card allows to add the constraint to previous constraints. For example if the old constraint is $\mathbf{x} = \mathbf{a}$ and we add the constraint $\mathbf{x} = \mathbf{b}$, the new constraint will be $\mathbf{x} = \text{old constraint} + \mathbf{b} = \mathbf{a} + \mathbf{b}$. This capability allows the user to define linear combinations of constraints. The constraint may also be imposed to the variation of the field with the “SUP” flag. If this capability is used, we have $\mathbf{x} = \mathbf{x}_{\text{old}} + \mathbf{a}$ instead of $\mathbf{x} = \mathbf{a}$. For constraints of the form $z_n = \beta$, “BEVAXS” cards are used.

A.2 Resolution of the nonlinear system

The discretization of the governing equations and the selection of a finite element representation of the unknown fields provide a set of nonlinear algebraic equations in the nodal values. In order to solve the nonlinear system, an appropriate iterative scheme is introduced. Polyflow uses two basic schemes: the Newton-Raphson algorithm, and the Picard method.

The nonlinear system may be written as follows:

$$\mathbf{r}(\mathbf{x}) = \mathbf{K}(\mathbf{x})\mathbf{x} + \mathbf{f}(\mathbf{x}) = \mathbf{0}, \quad (\text{A.1})$$

where $\mathbf{K}(\mathbf{x})$ is usually called the “stiffness” matrix. We start from the solution vector \mathbf{x}_{n-1} to calculate an improved estimate of the solution \mathbf{x}_n : the system (A.1) is linearized around the old solution \mathbf{x}_{n-1} , and we hope to find $\mathbf{x}_n = \mathbf{x}_{n-1} + \delta\mathbf{x}$. We have

$$\mathbf{r}(\mathbf{x}_n) = \mathbf{r}(\mathbf{x}_{n-1} + \delta\mathbf{x}) \approx \mathbf{r}(\mathbf{x}_{n-1}) + \nabla\mathbf{r}(\mathbf{x}_{n-1})\delta\mathbf{x} \quad (\text{A.2})$$

in which $\nabla\mathbf{r}$ is the Jacobian matrix. We hope that $\mathbf{r}(\mathbf{x}_n)$ vanishes. So an increment $\delta\mathbf{x}$ is calculated by solving

$$\nabla\mathbf{r}(\mathbf{x}_{n-1})\delta\mathbf{x} = -\mathbf{r}(\mathbf{x}_{n-1}), \quad (\text{A.3})$$

and the new estimate of the solution is given by $\mathbf{x}_n = \mathbf{x}_{n-1} + \delta\mathbf{x}$.

The Newton-Raphson algorithm is endowed with a quadratic convergence rate, provided the initial solution is located in the disk of convergence. However, it is frequent that the disk of convergence is too small. For such cases, a continuation method has to be used: a parameter related to the nonlinearity of the problem is progressively increased, and intermediate solutions are calculated with the Newton-Raphson algorithm, and starting from the last converged solution.

Note that in Polyflow, the equations are built in a way similar to that of equation (A.3): the right hand side contains the residue $-\mathbf{r}(\mathbf{x}_{n-1})$, and a Jacobian matrix $\nabla\mathbf{r}(\mathbf{x}_{n-1})$ is derived from the expression of the residue (i.e. the derivative of the residue is calculated for all the unknowns of the system).

The radius of the disk of convergence of Newton-Raphson algorithm may be very small, for example when a Newtonian fluid exhibits an important shear thinning character. The lack of convergence of Newton's algorithm may be avoided by using a matrix \mathbf{A} different than the Jacobian matrix $\nabla\mathbf{r}$ in the iterative scheme. Generally \mathbf{A} is obtained by an incomplete derivation of \mathbf{r} with respect to nodal unknowns. For example, when the lack of convergence of Newton-Raphson algorithm is related to the shear thinning character of a fluid, viscosity is not derived with respect to nodal values of the velocity field. This new scheme is called "Picard iterative scheme". The radius of this scheme is larger, but it does not enjoy the quadratic convergence property.

A.3 Adaptive time stepping algorithm

We present here the adaptive time-stepping strategy proposed by Gresho, Lee and Sani [GLS80] and later used by Christine Bodart [BC94, Bod94]. The principle of the strategy is simple: an explicit scheme is used to predict the solution at time step $n + 1$. Then the explicit prediction is corrected with an implicit scheme. The difference between the predicted and corrected solutions at time t_{n+1} is used to calculate the next time step Δt_{n+2} .

Introducing the notations

$$\dot{\mathbf{z}}^{n+1} = \mathbf{M}^{-1}(\mathbf{z}^{n+1})\mathbf{g}(\mathbf{z}^{n+1}), \quad (\text{A.4})$$

$$\dot{\mathbf{z}}^n = \mathbf{M}^{-1}(\mathbf{z}^n)\mathbf{g}(\mathbf{z}^n), \quad (\text{A.5})$$

expression (1.37) may be written

$$\mathbf{z}^{n+1} + \theta\Delta t_{n+1}\dot{\mathbf{z}}^{n+1} = \mathbf{z}^n - (1 - \theta)\Delta t_{n+1}\dot{\mathbf{z}}^n. \quad (\text{A.6})$$

By multiplying this expression by $\mathbf{M}(\mathbf{z}^{n+1})$ and introducing the notation $\mathbf{z}^r = \mathbf{z}^n - (1 - \theta)\Delta t\mathbf{M}^{-1}(\mathbf{z}^n)\mathbf{g}(\mathbf{z}^n)$, we obtain

$$\frac{1}{\theta\Delta t_{n+1}}\mathbf{M}(\mathbf{z}^{n+1})(\mathbf{z}^{n+1} - \mathbf{z}^r) + \mathbf{g}(\mathbf{z}^{n+1}) = \mathbf{0}. \quad (\text{A.7})$$

\mathbf{z}^r only depends on the solution at time step n , and is called the “explicit part” of the corrector. Equation (A.7) is solved with a Newton-Raphson algorithm and gives the solution \mathbf{z}^{n+1} . Note that equation (A.7) only exists if the method is implicit ($\theta > 0$).

The initial value \mathbf{z}^p used to start the Newton-Raphson algorithm is predicted with an explicit predictor. For example the use of an Euler explicit scheme gives

$$\mathbf{z}^p = \mathbf{z}^n + \Delta t \dot{\mathbf{z}}^n. \quad (\text{A.8})$$

A second order predictor explicit scheme is the Adams-Bashforth scheme:

$$\mathbf{z}_{n+1}^p = \mathbf{z}_n + \frac{\Delta t_{n+1}}{2} \left(2\dot{\mathbf{z}}_n + \frac{\Delta t_{n+1}}{\Delta t_n} (\dot{\mathbf{z}}_n - \dot{\mathbf{z}}_{n-1}) \right) \quad (\text{A.9})$$

To calculate the Euler explicit prediction (A.8), the time derivative of \mathbf{z} at time t_n must be known a priori. To calculate the second order prediction (A.9), the two last time derivatives of the solution must be known.

For the current time step, $\dot{\mathbf{z}}^{n+1}$ may be estimated with equations (A.4) and (A.7). This gives

$$\dot{\mathbf{z}}^{n+1} = \frac{\mathbf{z}^{n+1} - \mathbf{z}^r}{\theta \Delta t}. \quad (\text{A.10})$$

The local error of time discretization defined as

$$\mathbf{d}^{n+1} = \mathbf{z}^{n+1} - \mathbf{z}(t_{n+1}) \quad (\text{A.11})$$

is used to calculate the next time step Δt_{n+2} . Assuming that $\mathbf{z}^n, \mathbf{z}^{n+1}, \dots, \dot{\mathbf{z}}^n, \dot{\mathbf{z}}^{n+1}, \dots$ are exact, it is possible to determine a local estimate of the time discretization error by an expansion in Taylor series. With a θ method like (A.6), the generic form of the discretization error is

$$\mathbf{z}^{n+1} - \mathbf{z}(t_{n+1}) = \left(\theta - \frac{1}{2} \right) \Delta t_{n+1}^2 \ddot{\mathbf{z}}^n + \frac{1}{2} \left(\theta - \frac{1}{3} \right) \Delta t_{n+1}^3 \dddot{\mathbf{z}}^n + \mathcal{O}(\Delta t_{n+1}^4). \quad (\text{A.12})$$

We see that only the Crank-Nicolson scheme ($\theta = 1/2$) is of the second order (error as Δt^3). A local estimate of the local error of this method is given by

$$\mathbf{z}^{n+1} - \mathbf{z}(t_{n+1}) = \frac{1}{12} \Delta t_{n+1}^3 \dddot{\mathbf{z}}^n + \mathcal{O}(\Delta t_{n+1}^4). \quad (\text{A.13})$$

For the implicit Euler scheme, one has

$$\mathbf{z}^{n+1} - \mathbf{z}(t_{n+1}) = \frac{1}{2} \Delta t_{n+1}^2 \ddot{\mathbf{z}}^n + \mathcal{O}(\Delta t_{n+1}^3). \quad (\text{A.14})$$

Similar estimates of the local error may be calculated for the explicit Euler and Adams-Bashforth predictors. One obtains

$$\mathbf{z}_P^{n+1} - \mathbf{z}(t_{n+1}) = -\frac{1}{2} \Delta t_{n+1}^2 \ddot{\mathbf{z}}^n + \mathcal{O}(\Delta t_{n+1}^3) \quad (\text{A.15})$$

and

$$\mathbf{z}_P^{n+1} - \mathbf{z}(t_{n+1}) = -\frac{1}{12} \left(2 + 3 \frac{\Delta t_n}{\Delta t_{n+1}} \right) \Delta t_{n+1}^3 \ddot{\mathbf{z}}^{..n} + \mathcal{O}(\Delta t_{n+1}^4) \quad (\text{A.16})$$

respectively.

By combining the error expressions of the second order predictor-corrector (A.13) and (A.16), one obtains the discretization error given by

$$\mathbf{d}^{n+1} = \frac{\mathbf{z}^{n+1} - \mathbf{z}_P^{n+1}}{3 \left(1 + \frac{\Delta t_n}{\Delta t_{n+1}} \right)} + \mathcal{O}(\Delta t_{n+1}^4). \quad (\text{A.17})$$

A similar expression may be calculated for the first order predictor-corrector scheme:

$$\mathbf{d}^{n+1} = \frac{\mathbf{z}^{n+1} - \mathbf{z}_P^{n+1}}{2} + \mathcal{O}(\Delta t_{n+1}^3). \quad (\text{A.18})$$

Vector \mathbf{d}^{n+1} may be used to estimate the next time step by imposing that the error of the time step is equal to a parameter ϵ . From (A.17), one obtains

$$\frac{|\mathbf{d}^{n+2}|}{|\mathbf{d}^{n+1}|} \left(\frac{\Delta t_{n+2}}{\Delta t_{n+1}} \right)^3 \frac{\left| \ddot{\mathbf{z}}^{..n+1} \right|}{\left| \ddot{\mathbf{z}}^{..n} \right|}. \quad (\text{A.19})$$

Noting that $\ddot{\mathbf{z}}^{..n+1} = \ddot{\mathbf{z}}^{..n} + \mathcal{O}(\Delta t_n)$, we may replace $\ddot{\mathbf{z}}^{..n+1}$ in (A.19) by ϵ . Neglecting higher order terms, one has

$$\Delta t_{n+2} = \Delta t_{n+1} \left(\frac{\epsilon}{|\mathbf{d}^{n+1}|} \right)^{1/3}. \quad (\text{A.20})$$

Thus we have an estimate of the next time step. Actually this operation is done separately for all fields influencing the transient evolution. The smallest time step obtained is selected as the new time step. The same method is used for the first order predictor-corrector scheme. One obtains easily

$$\Delta t_{n+2} = \Delta t_{n+1} \left(\frac{\epsilon}{|\mathbf{d}^{n+1}|} \right)^{1/2}. \quad (\text{A.21})$$

Note that equations (A.20) and (A.21) are not used without additional tests. For example, one tests the convergence of Newton-Raphson schemes before going to the next time step. If one SOLVER does not converge, the step is recalculated with a smaller time step. One also checks that the difference between the new time step and the current one is not too large. If the difference is too large, it may mean that the last calculated solution is not very good. Therefore, additional tests are added to the algorithm. More information about practical details may be found in [Bod94].

Appendix B

More information on multilayer flows

This appendix is devoted to the presentation of additional informations to the chapter 2. We present in sections B.1.1 and B.1.2 the expressions of the velocity and pressure fields for the two-layer planar Poiseuille flow, and core-annular flows respectively (Figures 2.1 and 2.28). In section B.2, we summarize the various nonlinear phenomena observed in multilayer transient calculations.

B.1 Base flows

B.1.1 Two layer planar Poiseuille flow

The equations are solved in a cartesian coordinates system. The flow is horizontal and parallel to the x axis. The vertical component of the velocity vanishes. The horizontal component only depends on y , and consists of two parabolic profiles given respectively by

$$u_1(y) = 1 + \frac{m - n^2}{n(n+1)}y - \frac{m+n}{n(n+1)}y^2,$$
$$u_2(y) = 1 + \frac{m - n^2}{mn(n+1)}y - \frac{m+n}{mn(n+1)}y^2.$$

The horizontal pressure gradient is constant on the domain. We find

$$\begin{aligned} \frac{\partial p}{\partial x} &= \frac{\partial^2 u_1}{\partial y^2}, \\ &= m \frac{\partial^2 u_2}{\partial y^2}, \\ &= -\frac{2(m+n)}{n(n+1)}. \end{aligned} \tag{B.1}$$

If gravity is neglected, the pressure field is independent of y . Otherwise, a constant vertical pressure gradient, given in both layers respectively by $\partial p/\partial y = -G$ and $\partial p/\partial y = -\zeta G$, is to be added to (B.1). The total flow rate in the two layers is obtained by integration of the velocity profile along a vertical section:

$$\begin{aligned}\dot{Q} &= \int_{-n}^0 u_2(y)dy + \int_0^1 u_1(y)dy \\ &= \frac{4mn^3 + 3mn^2 + n^4}{6mn(n+1)} + \frac{3n^2 + 4n + m}{6n(n+1)}, \\ &= \frac{4mn^3 + 6mn^2 + n^4 + 4mn + m^2}{6mn(n+1)}.\end{aligned}\quad (\text{B.2})$$

B.1.2 Core-annular flow

In each layer, the velocity and the pressure satisfy the Navier-Stokes equations. For the base flow, we have

$$\frac{dp_1}{dz} = \frac{dp_2}{dz} = -f.$$

The axial component of the velocity is in each layer respectively given by

$$\begin{aligned}v_1(r) &= \frac{f + \rho_1 g}{4\mu_1} (R_1^2 - r^2) + \frac{f + \rho_2 g}{4\mu_2} (R_2^2 - R_1^2) + \frac{R_1^2 \llbracket \rho \rrbracket g}{2\mu_2} \ln \frac{R_2}{R_1}, \\ v_2(r) &= \frac{f + \rho_2 g}{4\mu_2} (R_2^2 - r^2) - \frac{R_1^2 \llbracket \rho \rrbracket g}{2\mu_2} \ln \frac{r}{R_2},\end{aligned}\quad (\text{B.3})$$

where $\llbracket (\cdot) \rrbracket = (\cdot)_1 - (\cdot)_2$.

The flow rates are given by integration of the velocity on each layer:

$$\begin{aligned}Q_1 &= \int_0^{R_1} 2\pi r v_1(r) dr \\ &= \pi R_1^2 \left(\frac{f + \rho_1 g}{8\mu_1} R_1^2 + \frac{f + \rho_2 g}{4\mu_2} (R_2^2 - R_1^2) + \frac{\llbracket \rho \rrbracket g R_1^2}{2\mu_2} \ln \frac{R_2}{R_1} \right) \\ &= \pi \frac{f + \rho_1 g}{8\mu_1} R_1^4 + \pi \frac{f + \rho_2 g}{4\mu_2} (R_1^2 R_2^2 - R_1^4) + \pi \frac{\llbracket \rho \rrbracket g}{4\mu_2} R_1^4 \ln \frac{R_2}{R_1}.\end{aligned}$$

$$\begin{aligned}Q_2 &= \int_{R_1}^{R_2} 2\pi r v_2(r) dr \\ &= \pi \frac{f + \rho_2 g}{8\mu_2} (R_1^2 - R_2^2)^2 + \pi \frac{R_1^2 \llbracket \rho \rrbracket g}{4\mu_2} \left(R_1^2 \ln \frac{R_1}{R_2} + R_2^2 - R_1^2 \right) \\ &= \pi \frac{f + \rho_2 g}{8\mu_2} (R_1^4 - 2R_1^2 R_2^2 + R_2^4) + \pi \frac{\llbracket \rho \rrbracket g}{4\mu_2} \left(R_1^2 R_2^2 - R_1^4 \ln \frac{R_2}{R_1} - R_1^4 \right).\end{aligned}$$

$$\begin{aligned}
Q &= Q_1 + Q_2 \\
&= \pi \frac{f + \rho_1 g}{8\mu_1} R_1^4 + \pi \frac{f + \rho_2 g}{8\mu_2} (R_2^4 - R_1^4) + \pi \frac{[\rho]g}{4\mu_2} (R_1^2 R_2^2 - R_1^4). \quad (\text{B.4})
\end{aligned}$$

B.2 Nonlinear phenomena

Our transient calculations allow us to observe phenomena that cannot be predicted with a linear theory. The most evident nonlinearity we expect to see in our transient calculations is the nonlinearity related to the growth of an unstable perturbation in the nonlinear domain. This point is discussed in section B.2.1. But other nonlinear phenomena may be observed. For example the frequency of the oscillations in amplitude curves for $n = \sqrt{m}$ depends on the amplitude of the initial perturbation (see section B.2.3). Moreover, we demonstrate in section B.2.2 that the higher order harmonics observed in the perturbation are originated by nonlinearities of the governing equations.

B.2.1 Large amplitude perturbations

The unstable perturbations grow. At the beginning of their growth, their behaviour is essentially linear if their amplitude is sufficiently small. But they finally reach an amplitude for which their behaviour cannot be described with a linear theory.

For unstable flows, we may distinguish two different situations: the most unstable mode may be either of the first harmonic or of a higher order harmonic.

For $n = 2.63$, the amplitude of the first harmonic of the perturbation increases with time. For large values of t , the amplitude of the perturbation becomes so large that the interface flattens close to the upper plate, and departs from a sinusoidal shape (figure 2.17). If we want to describe the shape of the interface with sinusoidal functions, a spectrum of wavelength must be introduced: $h(x) = g_1 \sin(\alpha x + \beta_1) + g_2 \sin(2\alpha x + \beta_2) + \dots$. In the last expansion, g_1 and g_2 correspond respectively to the amplitudes A and A_2 of the first and second harmonics. Therefore, we expect the higher order harmonics to grow with time when the amplitude A of the perturbation becomes large.

In Figure B.1, we plot the amplitude of the three first harmonics as a function of time. As the amplitude of the perturbation (i.e. of the first harmonic) tends towards 1, the amplitude of the higher order harmonic curves grow smoothly.

In the curves giving the amplitude of the harmonics as a function of time for $n = 8$ (figure B.2), we see that only the first harmonic is stable. Several modes of the second and third harmonics are originated at the beginning of the calculation. For small values of t , the amplitude of those modes is small, and they interfere. But, for both second and third harmonics, at least one of the modes is unstable; during their growths, the most unstable modes of each harmonic progressively dominates and the oscillations of the related amplitude curves progressively vanish.

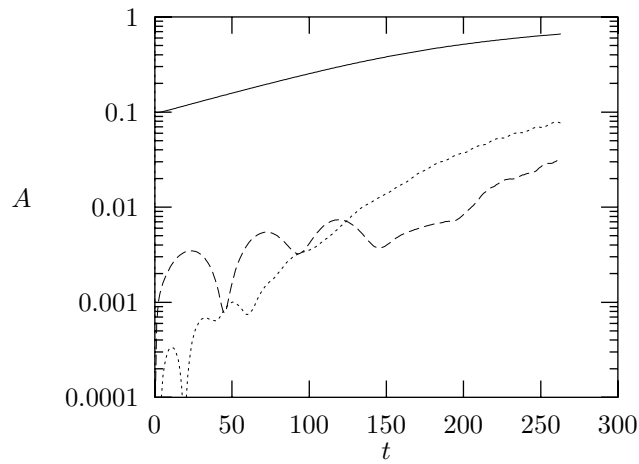


Figure B.1: *Amplitude of the three first harmonics as a function of time ($\alpha = 0.4$, $n = 2.63$, $m = 20$, $\mathbb{R} = 10$, $A_{\text{init}} = 0.1$ and $\Delta t = 0.25$). The continuous, dashed and dotted lines correspond respectively to the first, second and third harmonics.*

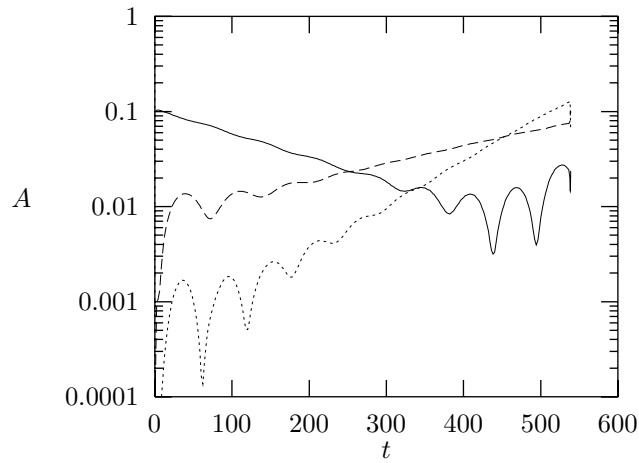


Figure B.2: *Amplitude of the three first harmonics as a function of time ($\alpha = 0.4$, $n = 8$, $m = 20$, $\mathbb{R} = 10$, $A_{\text{init}} = 0.1$ and $\Delta t = 0.25$). The continuous, dashed and dotted lines correspond respectively to the first, second and third harmonics.*

In Figure B.3 we plot the shape of the interface for two values of t . For $t = 380$ and $t = 562.5$, the flow is dominated by the second and the third harmonic respectively. But in both cases, modes of other harmonics also are present in the flow.

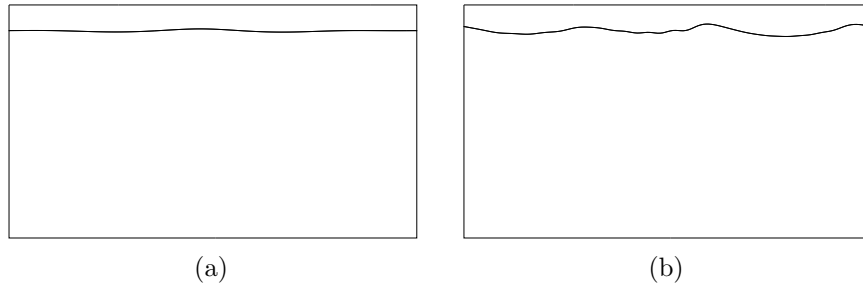


Figure B.3: Configuration of the two layers for $t = 380$ (a) and $t = 562.5$ (b). ($\alpha = 0.4$, $n = 8$, $m = 20$, $\mathcal{R} = 10$, $A_{\text{init}} = 0.1$ and $\Delta t = 0.25$).

For large values of t oscillations appear in the amplitude curve of the first harmonic. This gives us the impression that an unstable mode of the first harmonic grows in the flow. When this occurs, the amplitude of the high order harmonics already is large. We think that the perturbations of the first harmonic are destabilized by the non linearities of the flow generated by the growth of higher order harmonics.

B.2.2 Unstable higher order harmonics for $n = 8$

The fact that for $n = 8$ the amplitude of the second harmonic oscillates for small values of t in Figure B.4 proves that various modes of the second harmonic are present in the flow. But one of the modes grows faster than the others and the oscillations vanish for larger values of t . It is not surprising that some modes of the second harmonic are unstable, for the second harmonic corresponds to a perturbation of wavenumber $\alpha = 0.8$ for which the linear stability theory predicts a growth rate $\alpha c_i > 0$ (figure 2.7).

We also see that for $n = 8$ and $t \lesssim 250$, the ratio of the amplitudes $A(t)$ taken respectively for $A_{\text{init}} = 0.1$ and $A_{\text{init}} = 0.05$ is approximately equal to 2. But the corresponding ratio for the second harmonic is approximately 4. (A similar observation has been done for $n = 2.63$.) We conclude that higher order harmonics are originated in the flow by the nonlinearities of the governing equations (i.e. by inertia terms).

B.2.3 The peculiar case $n = \sqrt{m}$

The low frequency oscillations observed in Figures 2.19 and 2.21 only occur for $n = \sqrt{m}$, value for which all linear stability analyses predict a neutral stability. For the other values of n , we always obtain high frequency oscillations. The

peculiar behaviour of the oscillations for $n = \sqrt{m}$ is probably related to its neutral interfacial stability.

Actually, the linear stability analyses also predict a peculiar translation velocity of the perturbations for $n = \sqrt{m}$. For example, the long wavelength asymptotic analysis of Yiantsios and Higgins [YH88b] predicts a translation velocity c_{tr} given by

$$c_{\text{tr}} = 1 + \frac{2(m - n^2)(m - 1)(n^3 + n^2)}{(n^2 + n)(n^4 + 4n^3m + 6n^2m + 4nm + m^2)}.$$

For $n = \sqrt{m}$, this equation simply gives $c_{\text{tr}} = 1$. Thus, it seems that for $n = \sqrt{m}$ the perturbations are transported by the flow, at the velocity of the interface, without increasing or decreasing.

If all modes were translated at the same velocity, oscillations could not be observed in amplitude curves. Nevertheless, oscillations occur in our curves for $n = \sqrt{m}$, though at very small frequency. That makes us think that the translation velocity of the various modes present in the flow is not exactly equal to one. An explanation of that, may be found in the nonlinearity of the behaviour of the modes present in the flow.

If we write the translation velocity of the perturbations as a function of the amplitude, we obtain something like

$$c_{\text{tr}} = c_{\text{tr}}^{\text{lt}}(\alpha, n, k) + f(A, \alpha, n, k),$$

in which $\alpha c_{\text{tr}}^{\text{lt}}$ is the translation velocity of the perturbation predicted with the linear theory, $f(A, \alpha, n, k)$ represents the effect of the nonlinearities on the translation velocity of the mode (and thus f decreases with A), and k denotes the observed mode.

The difference between the translation velocities of two modes is given by

$$c_{\text{tr}}^{\text{lt}}(\alpha, n, k_1) - c_{\text{tr}}^{\text{lt}}(\alpha, n, k_2) + f(A, \alpha, n, k_1) - f(A, \alpha, n, k_2). \quad (\text{B.5})$$

For small amplitude modes, the nonlinearities are small and $f(A, \alpha, n, k_1) - f(A, \alpha, n, k_2)$ is generally small compared to $c_{\text{tr}}^{\text{lt}}(\alpha, n, k_1) - c_{\text{tr}}^{\text{lt}}(\alpha, n, k_2)$. Therefore, we do not expect the frequency of the amplitude oscillations to be very different than the frequency we could predict with a linear theory. Moreover, the frequency will remain approximately independent of the amplitude for moderate values of A .

But there is one exception to this theory: if $c_{\text{tr}}^{\text{lt}}(\alpha, n, k_1) - c_{\text{tr}}^{\text{lt}}(\alpha, n, k_2)$ vanishes or becomes very small (and this occurs for $n = \sqrt{m}$), $f(A, \alpha, n, k_1) - f(A, \alpha, n, k_2)$ may no longer be neglected. Actually, for $n = \sqrt{m}$, this term will be responsible of the difference of translation velocity between the modes. Thus, $f(A, \alpha, n, k_1) - f(A, \alpha, n, k_2)$ is clearly related to the frequency of the oscillations. Therefore, we may expect the frequency to decrease with the amplitude of the perturbation A for $n = \sqrt{m}$.

In order to check this assumption, we plot in Figures B.4 and B.5 the amplitude curves for the first and second harmonic, and for two different initial

values of the perturbation's amplitude. (To clarify Figure B.5, we do not plot the curves for $n = 2.63$. The effect of the initial amplitude on the amplitude curve for $n = 2.63$ is qualitatively identical to its effect on the curves for $n = 8$.)

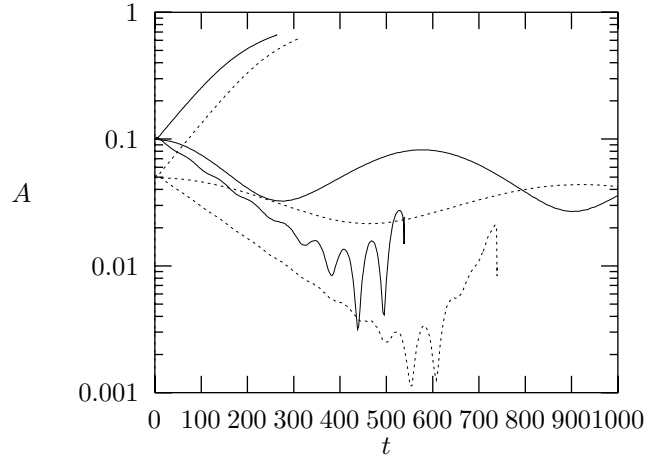


Figure B.4: *Amplitude of the first harmonic of the perturbation as a function of time for various values of n and A_{init} ($\alpha = 0.4$, $m = 20$, $\mathcal{R} = 10$, $n = 2.63$, 8 or $\sqrt{20}$, $A_{\text{init}} = 0.1$ or 0.05 and $\Delta t = 0.25$).*

We observe the expected phenomena: the frequency of the oscillations decreases with A_{init} for $n = \sqrt{m}$, but remains independent of the initial amplitude for other values of n .

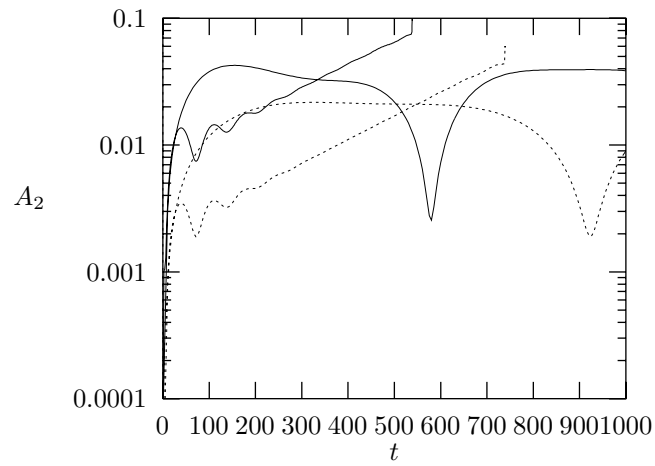


Figure B.5: *Amplitude of the second harmonic of the perturbation as a function of time for various values of n and A_{init} ($\alpha = 0.4$, $m = 20$, $\mathcal{R} = 10$, $n = 8$ or $\sqrt{20}$, $A_{\text{init}} = 0.1$ or 0.05 and $\Delta t = 0.25$).*

Appendix C

Contact line problem in Polyflow

C.1 Line dynamic condition with constraints

C.1.1 Dirichlet boundary conditions and contact force

We have seen in section 1.3.1 how the integration by parts of the weak formulation of the Galerkin equations allows us to identify a natural boundary condition involving the contact force $\mathbf{t} = \boldsymbol{\sigma} \cdot \mathbf{n}$. The strong formulation of the momentum equation may be written

$$\nabla \cdot \boldsymbol{\sigma}(\mathbf{v}, p, \mathbf{T}, \dots) + \mathbf{f} = \mathbf{0}.$$

The weak formulation, after integration by parts simply gives

$$\int_{\Gamma} \psi_j \cdot [\boldsymbol{\sigma}(\mathbf{v}, p, \mathbf{T}, \dots) \cdot \mathbf{n}] d\Gamma - \int_{\Omega} \nabla \psi_j : \boldsymbol{\sigma}(\mathbf{v}, p, \mathbf{T}, \dots) d\Omega = \mathbf{0}. \quad (\text{C.1})$$

When Neumann boundary conditions are applied along the boundary, a force repartition $\mathbf{t} = \boldsymbol{\sigma}(\mathbf{v}, p, \mathbf{T}, \dots) \cdot \mathbf{n}$ is prescribed, and equation (C.1) becomes

$$\int_{\Omega} \nabla \psi_j : \boldsymbol{\sigma}(\mathbf{v}, p, \mathbf{T}, \dots) d\Omega = \int_{\Gamma} \psi_j \cdot \mathbf{t} d\Gamma. \quad (\text{C.2})$$

If Dirichlet conditions are applied, the left hand side of (C.2) is not calculated, and the discretized equations before the imposition of constraints are given by

$$\int_{\Omega} \nabla \psi_j : \boldsymbol{\sigma}(\mathbf{v}, p, \mathbf{T}, \dots) d\Omega = \mathbf{0}. \quad (\text{C.3})$$

Then, the three steps presented in section A.1 may be used to impose a Dirichlet condition of the type $z_n = \beta$.

Instead of imposing the velocity field with constraints, an appropriate contact force \mathbf{t} may be applied along the boundary Γ in order to impose the velocity on that boundary. In such a formulation, \mathbf{t} is *a priori* unknown; it is the Lagrange multiplier of the constraint on the velocity, and its calculation is coupled with the resolution of the others governing equations.

In Polyflow, we use a Newton-Raphson algorithm (see section A.2) and actually, before imposition of the constraints, the left hand sides of the discretized equations for both methods are

$$\int_{\Gamma} \psi_j \cdot \mathbf{t} d\Gamma - \int_{\Omega} \nabla \psi_j : \sigma(\mathbf{v}, p, \mathbf{T}, \dots) d\Omega \quad (\text{C.4})$$

and

$$- \int_{\Omega} \nabla \psi_j : \sigma(\mathbf{v}, p, \mathbf{T}, \dots) d\Omega \quad (\text{C.5})$$

respectively.

Of course, the imposition of the velocity along the boundary must give exactly the same result with both methods. With the Lagrange multiplier method, when convergence occurs, the left hand side (C.4) vanishes. Thus, for a converged solution, the left hand side (C.5) must be equal to the integration of the contact force

$$- \int_{\Gamma} \psi_j \cdot \mathbf{t} d\Gamma. \quad (\text{C.6})$$

Note that \mathbf{t} is the force applied by the boundary on the fluid. Thus (C.5) is equal to the resultant of the force imposed by the fluid on the boundary.

This property may be used to calculate with a postprocessor the resulting force on a boundary on which Dirichlet boundary conditions are imposed. (Actually, this is done in Polyflow with the “DUAL” cards.)

C.1.2 Contact forces and constraints

The properties of the converged left hand side (C.5) before imposition of the constraints also may be used to recover an estimate of the contact force during the elimination of the system. (We mean: in such a way that the calculation of the contact force is coupled with the Gaussian elimination and not performed during a post-processing step.)

The strategy we have developed to calculate the position of the contact line, is inspired by the way the position of the contact point of a free surface to a wall was calculated in two dimensional cases by Vincent Legat in his PHD thesis [Leg92]. In order to simplify the notations, we first examine how the expression $\int_{\Gamma} \psi_j \cdot \mathbf{t} d\Gamma$ may be recovered on one node. We also assume that the node for which we want to recover the force is the last one; this last assumption does not involve any loss of generality, because it may be achieved by a renumbering of the unknowns of the system.

To the governing equations of the problem, we add the equation $\pi \mathbf{f}_k = \mathbf{0}$, in which \mathbf{f}_k is the nodal value that represents the resulting force on node k we are

looking for, and π is an arbitrary parameter, but sufficiently large (this point will be discussed later). The system of equations we are solving looks like

$$\begin{pmatrix} \ddots & \vdots & \vdots & \vdots & \vdots & \vdots & \vdots \\ \cdots & A_{11} & A_{12} & A_{13} & 0 & 0 & 0 \\ \cdots & A_{21} & A_{22} & A_{23} & 0 & 0 & 0 \\ \cdots & A_{31} & A_{32} & A_{33} & 0 & 0 & 0 \\ \cdots & 0 & 0 & 0 & \pi & 0 & 0 \\ \cdots & 0 & 0 & 0 & 0 & \pi & 0 \\ \cdots & 0 & 0 & 0 & 0 & 0 & \pi \end{pmatrix} \begin{pmatrix} \vdots \\ \Delta u_k \\ \Delta v_k \\ \Delta w_k \\ \Delta f_u^k \\ \Delta f_v^k \\ \Delta f_w^k \end{pmatrix} = \begin{pmatrix} \vdots \\ -r_u^k \\ -r_v^k \\ -r_w^k \\ -\pi f_u^k \\ -\pi f_v^k \\ -\pi f_w^k \end{pmatrix}. \quad (\text{C.7})$$

The A_{ij} elements represent the momentum equation. We only have represented a small part of the matrix in order to simplify the notations.

Now we add the constraints $\mathbf{v}_k = \mathbf{f}_k$ to the system. After the line operation, we have

$$\begin{pmatrix} \ddots & \vdots & \vdots & \vdots & \vdots & \vdots & \vdots \\ \cdots & A_{11} & A_{12} & A_{13} & 0 & 0 & 0 \\ \cdots & A_{21} & A_{22} & A_{23} & 0 & 0 & 0 \\ \cdots & A_{31} & A_{32} & A_{33} & 0 & 0 & 0 \\ \cdots & A_{11} & A_{12} & A_{13} & \pi & 0 & 0 \\ \cdots & A_{21} & A_{22} & A_{23} & 0 & \pi & 0 \\ \cdots & A_{31} & A_{32} & A_{33} & 0 & 0 & \pi \end{pmatrix} \begin{pmatrix} \vdots \\ \Delta u_k \\ \Delta v_k \\ \Delta w_k \\ \Delta f_u^k \\ \Delta f_v^k \\ \Delta f_w^k \end{pmatrix} = \begin{pmatrix} \vdots \\ -r_u^k \\ -r_v^k \\ -r_w^k \\ -r_u^k - \pi f_u^k \\ -r_v^k - \pi f_v^k \\ -r_w^k - \pi f_w^k \end{pmatrix}, \quad (\text{C.8})$$

and after the column operation

$$\begin{pmatrix} \ddots & \vdots & \vdots & \vdots & \vdots & \vdots & \vdots \\ \cdots & A_{11} & A_{12} & A_{13} & A_{11} & A_{12} & A_{13} \\ \cdots & A_{21} & A_{22} & A_{23} & A_{21} & A_{22} & A_{23} \\ \cdots & A_{31} & A_{32} & A_{33} & A_{31} & A_{32} & A_{33} \\ \cdots & A_{11} & A_{12} & A_{13} & \pi - A_{11} & -A_{12} & -A_{13} \\ \cdots & A_{21} & A_{22} & A_{23} & -A_{21} & \pi - A_{22} & -A_{23} \\ \cdots & A_{31} & A_{32} & A_{33} & -A_{31} & -A_{32} & \pi - A_{33} \end{pmatrix} \begin{pmatrix} \vdots \\ \Delta u_k \\ \Delta v_k \\ \Delta w_k \\ \Delta f_u^k \\ \Delta f_v^k \\ \Delta f_w^k \end{pmatrix} = \begin{pmatrix} \vdots \\ -r_u^k \\ -r_v^k \\ -r_w^k \\ -r_u^k - \pi f_u^k \\ -r_v^k - \pi f_v^k \\ -r_w^k - \pi f_w^k \end{pmatrix}. \quad (\text{C.9})$$

Finally, the constrained variables are eliminated from the system, and we

solve

$$\begin{pmatrix} \ddots & \vdots & \vdots & \vdots \\ \cdots & \pi - A_{11} & -A_{12} & -A_{13} \\ \cdots & -A_{21} & \pi - A_{22} & -A_{23} \\ \cdots & -A_{31} & -A_{32} & \pi - A_{33} \end{pmatrix} \begin{pmatrix} \vdots \\ \Delta f_u^k \\ \Delta f_v^k \\ \Delta f_w^k \end{pmatrix} = \begin{pmatrix} \vdots \\ -r_u^k - \pi f_u^k \\ -r_v^k - \pi f_v^k \\ -r_w^k - \pi f_w^k \end{pmatrix}. \quad (\text{C.10})$$

After convergence, \mathbf{f}_k satisfies the relations

$$\begin{aligned} \pi f_u^k &= -r_u^k, \\ \pi f_v^k &= -r_v^k, \\ \pi f_w^k &= -r_w^k. \end{aligned}$$

It is clear that for a very large parameter π , \mathbf{f}_k tends towards zero, and the same is true for \mathbf{v}_k . Thus, by increasing π the solution tends to what is obtained when a vanishing Dirichlet boundary condition is imposed to \mathbf{v}_k . We have seen in section C.1.1 that in such circumstances, after convergence, \mathbf{r}_k contains the resultant of the force imposed by the fluid on the boundary. Thus for large values of π , \mathbf{f}_k and \mathbf{v}_k become proportional to the contact force in the area of the node.

Actually, by introducing a penalty equation for the nodal force and a constraint for the velocity, we introduce a sort of slip condition at the node. But we have not the assurance yet that the component of \mathbf{f}_k normal to the surface vanishes (and in fact the normal component does not vanish). In order to compensate that component, we had a new unknown f_k^n to the problem. This unknown is the Lagrange multiplier of the constraint on the normal component to the surface.

C.1.3 Implementation of the line dynamic condition

For the implementation of the line dynamic condition, we use the method derived of what is presented in section C.1.2. Along the walls, Dirichlet Boundary conditions of the type $\mathbf{v} = \mathbf{0}$ are imposed with a BEVAXS card. Along the contact line, we integrate the equation $\pi \mathbf{f}_l = \mathbf{0}$, where \mathbf{f}_l is the field in which we try to recover the contact force between the fluids and the wall.

We want this contact force to be tangent to the cylindrical surface. Thus we want to compensate the radial component of \mathbf{f}_l by applying a lineic radial force f_r on the contact line. This radial force is the Lagrange multiplier of the constraint on the radial component of \mathbf{f}_l . Thus the equations added to the system are

$$\begin{aligned} \pi \mathbf{f}_l + f_r &= \mathbf{0}, \\ \mathbf{f} \cdot \mathbf{r}(x, y) &= 0. \end{aligned}$$

The first part of the equation is vectorial. The second part is a scalar constraint.

The vector \mathbf{r} is a radial unit vector defined as

$$\mathbf{r}(x, y) = \frac{(x, y, 0)^T}{x^2 + y^2}.$$

Thus we take the cylindrical form of the die into account for the mathematical formulation. In our problem, no variable corresponds to field $\mathbf{r}(x, y)$. The constraint on \mathbf{f}_l is directly expressed as a function of the coordinates x and y .

Now we add the constraint $\mathbf{v}_l = \mathbf{f}_l$ along the contact line with a CTRRHS card. The constraint is such that a linear combination is done with the previous constraints on the velocity field (i.e. $\mathbf{v} = \mathbf{0}$ with the BEVAXS card). The new constraint added to the velocity unknowns is such that it is added to the old constraint $\mathbf{v} = \mathbf{0}$. Thus we have $\mathbf{v}_l = \mathbf{0}$ for all nodes of the walls that are not on the contact line, and $\mathbf{v}_l = \mathbf{f}_l$ for all nodes pertaining to the contact line.

After convergence of the Newton-Raphson iterations, the field $\mathbf{v}_l = \mathbf{f}_l$ is proportional to the tangential component of the contact force along the wall, but very small. Actually, we have introduced a sort of slip along the walls, but only on the contact line.

Nothing more has to be done to obtain the motion of the contact line for the line kinematic condition is defined on the whole interface, and the contact lines belongs to this interface.

Some additional comments

Normally, it would have been possible to express the constraint with a vector \mathbf{n} normal to the wall, and it may be a good method to use for a complex geometry. But two problems have to be solved in order to use the normal vector instead of the radial one:

1. The normal vector has to be calculated on a surface, thus on the wall. That means that an additional field has to be defined on the boundary corresponding to the walls in the area of the contact line, and a problem must be solved to calculate the normal in that area. This results in an increase of the computational cost.
2. The calculation of the normal is very sensitive to the motion of the mesh when this mesh is too coarse. The computational cost of our calculations is very high, and the use of a refined mesh involves a prohibitive cost.

As a conclusion, we can say that the use of the radial vector is easy to implement, cheap, and well adapted to our peculiar problem. For complicated geometries, an additional description of the dependence of the normal on the coordinates should be given in one or other way.

Appendix D

More information on molecular effects

D.1 Fit with the sum of two exponentials

We try to fit the relaxation curve corresponding to $t_{\text{stop}} = 1.2350$ s in figure 5.5 by a least square method. The fit function is

$$f(t) = A \exp(-t/a) + B \exp(-t/b).$$

We use a reinterpolation technique to calculate the value of the tension σ_{zz} every $\Delta t_{\text{sampling}}$ seconds. For our calculations, we consider that the force is measured every 0.01 s. The relaxation curve is fitted between $t_{\text{stop}} + \Delta t_{\text{stop}}$ and $t_{\text{end}} = 2$ s. We try to find A , a , B and b that minimize the residue

$$R(A, a, B, b) = \sum_{i=1}^n \left\{ \log(A \exp(-t_i/a) + B \exp(-t_i/b)) - \log(\sigma_{zz}^i(t_i)) \right\}^2,$$

in which n is the number of data points.

To minimize $R(A, a, B, b)$, we must solve a nonlinear system of equations, A , a , B and b being the unknowns. The system is solved with a Newton-Raphson algorithm.

D.2 Identification of a viscous stress

What we try to do here, is to “simulate” the identification of the viscous and elastic parts of the tensile stress with the method of Orr and Sridhar. For each simulation, we select an initial value of the solution on the extension curve in figure 5.5. Then, we calculate the relaxation of the tension by a numerical integration of the constitutive equations. During the relaxation, the stretch rate as a function of time is given by (5.4).

The time integration is done until $t_{\text{end}} = t_{\text{stop}} + \Delta t_{\text{stab}}$, in which Δt_{stab} is the interval of time necessary to obtain a fit function f close to the data points. (In most calculations, we use $\Delta t_{\text{stab}} = 0.15$ s). We assume that for t between $t_{\text{stop}} + \Delta t_{\text{stop}}$ and $t_{\text{stop}} + \Delta t_{\text{stab}}$, the stress decreases exponentially. We use this assumption to reinterpolate the stress back from $t = t_{\text{stop}} + \Delta t_{\text{stab}}$ to $t = t_{\text{stop}} + \Delta t_{\text{stop}}$. The value obtained by this calculation is assumed to be the elastic portion of the stress $\sigma_{zz}^{\text{elast}}(t_{\text{stop}})$. The viscous part of the tensile stress is then given by $\sigma_{zz}^{\text{visc}}(t_{\text{stop}}) = \sigma_{zz}(t_{\text{stop}}) - \sigma_{zz}^{\text{elast}}(t_{\text{stop}})$.

The method we use to determine $\sigma_{zz}^{\text{elast}}$ and $\sigma_{zz}^{\text{visc}}$ only approximates the method of Orr and Sridhar. However, it is a sufficiently good approximation for our purpose.

D.2.1 Transient viscous and elastic stresses

We can use the procedure described above to estimate the viscous and elastic contributions to the tensile stress during the stretching. We present the results obtained for fluid “B” at stretch rates $\dot{\epsilon} = 2.1 \text{ s}^{-1}$ and $\dot{\epsilon} = 3.0 \text{ s}^{-1}$ respectively in figures D.1 and D.2.

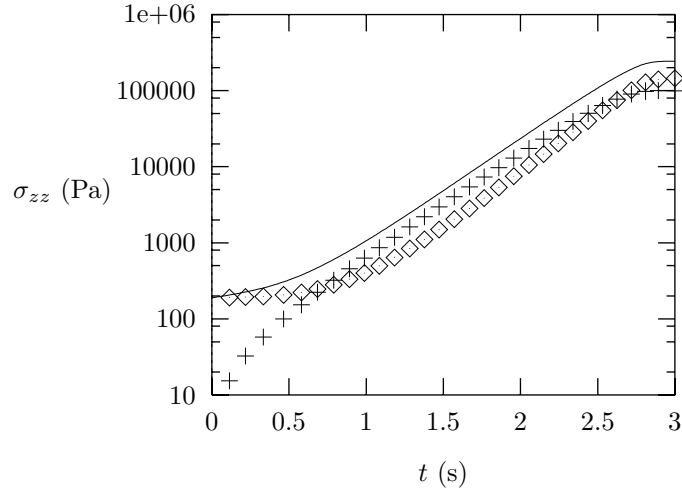


Figure D.1: *Separation between the elastic and viscous contributions to the tensile stress in the filament. The fluid “B” is used for the calculation and the strain rate is $\dot{\epsilon} = 2.1 \text{ s}^{-1}$. To estimate the elastic contribution, we use the linear reinterpolation with $\Delta t_{\text{stop}} = 0.05 \text{ s}$ and $\Delta t_{\text{stab}} = 0.15 \text{ s}$.*

For small values of the deformation, the tensile stress is dominated by the solvent contribution. For Hencky strains larger than 1.5 the elastic and viscous parts of the polymer contribution dominate. Close to the horizontal plateau, the viscous polymer contribution becomes larger than the elastic polymer part of the tensile stress. The comparison of figures D.1 and D.2 also shows that the viscous polymer part increases with the strain rate, while the elastic part does not seem to depend on $\dot{\epsilon}$.

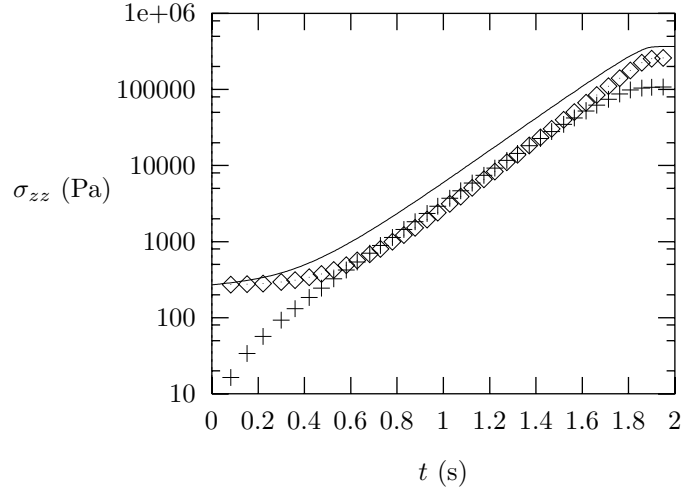


Figure D.2: Separation between the elastic and viscous contributions to the tensile stress in the filament. The fluid “B” is used for the calculation and the strain rate is $\dot{\epsilon} = 3 \text{ s}^{-1}$. To estimate the elastic contribution, we use the linear reinterpolation with $\Delta t_{\text{stop}} = 0.05 \text{ s}$ and $\Delta t_{\text{stab}} = 0.15 \text{ s}$.

Thos results are in qualitative agreement with the results of Orr and Sridhar.

D.3 Origin of the hysteretic behaviour

To better understand how dispersion can generate hysteresis, we first show that the combination of the FENE stress law and of a dispersion of the extension of the molecules leads to an increase of the mean value of the stress. To simplify the explanation, we make the following simplifications:

1. We assume that a simple relation exists between A_{zz} and σ_{zz} . Though we know that actually A_{xx} and A_{yy} also influence the value of the axial component of the stress, this assumption will not change the conclusions of our explanation.
2. We represent the dispersion of the extension of the molecules with a distribution function $W_A(A_{zz})$. This function is such that

$$\int_0^{\infty} W_A(A_{zz}) dA_{zz} = 1, \quad (\text{D.1})$$

and gives the probability to find an extension equal to A_{zz} .

With the simplifications presented here above, the relation between σ_{zz} and A_{zz} may be represented by a growing curve with concavity oriented towards the positive values of σ_{zz} (figure D.3). The A_{zz} distribution is represented on

the lower part of the same figure with a bell shaped function. Let us define the mean value of the extension of the molecules:

$$\langle A_{zz} \rangle \triangleq \int_0^\infty A_{zz} W_A(A_{zz}) dA_{zz}. \quad (\text{D.2})$$

Note that a tension distribution $W_\sigma(\sigma_{zz})$ similar to the extension distribution $W_A(A_{zz})$ may be defined. We also may calculate a mean value $\langle \sigma_{zz} \rangle$ of the tension with a formula similar to (D.2).

Besides the FENE stress-extension relation, we define an ‘‘affine’’ relation between stress and extension by

$$\sigma_{zz}^{\text{affine}}(A_{zz}) = \alpha A_{zz} + \beta, \quad (\text{D.3})$$

in which α and β are selected in such a way that the FENE and affine stress functions have identical value and derivative for $A_{zz} = \langle A_{zz} \rangle$ (figure D.3).

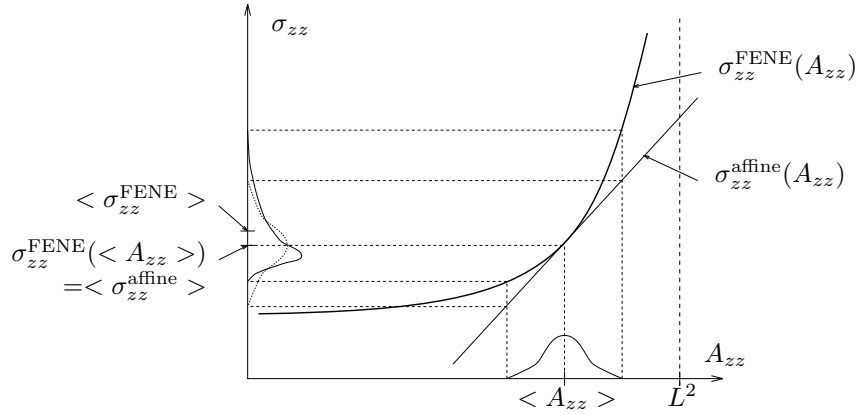


Figure D.3: Relations between the mean values of σ_{zz} and A_{zz} when a nonlinear model is used, and dispersion is present.

Now let us compare the tension distributions corresponding to $W_A(A_{zz})$ and obtained with the affine and FENE stress laws respectively:

- Because of the affine character of the stress law, the affine tension distribution $W_\sigma^{\text{affine}}(\sigma_{zz})$ simply is an affine transformation of the extension distribution. Consequently, the mean value of the affine tension is equal to the affine tension corresponding to the mean value of the extension: $\langle \sigma_{zz}^{\text{affine}} \rangle = \sigma_{zz}^{\text{affine}}(\langle A_{zz} \rangle)$; because of the peculiar way we construct the affine stress law, we also have $\langle \sigma_{zz}^{\text{affine}} \rangle = \sigma_{zz}^{\text{FENE}}(\langle A_{zz} \rangle)$.
- For the peculiar value of $\langle A_{zz} \rangle$, we have $\sigma_{zz}^{\text{affine}}(\langle A_{zz} \rangle) = \sigma_{zz}^{\text{FENE}}(\langle A_{zz} \rangle)$. But it easily can be seen on figure D.3, that for all other values of A_{zz} , the FENE stress law gives larger values of the tension than the

affine stress law. Consequently, the mean value $\langle \sigma_{zz}^{\text{FENE}} \rangle$ will be larger than $\langle \sigma_{zz}^{\text{affine}} \rangle$. Therefore, we always have the relation

$$\langle \sigma_{zz}^{\text{FENE}} \rangle \geq \sigma_{zz}^{\text{FENE}}(\langle A_{zz} \rangle). \quad (\text{D.4})$$

There is only one case for which we have equality: when all molecules have the same extension and the distribution reduces to a Dirac function.

Inequality (D.4) is a consequence of the dispersion of the A_{zz} distribution and of the fact that FENE stress law has a concavity oriented towards the positive values of σ_{zz} .

During the stretching, the dispersion of extension is important, and we have the relation

$$\langle \sigma_{zz} \rangle > \sigma_{zz}(\langle A_{zz} \rangle).$$

At the end of the stretching, (at least partial) saturation occurs, and the extension distribution gathers in a Dirac function. The distribution more or less keeps the shape of a Dirac function during relaxation. Thus for a given value of $\langle A_{zz} \rangle$, we have a larger value of the tension during extension than during relaxation. This explains the hysteretic behaviour and why it always turn clockwise.

Bibliography

- [AH94] J. Azaiez and G. M. Homsy. *Journal of Non-Newtonian Fluid Mechanics*, 54:333, 1994. [33](#)
- [APW90] N. R. Anturkar, T. C. Papanastasiou, and J. O. Wilkes. Linear Stability Analysis of Multilayer Plane Poiseuille Flow. *Phys. Fluids*, A2(4):530–541, 1990. [56](#)
- [BC94] C. Bodart and M. J. Crochet. The time-dependent flow of a viscoelastic fluid around a sphere. *Journal of Non-Newtonian Fluid Mechanics*, 54:303–329, 1994. [199](#)
- [BCAH87] R. B. Bird, C. F. Curtiss, R. C. Armstrong, and Ole Hassager. *Dynamics of Polymeric liquids*, volume 2 Kinetic Theory. John Wiley & Sons, 1987. [21](#), [175](#)
- [BCJ92] R. Bai, K. Chen, and D. D. Joseph. Lubricated Pipelining V: Stability of Core-Annular Flow. Experiments and comparison with theory. *J. Fluid Mech.*, ???:???, 1992. [81](#), [83](#), [86](#), [89](#)
- [BDJ80] R. B. Bird, P. J. Dotson, and N. L. Johnson. Polymer solution rheology based on a finitely extensible bead-spring chain model. *Journal of Non-Newtonian Fluid Mechanics*, 7:213–235, 1980. [33](#)
- [Ber91] D. Berghezan. *Simulation numérique d'écoulements en couches intervenant dans l'industrie photographique*. PhD thesis, Université Catholique de Louvain, 1991. [46](#)
- [BH82] A. N. Brooks and T. J. R. Hughes. Streamline Upwind/Petrov-Galerkin Formulations for Convection Dominated Flows with Particular Emphasis on the Incompressible Navier-Stokes Equations. *Computer Methods in Applied Mechanics and Engineering*, 32:199–259, 1982. [38](#)
- [BHAC77] R. B. Bird, O. Hassager, R. C. Armstrong, and C. F. Curtiss. *Dynamics of Polymeric liquids*, volume 2 Kinetic Theory. John Wiley & Sons, 1977. [21](#), [28](#), [29](#)

- [BM84] J. W. Barret and K. W. Morton. Approximate Symmetrization and Petrov-Galerkin Methods for Diffusion-Convection Problems. *Computer Methods in Applied Mechanics and Engineering*, 45:97–122, 1984.
- [BM92] P. A. M. Boomkamp and R. H. M. Miesen. Nonaxisymmetric waves in core-annular flow with a small viscosity ratio. *Phys. Fluids A*, 4(8):1627–1636, 1992.
- [Bod94] C. Bodart. *Écoulements Viscoélastiques transitoires et Sédimentation*. PhD thesis, Université Catholique de Louvain, décembre 1994. [21](#), [199](#), [201](#)
- [Bre74] F. Brezzi. On the existence, Uniqueness and Approximation of Saddle-point Problem Arising from Lagrange Multipliers. *Revue Française 'Automatique Inform. Rech. Opér., Série Rouge Anal. Numér.*, R-2:129–151, 1974. [35](#)
- [BS78] A. J. Baker and M. O. Soliman. Utility of a Finite Element Solution Algorithm for Initial-Value Problems. *Journal of Computational Physics*, 32:289–324, 1978.
- [CAD⁺95a] J. A. Covas, J. F. Agassant, A. C. Diogo, J. Vlachopoulos, and K. Walters, editors. *Rheological Fundamentals of Polymer Processing*, volume 302 of *NATO ASI Series*. Kluwer Academic Publishers, 1995. [21](#), [39](#)
- [CAD⁺95b] J. A. Covas, J. F. Agassant, A. C. Diogo, J. Vlachopoulos, and K. Walters, editors. *Rheological Fundamentals of Polymer Processing*, volume 302 of *NATO ASI Series*, pages 265–288. Kluwer Academic Publishers, 1995. [49](#), [50](#), [100](#), [102](#)
- [Cas96] B. Caswell. Report on the IXth International Workshop on Numerical Methods in Non-Newtonian Flows. *Journal of Non-Newtonian Fluid Mechanics*, 62:99–110, 1996. [147](#), [149](#)
- [CBJ90] K. Chen, R. Bai, and D. D. Joseph. Lubricated Pipelining III: Stability of Core-Annular Flow in Vertical Pipes. *J. Fluid Mech.*, 214:251–286, 1990. [81](#), [83](#), [86](#)
- [CGH61] M. E. Charles, G. W. Govier, and G. W. Hodgson. The Horizontal Pipeline Flow of Equal Density of Oil-Water Mixtures. *The Canadian Journal of Chemical Engineering*, 39:17–36, 1961. [81](#), [86](#), [87](#)
- [CGMZ76] I. Christie, D. F. Griffiths, A. R. Mitchell, and O. C. Zienkiewicz. Finite Element Methods for Second Order Differential Equations with Significant First Derivatives. *International Journal for Numerical Methods in Engineering*, 10:1389–1396, 1976.

- [CJ88] G. F. Carey and B. N. Jiang. Least-Squares Finite Elements for First-Order Hyperbolic Systems. *International Journal for Numerical Methods in Engineering*, 26:81–93, 1988.
- [CJ91a] K. Chen and D. D. Joseph. Long wave and lubrication theories for core-annular flows. *Phys. Fluids A*, 3(11):2672, 1991.
- [CJ91b] K. Chen and D. D. Joseph. Lubricated Pipelining IV: Stability of Core-Annular Flow: Guinzburg-Landau equations. *J. Fluid Mech.*, 227:587, 1991.
- [CK80] M. J. Crochet and R. Keunings. Die Swell of a Maxwell Fluid: Numerical Prediction. *Journal of Non-Newtonian Fluid Mechanics*, 7:199–212, 1980. [35](#)
- [CM79] M. J. P. Cullen and K. W. Morton. Analysis of Evolutionary Error in Finite Element and Other Methods. *Journal of Computational Physics*, 34:245–267, 1979.
- [Cou94] W. Couzy. Higher-order splitting methods for the discretized Navier-Stokes equations. *CESAME-UCL*, 1994.
- [CR88] M. D. Chilcott and J. N. Rallison. Creeping flow of dilute polymer solutions past cylinders and spheres. *Journal of Non-Newtonian Fluid Mechanics*, 29:381–432, 1988. [33](#), [151](#)
- [CTW93] E. O. A. Carew, P. Townsend, and M. F. Webster. A Taylor-Petrov-Galerkin Algorithm for Viscoelastic Flow. *Journal of Non-Newtonian Fluid Mechanics*, 50:253–287, 1993.
- [DADH97] B. Debbaut, T. Avalosse, J. Dooley, and K. Hughes. On the development of secondary motions in straight channels induced by the second normal stress difference: experiments and simulations. *Journal of Non Newtonian Fluid Mechanics*, 69:255–271, 1997. [139](#)
- [DC87] J. Dheur and M. J. Crochet. Newtonian stratified flow through an abrupt expansion. *Rheologica Acta*, 26:401–413, 1987. [118](#)
- [DC88] B. Debbaut and M. J. Crochet. Extensional effects in complex flows. *Journal of Non-Newtonian Fluid Mechanics*, 30:169–184, 1988. [147](#)
- [DG84] D. B. Duncan and D. F. Griffiths. The Study of a Petrov-Galerkin Method for First-Order Hyperbolic Equations. *Computer Methods in Applied Mechanics and Engineering*, 45:147–166, 1984.
- [DGL82] J. Donea, S. Giuliani, and H. Laval. Finite Element Solution of the Unsteady Navier-Stokes Equation by a Fractional Step Method. *Computer Methods in Applied Mechanics and Engineering*, 30:53–73, 1982.

- [DGLQ84] J. Donea, S. Giuliani, H. Laval, and L. Quartapelle. Time-Accurate Solution of Advection-Diffusion Problems by Finite Elements. *Computer Methods in Applied Mechanics and Engineering*, 45:123–145, 1984.
- [DQS87] J. Donea, L. Quartapelle, and V. Selmin. An analysis of Time Discretization in the Finite Element Solution of Hyperbolic Problems. *Journal of Computational Physics*, 70:463–499, 1987.
- [DS97] P. S. Doyle and E. S. G. Shaqfeh. Dynamic Simulation of Freely-Draining, Flexible Bead-Rod Chains: Start-up of Extensional and Shear Flow. *Submitted to the Journal of Non-Newtonian Fluid Mechanics*, June 1997. [147](#), [173](#), [184](#)
- [DSMS97] P. S. Doyle, E. S. G. Shaqfeh, G. H. McKinley, and S. H. Spiegelberg. Relaxation of Dilute Polymer Solutions Following Extensional Flow. *Submitted to the Journal of Non-Newtonian Fluid Mechanics*, June 1997. [147](#), [173](#), [184](#)
- [DW84] T. F. Dupont and L. B. Wahlbin. An Analysis of Dendy’s Piecewise Polynomial Petrov-Galerkin Method for a Hyperbolic Equation with Stagnation Points. *Computer Methods in Applied Mechanics and Engineering*, 45:165–175, 1984.
- [Eve73] A. E. Everage. Theory of Stratified Bicomponent Flow of Polymer Melts. I. Equilibrium Newtonian Tube Flow. *Transactions of the Society of Rheology*, 17:629–646, 1973. [99](#)
- [Eve75] A. E. Everage. Theory of Stratified Bicomponent Flow of Polymer Melts. II. Interface Motion in Transient Flows. *Transactions of the Society of Rheology*, 19:509–522, 1975. [49](#), [99](#), [100](#), [101](#)
- [FBL⁺87] A. L. Frenkel, A. J. Babchin, B. G. Levich, T. Shlang, and G. I. Sivashinsky. Annular flows can keep unstable films from breakup: nonlinear saturation of capillary instability. *J. Colloid. Interface Sci.*, 115:225–233, 1987.
- [For81] M. Fortin. Old and New Finite Elements for Incompressible Flows. *International Journal for Numerical Methods in Fluids*, 1:347–364, 1981. [38](#), [118](#)
- [GCLU84a] P. N. Gresho, S. T. Chan, R. L. Lee, and C. D. Upson. A Modified Finite Element Method for Solving the Time-Dependent Incompressible Navier-Stokes Equations. Part 1: Theory. *International Journal for Numerical Methods in Fluids*, 4:557–598, 1984.
- [GCLU84b] P. N. Gresho, S. T. Chan, R. L. Lee, and C. D. Upson. A Modified Finite Element Method for Solving the Time-Dependent Incompressible Navier-Stokes Equations. Part 2: Applications. *International Journal for Numerical Methods in Fluids*, 4:619–640, 1984.

- [GF95] R. Guénette and M. Fortin. A new mixed finite element method for computing viscoelastic flows. *Journal of Non-Newtonian Fluid Mechanics*, 60(1):27–52, 1995. [37](#)
- [GLS80] P. M. Gresho, R. L. Lee, and R. L. Sani. *Recent Advances in Numerical Methods in Fluids*, volume 1, chapter 2 On the Time dependent Solution of the Incompressible Navier-Stokes Equations in two or three Dimensions, pages 27–80. Pineridge, Swansea, 1980. [199](#)
- [GNOZ82] R. H. Gallagher, D. H. Norrie, J. T. Oden, and O. C. Zienkiewicz. *Finite Elements in Fluids*, volume 4. John Wiley and sons, 1982.
- [GS87] P. M. Gresho and R. L. Sani. On Pressure Boundary Conditions for the Incompressible Navier-Stokes Equations. *International Journal for Numerical Methods in Fluids*, 7:1111–1145, 1987.
- [Han73] Chang Dae Han. A Study of Bicomponent Coextrusion of Molten Polymers. *Journal of Applied Polymer Science*, 17:1289–1303, 1973. [99](#), [110](#), [111](#), [132](#), [138](#), [141](#), [143](#)
- [HB83] A. P. Hooper and W. G. C. Boyd. Shear-Flow Instability at the Interface Between two Viscous Fluids. *J. Fluid Mech.*, 128:507–528, 1983. [57](#), [84](#)
- [HB87] A. P. Hooper and W. G. C. Boyd. Shear-Flow Instability Due to a Wall and a Viscosity Discontinuity at the Interface. *J. Fluid Mech.*, 179:201–225, 1987. [53](#), [56](#), [57](#)
- [HG85] A. P. Hooper and R. Grimshaw. Nonlinear instability at the interface between two viscous fluids. *Phys. Fluids*, 28:37–45, 1985.
- [Hic71] C. E. Hickox. Instability Due to Viscosity and Density Stratification in Axisymmetric Pipe Flow. *Phys. Fluids*, 14:251–262, 1971. [84](#)
- [HJ90] H. H. Hu and D. D. Joseph. Lubricated Pipelining II: Stability of Core-Annular Flows. *J. Fluid Mech.*, 205:358–396, 1990.
- [HK76a] C. D. Han and Y. W. Kim. Further Observations of the Interface of Conjugate Fibers. *Journal of Applied Polymer Science*, 20:2609–2614, 1976. [102](#), [110](#)
- [HK76b] C. D. Han and Y. W. Kim. Use of the Coextrusion Technique for Producing Flame-Retardant and Antistatic Fibers. *Journal of Applied Polymer Science*, 20:2913–2918, 1976. [102](#)
- [HK81] J. P. Hufenus and D. Khaletzky. The Lagrangian Approach of Advective Term Treatment and its Application to the Solution of Navier-Stokes Equations. *International Journal for Numerical Methods in Fluids*, 1:365–387, 1981.

- [HLB79] T. J. R. Hughes, W. K. Liu, and A. Brooks. Finite Element Analysis of Incompressible Viscous Flows by the Penalty Function Formulation. *Journal of Computational Physics*, 30:1–60, 1979.
- [HLZ81] T. J. R. Hughes, W. K. Liu, and T. K. Zimmermann. Lagrangian-Eulerian Finite Element Formulation for Incompressible Viscous Flows. *Computer Methods in Applied Mechanics and Engineering*, 29:329–349, 1981.
- [HMM86] T. J. R. Hughes, M. Mallet, and A. Mizukami. A New Finite Element Formulation for Computational Fluid Dynamics: II. Beyond SUPG. *Computer Methods in Applied Mechanics and Engineering*, 54:341–355, 1986.
- [HMN70] D. Hasson, U. Mann, and A. Nir. Annular Flow of Two Immiscible Liquids I: Mechanisms. *The Canadian Journal of Chemical Engineering*, 48:514–520, 1970.
- [Hoo85] A. P. Hooper. Long-Wave Instability at the Interface Between Two Viscous Fluids: Thin Layer Effects. *Phys. Fluids*, 28(5):1613–1618, 1985. 56
- [Hoo89] A. P. Hooper. The stability of two superposed viscous fluids in a channel. *Phys. Fluids A*, 1(7):1133–1142, 1989. 56
- [HPP86] I. I. Hesla, F. R. Pranckh, and L. Preziosi. Squire’s Theorem for two Stratified Fluids. *Phys. Fluids*, 29(9):2808–2811, 1986.
- [HPT79] T. J. R. Hughes, K. S. Pister, and R. L. Taylor. Implicit-Explicit Finite Elements in Nonlinear Transient Analysis. *Computer Methods in Applied Mechanics and Engineering*, 17/18:159–182, 1979.
- [HTJTW90] D. M. Hawken, H. R. Tamaddon-Jahromi, P. Townsend, and M. F. Webster. A Taylor-Galerkin-Based Algorithm for Viscous Incompressible Flow. *International Journal for Numerical Methods in Fluids*, 10:327–351, 1990.
- [Hug78] T. J. R. Hughes. A Simple Scheme for Developing ‘Upwind’ Finite Elements. *International Journal for Numerical Methods in Engineering*, 12:1359–1365, 1978.
- [Hug87] T. J. R. Hughes. Recent Progress in the Development and Understanding of SUPG Methods with Special Reference to the Compressible Euler and Navier-Stokes Equations. *International Journal for Numerical Methods in Fluids*, 7:1261–1275, 1987.
- [JC88] B. N. Jiang and G. F. Carey. A Stable Least-Squares Finite Element Method for Non-Linear Hyperbolic Problems. *International Journal for Numerical Methods in Fluids*, 8:933–942, 1988.

- [JNP84] C. Johnson, U. Nävert, and J. Pitkäranta. Finite Element Methods for Linear Hyperbolic Problems. *Computer Methods in Applied Mechanics and Engineering*, 45:285–312, 1984.
- [JR93a] D. D. Joseph and Y. Y. Renardy. *Fundamentals of Two Fluids Dynamics. Part I: Mathematical Theory and Applications*. Springer-Verlag, 1993. 49, 55
- [JR93b] D. D. Joseph and Y. Y. Renardy. *Fundamentals of Two Fluids Dynamics. Part II: Lubricated Pipelining and Immiscible Liquids*. Springer-Verlag, 1993. 49, 81, 83, 86, 89
- [JRR84] D. D. Joseph, M. Renardy, and Y. Renardy. Instabilities of the Flow of two Immiscible Liquids with Different Viscosities in a Pipe. *J. Fluid Mech.*, 141:309–317, 1984. 84
- [Keu86] R. Keunings. An algorithm for the simulation of transient viscoelastic flows with free surfaces. *Journal of Computational Physics*, 62:199–220, 1986. 43, 46
- [Keu89] R. Keunings. Simulation of viscoelastic fluid flow. In C.L. Tucker III, editor, *Fundamentals of Computer Modeling for Polymer Processing*, pages 403–470. Carl Hanser Verlag, 1989. 36
- [KH76] A. A. Khan and C. D. Han. On the Interface Deformation in the Stratified Two-Phase Flow of Viscoelastic Fluids. *Transactions of the Society of Rheology*, 20:595–621, 1976. 100, 102
- [Kho90a] B. Khomami. Interfacial Stability and Deformation of Two Stratified Power Law Fluids in Plane Poiseuille Flow. Part I. Stability Analysis. *Journal of Non-Newtonian Fluid Mechanics*, 36:289–303, 1990.
- [Kho90b] B. Khomami. Interfacial Stability and Deformation of Two Stratified Power Law Fluids in Plane Poiseuille Flow. Part II. Interface Deformation. *Journal of Non-Newtonian Fluid Mechanics*, 37:19–36, 1990.
- [KHV90] A. Karagiannis, A. N. Hrymak, and J. Vlachopoulos. Three dimensional studies on bicomponent extrusion. *Rheologica Acta*, 29:71–87, 1990. 100, 101, 102, 123
- [Kra44] H. A. Kramers. *Physica*, 11:1, 1944. 31
- [KT77] M. Kawahara and N. Takeuchi. Mixed Finite Element Method for Analysis of Viscoelastic Fluid Flow. *Computers and Fluids*, 5:33–45, 1977. 35
- [L89] R. Löhner. Adaptative Remeshing for Transient Problems. *Computer Methods in Applied Mechanics and Engineering*, 75:195–214, 1989.

- [Lar88] R. G. Larson. *Constitutive Equations for Polymer Melts and Solutions*. Butterworths:Boston, 1988. 21, 28
- [Leg92] V. Legat. *Méthodes d'éléments finis pour le calcul d'écoulements tridimensionnels à surfaces libres*. PhD thesis, 1992. ix, 21, 43, 198, 212
- [LHJ⁺97] G. Lielens, P. Halin, I. Jaumain, R. Keunings, and V. Legat. New closure approximations for the kinetic theory of finitely extensible dumbbells,. *J. Non-Newtonian Fluid Mech.*, in press 1997. 147, 187, 189, 191, 193
- [LKLon] G. Lielens, R. Keunings, and V. Legat. Evaluation of the FENE-L model in three-dimensional flow fields,. in preparation. 147, 189, 191
- [LMZ84] R. Löhner, K. Morgan, and O. C. Zienkiewicz. The Solution of Non-Linear Hyperbolic Equation Systems by the Finite Element Method. *International Journal for Numerical Methods in Fluids*, 4:1043–1063, 1984.
- [LQ91] H. Laval and L. Quartapelle. A Fractional-Step Taylor-Galerkin Method for Unsteady Incompressible Flows. *International Journal for Numerical Methods in Fluids*, 11:501–513, 1991.
- [LW74] B. L. Lee and J. L. White. An experimental Study of Rheological Properties of Polymer Melts in Laminar Shear Flow and of Interface Deformation and Its Mechanisms in Two-Phase Stratified Flow. *Transactions of the Society of Rheology*, 18:467–492, 1974. 99, 102
- [Mac94] C. W. Macosko. *Rheology: Principles, Measurements and Applications*. VCH Publishers, 1994. 21, 25
- [MBD⁺92] R. Miesen, G. Beijnon, P. E. M. Duijvestijn, R. V. A. Olie-mans, and T. Verheggen. Interfacial waves in core-annular flow. *J. Fluid Mech.*, 238:97–117, 1992. 81
- [MC86] J. M. Marchal and M. J. Crochet. Hermitian Finite Element for Calculating Viscoelastic Flow. *Journal of Non-Newtonian Fluid Mechanics*, 20:187–207, 1986. 36
- [MC87] J. M. Marchal and M. J. Crochet. A new mixed finite element for calculating viscoelastic flow. *Journal of Non-Newtonian Fluid Mechanics*, 26:77–114, 1987. 36, 147
- [McK95] G. H. McKinley. Steady and transient motion of a sphere sedimenting through shear-thinning and constant-viscosity elastic fluids. *BSR Annual Award Lecture, IXth International Workshop on Numerical Methods in Non-Newtonian Flows*, 1995. 149, 153, 154, 166

- [Miz94] A. Mizukami. Element by element penalty/Uzawa formulation for large scale flow problems. *Computer Methods in Applied Mechanics and Engineering*, 112:283–289, 1994.
- [Mor85] K. W. Morton. Generalised Galerkin Methods for Hyperbolic Problems. *Computer Methods in Applied Mechanics and Engineering*, 52:847–871, 1985.
- [MP80] K. W. Morton and A. K. Parrot. Generalised Galerkin Methods for First-Order Hyperbolic Equations. *Journal of Computational Physics*, 36:249–270, 1980.
- [Old50] J. G. Oldroyd. *Proceedings of the Royal Society*, A200:523, 1950. [25](#)
- [OS94] Y. W. Ooi and T. Sridhar. Extensional rheometry of fluid S1. *Journal of Non-Newtonian Fluid Mechanics*, 52:153–162, 1994. [147](#), [180](#)
- [OS96] N. V. Orr and T. Sridhar. Stress relaxation in uniaxial extension. *Journal of Non-Newtonian Fluid Mechanics*, 67:77–103, 1996. [147](#), [173](#), [178](#), [179](#), [180](#)
- [P. 62] P. D. Lax and B. Wendroff. On the stability of difference schemes. *Communication in Pure Applied Mathematics*, 15:363, 1962.
- [PCa] B. Purnode and M. J. Crochet. Flows of polymer solution through contractions, part I: Flows of polyacrylamide solutions through planar contractions. *to be published in Journal of Non-Newtonian Fluid Mechanics*. [191](#)
- [PCb] B. Purnode and M. J. Crochet. Flows of polymer solution through contractions, part II: Flows of fluid M1 through axisymmetric contractions. *to be published in Journal of Non-Newtonian Fluid Mechanics*. [147](#), [191](#)
- [PCc] B. Purnode and M. J. Crochet. Polymer solution characterization with the FENE-P model. *to be published in Journal of Non-Newtonian Fluid Mechanics*. [147](#)
- [PCJ89] L. Preziosi, K. Chen, and D. D. Joseph. Lubricated pipelining I: stability of core-annular flow. *J. Fluid Mech.*, 201:323–356, 1989. [82](#), [83](#), [85](#), [86](#), [87](#), [88](#)
- [Pea85] A. J. Pearlstein. On the Two-Dimensionality of the Critical Disturbances for Stratified Viscous Plane Parallel Shear Flows. *Phys. Fluids*, 28:751, 1985.
- [Per93] J. B. Perot. An analysis of the Fractional Step Method. *Journal of Computational Physics*, 108:51–58, 1993.

- [Pet66] A. Peterlin. *Journal of Polymer Science, Polymer Letters*, 4B:287, 1966. [32](#)
- [PMR90] D. T. Papageorgiou, C. Maldarelli, and D. S. Rumschitzki. Non-linear interfacial stability of core annular film-flows. *Phys. Fluids*, A2:340–352, 1990.
- [PN95] J. Petera and V. Nassehi. Use of the finite element modelling for the improvement of viscometry results obtained by cone-and-plate rheometers. *Journal of Non-Newtonian Fluid Mechanics*, 58:1–24, 1995. [147](#)
- [Pur96] B. Purnode. *Vortices and Change of Type in Contraction Flows of Viscoelastic Fluids*. PhD thesis, Université Catholique de Louvain, february 1996. [21](#), [29](#)
- [Ray79] Lord Rayleigh. On the instability of jets. *Proc. Roy. London. Math. Soc.*, 10:4, 1879.
- [RBA90] D. Rajagopalan, R.A. Brown, and R.C. Armstrong. Finite element methods for calculations of steady viscoelastic flow using constitutive equations with a Newtonian viscosity. *Journal of Non-Newtonian Fluid Mechanics*, 36:159–192, 1990. [37](#)
- [Ren88] Y. Renardy. Stability of the Interface in Two-Layer Couette Flow of Upper Convected Maxwell Liquids. *Journal of Non-Newtonian Fluid Mechanics*, 282:359–375, 1988.
- [Rou53] P. E. Rouse. *Journal of Chemical Physics*, 21:1272, 1953. [29](#), [175](#)
- [RS85] J. G. Rice and R. J. Schnipke. A Monotone Streamline Upwind Finite Element Method for Convection-Dominated Flows. *Computer Methods in Applied Mechanics and Engineering*, 48:313–327, 1985.
- [Rus80] K. J. Ruschak. A method for incorporating free boundaries with surface tension in finite element fluid flow simulators. *International Journal for Numerical Methods in Engineering*, 15:639–648, 1980. [43](#)
- [SAM96] S. H. Spiegelberg, D. C. Ables, and G. H. McKinley. The role of end effects on measurements of extensional viscosity in filament stretching rheometers. *Journal of Non-Newtonian Fluid Mechanics*, 64:229–267, 1996. [147](#), [149](#), [150](#), [158](#), [163](#), [164](#), [166](#)
- [SB73] J. H. Southern and R. L. Ballman. Stratified Bicomponent Flow of Polymer Melts in Tube. *Applied Polymer Science*, 20:175–189, 1973. [49](#), [99](#)

- [SB75] J. H. Southern and R. L. Ballman. Additional Observations on Stratified Bicomponent Flow of Polymer Melts in Tube. *Journal of Polymer Science*, 13:863–869, 1975. [49](#), [99](#)
- [SDK91] R. W. G. Shipman, M. M. Denn, and R. Keunings. Mechanics of the “falling plate extensional” rheometer. *Journal of Non-Newtonian Fluid Mechanics*, 40:281–288, 1991. [147](#)
- [SDQ85] V. Selmin, J. Donea, and L. Quartapelle. Finite Element Methods for Nonlinear Advection. *Computer Methods in Applied Mechanics and Engineering*, 52:817–845, 1985.
- [SK92] Y.-Y. Su and B. Khomami. Interfacial Stability of Multilayer Viscoelastic Fluids in Slit and Converging Channel Die Geometries. *Journal of Rheology*, 36(2):357–387, 1992. [49](#)
- [SL97] R. Sizaire and V. Legat. Finite element simulation of a filament stretching rheometer. *Journal of Non-Newtonian Fluid Mechanics*, 71:89–107, 1997. [149](#)
- [SL98] R. Sizaire and V. Legat. Calculation of 3D encapsulation flows with the finite element method. *in preparation*, 1998. [99](#)
- [SLJ+98] R. Sizaire, G. Lielens, I. Jaumain, R. Keunings, and V. Legat. Influence of non-linearity and dispersity on the behaviour of viscoelastic fluids in rheometrical extensional flows. *in preparation*, 1998. [174](#), [188](#), [189](#), [190](#)
- [SM96a] M. J. Solomon and S. J. Muller. The transient extensional behavior of polystyrene-based Boger fluids of varying solvent quality and molecular weight. *Journal of Rheology*, 40:837–856, 1996. [147](#), [149](#), [163](#), [164](#), [166](#)
- [SM96b] S. H. Spiegelberg and G. H. McKinley. Stress relaxation and elastic decohesion of viscoelastic polymer solutions in extensional flows. *Journal of Non-Newtonian Fluid Mechanics*, 67:49–76, 1996. [156](#)
- [SPTT96] J. Sun, N. Phan-Thien, and R.I. Tanner. An adaptive viscoelastic stress splitting scheme and its applications: AVSS/SI and AVSS/SUPG. *Journal of Non-Newtonian Fluid Mechanics*, 65:75–91, 1996. [37](#)
- [Squ33] H. B. Squire. On the Stability of Three Dimensional Disturbances for Stratified Viscous Flow Between Parallel Walls. *Proc. Roy. Soc.*, A142:621, 1933.
- [SS80] W. J. Silliman and L. E. Scriven. Separating Flow Near a Static Contact Line: Slip at a Wall and Shape of a Free Surface. *Journal of Computational Physics*, 34:287–313, 1980. [118](#), [119](#)

- [SSBF85] T. Shlang, G. I. Sivashinsky, A. J. Babchin, and A. L. Frenkel. Irregular wavy flow due to viscosity stratification. *J. Phys. Paris*, 46:863–866, 1985.
- [THV⁺93] A. Torres, A. N. Hrymak, J. Vlachopoulos, J. Dooley, and B. T. Hilton. Boundary conditions for contact lines in coextrusion flows. *Rheologica Acta*, 32:513–525, 1993. [50](#), [118](#), [119](#)
- [TJTW92] H. R. Tamaddon-Jahromi, P. Townsend, and M. F. Webster. Numerical Solution of Unsteady Viscous Flows. *Computer Methods in Applied Mechanics and Engineering*, 95:301–315, 1992.
- [TN65] C. Truesdell and W. Noll. *The Non-Linear Field Theories of Mechanics*. Springer-Verlag, 1965. [25](#)
- [Tro06] F. T. Trouton. *Proceedings of the Royal Society*, A77:426, 1906. [25](#)
- [TS93] V. Tirtaatmadja and T. Sridhar. A filament stretching device for measurement of extensional viscosity. *Journal of Rheology*, 37:1081–1102, 1993. [147](#), [149](#)
- [TWM82] J. F. Thompson, Z. U. A. Warsi, and C. W. Mastion. Boundary-fitted coordinate systems for numerical solutions of partial differential equations - A review. *Journal of computational physics*, 47:1, 1982. [45](#)
- [TWM85] J. F. Thompson, Z. U. A. Warsi, and C. W. Mastion. *Numerical grid generation, foundations and applications*. North-Holland, 1985. [45](#)
- [Uwa95] T. Uwaji. Studies on wrap around phenomena of stratified two phase flow. Master’s thesis, Université Catholique de Louvain, October 1995. [99](#), [102](#), [123](#)
- [War96] V. Warichet. *hp-Adaptivity in Finite Element Methods for Viscoelastic Flow Simulation*. PhD thesis, Université Catholique de Louvain, Novembre 1996. [21](#)
- [WH74] R. F. Warming and B. J. Hyett. The Modified Equation approach to the Stability and Accuracy Analysis of Finite-Difference Methods. *Journal of Computational Physics*, 14:159–179, 1974.
- [Wil75] M. C. Williams. Migration of Two Liquid Phases in Capillary Extrusion: An Energy Interpretation. *A. I. Ch. E. Journal*, 21:1204–1207, 1975.
- [WJ87] W. T. Wong and C. C. Jeng. The Stability of Two Concentric Non-Newtonian Fluids in Circular Pipe Flow. *Journal of Non-Newtonian Fluid Mechanics*, 22:359–380, 1987.

- [WK93a] G. M. Wilson and B. Khomami. An Experimental Investigation of Interfacial Instabilities in Multilayer Flow of Viscoelastic Fluids. II. Elastic and Nonlinear Effects in Incompatible Polymer Systems. *Journal of Rheology*, 37(2):315–339, 1993. 49, 143
- [WK93b] G. M. Wilson and B. Khomami. An Experimental Investigation of Interfacial Instabilities in Multilayer Flow of Viscoelastic Fluids. III. Compatible Polymer Systems. *Journal of Rheology*, 37(2):341–354, 1993. 49
- [WOB91] L. E. Wedgewood, D. N. Ostrov, and R. B. Bird. A finitely extensible bead-spring chain model for dilute polymer solutions. *Journal of Non-Newtonian Fluid Mechanics*, 40:119–139, 1991. 173, 176
- [WUDP72] J. L. White, R. C. Ufford, K. R. Dharod, and R. L. Price. Experimental and Theoretical Study of the Extrusion of Two-Phase Molten Polymer Systems. *Journal of Applied Polymer Science*, 16:1313–1330, 1972. 99, 100, 102, 103
- [YH86] C. C. Yu and J. C. Heinrich. Petrov-Galerkin Methods for the Time-Dependent Convective Transport Equation. *International Journal for Numerical Methods in Engineering*, 23:883–901, 1986.
- [YH87a] S. Yiantsios and B. G. Higgins. Analysis of Superposed Fluids by the Finite Element Method: Linear Stability and Flow Development. *International Journal for Numerical Methods in Fluids*, 7:247–261, 1987. 55, 56, 60, 61
- [YH87b] C. C. Yu and J. C. Heinrich. Petrov-Galerkin Method for Multidimensional, Time-Dependent Convective-Diffusion Equations. *International Journal for Numerical Methods in Engineering*, 24:2201–2215, 1987.
- [YH88a] S. G. Yiantsios and B. G. Higgins. . *Journal of Computational Physics*, 74:25, 1988. 55
- [YH88b] S. G. Yiantsios and B. G. Higgins. Linear Stability of Plane Poiseuille Flow of Two Superposed Fluids. *Phys. Fluids*, 31(11):3225–3238, 1988. 51, 52, 55, 56, 57, 58, 59, 208
- [Yih67] C.-S. Yih. Instability Due to Viscosity Stratification. *Journal of Fluid Mechanics*, 27(2):337–352, 1967. 51, 55, 56, 57
- [Zie77] O. C. Zienkiewicz. *The Finite Element Method*. McGRAW-HILL, 1977.
- [ZSP90] O. C. Zienkiewicz, J. Szmelter, and J. Peraire. Compressible and Incompressible Flow; an Algorithm for all Seasons. *Computer Methods in Applied Mechanics and Engineering*, 78:105–121, 1990.

- [ZT89] O. C. Zienkiewicz and R. L. Taylor. *The Finite Element Method*, volume 1 Basic Formulation and Linear Problems, chapter A8, pages 605–610. McGRAW-HILL, fourth edition, 1989.
- [ZT91a] O. C. Zienkiewicz and R. L. Taylor. *The Finite Element Method*, volume 2 Solid and Fluid Mechanics Dynamics and Non-linearity, chapter 12, pages 438–505. McGRAW-HILL, fourth edition, 1991.
- [ZT91b] O. C. Zienkiewicz and R. L. Taylor. *The Finite Element Method*, volume 2 Solid and Fluid Mechanics Dynamics and Non-linearity, chapter 13, pages 506–556. McGRAW-HILL, fourth edition, 1991.
- [ZVTN85] O. C. Zienkiewicz, J. P. Vilotte, S. Toyoshima, and S. Nakazawa. Iterative Method for Constrained and Mixed Approximation. An inexpensive Improvement of F.E.M. Performance. *Computer Methods in Applied Mechanics and Engineering*, 51:3–29, 1985.